

**The Effect of Oil on Foam for Enhanced Oil Recovery
Theory and Measurements**

Tang, Jinyu

DOI

[10.4233/uuid:49763197-fec0-49e6-a496-6ac0068585db](https://doi.org/10.4233/uuid:49763197-fec0-49e6-a496-6ac0068585db)

Publication date

2019

Document Version

Final published version

Citation (APA)

Tang, J. (2019). *The Effect of Oil on Foam for Enhanced Oil Recovery: Theory and Measurements*. [Dissertation (TU Delft), Delft University of Technology]. <https://doi.org/10.4233/uuid:49763197-fec0-49e6-a496-6ac0068585db>

Important note

To cite this publication, please use the final published version (if applicable).
Please check the document version above.

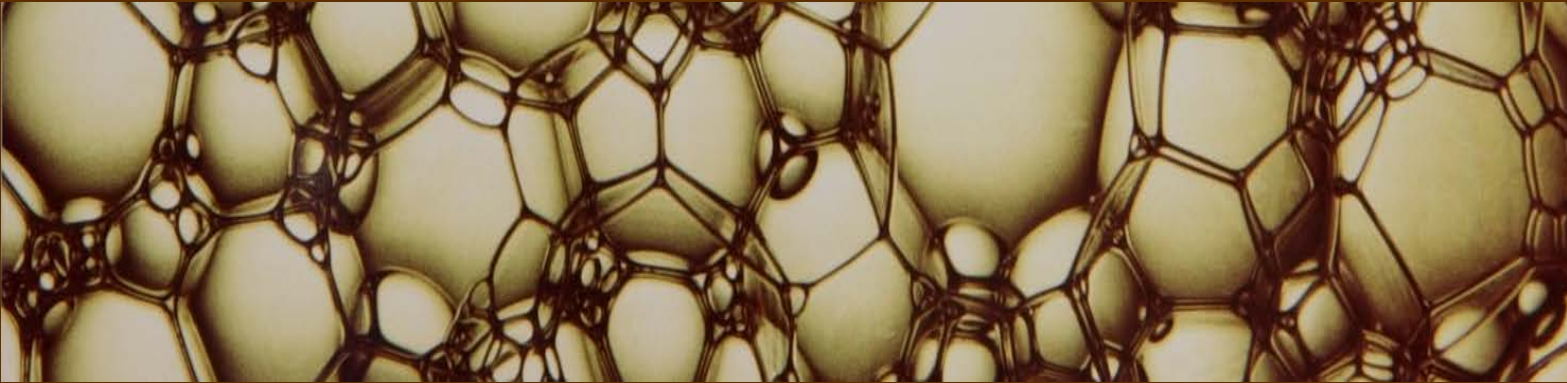
Copyright

Other than for strictly personal use, it is not permitted to download, forward or distribute the text or part of it, without the consent of the author(s) and/or copyright holder(s), unless the work is under an open content license such as Creative Commons.

Takedown policy

Please contact us and provide details if you believe this document breaches copyrights.
We will remove access to the work immediately and investigate your claim.

**THE EFFECT OF OIL ON FOAM FOR
ENHANCED OIL RECOVERY:
THEORY AND MEASUREMENTS**



Jinyu Tang



Challenge the Future

**THE EFFECT OF OIL ON FOAM FOR
ENHANCED OIL RECOVERY:
THEORY AND MEASUREMENTS**

THE EFFECT OF OIL ON FOAM FOR ENHANCED OIL RECOVERY: THEORY AND MEASUREMENTS

Proefschrift

ter verkrijging van de graad van doctor
aan de Technische Universiteit Delft,
op gezag van de Rector Magnificus Prof. dr. ir. T.H.J.J. van der Hagen,
voorzitter van het College voor Promoties,
in het openbaar te verdedigen op
maandag 17 juni 2019 om 10:00 uur

door

JINYU TANG

Master of Engineering in Oil and Gas Field Development Engineering
China University of Petroleum, China
Geboren te Shandong, China

Dit proefschrift is goedgekeurd door de promotoren:

Prof. dr. W. R. Rossen

Samenstelling promotiecommissie:

Rector Magnificus,	voorzitter
Prof. dr. W.R. Rossen,	Technische Universiteit Delft, promotor

Onafhankelijke leden:

Prof. dr. P.L.J. Zitha	Technische Universiteit Delft
Prof. dr. M. Bakker	Technische Universiteit Delft
Dr. D.V. Voskov	Technische Universiteit Delft
Prof. dr. P.R. King	Imperial College London, UK
Prof. dr. D. Marchesin	Overige leden, Instituto Nacional de Matemática Pura e Aplicada, Brazil
Dr. S. Vincent-Bonnieu	Overige leden, Shell Global Solutions International, the Netherlands

The work presented in this thesis was conducted in the Department of Geoscience and Engineering, Delft University of Technology, Delft, the Netherlands, and partly in the Instituto Nacional de Matemática Pura e Aplicada (IMPA), Rio de Janeiro, Brazil, hosted by Prof. Dan Marchesin. The research was funded by the Joint Industry Project (JIP) on Foam for Enhanced Oil Recovery at Delft University of Technology, and partly by China Scholarship Council (funding code: 201406450034), the Ministry of Education, China.

Key words: Enhanced oil recovery, Foam flow in porous media with oil, Coreflood study, Implicit-texture modeling, Fractional-flow theory, Capillary number for micromodels

Copyright © 2019 by Jinyu Tang (Jinyu.tang12@gmail.com)

All rights reserved. No part of the material protected by this copyright notice may be reproduced or utilized in any form or by any means, electronic or mechanical, including photocopying, recording or by any information storage and retrieval system, without written permission from the author.

Cover design by Xuhong Zhuang and Jinyu Tang

Printed by GILDEPRINT in the Netherlands

An electronic version of this dissertation is available at:

<http://repository.tudelft.nl>

ISBN: 978-94-6366-179-9

CONTENTS

CONTENTS	v
CHAPTER 1 INTRODUCTION	1
1.1 Gas injection EOR.....	1
1.2 Foam EOR.....	2
1.2.1 Foam definition.....	2
1.2.2 Mobility of phases with foam	3
1.2.3 Foam-flow regimes at steady state	4
1.2.4 Engineering applications.....	5
1.3 Research techniques for foam EOR.....	6
1.3.1 Measurements	6
1.3.2 Foam modeling	6
1.4 Current challenges in foam EOR.....	7
1.4.1 Issues in physical dynamics of foam EOR.....	7
1.4.2 Issues in foam-oil modeling	8
1.5 Research objectives	9
1.6 Thesis outline	10
CHAPTER 2 IMPLICIT-TEXTURE MODELING OF THE EFFECT OF OIL ON FOAM EOR	13
2.1 Introduction	14
2.2 Results and analysis.....	16
2.2.1 The oil effect represented in foam model – STARS	17
2.2.1.1 Oil effect predicted by wet-foam model	17
2.2.1.2 Oil effect predicted by dry-out model.....	21
2.2.1.3 Foam quality scan with varying ratios of U_o to U_w	21
2.2.2 Multiple steady states.....	21
2.2.2.1 Wet-foam model	21
2.2.2.2 Dry-out model.....	22
2.2.3 Simulation analysis of multiple steady states.....	24
2.2.3.1 Stability analysis	24
2.2.3.2 Third ∇p contour	28
2.2.3.3 Multiple steady states as folds in a surface.....	29
2.3 Discussion and remarks.....	31
2.4 Conclusions	32
2.5 Nomenclature	33
CHAPTER 3 STEADY-STATE FOAM-FLOW REGIMES WITH OIL IN POROUS MEDIA	35
3.1 Introduction	36
3.1.1 Foam models	37

CONTENTS

3.1.2	Experimental method	39
3.1.2.1	Experimental scheme	39
3.1.2.2	Apparatus and materials	41
3.2	Results	42
3.2.1	Oil screening	42
3.2.2	Two foam regimes with and without oil	43
3.2.2.1	LE foam flow without oil	43
3.2.2.2	LE foam flow with C ₁₆	44
3.2.2.3	LE foam flow with 10 wt% OA in model oil.....	45
3.2.2.4	LE foam flow with 20 wt% OA in model oil.....	46
3.2.3	Fit of model parameters to data.....	47
3.2.3.1	Model fit results	47
3.2.3.2	Attempt to fit oil-related parameters in the model.....	51
3.3	Discussion and remarks	52
3.4	Conclusions	53
3.5	Nomenclature	54
CHAPTER 4 FRACTIONAL-FLOW MODEL INSIGHTS INTO FOAM-OIL DISPLACEMENT		56
4.1	Introduction	57
4.2	Theoretical background and foam model	59
4.2.1	Three-phase fractional-flow theory.....	59
4.2.2	Foam model	62
4.3	Results and discussion.....	63
4.3.1	Structure of foam displacement with oil	64
4.3.1.1	Scenario 1 for J_{nf} displacing I_{nf}	64
4.3.1.2	Scenario 2 for J_{nf} displacing I_{fm}	66
4.3.1.3	Scenario 3 for J_{fm} displacing I_{fm}	67
4.3.1.4	Scenario 4 for J_{fm} displacing I_{nf}	68
4.3.2	Foam formulations with improved tolerance to oil	70
4.3.2.1	Scenario 3 with J_{fm} displacing I_{fm}	70
4.3.2.2	Scenario 4 with J_{fm} displacing I_{nf}	71
4.3.2.3	Numerical artifact in foam simulation with oil	73
4.3.3	Foam-bank propagation with oil	74
4.4	Conclusions	75
CHAPTER 5 FRACTIONAL-FLOW THEORY OF FOAM-OIL DISPLACEMENT WITH MULTIPLE STATES		77
5.1	Introduction	78
5.2	Theory and mathematical approach.....	81
5.2.1	Three-phase fractional-flow theory.....	81

CONTENTS

5.2.2	Wave-curve method	84
5.3	Foam model	86
5.3.1	Foam representation on ternary diagram	87
5.3.2	Multiple steady states in foam model	88
5.4	Displacing state among multiple steady states	89
5.4.1	Initial state outside foam region	91
5.4.2	Initial state inside foam region	94
5.4.3	Boundary curve for the dependence of the nature of the displacement on I	95
5.5	Discussion	97
5.5.1	Significance for field applications	97
5.5.2	Experimental verification of multiple steady states	97
5.6	Conclusions	98
CHAPTER 6 CT COREFLOOD STUDY OF TRANSIENT FOAM FLOW WITH OIL		99
6.1	Introduction	100
6.2	Experimental design	101
6.2.1	Materials and apparatus	101
6.2.1.1	Materials	101
6.2.1.2	CT coreflood apparatus	102
6.2.2	CT measurements	103
6.2.3	Experimental procedures	104
6.3	Results and discussion	106
6.3.1	Model oil – C ₁₆	106
6.3.1.1	In-situ-generated foam	106
6.3.1.2	Pre-generated foam	107
6.3.2	Model oil – mixture of 80wt% C ₁₆ and 20wt% OA	109
6.3.2.1	In-situ-generated foam	109
6.3.2.2	Pre-generated foam	111
6.3.3	Implications for foam EOR and modeling	113
6.3.3.1	Implications for applications of foam EOR	113
6.3.3.2	Implications for modeling of foam flow with oil	113
6.4	Conclusions	114
CHAPTER 7 NEW CAPILLARY NUMBER DEFINITION FOR MICROMODELS		116
7.1	Introduction	117
7.2	New capillary number definition	120
7.2.1	Derivation from a force balance	120
7.2.2	Comparison of the new and conventional N_{ca}	121
7.2.3	Calculation of parameters in the new N_{ca}	123
7.3	Test of the new N_{ca} definition	123

CONTENTS

7.4 Discussion	127
7.5 Conclusions	128
7.6 Nomenclature	129
CHAPTER 8 CONCLUSIONS AND RECOMMENDATIONS	131
8.1 Contributions of the study to foam EOR	131
8.2 Summary of conclusions	131
8.2.1 Implicit-texture modeling of the effect of oil on foam	132
8.2.2 Steady-state foam-flow regimes with oil	132
8.2.3 Fractional-flow model insights into transient foam flow with oil	133
8.2.4 Fractional-flow theory of foam-oil displacement with multiple states	133
8.2.5 CT coreflood study of transient foam flow with oil	134
8.2.6 New N_{ca} definition for micromodels	135
8.3 Recommendations for further research	135
8.3.1 Further research on implicit-texture foam modeling	135
8.3.2 Further research on foam dynamics with oil	136
BIBLIOGRAPHY	138
APPENDIX A IMPLICI-TEXTURE FOAM MODEL – STARS	151
APPENDIX B STEADY-STATE DATA ADAPTED FOR MODEL FIT	154
APPENDIX C FOAM-SIMULATION-PARAMETER FITTING METHOD	156
APPENDIX D FOAM MODEL FOR THEORETICAL ANALYSIS OF FOAM-OIL DISPLACEMENT	160
APPENDIX E FOAM MODEL FOR THEORETICAL ANALYSIS OF MULTIPLE STATES	163
APPENDIX F CT IMAGING OF THREE-PHASE SATURATIONS USING DUAL-ENERGY	166
APPENDIX G MICROFLUIDIC DEVICES IN THE LITERATURE	168
SCIENTIFIC CONTRIBUTIONS	169
ACKNOWLEDGEMENTS	171
SUMMARY	174
SAMENVATTING	178

INTRODUCTION

1.1 Gas injection EOR

According to *World Energy Outlook 2018* by the International Energy Agency, nearly 53.9% of world primary energy consumption in 2018 (**Fig. 1.1a**) was supplied by oil and gas. Green energies, e.g. bioenergy, hydro or other renewables, will experience an increasing demand, but cannot be an absolute alternative in the near future. Oil and gas demand is projected still to be 52.6% by 2040 (**Fig. 1.1b**). Nevertheless, the climate impact of fossil fuels and continuously increasing energy demand drive oil production in a more efficient and environmentally-friendly manner.

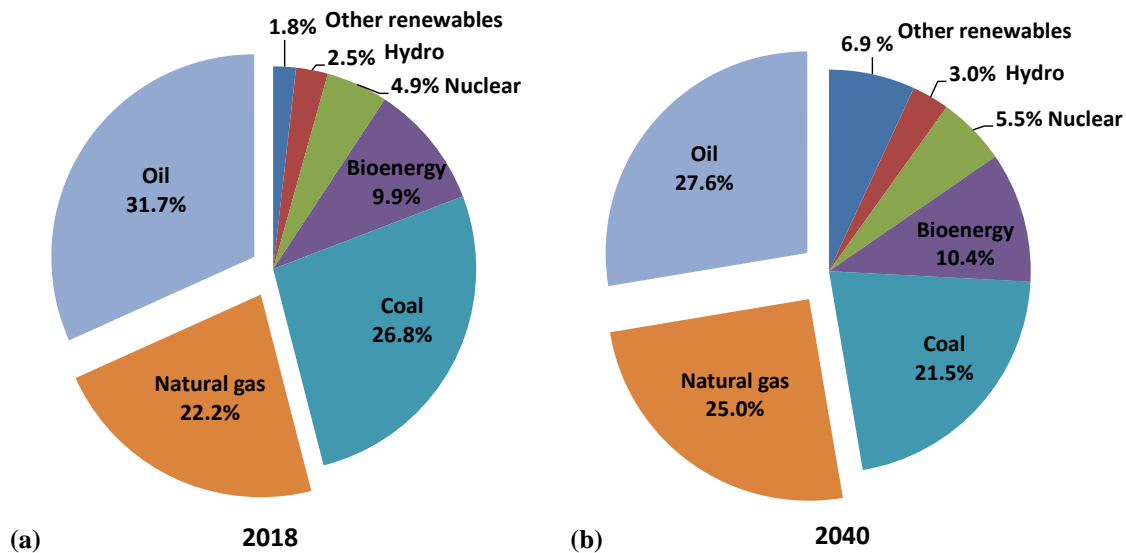


Figure 1.1 World primary energy consumption: (a) 2018, and (b) 2040 projections; statistical data and analysis from *World Energy Outlook* (2018) by the International Energy Agency.

The life cycle of oil recovery in a reservoir in general comprises three phases (Lake et al. 2014): primary recovery, secondary recovery and tertiary recovery. Primary recovery relies on natural drive mechanisms, e.g. expansion of solution gas, gravity drainage or rock compressibility (Green and Willhite, 1998; Lake et al., 2014). Secondary recovery mainly comes from water or gas injection intended to maintain reservoir pressure and displace oil. All subsequent techniques, e.g. thermal methods (Stahl, 1987), chemical flooding (Shah, 2012) or foam (Rossen, 1996), contribute to tertiary recovery. Enhanced oil recovery (EOR) is referred to as oil production by injection of external agents originally not belonging to a reservoir; this is tertiary recovery. Roughly 10% of OOIP (Oil Originally In Place) is produced during primary recovery. Waterfloods contribute a typical ultimate recovery of 25%. Nearly 65% of OOIP left in reservoirs needs to rest on EOR techniques; thus EOR is key to enhance oil production.

The U.S. Department of Energy (2016) reports that three categories of EOR techniques have been found to be commercially successful to varying degrees: thermal methods, gas injection and chemical injection. Among others, injection of gases (e.g. N₂, air, CO₂, steam or hydrocarbon gases) contributes significantly to the overall oil production during EOR processes (Oil and Gas Journal, 2010). Manrique et al. (2010) find, based on statistics of 1507 international field EOR projects shown in **Fig. 1.2**, that about 25% implement gas injection in either sandstone or carbonate reservoirs. Gas EOR is nowadays a mature technique and very efficient in displacing oil: nearly 100% in the oil zone where oil is swept by gas (Orr 2007). However, most gas-injection processes are subject to poor sweep efficiency, which arises mainly from three issues: gravity override caused by the density difference between gas and liquid phases; gas fingering due to viscosity instability; and gas channelling owing to geological heterogeneity. These three prominent issues in gas injection alone greatly limit its EOR potential.

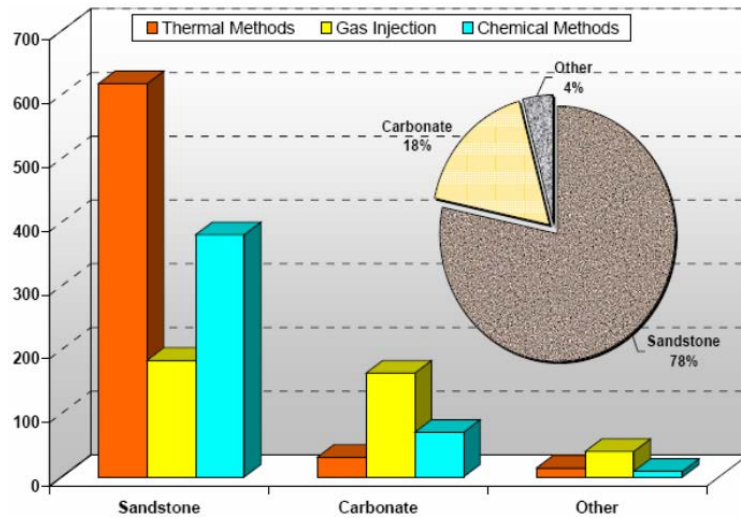


Figure 1.2 Statistics of EOR implementations in worldwide 1507 field projects; by Manrique et al. (2010).

To maximize the benefit of gas EOR, several technologies have been developed to improve the sweep efficiency of gas injection, e.g. supercritical CO₂ (Orr and Taber, 1984) and WAG (Water-Alternating-Gas), where water and gas are injected in alternating slugs (Christensen et al., 1998). These technologies mitigate partly one or two of the three issues in gas injection. Introduction of foam can address all the three issues simultaneously; it is thought to be a promising technology in assisting gas injection EOR (Rossen, 1996).

1.2 Foam EOR

1.2.1 Foam definition

Foam here is defined as a dispersion of gas in liquid, where gas bubbles are separated by interconnected thin aqueous films, called lamellae, stabilized by surfactants (Rossen 1996; Gauglitz et al. 2002). The properties of foam are characterized mainly through foam texture, bubble density (bubbles per unit volume), foam quality and foam stability (Schramm and Wassmuth 1994; Rossen 1996). Foam “quality” throughout our study refers to gas volumetric fractional flow in foam, i.e. $f_g = u_g / (u_g + u_w)$ where u_g and u_w are the Darcy’s velocity for gas and water phases. Higher foam quality means larger gas fractional flow. In steam foam it can mean the mass fraction of steam in foam (Hirasaki, 1989).

Generally, there are two categories of foams in the petroleum industry: bulk foam, of which the bubble size is much smaller than the diameter of a container, and foam in porous media, in which the individual bubble size is close to or greater than the size of a single pore where it resides (Rossen, 1996). This distinction gives special properties to foam in porous media, that are controlled by capillary processes (Alvarez et al., 2001). The study in this thesis concerns foam behavior in porous media.

1.2.2 Mobility of phases with foam

Foam in rock pore space is not a single phase, but a phenomenon that comprises two individual phases, i.e. aqueous and gaseous phases. Because of its unique microstructure (Weaire and Hutzler 2001), the formation of foam has a significant influence on the mobility of phases present and flowing through geological formations. In particular, compared with gas mobility without foam, the mobility of gas with foam is substantially reduced. In foam flow, the gas phase comprises flowing and trapped gas bubbles, as schematically illustrated in **Fig. 1.3** (Kovscek and Radke, 1993). The reduction in gas mobility by foam primarily results from two mechanisms (Tang and Kovscek, 2006; Rossen, 1996): a large increase in trapped residual-gas saturation, and a dramatic rise in flow resistance caused by capillary and dragging effects as gas bubbles mobilize through constricted pore throats and pore bodies.

The presence of foam also affects the mobility of liquid phases. With foam, the increase in the residual gas saturation reduces the pore space for the liquid phases (water and oil), and the enhanced resistance to gas flow causes the saturations of liquid phases to remain very low. However, a number of studies show that only the mobility function of the gas phase is altered by foam, but not those of the liquid phases (Bernard and Jacobs, 1965; Holm, 1968). This is widely accepted to be true and facilitates greatly the modeling of foam flow and transport (Rossen et al., 1999).

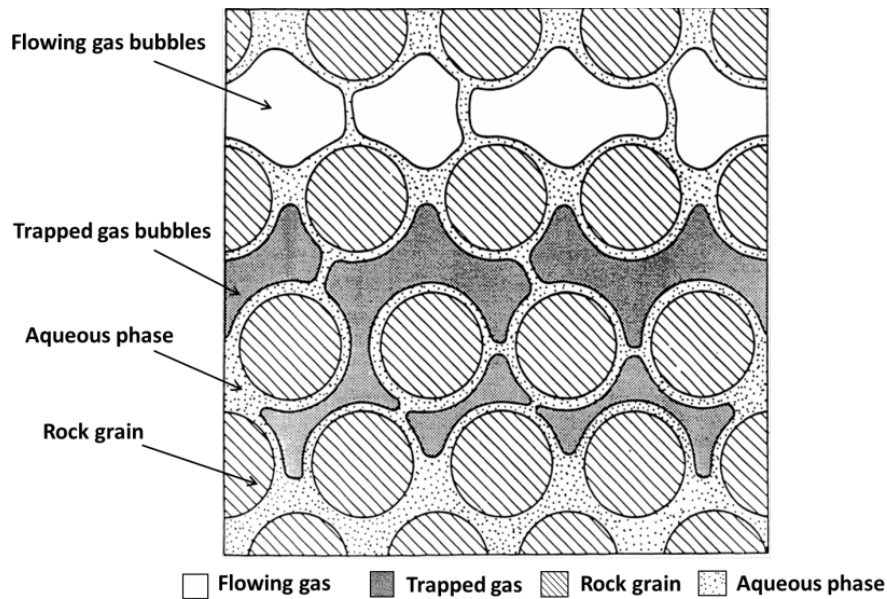


Figure 1.3 Schematic of phase distribution in foam flow through porous media (without oil); adapted from Kovscek and Radke (1993).

1.2.3 Foam-flow regimes at steady state

Foam flow through porous media, in the absence of oil, shows fundamentally two regimes depending on foam quality (Osterloh and Jante 1992): the high- and low-quality regimes. As illustrated in **Fig. 1.4a**, the high-quality regime, also called the “dry-out” or “coalescence” regime, is represented by the upper-left vertical contours, where pressure gradient is independent of gas superficial velocity. This regime is mainly dominated by foam stability, controlled by the limiting capillary pressure, which in turn corresponds to the limiting water saturation, the water saturation below which foam collapses abruptly (Alvarez et al., 2001). The low-quality regime, also called the “wet” regime, is denoted by the lower-right contours, where pressure gradient is largely independent of water superficial velocity. The low-quality regime is dominated by foam strength which is related to bubble size and density; this is reflected implicitly through foam apparent viscosity (i.e. the inverse of total relative mobility of phases). The two regimes usually feature a sharp transition from high to low foam qualities. In the high-quality regime, decreasing foam quality increases gas-mobility reduction, as seen from the increasing pressure gradient as one moves diagonally down and to the right in **Fig. 1.4a**. In the low-quality regime, decreasing foam quality reduces gas mobility reduction. The rheology of foam in each regime is not necessarily Newtonian (Tang et al., 2018). In most cases, the high-quality regime shows roughly Newtonian behavior and the low-quality regime exhibits shear-thinning behavior.

Another popular way to represent the two regimes is the single foam-quality scan plot at fixed total superficial velocities of water and gas, as shown in **Fig. 1.4b**. **Figure 1.4b** is a diagonal line cutting through **Fig. 1.4a** at a given total superficial velocity. The right side of **Fig. 1.4b**, starting from the lower-right corner until maximum pressure gradient, corresponds to the high-quality regime, and the left side of **Fig. 1.4b** marks the low-quality regime. The contour plot in **Fig. 1.4a** contains the most complete information regarding steady-state foam flow. The foam-quality scan plot in **Fig. 1.4b** requires fewer data points to be constructed, and is thus commonly used in studying steady-state foam behavior. These two regimes in **Figs. 1.4a** or **1.4b** are usually a starting point for the deeper exploration of foam behavior in geological formations.

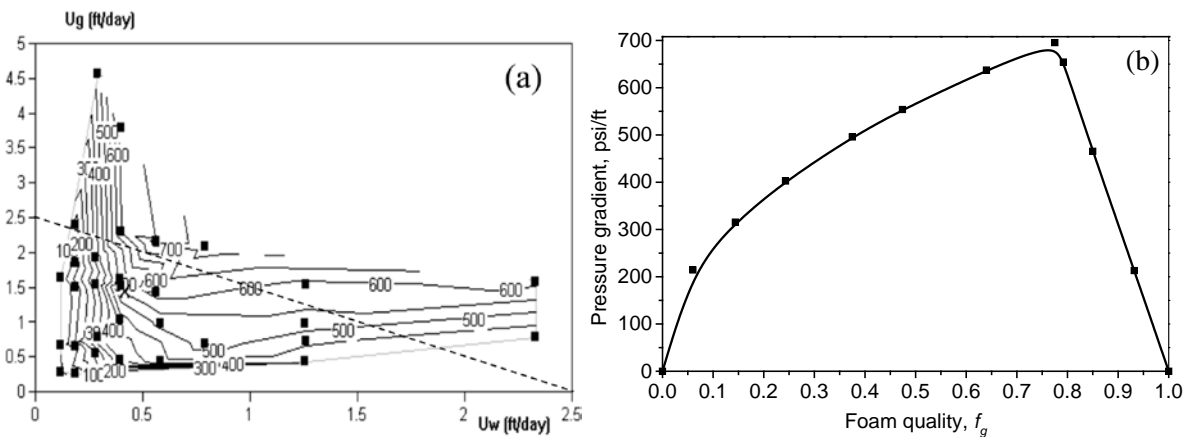


Figure 1.4 Steady-state foam-flow regimes in porous media (data from Alvarez et al. (2001) in Berea sandstone): (a) pressure gradient (psi/ft) as a function of water and gas superficial velocities (ft/day); each symbol represents a steady-state measurement at the given water and gas superficial velocities. (b) pressure gradient (psi/ft) with respect to a scan of foam quality at a fixed total superficial velocity of 2.5 ft/day.

1.2.4 Engineering applications

The effectiveness of foam in reducing gas mobility gives foam injection into geological formations broad engineering applications in a variety of fields. These applications include EOR in the oil industry (Lake et al. 2014), removal of DNAPL (Dense Non-aqueous Phase Liquid) contaminants in environmental remediation (Hirasaki et al., 1997), and more recently CCUS (Carbon Capture, Utilization and Storage) for mitigating the impact of CO₂ emission on global climate (Bui et al., 2018).

The purposes of applying foam for EOR primarily lie in conformance improvement in the near-well region or deep in a reservoir and gas-mobility control for oil displacement. In the former application, foam preferably flows into high-permeability zones and diverts subsequently injected agents into low-permeability regions. This application also includes acid diversion for near-well stimulation (Zhou and Rossen, 1994; Rossen and Wang, 1999). In the latter application, foam is used directly as a displacing agent that both improves gas-injection sweep efficiency and makes full use of efficient displacement by gas. In principle, oil reservoirs suitable for gas injection EOR are also applicable for implementation of foam, and various benefits of other EOR methods can all be seen in foam as well. A number of field pilots have been demonstrating that foam injection is a promising EOR technology (Patil et al., 2018; Carpenter, 2018; Alcorn et al., 2018).

Table 1.1 Current techniques for foam flow through porous media

Perspectives	Techniques		Remarks
Measurements	Bulk tests		Quick screening of foaming agents
	Pore scale	2D microfluidics	Showing pore-scale mechanisms
		3D micro-CT imaging	
	Core scale	Foam corefloods	Supporting validation of models and parameter fit for upscaling to field applications
CT coreflood imaging			
Modeling	Pore-scale models		Supporting data interpretation and project design
	Foam representation	Implicit-texture (IT) models	
		Population-balance (PB) models	
	Steady-state flow	Local-equilibrium IT modeling	
		Population balance modeling	
	Transient displacements	Numerical simulation	
Fractional-flow theory/ the MOC (Method of Characteristics)			
Pilots	Pilot-scale tests		Testing effectiveness prior to EOR implementations

1.3 Research techniques for foam EOR

Successful engineering applications of foam for EOR rest on comprehensive understanding of fundamentals of foam behavior in reservoirs. **Table 1.1** summarizes current techniques for understanding foam flow through porous media from two perspectives: measurements and modeling. The purpose and contribution of each technique is briefly reviewed as follows.

1.3.1 Measurements

Experimental techniques for foam EOR involve in general bulk tests, pore-scale imaging, coreflood study and field pilots, as listed in **Table 1.1**. Each technique offers crucial physical insights on foam behavior in porous media. Bulk tests (i.e., foam in columns or test tubes much larger than the bubbles) serve for a rough but quick evaluation of foam properties, in particular the influence of factors on foam stability. Bulk-test results can be used as a quick screening of foaming agents, before conducting corefloods, which are usually time-consuming.

Imaging analysis on a pore scale includes 2D microfluidic study (e.g. Conn et al., 2014) and 3D micro-CT study (e.g. Blunt et al., 2013). This technique is appealing in that phase interactions as well as flow and transport can be seen directly or visualized. The experimental observations provide direct evidence of foam dynamics (e.g. generation, destruction, coarsening and flow) in pore or fracture networks (Sian et al., 2018; AlQuaimi and Rossen, 2018). When intending to interpret foam behavior in geological formations using microfluidic and micro-CT results, one needs to account for geometrical factors of physical models used. 2D micromodels (with flow geometry very different from 3D networks) and core-sample sizes for 3D micro-CT study may give results deviating from that at a reservoir scale.

Lab investigation on a core scale, with core samples roughly ranging from 5 to 100 cm in length and 1 to 5cm in diameter, is most indicative of foam flow in reservoir rocks. Coreflood measurements can mimic reservoir conditions (e.g. pressure and temperature). Since the 1980s, advanced imaging techniques have been developed to assist in coreflood study, e.g. CT (Computed Tomography) and NMR (Nuclear Magnetic Resonance) imaging. In particular, CT foam corefloods are capable of monitoring in-time phase saturations during corefloods. This allows one to relate quantitatively foam properties to phase distributions, which is very important in the modeling of foam EOR.

1.3.2 Foam modeling

Foam models, e.g. pore-network models, are developed to describe foam formation and propagation on a pore-scale (Kharabaf and Yortsos 1998; Blunt; 2001). On a larger scale (e.g. centimeters to kilometers), the representation of foam currently falls into two groups of models that are categorized by implicit or explicit description of foam texture: implicit-texture (IT) foam models (Computer Modeling Group 2015), and population-balance foam models (Kovscek et al., 1995; Kam et al., 2007). IT models describe foam using a mobility-reduction factor FM that reduces gas mobility according to a function of local phase saturations and other factors. Foam texture (bubble size and density) in IT models is not explicitly incorporated, but implicitly reflected by the values of factor FM that represent the effects of a given foam texture. IT models delineate foam properties at local equilibrium, where generation and destruction rates of bubbles are instantly identical

everywhere at all times. Population-balance models explicitly incorporate foam texture in associated algorithms, based on dynamic modeling of the bubble population. This group of models is usually used to describe the dynamics of foam generation and destruction. At local equilibrium, population-balance models describe similar behavior to the IT models. Nevertheless, IT models are much simpler to use than population balance models (Lotfollahi et al., 2016).

Steady-state foam flow in porous media, which features two regimes (as shown in **Fig. 1.4a** or **1.4b**), is in general modelled through IT models. The validity of IT models in representing steady-state foam behavior without oil is justified by a good match between model-fitted results and lab data (Cheng et al., 2000).

The modeling of transient foam flow through geological formations includes two major techniques (Rossen, 2013; Ashoori et al., 2010): numerical simulation and fractional-flow theory, also called the Method of Characteristics (MOC). Both techniques may each adopt either IT models or population-balance models depending on purposes of studies (Lotfollahi et al., 2016). In numerical simulators, transient foam flow and transport are numerically solved, primarily for predicting foam performance at field conditions and then optimizing the design of foam EOR projects. Numerical solutions for foam EOR are subject to issues of stability and accuracy (Rossen, 2013). Fractional-flow theory is a powerful analytical approach that yields additional physical insights into transient foam dynamics. Furthermore, analytical solutions solved by this theory act as a benchmark for numerically solved results. The application of fractional-flow theory to a two-phase system is elegant and mature (Pope, 1980), whereas, for a three-phase system, its applications are under development, given the difficulty in finding theoretical solutions.

Lab measurements and foam modeling are complementary techniques in exploring foam in porous media. Data obtained in the lab assist in the development and validation of foam models, and are used to fit foam-simulation-model parameters for upscaling to field applications. Model fit to data helps us to interpret the mechanisms as implied in the data. When lab measurements and modeling are in agreement and suggest success in the field, the next step is pilot-scale tests before implementation of foam EOR.

1.4 Current challenges in foam EOR

Numerous lab investigations (Rossen, 1996; Simjoo et al., 2012; Tang et al. 2018) and recent field pilots (Sharma et al, 2017; Rognmo et al., 2018; Alcorn et al., 2018) demonstrate that foam EOR technology possesses remarkable potential in improving oil production. Nevertheless, the commercially widespread application of this technology still faces some challenges, because subsurface foam behavior is very complex and associated knowledge is still progressing. Those challenges primarily surround the fundamental understanding of foam dynamics in EOR processes, as well as precise and efficient modeling of these processes.

1.4.1 Issues in physical dynamics of foam EOR

The physical dynamics of foam in EOR processes involves foam generation and destruction, steady-state and transient flow behavior, and foam interaction with oil (stabilization and destabilization of foam) (Rossen, 1996). Lamella creation for foam generation have four mechanisms: leave behind, lamella division, snap off and gas

evolution within liquid (Rossen 1996). For foam flow at steady-state without oil, the fundamentals (as shown in **Figs. 1.4a** and **1.4b**) are well understood, whereas our current understanding of transient behavior is limited, especially in long-distance foam propagation. Major issues concern, e.g., whether foam propagation deep in a reservoir arises from propagation of foam generation near-well, or from newly generated foam in situ, or both, and associated gravity effects (Hussain et al., 2017; Shah et al., 2018). An additional issue is injectivity of gas and liquid slugs in SAG (Surfactant-Alternating-Gas) processes, including the influence of fingering, gas dissolution and water vaporization on the injectivity in these processes (Farajzadeh et al., 2016; Al Ayesh et al., 2017, Gong et al., 2018) .

Foam in most EOR applications contacts oils; these interactions are complicated and not yet fully understood (Farajzadeh et al., 2012). The effect of oil on foam can be roughly regarded as anti-foaming, through which oil prevents foam from being generated, and de-foaming, through which oil destabilizes generated foam. Regarding the anti-foaming effect, Sanchez and Hazlett (1992) conclude foam can be generated in oil-wet reservoirs without oil only when the wettability is altered to be water wet; at oil-wet conditions with oil present, foam cannot be generated. The generality of these conclusions needs to be demonstrated. Regarding the de-foaming effect, lab observations show that most oils destabilize foam (Farajzadeh et al., 2012). Several coefficients are proposed to describe the destabilizing effect of oil on foam through surface phenomena, e.g., spreading coefficient (Harkins and Feldman, 1922), bridging coefficient (Aveyard et al. 1994), or lamella number (Schramm and Novosad 1990, 1992). However, these coefficients, either individually or in a combination, cannot yet predict the detrimental effect of a given oil. Furthermore, these findings are mainly based on bulk column tests that are not always consistent with behavior in porous media. In prior foam coreflood studies (references), with oil both immobile and mobile, the oil effect was interpreted qualitatively; no quantitative correlations have been formulated between foam-flow dynamics and oil-related factors (oil saturation and composition). These issues above are a primary knowledge gap that needs to be filled concerning foam EOR.

1.4.2 Issues in foam-oil modeling

The quantitative modeling of the effect of oil on foam flow, and displacement of oil by foam remains a challenge. Among the two groups of current foam models, the IT model STARS (Computer Modeling Group 2015), that is representative of current IT models, includes two algorithms that incorporate the effect of oil on foam for EOR: the “wet-foam” algorithm and “dry-out” algorithm. However, the specific impacts of oil on foam as represented in the two algorithms and their validity in representing physical behavior were not reported in the literature. These unknowns impose large uncertainty in the choice of the two algorithms in foam-oil modeling and interpretation of foam behavior with oil.

Most current population-balance foam models do not include the effect of oil, except for the earlier model of Myers and Radke (2000) and a recent model of Ma et al. (2018). The model of Myers and Radke incorporates the effect of oil on foam by reducing bubble-generation rate, to account for the reduction in foam-generation sites caused by the occupancy of oil. This model does not capture the impact of oil on foam stability. The model proposed by Ma et al. is expected to represent the two regimes, such as in **Figs. 1.4a** and **1.4b**, but the validity of the model has not been tested yet.

For modeling steady-state foam flow with oil, the representation of the oil effect and whether and how oil affects the two foam regimes remain unknown in both groups of foam models. For modeling transient foam flow with oil, numerical simulation faces a number of numerical challenges and numerical artifacts. This is partly because the presence of foam makes a huge difference to gas mobility relative to that without foam, which may cause inaccuracy or instability in numerical simulations (Rossen, 2013). Fractional-flow modeling, as an analytical approach, can give additional physical insights regarding dynamic foam-oil behavior in a simplified system, assuming 1D flow, incompressible phases and uniform initial conditions. The challenge is that finding the theoretical solutions for a three-phase flow is mathematically difficult and time consuming.

1.5 Research objectives

Foam injected into geological formations for EOR is in direct contact with oil in most contexts. The effectiveness of foam for gas-mobility reduction in the presence of oil is key to success of foam EOR processes. The central scope of this study concerns a systematic understanding of the effect of oil on foam-flow dynamics through both theory and measurements. Three major aspects are addressed: steady-state behavior, transient behavior, and microfluidics.

The objectives of the thesis are listed as follows:

- Steady-state behavior:
 - Review current implicit-texture (IT) and population-balance models for the representation of foam during EOR processes, in particular regarding the incorporation of oil in these two groups of models.
 - Propose a practical approach to quantitatively measure the oil effect in steady-state foam-flow systems. Then, examine how the two algorithms (wet-foam algorithm and “dry-out” algorithm) in the widely used IT foam model STARS (Computer Modeling Group 2015) quantify the effect of oil on foam for EOR.
 - Collect coreflood data on steady-state foam flow with oil, to verify whether the two regimes (as in **Figs. 1.4a** and **1.4b**) that exist for foam without oil also apply to foam with oil, and analyze how the introduction of oil (saturation and type) shifts the two regimes.
 - Fit the IT model STARS to the steady-state data with oil, to assess the suitability of the model for representing the effect of oil on the two regimes; determine foam-oil interactions in each regime through the match between data and model fit.
- Transient behavior
 - Solve for transient foam flow with oil using three-phase fractional-flow theory / the MOC with the local-equilibrium approximation, to get insights on two major aspects concerning foam EOR processes: dependence of the displacement on initial and injection conditions and the effects of foam tolerance for oil on the propagation velocities of foam and of the oil bank.
 - Identify the physically-acceptable foam-oil displacement, for given injection conditions (defined by phase fractional flows) that correspond to multiple possible injection states, i.e. different phase saturations (as predicted by the IT model), using three-phase fractional-flow theory. Determine the nature of the dependence of the foam-oil displacement on initial state.

- Investigate transient foam-oil dynamics using CT corefloods, where phase distributions can be monitored during the corefloods; relate foam properties that are reflected through sectional pressure-drop measurements, in particular, directly to oil saturations calculated from CT data.

- Microfluidics:
 - Analyze the suitability of conventional capillary-number definitions (representing a ratio of viscous to capillary forces) as a criterion for non-wetting phase mobilization in 2D microfluidics.
 - Propose a new capillary-number model for 2D micromodels. Verify the validity of the new model in evaluating the potential of non-wetting-phase mobilization in 2D microfluidic systems.

1.6 Thesis outline

This thesis is based upon six journal articles published or to be published, concerned with foam-oil dynamics in EOR processes. The thesis comprises eight chapters, starting with this **Chapter 1** as the Introduction. The description of problem background in the some chapters may overlap, to maintain the discussion flow.

Chapter 2 examines how the wet-foam algorithm and dry-out algorithm in the IT foam model STARS (Computer Modeling Group 2015) represent the effect of oil on foam, respectively. An approach is proposed to measure the effect of oil in steady-state foam-flow corefloods through data at fixed oil saturation, fixed oil superficial velocity, or a fixed ratio of oil/water superficial velocities. The oil effect as represented in each algorithm is illustrated by how oil shifts the two foam regimes. In addition, the IT model predicts multiple steady states in both algorithms, i.e. that the constant pressure-gradient contours, as function of gas and water superficial velocities in **Fig. 1.4a**, cross when oil is present. When the results are plotted in a manner similar to **Fig. 1.4b** but with apparent foam viscosity vs. foam quality, the plot folds on itself. The folding means that some injection conditions (defined in terms of phase fractional flows or superficial velocities) may correspond to multiple possible displacing states. A simple 1D foam simulator is then developed to conduct a numerical stability analysis of the multiple steady states, with and without including capillary diffusion in the simulations. The results indicate which of the multiple steady states are stable and which stable state makes the displacement depends on initial state.

Chapter 3 shows an experimental investigation of the effect of oil on steady-state foam flow through its effect on the two foam regimes. The experimental design implements two types of model oils: hexadecane (C_{16}), which is relatively benign to foam stability, and oleic acid (OA), which is greatly harmful to foam stability. Data are collected on the two regimes with pure C_{16} , mixture oil with 10% OA and mixture oil with 20% OA, respectively. In each case, oil is co-injected with foam at a fixed oil/water superficial velocity ratio. The influence of oil on the two regimes is determined through a comparison with the reference two regimes without oil obtained at similar experimental conditions. The widely used IT model analysed in Chapter 2 is then fitted to the data with and without oil, using a method similar to that of Cheng et al. (2000). The validity of the IT model for representing the two regimes with oil is demonstrated by a good match between the fitted results and data. The match also assists in interpreting the mechanisms of foam-oil interaction in each regime. Initial efforts are made to estimate

oil-related foam-simulation parameters, without information on oil saturation during the steady-state coreflood measurements.

Chapter 4 provides physical insights on foam displacement with oil from the view of wave propagation, through three-phase fractional-flow theory. Mathematically, conservation equations (coupled with the IT foam model) that govern a system of 1D transient foam flow with oil are solved by the wave-curve method (WCM) (Liu, 1974; Castañeda et al., 2016). The WCM produces two major outputs that define any particular displacement: a composition path from an injection (J) to initial (I) condition in ternary saturation space, and associated wave velocities of saturations along the path. In general, insights on two crucial aspects concerning foam EOR are derived from the theoretical solutions. 1. The foam-oil displacement structures are revealed for four representative scenarios that are defined by different combinations of injection state J and initial state I , each either allowing or killing foam. The desirability of the structure in each scenario is analysed in terms of foam-propagation velocity, oil-displacement rate and mobility ratio of displacing to displaced fluids at the displacement front. 2. A key issue is resolved that concerns whether oil saturation within an oil bank, when displaced by foam, can exceed an upper-limiting oil saturation above which foam is killed completely. 3. We show the impacts of oil-related foam model parameters on foam-bank propagation, to guide improving foam propagation through some controllable factors, e.g. improving surfactant formulation for better tolerance to oil.

Chapter 5 addresses an issue of oil displacement by foam with multiple steady states as predicted by the IT model (Chapter 2), again from the perspective of wave propagation as suggested by three-phase fractional-flow theory. We find that the problem definition that the WCM solves is different than a physical coreflood with specified injection rates of phases. The difference in the problem definition between the two makes the WCM capable of identifying the unique displacing state among multiple possible injection states that fit to same injected fractional flows. Theoretical solutions suggest that the choice of the displacing state among multiple steady states shows a dependence on initial state. This argument is consistent with the simulation analysis in Chapter 2. In the solutions by the WCM, a physically-acceptable displacement path features only positive wave velocities along the whole path. A path with negative wave velocities does not fit the injection conditions in physical corefloods. More fundamentally, a boundary curve is defined in a ternary saturation space that captures the nature of the dependence of the displacement on initial state. We show then the implications of the findings for field applications, and give suggestions for laboratory verification of the multiple steady states.

Chapter 6 presents a CT coreflood study of foam displacement with oil, seeking to understand the transient foam dynamics as a function of oil type and oil saturation. Two types of model oils are used, i.e. C_{16} and a mixture oil with 20% OA and 80% C_{16} whose effects on steady-state foam flow have been examined in Chapter 3. For each model oil, foam is injected into a core at waterflood-residual oil saturation, through two ways: co-injection of surfactant solution and gas to generate foam in-situ, and direct injection of pre-generated foam. Dual-energy CT scanning is implemented during the corefloods to distinguish and monitor three-phase saturations. Foam dynamics is quantitatively related to oil saturation and oil type, including the impacts of oil on in-situ foam generation and propagation of pre-generated foam. Experimental observations give also insights on oil-type-dependent displacement processes in both types of foam injection, e.g. oil drainage and oil-bank

creation. Based on these findings, it is doubtful that IT models represent transient dynamics of in-situ-generated foam in presence of very harmful oils in some cases.

Chapter 7 defines a new capillary number (N_{ca}) for 2D micromodels, specifically to account for the impact of pore microstructures, i.e. the pore throats and pore bodies that control capillary trapping. The conventional capillary-number definitions originally proposed for 3D geological formations do not work for 2D pore networks, because the flow in 2D and 3D pore networks is very different. The new definition is developed based on a force balance on a ganglion trapped in a single pore by capillarity. The validity of the new definition is confirmed by yielding a converging trend on the capillary-desaturation curve (i.e. non-wetting phase saturation vs. N_{ca}) for 2D micromodels. using published data.

Chapter 8 summarizes the major conclusions of the thesis, and give recommendations for those aspects that need further research in the area of foam-oil dynamics during EOR processes.

IMPLICIT-TEXTURE MODELING OF THE EFFECT OF OIL ON FOAM EOR

Summary

The effectiveness of foam for mobility control in the presence of oil is key to foam EOR. A fundamental property of foam EOR is the existence of two steady-state flow regimes: the high-quality regime and the low-quality regime. Experimental studies have sought to understand the effect of oil on foam through its effect on these two regimes. Here we explore the effect of oil on the two flow regimes for one widely used foam model.

The STARS foam model includes two algorithms for the effect of oil on foam: in the "wet-foam" model, oil changes the mobility of full-strength foam in the low-quality regime; in the "dry-out" model, oil alters the limiting water saturation around which foam collapses. We examine their effects as represented in each model on the two flow regimes using a Corey relative-permeability function for oil. Specifically, we plot the pressure-gradient contours that define the two flow regimes as a function of superficial velocities of water, gas and oil and show how oil shifts behavior in the regimes.

The wet-foam model shifts behavior in the low-quality regime with no direct effect on the high-quality regime. The dry-out model shifts behavior in the high-quality regime but not the low-quality regime. At fixed superficial velocities, both models predict multiple steady states at some injection conditions. We carry out a stability analysis of these states using a simple 1D simulator with and without incorporating capillary diffusion. The steady state attained after injection depends on the initial state. In some cases, it appears that the steady state at intermediate pressure gradient is inherently unstable as represented in the model. In some cases introduction of capillary diffusion is required to attain a uniform steady-state in the medium. The existence of multiple steady states, with the intermediate one unstable, is reminiscent of catastrophe theory and of studies of foam generation without oil.

2.1 Introduction

Injected gas (CO₂, steam, or hydrocarbon gas) can be very efficient in displacing oil in enhanced oil recovery but suffers from poor sweep efficiency (Lake et al. 2014). Foam is one promising means of increasing the sweep efficiency of injected gas (Schramm 1994; Rossen 1996).

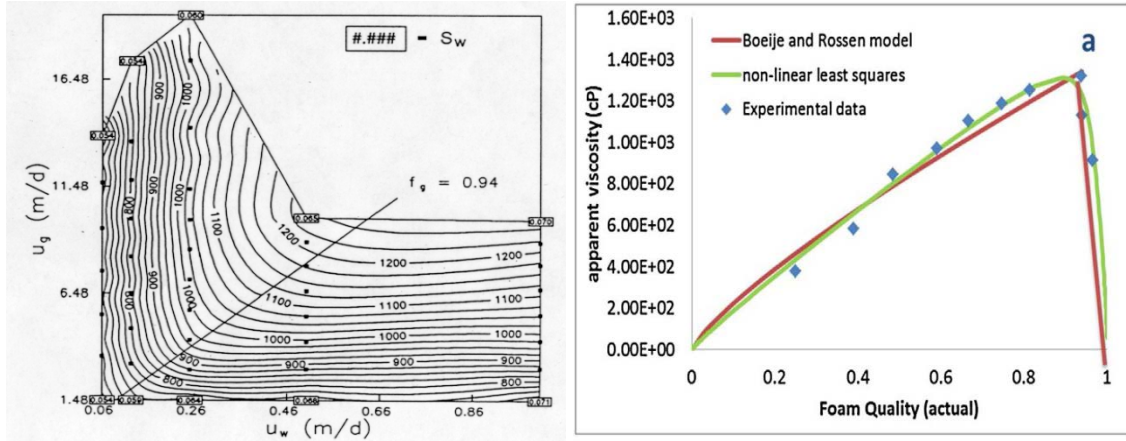


Figure 2.1 (left) Pressure drop across a 2-ft sandpack as a function of superficial velocities of gas (U_g) and water (U_w). Pressure gradient in psi/ft is half the values shown. Boxed numbers are the water saturation S_w . Contours of equal pressure drop are plotted through steady-state data, which are represented by black points. From Osterloh and Jante (1992).

Figure 2.2 (right) Apparent viscosity (Eq. 2.1) of foam without oil at fixed total superficial velocity (0.671 ft/D) in a 90-md Berea core, as a function of foam quality, from Kapetas et al. (2017). The green least-squares model fit finds an abrupt, though continuous, transition between the two flow regimes; the red fit assumes an infinitely abrupt transition.

A fundamental property of steady-state foam behavior in porous media, in the absence of oil, is the existence of two steady-state flow regimes: the high- and low-quality regimes (**Fig. 2.1**). Foam "quality" means gas fractional flow f_g . At high foam quality (upper left portion of diagram) pressure gradient $\bar{\nabla}p$ is nearly independent of gas superficial velocity U_g . Behavior in this regime is thought to be controlled by foam stability, specifically by foam collapse at a limiting capillary pressure (Khatib et al. 1988; Alvarez et al. 2001). At low foam quality (lower right portion), $\bar{\nabla}p$ is nearly independent of liquid superficial velocity U_w . In this regime, foam bubble size is thought to be fixed at a minimum size, close to pore size, and foam mobility to be controlled by capillary trapping and mobilization of bubbles as well as drag on moving bubbles ((Hirasaki and Lawson 1985; Falls et al. 1988; Rossen and Wang 1997; Xu and Rossen 2003). The rheology of foam in the two flow regimes of **Fig. 2.1** is usually not consistent (Osterloh and Jante 1992; Cheng et al. 2000; Kim et al. 2005). Foam in the low-quality regime in the absence of oil usually shows shear-thinning behavior with respect to U_g . At fixed f_g , this implies shear-thinning behavior with respect to total superficial velocity U_t . The high-quality regime, in contrast, could be Newtonian, shear-thinning or shear-thickening with respect to U_w . One way to examine the rheology in each regime is to measure pressure gradient by varying total superficial velocity at fixed foam quality. One recent study plotted effective viscosity v. foam quality at fixed pressure gradients (Cavalcante Filho et al., 2018), using information similar to that in **Fig. 2.1**. The alignment features of curves on such a plot suggest Newtonian

behavior, whereas separate curves reflect either shear-thinning or shear-thickening behavior, depending on the change of effective viscosity with pressure gradient. The rheology of foam can be seen on a contour plot such as **Fig. 2.1**. Evenly spaced contours, for the same increase in pressure gradient, imply Newtonian behavior. Increasingly sparse or dense contours in one of the flow regimes in **Fig. 2.1** suggests of either shear-thinning or shear-thickening behavior, respectively, in the given regime. Experimental observations (Tang et al. 2017) suggest that weaker foam with oil in the low-quality regime reflects either a destabilizing effect of oil or shear-thinning behavior, or maybe both. To avoid confusion, we exclude the factors for representation of non-Newtonian effects in each regime in this modeling study.

An alternative way to plot data and visualize the two flow regimes is in a scan of the apparent viscosity of foam μ_{app} as a function of foam quality f_g , at fixed total superficial velocity U_t (**Fig. 2.2**) (Ma et al. 2013; Boeije and Rossen, 2015). Foam apparent viscosity is defined as the viscosity of foam, treating it as a single phase:

$$\mu_{app} = -k\nabla p / U_t \dots\dots\dots (2.1)$$

where k is permeability. A plot like **Fig. 2.2** is in essence a diagonal slice, cutting through a plot like **Fig. 2.1** at fixed total superficial velocity $U_t = (U_g + U_w)$. In **Fig. 2.2**, the low-quality regime in **Fig. 2.1** corresponds to the left side of the plot, where μ_{app} increases with increasing f_g ; the high-quality regime the right side, where μ_{app} decreases with increasing f_g . The foam quality at which the transition from the low- to the high-quality regime occurs in **Figs. 2.1** and **2.2**, is defined as transition foam quality f_g^* . For the rest of this chapter, we assume that the transition between the two flow regimes is abrupt, giving a relatively sharp corner in the \sqrt{p} contours in **Fig. 2.1** and a relatively sharp peak in **Fig. 2.2**. This suggests a large value of adjustable foam parameter of $epdry$ used in our implicit-texture foam modeling (see **Table A-1** for its definition in Appendix A). Given commercial aspects concerning stability of numerical simulators and computational cost, some studies assume a small value of $epdry$ (Ma et al. 2013; Zeng et al. 2016; Farajzadeh 2015; Sumaiti et al. 2017), which sometimes does not give an ideal match to data.

Owing to the lack of data and complexity of interactions between foam and oil, the effect of oil on foam stability is not fully understood yet (Farajzadeh et al. 2012). Initial efforts to understand the effect of oil on foam represent surface phenomenon and phase behavior using, e.g., entering, spreading, and bridging coefficients as well as the "lamellae number" (Harkins and Feldman 1922; Kruglyakov and Vilkova 1999; Bergeron et al. 1993; Frye and Berg 1989; Garrett 1979; Dalland et al. 1994). However, none of these factors individually or in a combination yet discovered is a good criterion to predict the effect of oil on foam quantitatively (Basheva et al. 2000). One way to study the effect of oil on foam is to conduct dynamic coreflood displacements with an initial oil saturation in the core. Most of previous experimental studies, thus, focused on either foam displacements with oil (Hahn et al. 1985; Simjoo and Zitha 2013), or steady-state foam flow in the presence of residual oil (Myer and Radke 2000). Foam strength in these studies was mostly evaluated in terms of pressure-gradient responses with oil saturation either varying in a transient displacement or fixed at residual. However, none of these studies could effectively quantify the effect of oil on foam over a range of oil saturations or fractional flows. Interpreting these experiments in terms of the effect of oil saturation on foam is complicated by the change in oil saturation in the core during the displacement. This raises some key issues in simulating foam EOR processes, in particular, how to describe properly the effect of oil on foam in models, as well as whether current models represent the

effect of oil on foam suitably. Without answering these questions, selection of a suitable foam model for foam EOR and estimation of oil parameters in foam models cannot be done properly and efficiently. Since the two flow regimes identified for local-equilibrium foam flow in the absence of oil are already well understood, experiments have sought to understand the effect of oil on foam through its effect on the two foam flow regimes. In the experiments of Rong (2002) and of Shen et al. (2006), oil superficial velocity was maintained as a fixed fraction of water superficial velocity. Another possibility would be to maintain oil superficial velocity fixed, regardless of superficial velocities of water and gas. A third possibility is to represent the two flow regimes at fixed oil saturation. In general, however, oil saturation is not known or controlled in a coreflood experiment. The step after collecting experimental data is to fit a foam model to data and evaluate the suitability of current foam models for representing the effect of oil on foam.

To interpret such data in terms of models, it is necessary first to understand how those models represent the effect of oil foam when plotted in a manner of **Fig. 2.1** or **Fig. 2.2**. Among the two groups of foam models (implicit-texture (IT) and population-balance foam models), only the IT foam models in the STARS simulator describe the effect of oil on foam explicitly. A previous study (Myer and Radke 2000) incorporated the effect of oil on foam in a population-balance model, by reducing bubble-generation rate accounting for a reduction in generation sites due to occupancy by oil. This does not reflect the impact of oil saturation and composition on stability of foam with oil. Comparisons of the IT and "population-balance" approaches to foam modeling can be found in Ma et al. (2015) and Lotfollahi et al. (2016a). One major goal of this study is to show how the widely-used foam model in the STARS simulator (Computer Modeling Group 2015) represents foam behavior in the presence of oil. Other implicit-texture foam models have similar algorithms. The STARS model assumes instantaneous attainment of local equilibrium (LE) between rates of creation and destruction of foam. Specifically, we consider the three approaches proposed above to measure the effect of oil, in modeling the effect of oil on foam through its effect on the two flow regimes in **Fig. 2.1**: fixed oil saturation, fixed oil superficial velocity and fixed ratio of oil to water superficial velocity. Here we mainly illustrate how oil shifts the two flow regimes with changing values of the relevant parameters, rather than a sensitivity analysis of parameters. The theoretical analyses given below are mostly consistent with our experimental observations shown in Chapter 3 (Tang et al. 2017). In some cases we identify multiple steady states predicted by the model for the same injection conditions. A simple 1D incompressible simulator is then developed to analyze the stability of the multiple steady states. A third steady state is revealed by the simulation results.

In the end we present the multiple steady states as a surface of effective viscosity as a function of fractional flows and saturations on a ternary diagram, respectively. The folding of this surface is reminiscent of catastrophe theory (Zeeman 1977) and similar to the multiple steady states seen as a function of pressure gradient in studies of foam generation without oil (Gauglitz et al. 2002; Kam and Rossen 2003; Lotfollahi et al. 2016b). The multiple steady-states predicted in the foam models need more efforts to verify their existence, experimentally, and test their stability.

2.2 Results and analysis

Gas mobility, the ratio of gas permeability to gas viscosity, is reduced by foam. In simulation this mobility reduction can be represented either by reducing gas relative permeability or increasing gas viscosity. In the STARS foam model (Computer Modeling Group 2015; see appendix A), gas mobility reduction by foam is represented as a reduction in gas relative permeability. The effective gas relative permeability with foam is the product of the foam-free gas relative permeability and a mobility factor FM . FM in turn is inversely proportional to the product of a series of functions accounting for the effects of surfactant concentration, non-Newtonian foam mobility, water saturation (and, by implication, capillary pressure), and oil saturation. For simplicity we neglect all effects except the effects of water saturation ("dry-out") and oil saturation. The equations given in the STARS foam model account for the effect of oil on foam in two ways. In the "wet-foam" model, the mobility reduction of full-strength foam is reduced with increasing oil saturation. In the "dry-out model," increasing oil saturation causes the water saturation at which foam collapses to increase (by implication, reflecting a decrease in the limiting capillary pressure, and therefore less stable foam). Details are given in Appendix A. The definitions of all foam parameters involved in this study are given in **Table A-1** in Appendix A, the values of which used are provided in **Table A-2** in Appendix A. Note that different names are used for similar parameters in the two models. For instance, the limiting water saturation in the wet-foam model is $fmdry$, and in the dry-out model, $sfdry$. The oil parameters $fmoil$, $fmoil$, and $epoil$ in the wet-foam model are expressed as $sfoil$, $sloil$, and $efoil$ in the dry-out model, respectively.

2.2.1 The oil effect represented in foam model – STARS

2.2.1.1 Oil effect predicted by wet-foam model

Figure 2.3 illustrates how the wet-foam model reflects foam performance at fixed oil saturation when oil-related parameters $fmoil$, $fmoil$ and $epoil$ vary. The results in similar plots are obtained by collecting (U_w, U_g) at various fixed \bar{V}_p through a scan of saturations (S_w, S_g) . The LE foam-flow behavior implied by the wet-foam model continues to show the two flow regimes in the presence of oil. The nearly horizontal pressure-gradient contours in the low-quality regime shift upward or downward as the parameters in the wet-foam model vary. In contrast, the pressure-gradient contours in the high-quality regime remain unchanged as the model parameters change.

Figure 2.4 illustrates similar behavior for a fixed oil superficial velocity (5 ft/D). The contours in the low-quality regime shift up or down in response to model parameters, with little or no effect on the high-quality regime. In contrast to **Fig. 2.3**, oil saturation is not fixed in these plots, but depends on pressure gradient. With oil superficial velocity fixed, using a Corey expression for oil relative permeability, the oil saturation is fixed along a given pressure-gradient contour, but decreases with increasing pressure gradient. The effect of increasing oil saturation with decreasing \bar{V}_p is seen indirectly in the shift of the \bar{V}_p contours in the plots.

Figure 2.5 illustrates behavior when oil is injected at a fixed ratio of oil to water superficial velocity. In this case oil saturation increases along a \bar{V}_p contour as water superficial velocity increases in the low-quality regime. Thus, as illustrated in **Fig. 2.5b**, \bar{V}_p contours can bend upward in the low-quality regime, reflecting greater mobility of full-strength foam as oil saturation increases. Vertical contours in the high-quality regime are at nearly fixed water superficial velocity, and therefore oil superficial velocity and oil saturation are fixed as well. As a result, parameters in the wet-foam model again alter only the low-quality regime.

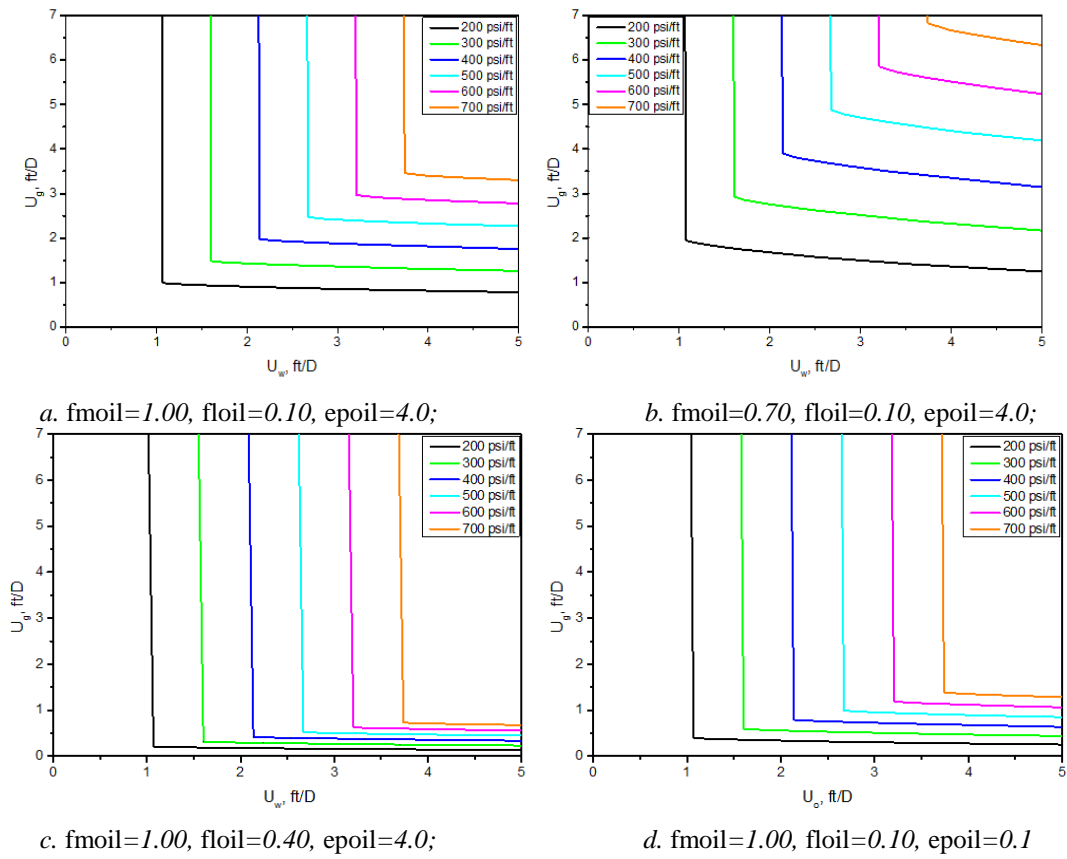


Figure 2.3 Pressure gradient as a function of water and gas superficial velocities predicted by the wet-foam model at fixed oil saturation $S_o=0.3$, with different values for the wet-foam model parameters.

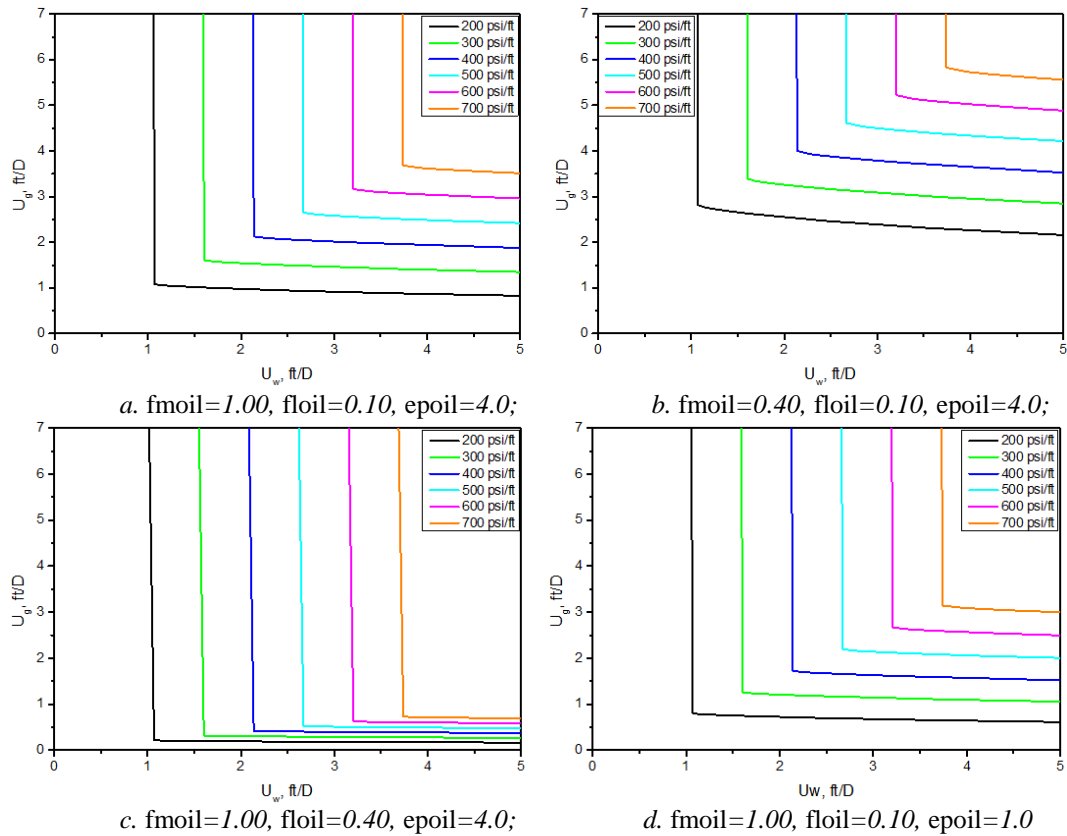


Figure 2.4 Pressure gradient as a function of water and gas superficial velocities predicted by the wet-foam model at fixed oil superficial velocity $U_o=5$ ft/D, with different sets of oil-related parameters.

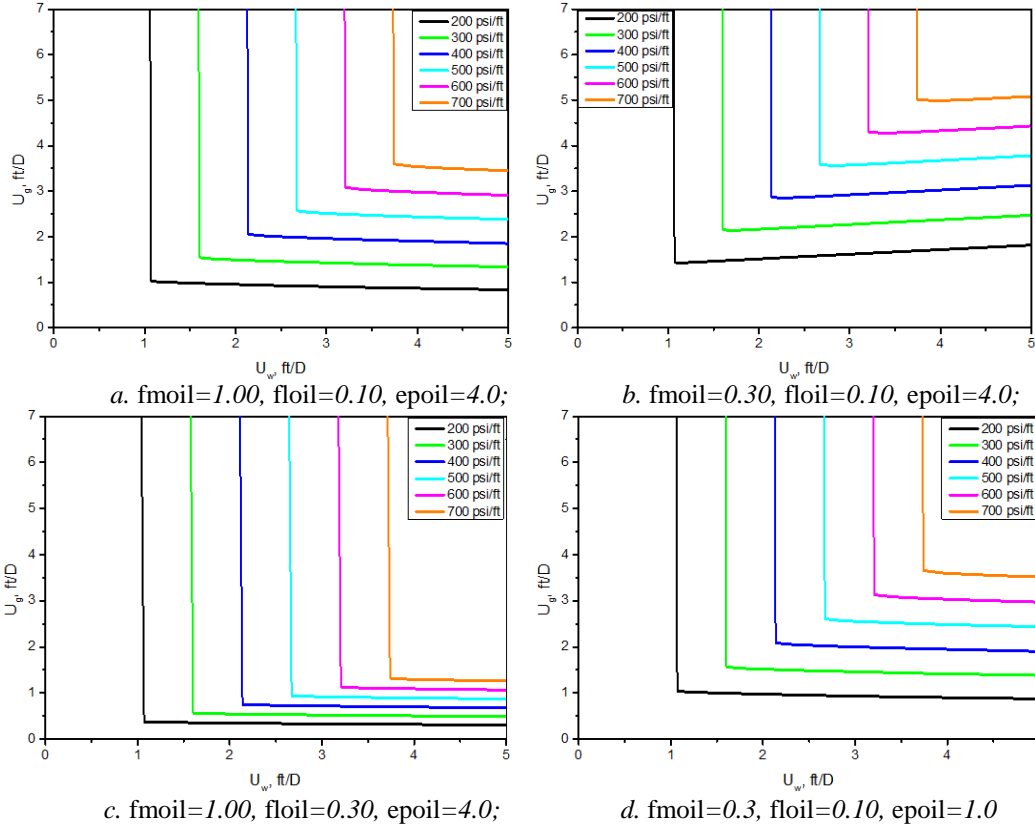


Figure 2.5 Pressure gradient as a function of water and gas superficial velocities predicted by the wet-foam model at fixed ratio of oil to water superficial velocities, $(U_o/U_w)=0.25$, with changing oil-related parameters.

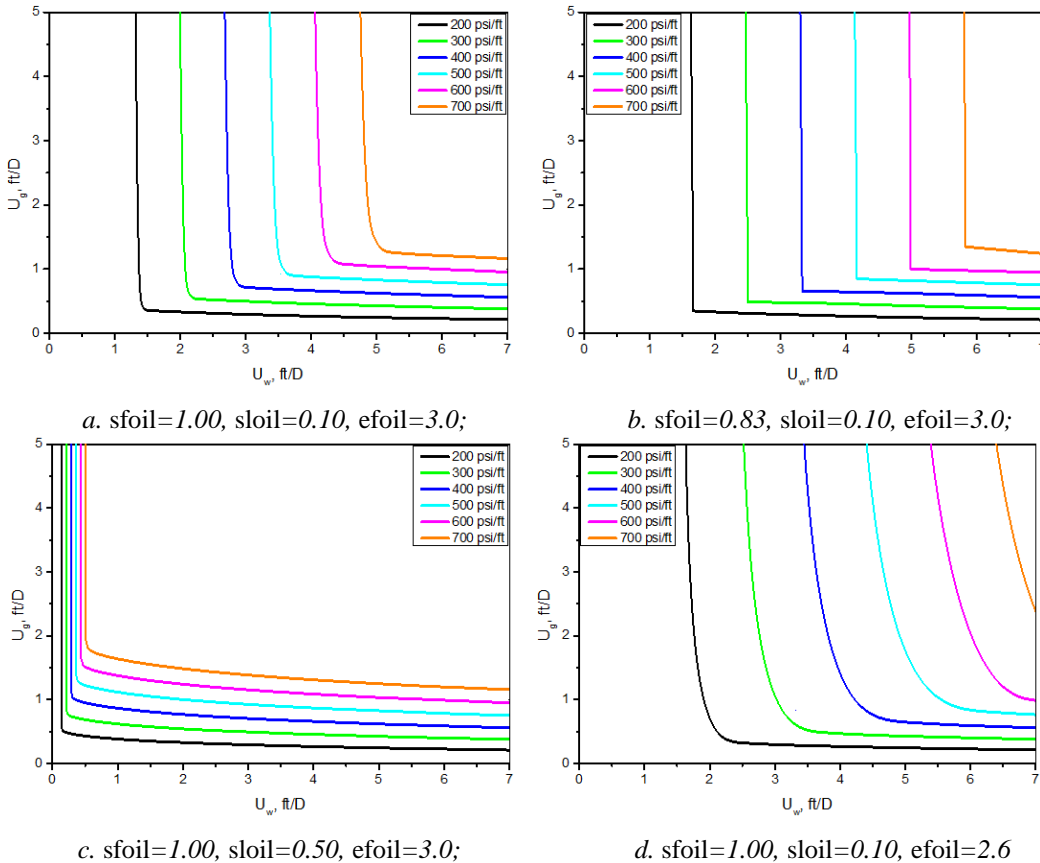


Figure 2.6 Pressure gradient as a function of water and gas superficial velocities predicted by the dry-out model at fixed oil saturation, $S_o=0.3$, with different values of oil-related parameters.

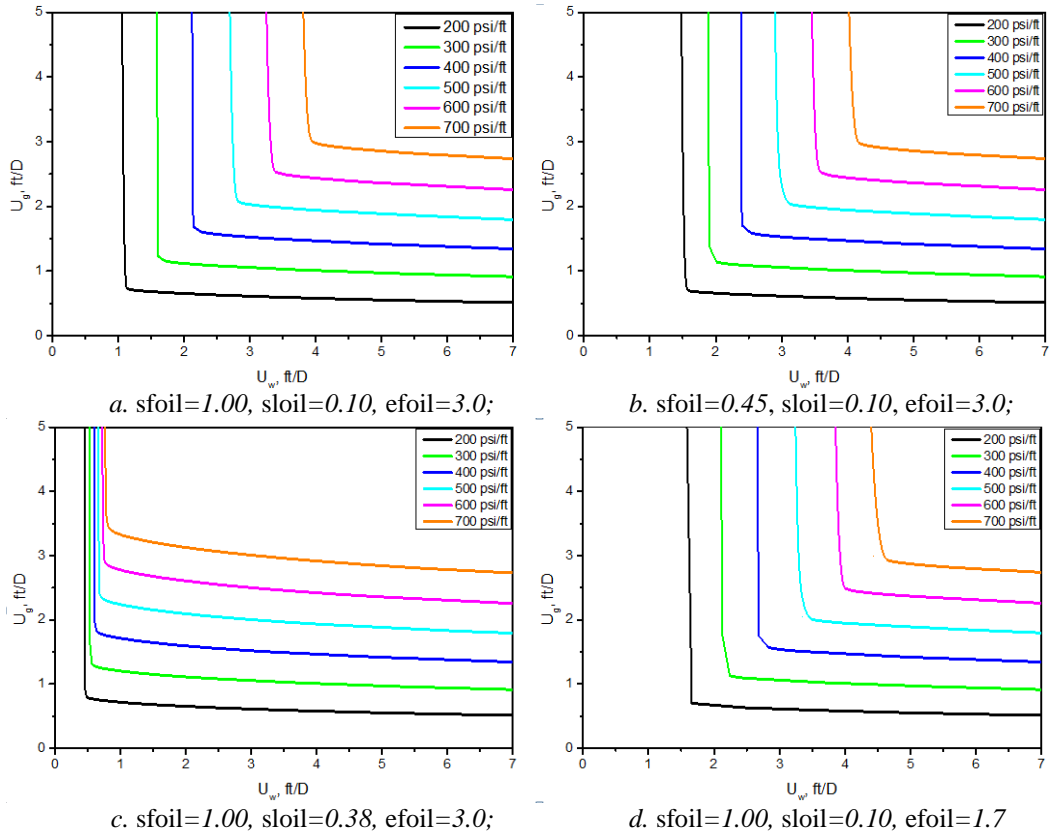
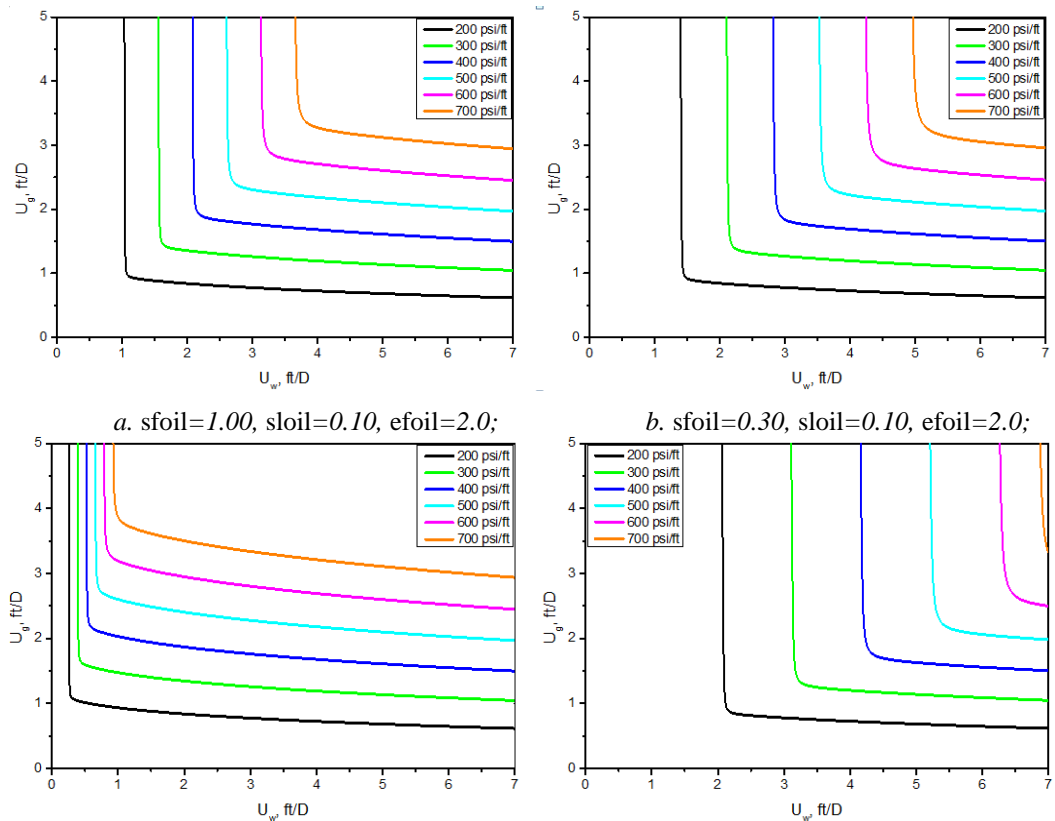


Figure 2.7 Pressure gradient as a function of water and gas superficial velocities predicted by the dry-out model at fixed oil superficial velocity, $U_o=5$ ft/D, with different sets of oil-related parameter.



c. $s_{foil}=1.00$, $s_{loil}=0.15$, $e_{foil}=1.0$; d. $s_{foil}=1.00$, $s_{loil}=0.10$, $e_{foil}=1.0$

Figure 2.8 Pressure gradient as a function of water and gas superficial velocities predicted by the dry-out model at fixed oil/water superficial velocity ratio of, $(U_o/U_w)=0.25$, with different sets of oil-related parameters.

2.2.1.2 Oil effect predicted by dry-out model

Figure 2.6 illustrates foam-flow behavior reflected by dry-out model at fixed oil saturation, corresponding to different sets of oil model parameters. As with the wet-foam model, the two flow regimes continue to appear as parameters change. However, in contrast to the wet-foam model, the parameters in the dry-out model affect only the high-quality regime. This is true also for plots at fixed oil superficial velocity (**Fig. 2.7**) and fixed ratio of oil to water superficial velocity (**Fig. 2.8**).

2.2.1.3 Foam quality scan with varying ratios of U_o to U_w

In plots of ∇p as a function of gas and water superficial velocities, if the boundary between foam regimes is sharp, then adjusting the parameters of the wet-foam model shifts the low-quality regime, and changing parameters in the dry-out model alters the high-quality regime. As noted, another popular way to represent the two regimes is in a scan of gas superficial velocity at fixed total superficial velocity (**Fig. 2.2**). In at least one case such a scan can be misleading when oil is included. **Figure 2.9** shows a plot of foam apparent viscosity as a function of foam quality f_g with varying ratios of oil to water superficial velocities. (In this case "foam quality" means gas superficial velocity as a fraction of total superficial velocity including oil; i.e. $[U_g/(U_g + U_w + U_o)]$.) Only the wet-foam model is implemented here, with the parameter values indicated. For these parameters, the effect of oil on the low-quality regime is modest. It appears that oil has a strong effect on the high-quality regime, but this is misleading. The water saturation at which foam collapses is independent of the ratio of oil to water superficial velocities (U_o/U_w) in this case. As this ratio increases, however, the superficial velocity of water at a given value of f_g decreases (since $f_g=U_g/(U_g+U_w+U_o)$). It is this decrease in water superficial velocity as (U_o/U_w) increases, not a collapse of foam, that causes the shift in this plot with (U_o/U_w) . In other words, (U_o/U_w) has no direct effect on the high-quality regime.

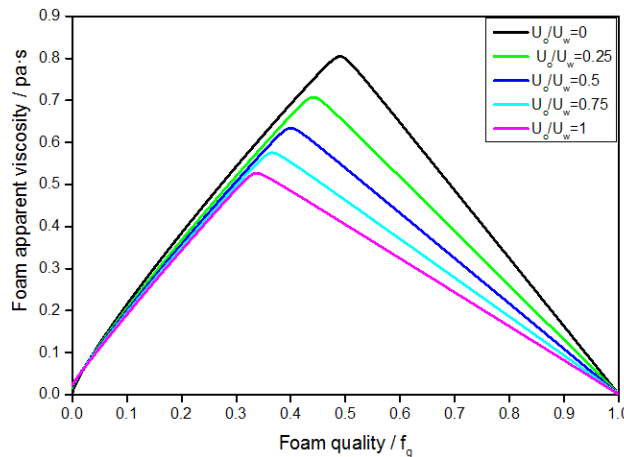


Figure 2.9 Foam apparent viscosity v. foam quality with varying ratio of oil to water superficial velocities with the wet-foam model. Parameter values $f_{moil}=1$, $f_{loil}=0.1$, $e_{poil}=4$; $U_t=13.56$ ft/D.

2.2.2 Multiple steady states

2.2.2.1 Wet-foam model

Figure 2.10 shows behavior in wet-foam model with oil superficial velocity fixed for one set of oil-related parameter values. As seen above, the pressure-gradient contours in the high-quality regime are independent of oil-related parameters in the wet-foam model. However, contours with lower pressure gradient in the low-quality regime, e.g. the contour of 200 psi/ft in **Fig. 2.10**, shift upward, crossing contours with higher pressure gradient in the high-quality regime: there are multiple steady states for the injection condition at the point of intersection.

Based on Darcy’s law, with a Corey function for oil relative permeability, oil superficial velocity is a function of oil saturation and pressure gradient. At fixed oil superficial velocity, decreasing pressure gradient means increasing oil saturation. In other words, the effect of oil on foam in the low-quality regime is greater along the lower-pressure-gradient contour. This contour in the low-quality regime moves upward, intersecting other pressure-gradient contours, thereby yielding multiple steady states.

Figure 2.11 shows the pressure-gradient contours for a case with fixed ratio of oil to water superficial velocity. Here, the pressure-gradient contours in the low-quality regime tilt upward at higher water superficial velocity, crossing other pressure-gradient contours. Along each pressure-gradient contour in the low-quality regime, with a fixed ratio of oil to water superficial velocity, oil saturation increases with increasing water superficial velocity, implying a greater effect on foam mobility. Oil saturation falls with increasing pressure gradient for a given water superficial velocity, with less effect on foam. This leads to multiple states for some injection conditions.

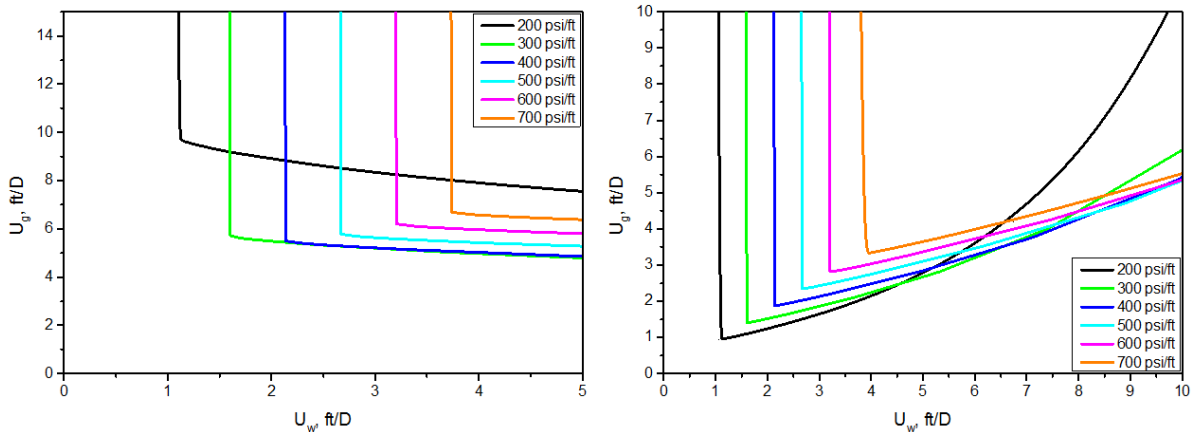


Figure 2.10 (left) Multiple steady states predicted by the wet-foam model: pressure-gradient contours plotted as a function of gas and water superficial velocities with fixed oil superficial velocity (5 ft/D). Parameter values $f_{moil}=0.2, f_{loil}=0.1, e_{poil}=1.3$.

Figure 2.11 (right) Multiple steady states predicted by the wet-foam model: pressure-gradient contours plotted as a function of gas and water superficial velocities with fixed ratio of oil to water superficial velocity (0.25). Parameter values $f_{moil}=0.2, f_{loil}=0.12, e_{poil}=4$.

2.2.2.2 Dry-out model

Figure 2.12 shows multiple steady states using the dry-out model with oil superficial velocity fixed. In the dry-out model, oil affects only the high-quality regime. Increasing water superficial velocity along a ∇p contour first leads the contours to a change from the high-quality regime to the low-quality regime. However, some contours with lower pressure gradient, e.g. contours of 200 psi/ft, 300 psi/ft, or 400 psi/ft, shift from the high- to low-

quality regimes at higher water superficial velocity than some other contours with higher pressure gradient (500 psi/ft, 600 psi/f or 700 psi/ft), resulting in intersections between the contours - multiple steady states.

The limiting water saturation in the dry-out model is not constant, but increases with increasing oil saturation. This increase in oil saturation destabilizes foam, causing pressure-gradient contours in the high-quality regime to shift to the right. With oil superficial velocity fixed in the dry-out model, oil saturation increases with decreasing pressure gradient: a lower pressure gradient thus yields a greater limiting water saturation and a weaker foam. If this effect is strong enough, a vertical contour in the high-quality regime can shift to a larger water superficial velocity with decreasing \sqrt{p} . This can cause multiple steady states.

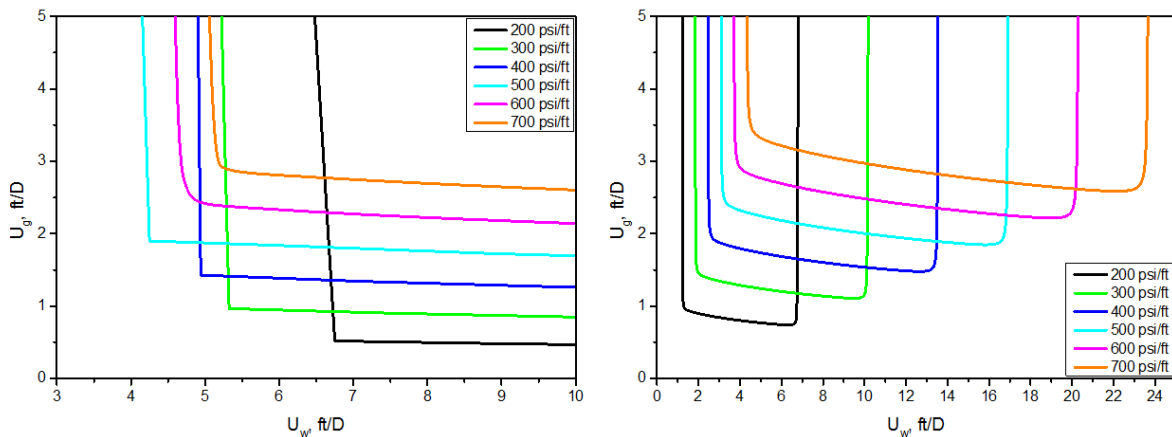


Figure 2.12 (left) Multiple steady states predicted by the dry-out model: pressure-gradient contours plotted as a function of gas and water superficial velocities with fixed oil superficial velocity (5 ft/D). Parameter values $s_{foil}=0.3$, $s_{loil}=0.1$, $e_{foil}=3$.

Figure 2.13 (right) Multiple steady states predicted by the dry-out model: pressure-gradient contours plotted as a function of gas and water superficial velocities with fixed ratio of oil to water superficial velocity (0.04). Parameter values $s_{foil}=0.144$, $s_{loil}=0.1$, $e_{foil}=3$.

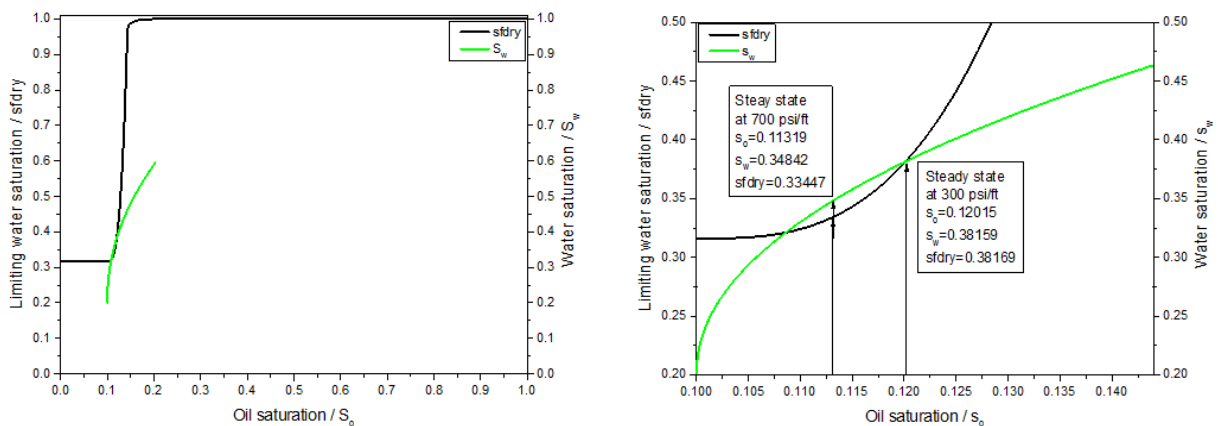


Figure 2.14 (left) Comparison between limiting water saturation s_{dry} (see Appendix A) and water saturation S_w as oil saturation changes in **Fig. 2.13**. The first high-quality regime is at the leftward intersection point, and the second at the rightward intersection point. The low-quality regime in **Fig. 2.13** is the interval between these two intersection points. Parameter values $s_{foil}=0.144$, $s_{loil}=0.1$, $e_{foil}=3$; $U_o/U_w=0.04$.

Figure 2.15 (right) Enlarged view of **Fig. 2.14** around intersection points and the interval between them.

With a fixed ratio of oil to water superficial velocity, oil saturation rises with increasing water superficial velocity along a $\bar{V}p$ contour. As a result, both oil and water saturations increase with increasing U_w in the low-quality regime. The increase in oil saturation causes an increase in limiting water saturation in the dry-out model. If the limiting water saturation increases enough, foam re-enters the high-quality regime again at higher U_w . The contours with lower pressure gradient re-enter the high-quality regime at a relatively lower water superficial velocity than the contours at higher pressure gradient, causing intersections of contours and multiple steady states. This shift of water saturation and limiting water saturation along the low-quality regime is illustrated in **Figs. 2.14** and **2.15**.

2.2.3 Simulation analysis of multiple steady states

2.2.3.1 Stability analysis

Both wet-foam and dry-out models, with fixed oil superficial velocity and fixed ratio of oil to water superficial velocity, predict multiple steady states for some injection conditions in the presence of oil. Each set of multiple steady states correspond to different foam strength, but have the same fractional flows.

Next we address the stability of the steady states at the intersection of pressure-gradient contours of 300 psi/ft and 700 psi/ft for dry-out model with fixed ratio of oil to water superficial velocity shown in **Fig. 2.13**, shown again in **Fig. 2.16**. We examine first which steady state is obtained for given initial conditions and then the stability of the two states to perturbations in 1D flow.

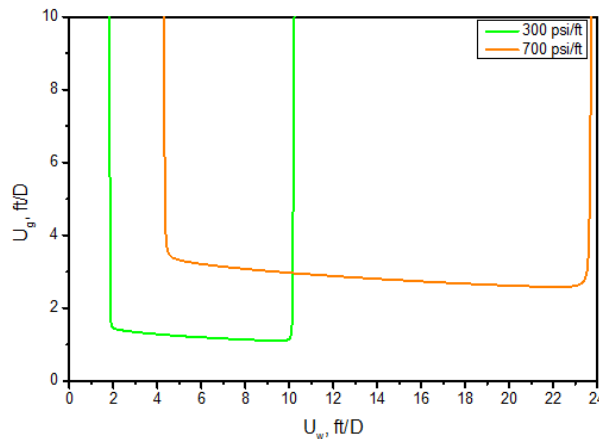


Figure 2.16 Intersection of contours of 300 psi/ft and 700 psi/ft, from **Fig. 2.13**.

A simple 1D simulator (100×1×1 grid blocks) was developed with the following assumptions: homogeneous reservoir, incompressible fluids and matrix, isothermal process, negligible effect of gravity, upstream weighting, and, initially, excluding capillary diffusion. It is further assumed that surfactant is present throughout the water phase, and foam immediately takes its local-equilibrium properties. The governing set of equations is then of the form:

$$S_{p,i}^{t+\Delta t} = S_{p,i}^t + \frac{\Delta t \cdot U_t}{\phi \cdot \Delta x} (f_{p,i-1}^t - f_{p,i}^t) \dots\dots\dots (2.2)$$

where subscript p denotes phase, i grid block (of length Δx), Δt time step, ϕ porosity, and f_p fractional flow for each phase in the given grid block at the given time. Both of the wet-foam and dry-out models were examined; they yield consistent results regarding the stability of the multiple steady states. Here we present the stability analysis using the dry-out model. For the purpose of our study, the dry-out foam model described in Appendix A is incorporated into the fractional flow expression of each phase in the simple 1D simulator. Gas mobility is modified by foam via the mobility-reduction factor $fmmob$ and limiting water saturation S_w^* , where water- and oil-saturation-dependent functions are considered in the simulation. All the parameters used in the numerical stability analysis are given in **Table A-2** in Appendix A. Specifically, the set of fractional flows into the first grid block, f_{p0} , was set at the injection condition for the steady states. For the stability analysis, the initial saturation is uniform at one of the steady states, with a small random perturbation in saturations (less than 0.01) added to 10 randomly selected grid blocks. We also tested what steady state the system reaches for three uniform initial states: each at residual saturation of all but one of the phases. **Table 2.1** specifies the injection and initial conditions for each case. Our interpolation for the superficial velocities at the intersection point in **Fig. 2.16** was inexact, so in fact the two steady states with the given superficial velocities have pressure gradients of 300 and about 706 psi/ft in the simulations.

Table 2.1 Overview of five simulation scenarios involving the two states at the intersection of 300 and 700 psi/ft contours from **Fig. 2.13**.

Scenario No.	Injection condition (ft/D)			Initial states			
	U_w	U_o	U_g	S_w	S_o	S_g	
1	$S_{w, \max}$			0.7	0.1	0.2	
2	$S_{o, \max}$			0.2	0.6	0.2	
3	$S_{g, \max}$	10.15110	0.40604	2.99894	0.2	0.1	0.7
4	300 psi/ft			0.38159	0.12015	0.49826	
5	700 psi/ft			0.34842	0.11319	0.53839	

Figure 2.17 shows the final states obtained after injecting 10 pore volumes corresponding to the five scenarios listed in **Table 2.1**, using the 1D simulator without capillary diffusion. During the process of three-phase flooding, some oscillations appear along reservoir moving downstream before reaching a steady state. By comparing all the ultimate saturation profiles achieved with the injection condition tested, the five scenarios starting with different initial states end up with two final states in terms of saturations: one final state close to the steady state of 700 psi/ft and a new steady state unidentified before. The steady state at 300 psi/ft is not present at the end in any case, even when it is the initial state. The steady state at 300 psi/ft is evidently unstable to perturbations; the stability of the state at 706 psi/ft is not clear.

The final states in the two stability tests (d and e) are not uniform. There is a jump from the state at 706 psi/ft to one at 11.33 psi/ft some distance down from the inlet, which appears to remain fixed in place over time. In the absence of diffusion or dispersion, with multiple steady states sharing the same fractional flows, it is possible that two consecutive grid blocks at different saturation could have the same fractional flows and thus not change with time. Nothing in our simulation model reflects a particular length scale, however. Thus, these fluctuations

could occur over lengths of mm or less, in which case capillary diffusion would be dominant. We then modify the simulator to allow in a qualitative manner for diffusion (which could arise from gradients in capillary pressure).

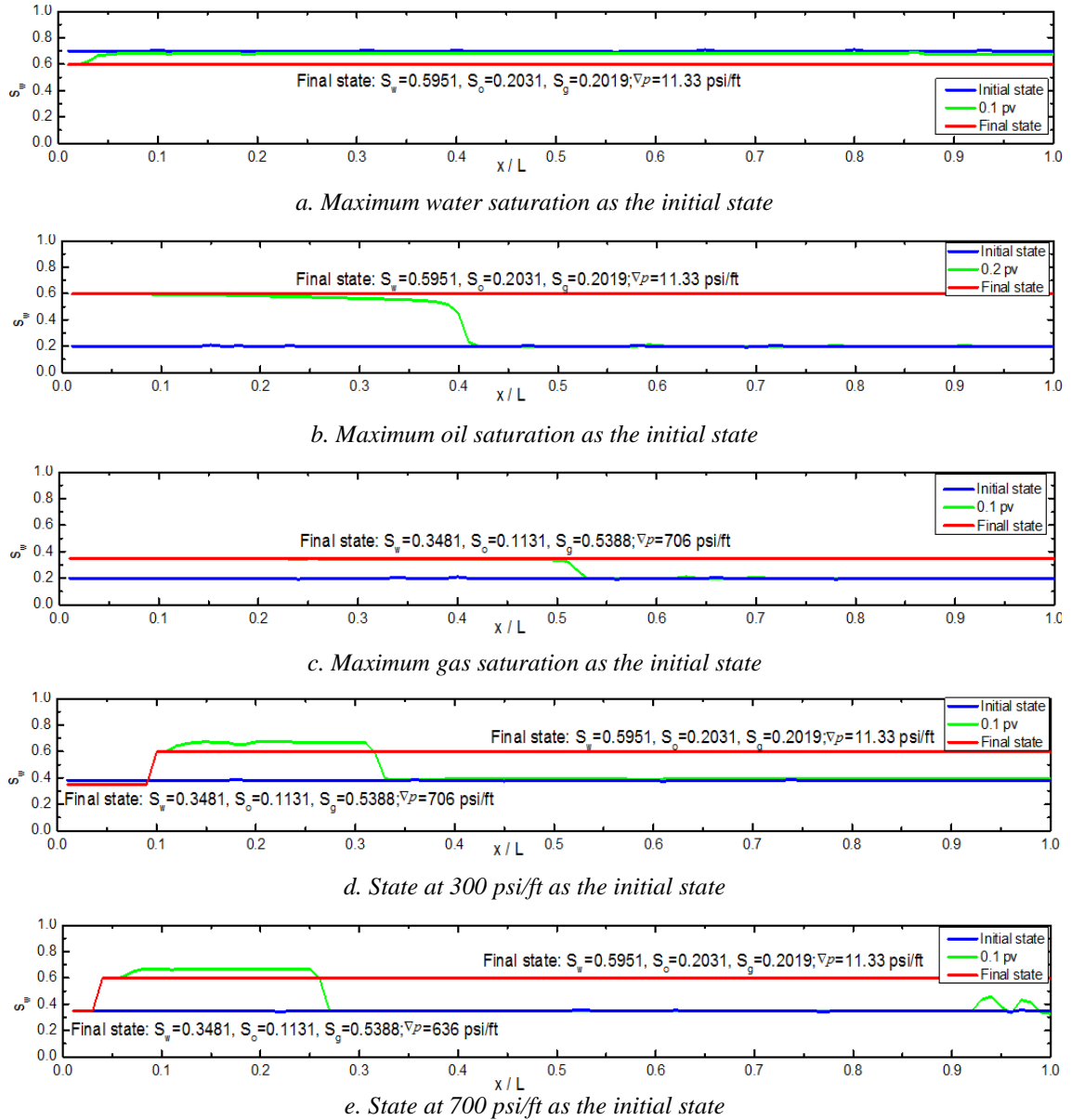


Figure 2.17 Final states achieved corresponding to different initial conditions during stability analysis of multiple steady states in **Fig. 2.16**, using the 1D simulator excluding capillary diffusion.

For simplicity we use constant diffusion coefficients, giving the following expressions for fractional flows:

$$\begin{aligned}
 f_{w,D}(i) &= f_w(i) - D_w \left(\frac{S_w(i+1) - S_w(i)}{\Delta x} \right) \\
 f_{g,D}(i) &= f_g(i) - D_g \left(\frac{S_g(i+1) - S_g(i)}{\Delta x} \right) \dots\dots\dots (2.3) \\
 f_{o,D}(i) &= 1 - f_{w,D}(i) - f_{g,D}(i)
 \end{aligned}$$

where subscript D indicates fractional flow accounting for diffusion and D_w and D_g are the diffusion coefficients for water and gas, respectively. The displacements in **Figs. 2.18a** through **2.18c** at 0.1 PV show that the diffusion coefficients are sufficient to disperse the front over several grid blocks but leave it otherwise intact. Displacements starting with high oil or water saturation end with the newly identified state, while one starting with maximum gas saturation ends at the 706 psi/ft state.

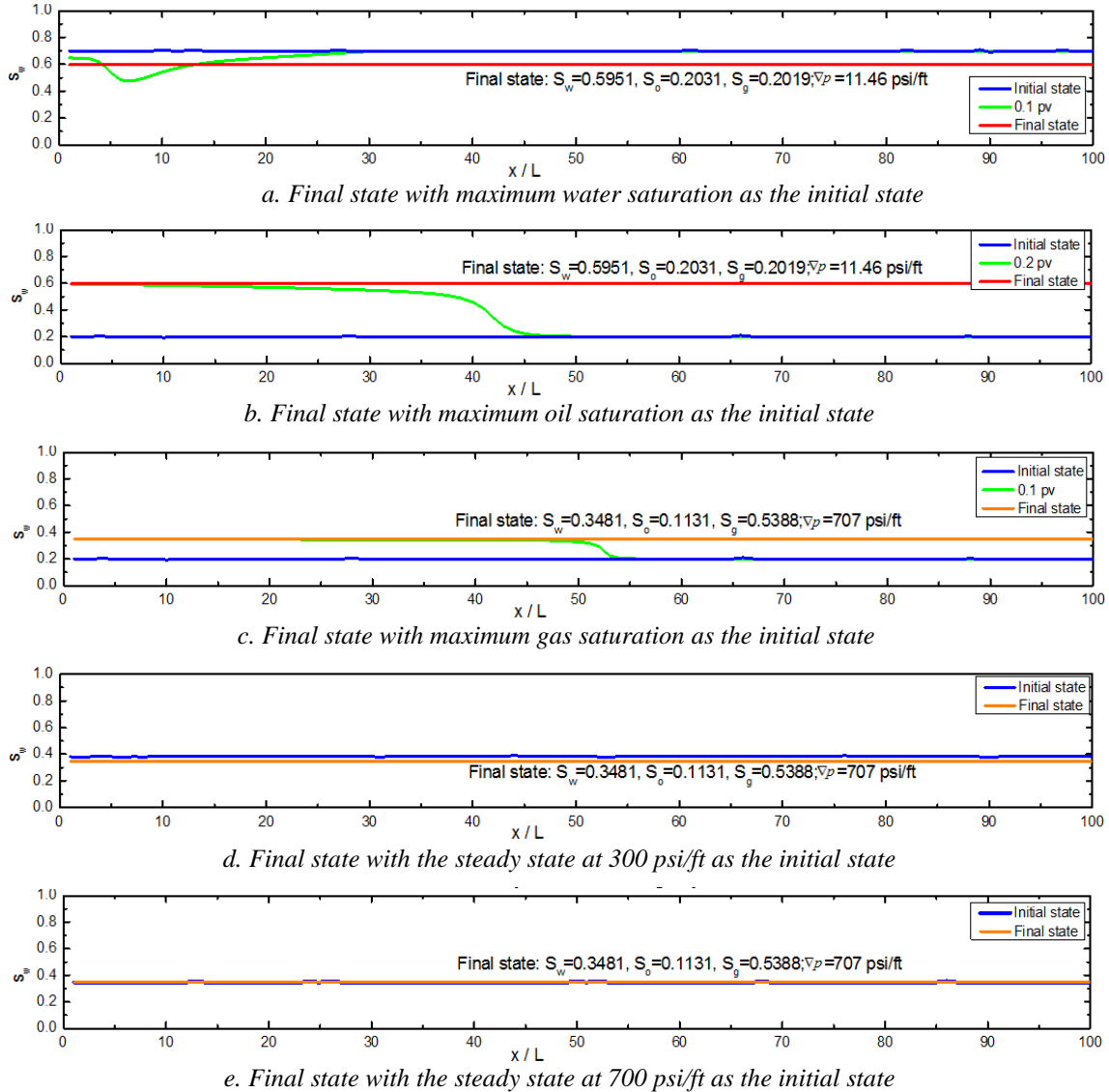


Figure 2.18 Final states achieved corresponding to different initial conditions during stability analysis of multiple steady states in **Fig. 2.13**, using the 1D simulator with capillary diffusion.

We note in **Fig. 2.18** that the jumps in the final case in the stability tests, as shown in **Figs. 2.17d** and **2.17e**, disappear with the following results: the 300 psi/ft steady state is unstable and the 706 psi/ft state stable. The newly identified steady state is at water saturation $S_w = 0.5951$. It shows a pressure gradient of only 11.33 psi/ft; oil saturation is above that at which foam is completely destroyed. We find this same steady state with the foam model disabled. To confirm that the form of the perturbations did not control stability, we conducted additional simulations with sinusoidal perturbations, of maximum magnitude 0.005 in saturation, of wavelength either twice or one-half the system length. The final results were the same as in **Figs. 2.18d** and **2.18e**. An additional

simulation with the newly identified steady state as initial state confirms that it is stable to small perturbations. Simulation stability analysis for another instance, i.e. the intersection of the 300 psi/ft and 600 psi/ft contours, achieves similar results, as shown in **Table 2.2**. Again, three steady states exist for the same injection condition, with steady states at upper and lower states stable to perturbation in saturations, but the intermediate steady state unstable.

Table 2.2 Results of numerical stability analysis to a different set of multiple steady states at the intersection of 300 and 600 psi/ft contours from **Fig. 2.13** (with diffusion)

Scenario No.	Injection condition (ft/D)			Initial state			Final state			∇p (psi/ft)	
	U_w	U_o	U_g	S_w	S_o	S_g	S_w	S_o	S_g		
1	$S_{w,max}$			0.7	0.1	0.2	0.59510	0.20310	0.20190	11.40	
2	$S_{o,max}$			0.2	0.6	0.2	0.59510	0.20310	0.20190	11.40	
3	$S_{g,max}$	10.42960	0.40572	2.47777	0.2	0.1	0.7	0.35393	0.11424	0.53184	600.00
4	300 psi/ft				0.38156	0.12014	0.49831	0.35393	0.11424	0.53184	600.00
5	600 psi/ft				0.35393	0.11424	0.53183	0.35390	0.11422	0.53184	600.00

The initial state plays an important role in which state one achieves for given injection conditions. If oil kills foam as in the dry-out model, it is reasonable that two final states could exist, one with strong foam and one with weak foam or no foam: it is not just an artifact of this model. If initial oil saturation is high, then oil might kill the foam; at the low pressure gradient without foam the small injected oil superficial velocity is sufficient to keep oil saturation constant. On the other hand, with little oil initially in the core, strong foam might carry the injected oil directly out of the core without allowing oil saturation to rise. Thus in an experimental study of steady-state behavior like that modeled here, one must be careful of the initial state of the core, as hysteresis could play a major part in the behavior observed. Thus, for this example, there exist three steady states corresponding to one injection condition: one at about 706 psi/ft, one at 300 psi/ft, and one at 11.33 psi/ft in this case. The previous analysis missed another intersection of contours at the same superficial velocities.

2.2.3.2 Third ∇p contour

The simulation results indicate that there must be a contour missing in **Fig. 2.13**. A clue comes from extending the range of water and gas superficial velocities in **Fig. 2.13** as illustrated in **Fig. 2.19**. Although such extreme values of U_w and U_g are not feasible physically, this plot shows the complete pressure-gradient contour predicted by dry-out model.

Each pressure-gradient contour in **Fig. 2.19** shifts from vertical in the high-quality regime to horizontal in the low-quality regime (extreme lower left on this plot) and then back to the high-quality regime with increasing water superficial velocity. Along this second ascent foam collapses completely; the remainder of the ascent and descent reflects three-phase flow without foam. Eventually, with increasing water superficial velocity, gas saturation drops to its immobile saturation and the superficial velocity of gas reaches zero.

Figure 2.20 shows the complete pressure-gradient contour for 11.45 psi/ft. It shows the same features as in Fig. 2.19, but at lower superficial velocities. Figure 2.21, plotted on the scale of Fig. 2.13, shows this contour and its intersection with the 300 and 700 psi/ft contours.

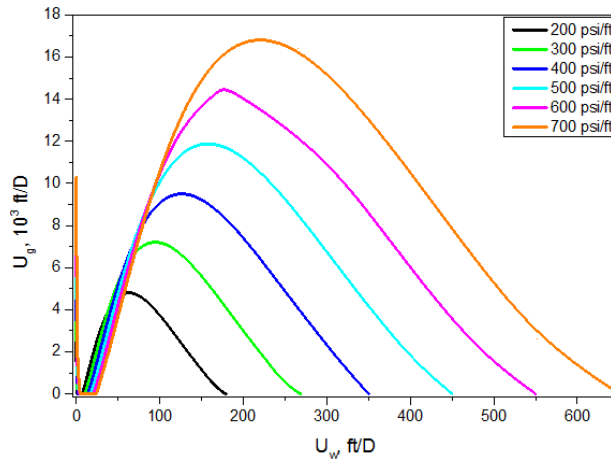


Figure 2.19 Extended plot with same parameter values as Fig. 2.13.

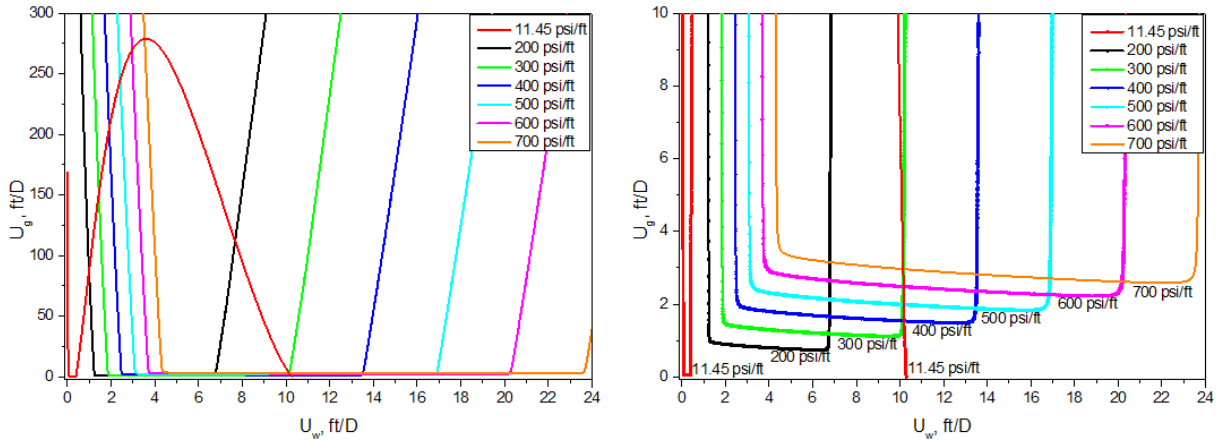


Figure 2.20 (left). Figure 2.13 replotted with the missing contour predicted by dry-out model.

Figure 2.21 (right). Replot of Fig. 2.20 focusing on lower range in gas superficial velocity.

2.2.3.3 Multiple steady states as folds in a surface

Because we exclude the factor for non-Newtonian effects in the STARS model, all of the contours in any plot shown here scale linearly with total superficial velocity. Each point on one contour corresponds to a point on another contour, with the same saturations, at a multiple of the superficial velocities of the first point. Therefore, apparent viscosity is independent of total superficial velocity. For a given model and set of parameters, one can plot μ_{app} (Eq. 2.1) as a function of the three fractional flows. Because the fractional flows must sum to one, it is convenient to plot this as a surface over a triangular diagram of fractional flows. An experiment at fixed (U_o/U_w) corresponds to a trace along this diagram at the same ratio of (f_o/f_w) , from the corner at $f_g = 1$ to the opposite side of the triangle. All the contours in a plot like Fig. 2.11 correspond to one such trace.

For one set of wet-foam parameters, Fig. 2.22 illustrates this surface using its traces at fixed (f_o/f_w) (equivalent to fixed (U_o/U_w)). The black curve, above the back edge of the triangle at $f_o = 0$, shows the two flow regimes without oil. The high-quality regime is the right side of this curve, at high gas fractional flow. As (U_o/U_w)

increases, a fold appears, starting from the bottom-right edge of the surface. The bottom, nearly flat, surface corresponds to complete foam collapse. As (U_o/U_w) increases further, the lobe representing foam shrinks until it disappears; at larger values of (U_o/U_w) , there is only one steady state, that of fully collapsed foam. **Figure 2.23** shows similar behavior for one set of parameters for the dry-foam model.

Further analysis shows that water saturation increases, following each trace in **Fig. 2.22** starting from the bottom-right edge of the surface (a-b-c-d-e), as illustrated in **Fig. 2.24**. As discussed in the section on multiple steady states, with fixed (U_o/U_w) , the increase in S_w also means an increase in S_o , suggesting weaker foam along trace until complete foam collapse, which leads to multiple steady states. The dry-out model predicts similar behavior for foam apparent viscosity plotted on a ternary diagram representing fractional flows, but the occurrence of multiple steady states in **Fig. 2.23** is due to the value of water saturation relative to limiting water saturation as the latter is modified by oil saturation.

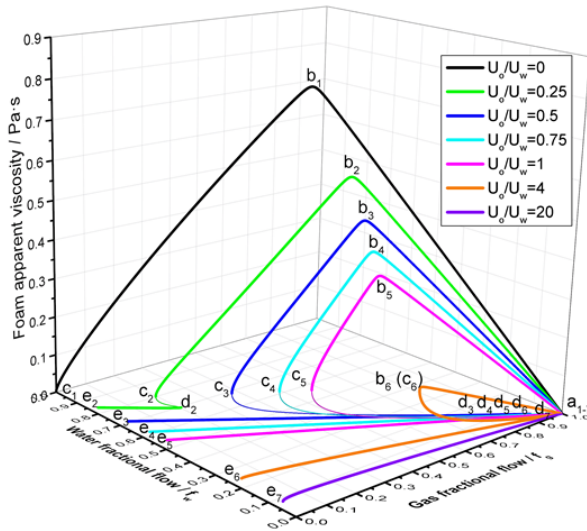


Figure 2.22 Foam apparent viscosity as a function of f_w , f_g and f_o predicted by wet-foam model with various ratios of oil to water superficial velocities ($f_{moil}=0.3$, $f_{loil}=0.1$, $e_{poil}=4$). Traces with multiple steady states follow a sequence a_i , b_i , c_i , d_i , e_i ; for $f_o = 0$: a_1 , b_1 , c_1 ; for $U_o/U_w = 20$: a_i , e_i .

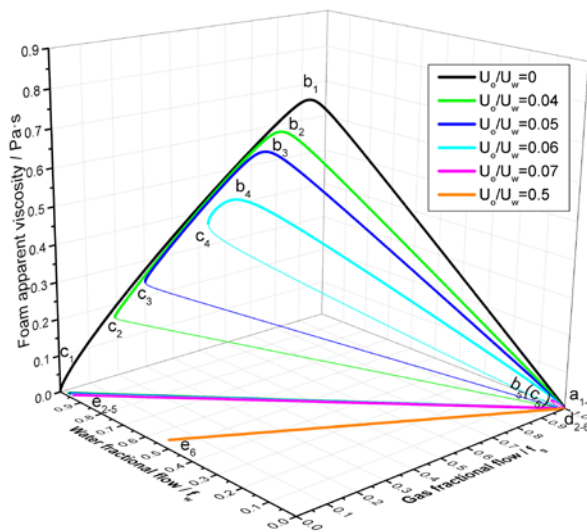


Figure 2.23 Foam apparent viscosity as a function of f_w , f_g and f_o predicted by dry-out model with various ratios of oil to water superficial velocity ($s_{foil}=0.144$, $s_{loil}=0.1$, $e_{foil}=3$). Traces with multiple steady states follow a sequence a_i , b_i , c_i , d_i , e_i ; for $f_o = 0$: a_1 , b_1 , c_1 ; for $U_o/U_w = 0.5$: a_i , e_i .

The identification of such multiple steady states is of interest in both theoretical study and practical applications. To verify the existence of the multiple steady states and test their stability, one can run experiments holding the same injection condition (co-injection of surfactant solution and gas) into a core initially at different conditions, e.g. a core initially saturated with oil or surfactant solution, where multiple steady states are predicted by the foam models under relevant experiment conditions. Given the stability of the multiple steady states, it is speculated that one may end up with the strong and greatly weakened foam state, whereas the middle state is unstable and therefore not observed.

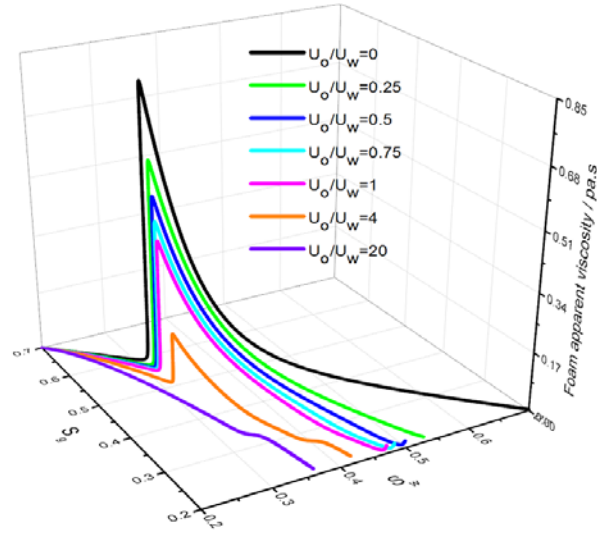


Figure 2.24 Foam apparent viscosity as a function of (S_w , S_g , S_o) predicted by wet-foam model for various ratios of oil to water superficial velocities. All the parameters used are the same as in **Fig. 2.22**. Each trace, starting from the bottom-left edge of the surface, corresponds to the path of a-b-c-d-e of the corresponding trace in **Fig. 2.22**.

This behavior is reminiscent of catastrophe theory (Zeeman 1977), with three steady states represented by a fold in the surface representing the behavior of the system, and the middle state unstable. Theory states that all equilibrium points of a dependent variable as a function of two independent variables can form a smooth surface, like an ‘S’ shape (Arnold et al. 1999; Wiggins 2013). It suggests that, for the region in between the two inflections of the ‘S’ shape surface, there exist three equilibrium points fitting a same set of the two independent variables, which are referred to as multiple steady states in our study. A special feature is that, due to instability of the middle state, only the upper and lower states can be observed depending on the path of independent variables. In consequence, there could be an abrupt change in behavior with a small variation in independent variables. This behavior is similar to the three steady states observed in studies of foam generation without oil (Gauglitz et al. 2002; Kam and Rossen 2003; Lotfollahi et al. 2016b). In that case, in both modeling and experiments, three steady states were observed, with the middle state unstable.

2.3 Discussion and remarks

This study reveals the way in which current implicit-texture foam models represent the effect of oil on steady-state foam flow dynamics in porous media. In numerical simulation, it is a necessary first step to understand the interaction dynamics of foam with oil as represented in the current models. Results obtained in this study can provide a guidance on fitting parameter values. This study does not tell us what model is valid. If this model is

valid, it tells how to adjust it to fit data, or helps guide this process, once one has experimental data on the effect of oil on foam. In an experimental study, knowing the effects of model parameters examined on the two foam regimes can assist in interpreting the experimental data. A comparison study (Tang et al. 2017) has gathered experimental evidence for the effect of oil on the two foam regimes. Most of analyses here are consistent with their experimental observations.

Specifically, this study suggests that the wet and dry-out models capture the effects of oil only on the low- and high-quality regimes, respectively. The data of Tang et al. (2017) give evidence for the actual effect of oil on the two regimes, which can guide modeling and numerical simulation for foam flow with oil. Furthermore, both models predict multiple steady states. In the dry-out model, the multiple steady states arise from the interplay between S_w and S_w^* . In the wet-foam model, they arise from the change in $fmmob$ with changes in S_o . Experimental evidence is needed to verify the existence of the multiple steady states for foam flow with oil. The stability analysis above suggests that the final state achieved for each set of multiple steady states depends on initial reservoir condition. If such multiples steady states do exist, injection strategy and initial reservoir conditions for implementing foam EOR, for instance where and when to inject foam, and foam quality to be injected, are key for effectiveness of foam for gas mobility control.

2.4 Conclusions

The STARS foam model has two algorithms to represent the effect of oil saturation on foam: the so-called wet-foam model and the dry-out model. If the transition between high- and low-quality regimes is abrupt, then the parameters in the wet-foam model alter only the low-quality regime, while the dry-out model alters the high-quality regime. This information can guide the fitting of model parameters to experimental data for steady-state foam mobility as a function of superficial velocities of water, gas and oil.

Plotting apparent foam mobility as a function of injected foam quality can be confusing if oil is injected as a fixed fraction of water injection rate in the experiment. The plot can give the incorrect impression that the wet-foam model parameters alter the high-quality regime.

The STARS foam model predicts that multiple steady states are possible for some injection conditions and some sets of model parameters. This is not necessarily an artifact of the model: it is plausible that the final steady state achieved with long-time injection of foam and oil might depend, for instance, on initial oil saturation. Multiple steady states are found for both the wet-foam and dry-out models. In this initial study, we find three steady states for some injection conditions: a strong-foam state, one of collapsed foam, and an intermediate state that is unstable to perturbations. If the apparent viscosity is plotted as a function of fractional flows of water, gas and oil these states appear as a fold in that surface. This behavior is reminiscent of catastrophe theory and of multiple steady states previously observed in studies of foam generation without oil.

Because of the possibility of multiple steady states, experimental studies of steady-state foam behavior with oil should check for hysteresis and the effect of initial state on their results.

2.5 Nomenclature

- D_w, D_g, D_o = capillary diffusion coefficient for water, gas and oil, dimensionless (**Eq. 2.3**)
 $epdry$ = water parameter in foam model (wet-foam model), dimensionless (**Eq. A-3**)
 $efoil$ = oil exponent (dry-out model), dimensionless (**Eq. A-10**)
 $epoil$ = oil exponent (wet-foam model), dimensionless (**Eq. A-4**)
 $fmdry$ = limiting water saturation (wet-foam model), dimensionless (**Eq. A-3**)
 $fmmob$ = reference mobility reduction factor, dimensionless (**Eq. A-2**)
 $fmoil$ = upper-limiting oil saturation on foam (wet-foam model), dimensionless (**Eq. A-4**)
 $floil$ = lower-limiting oil saturation on foam (wet-foam model), dimensionless (**Eq. A-4**)
 f_w, f_g, f_o = water, gas and oil fractional flow, fraction
 f_g^* = transition foam quality from low- to high-quality regime
 f_{p0} = fractional flows into first grid block, fraction
 F_1 = effect of surfactant concentration on foam, dimensionless (**Eq. A-2**)
 F_2 = effect of water saturation on foam, dimensionless (**Eq. A-3**)
 F_3 = effect of oil saturation on foam, dimensionless (**Eq. A-4**)
 F_4 = effect of gas superficial velocity on foam, dimensionless (**Eq. A-2**)
 F_5 = effect of shear-thinning rheology on foam, dimensionless (**Eq. A-2**)
 F_6 = effect of critical capillary number on foam, dimensionless (**Eq. A-2**)
 F_7 = effect of water saturation on foam (dry-out model), dimensionless (**Eq. A-9**)
 FM = mobility reduction factor, dimensionless (**Eq. A-2**)
 G_2 = effect of oil saturation on foam (dry-out model), dimensionless (**Eq. A-10**)
 k = permeability, m²
 $k_{rw}^0, k_{rg}^0, k_{ro}^0$ = endpoint relative permeabilities of water, gas and oil, dimensionless
 k_{rw}, k_{ro} = water and oil relative permeability, dimensionless
 k_{rg} = foam-free gas relative permeability, dimensionless
 k_{rg}^f = effective gas relative permeability with foam, dimensionless
 n_g = gas exponent for Corey relative permeability, dimensionless
 n_w = water exponent for Corey relative permeability, dimensionless
 n_o = oil exponent for Corey relative permeability, dimensionless
 PV = pore volumes injected, dimensionless
 ∇p = pressure gradient, Pa/m
 $sfdry$ = limiting water saturation (dry-out model), dimensionless (**Eq. A-11**)
 $sfbet$ = water parameter in foam model (dry-out model), dimensionless (**Eq. A-9**)
 $sfoil$ = upper-limiting oil saturation on foam (dry-out model), dimensionless (**Eq. A-10**)
 $sloil$ = lower-limiting oil saturation on foam (dry-out model), dimensionless (**Eq. A-10**)
 S_w, S_o, S_g = water, oil and gas saturation
 $S_{w,max}$ = maximum water saturation at residual of the other two phases, fraction
 $S_{o,max}$ = maximum oil saturation at residual of the other two phases, fraction

- $S_{g, max}$ = maximum gas saturation at residual of the other two phases, fraction
 S_{wc} = connate water saturation, fraction
 S_{or} = residual oil saturation, fraction
 S_{gr} = residual gas saturation, fraction
 Δt = time step of each iteration, s
 U_t = total superficial velocity, m/s
 U_w, U_g, U_o = water, gas and oil superficial velocity, m/s
 Δx = grid-block size, m
 μ_w, μ_g, μ_o = water, gas and oil viscosity, Pa s
 μ_{app} = foam apparent viscosity, Pa s
 ϕ = porosity, fraction

Superscripts and subscripts

- f = foam
 o = endpoint relative permeability
 p = water, gas or oil phase
 i = grid block of length Δx

STEADY-STATE FOAM-FLOW REGIMES WITH OIL IN POROUS MEDIA

Summary

Foam flow in porous media without oil shows two regimes, depending on foam quality (gas fractional flow). Complexity and limited data on foam-oil interactions in porous media greatly restrict understanding of foam in contact with oil. Distinguishing which regimes are affected by oil is key to modeling the effect of oil on foam. We report steady-state corefloods to investigate the effect of oil on foam through its effect on the two flow regimes. We fit parameters of a widely used local-equilibrium foam model to data for foam-oil concurrent flow. This research provides a practical approach and initial data for simulating foam EOR in the presence of oil.

To ensure steady state, oil is co-injected with foam at a fixed ratio of oil (U_o) to water (U_w) superficial velocities in a Bentheimer sandstone core. Model oils used here consist of a composition of hexadecane, which is benign to foam stability, and oleic acid, which can destroy foam. Varying the concentration of oleic acid in the model oil allows one to examine the effect of oil composition on steady-state foam flow. Experimental results show that oil impacts both high- and low-quality regimes, with the high-quality regime more sensitive to oil. In particular, oil increases the limiting water saturation (S_w^*) in the high-quality regime and also reduces gas mobility reduction in the low-quality regime. Unevenly spaced ∇p contours in the high-quality regime suggest either strongly shear-thinning behavior or an increasingly destabilizing effect of oil. Pressure gradient (∇p) in the low-quality regime, in some cases, decreases with increasing U_w at fixed gas superficial velocity (U_g), either with or without oil. This may reflect either an effect of oil, if oil is present, or easier flow of bubbles under wetter conditions. Increasing oleic-acid concentration extends the high-quality regime to lower foam qualities, indicating more difficulty in stabilizing foam. Thus oil composition plays as significant a role as oil saturation (S_o).

A model fit assuming a fixed S_w^* and including shear-thinning in the low-quality regime doesn't represent the two regimes when the oil effect is strong enough. In such cases, fitting S_w^* to each ∇p contour and excluding shear-thinning in the low-quality regime yields a better match to these data. The dependency of S_w^* on S_o is not yet clear, owing to absence of oil-saturation data in this study. Furthermore, none of the current foam simulation models can capture the upward-tilting ∇p contours in the low-quality regime.

3.1 Introduction

Numerous laboratory studies and field pilots demonstrate that steady-state foam flow comprises two regimes, depending on foam quality (gas fractional flow) (Osterloh and Jante 1992; Alvarez et al. 2001): the high-quality (or coalescence) regime, which is dominated by foam stability, and the low-quality (or wet) regime, where foam strength is controlled by a mobility-reduction factor. **Figure 3.1** illustrates this behavior. These two regimes are central to understanding of foam without oil and also modeling of foam with oil, but this fundamental property is identified in the absence of oil. Owing to limited data available and the complexity of foam-oil interactions, the effect of oil on foam is not fully understood yet. This knowledge gap greatly limits our ability to represent the effect of oil on foam in modeling (Farajzadeh et al. 2012; Bergeron et al. 1993; Harkins and Feldman 1922): in particular, its effect on the two regimes central to our understanding of foam without oil. The effectiveness of foam in the presence of oil is key to successful application of foam for enhanced oil recovery (EOR). This issue hinders reliable design of foam processes and effective prediction of foam performance.

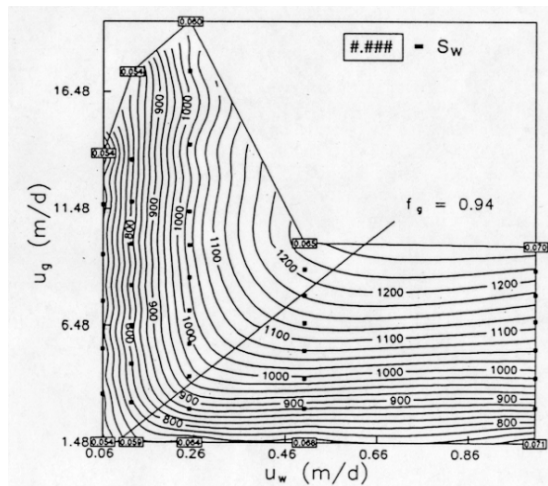


Figure 3.1 Pressure drop across a 2-ft sandpack as a function of superficial velocities of gas (U_g) and water (U_w). Pressure gradient in psi/ft is half the values listed. Contours of equal pressure drop are plotted through steady-state data represented by black points; from Osterloh and Jante (1992). The high-quality regime is to the upper left, and the low-quality regime is on the lower right.

Prior work on foam-oil interactions has identified some surface phenomenon and proposes some coefficients to represent them (Farajzadeh et al. 2012): e.g. entering coefficient (Bergeron et al. 1993), spreading coefficient (Harkins and Feldman 1922), bridging coefficient (Aveyard et al. 1994) and lamella number (Schramm and Novosad 1990, 1992). These coefficients can serve to represent the effects of oil on foam in bulk. However, foam behaviour identified in bulk is not necessarily consistent with that in porous media. In some cases, foam behaviour in these two scenarios contradicts each other. Besides, none of these coefficients is by itself a sufficient criterion for judging the stability of foam interacting with oil (Basheva et al. 2000). Moreover, these coefficients do not predict the effect of oil on foam quantitatively.

Some studies (Andrianov et al. 2011; Namdar Zanganeh et al. 2011) on the effect of oil on foam indicate that most of oils are detrimental to foam stability, and the lighter (also less viscous) the oil, the more harmful it is to

foam. But again, there is no quantitative, predictive model for the effect of oil on foam. Studies have shown that foam is destroyed when the oil saturation is above a critical oil saturation (Mannhardt et al. 1998). This critical oil saturation is used to model the oil effect on foam, as in the local-equilibrium implicit-texture (IT) model detailed in the Foam Models subsection. The critical oil saturation depends on the oil, rock and surfactant chemistry. For example, a critical oil saturation of 0.2 to 0.3 was used for the history-matching of the Snorre field pilot, (Spirov et al. 2012). However, there is no data on foam-oil interactions in steady-state flow documented in the literatures. Therefore oil parameters taken in simulating foam for EOR processes may not reflect the actual situation in the field.

A modeling study on the effect of oil on foam as discussed in Chater 2 (Tang et al. 2016) illustrates that foam-oil-interaction parameters in current foam models each shift one or the other of the two regimes. Depending on the model, the presence of oil shifts pressure gradient (∇p) contours in the high-quality regime to the right, indicating an increase in limiting water saturation below which foam collapses. Oil can also shift ∇p contours in the low-quality regime upwards, reflecting reduced resistance to bubble flow. Our goal here is to measure the effect of oil on foam in the laboratory to see whether the effect of oil can be represented by these models. Specifically, this study examines the effect of oil on foam through its effect on the two regimes initially identified in the absence of oil. A series of corefloods were carried out applying co-injection of foam and oil, with oil injected at a fixed ratio of oil superficial velocity (U_o) to water superficial velocity (U_w). Through this injection strategy, the effect of oil can be quantified. To examine the effect of oil composition on foam, for simplicity, two oil components were selected: one component, which is less destructive to foam (Simjoo and Zitha 2013), and the other one, which can destroy foam completely. Varying the proportion of these two oil components in the model oil allows one to examine the effect of oil composition on foam stability in media.

Then, applying a method similar to that of Cheng et al. (2000), for the first time, we fit a local-equilibrium IT foam model, adapted from widely used STARS model (Computer Modeling Group 2015), to experimental data for local-equilibrium (LE) foam flow in the presence of oil. (The acronym “LE” means generation and destruction rate of bubbles approach a balance immediately). This research provides a practical approach for measuring the effect of oil on foam in porous media. Initial data on foam-oil interactions obtained in this study give further insights for simulating foam for EOR in the presence of oil. Also, these data can serve as a case study for representing the behaviour of foam in contact with oil, and enhance the reliability of foam process design.

3.1.1 Foam models

Current foam models generally fall into two groups: “population-balance” models, characterizing the dynamics of bubble generation and destruction, coupled with gas mobility represented as a function of bubble size (Kovscek et al. 1995; Rossen 1996; Friedmann et al. 1991; Kam et al. 2007) and implicit-texture (IT) models, capturing effects of physical factors on LE foam flow, e.g. surfactant concentration, water saturation, oil saturation, salinity, capillary number and so forth (Cheng et al. 2000; Law et al. 1992; Patzek and Myhill 1989; Kular et al. 1989; Fisher et al. 1990; Islam and Ali 1988; Mohammadi et al., 1993). One earlier study (Myers and Radke 2000) attempted to incorporate the effect of oil on foam in a population balance model. However, the

effect of oil in their study is modeled by simply reducing bubble-generation rate, accounting for blockage of generation sites by the presence of residual oil. This approach is not sufficient to capture the actual interaction dynamics of foam and oil, e.g., effects of oil saturation and composition, or stability and strength of foam with oil, which are crucial for better understanding the fundamentals of foam with oil in porous media. This study focuses on fitting IT model parameters to experimental data.

In the local-equilibrium IT foam model studied here, foam reduces gas mobility by modifying gas relative permeability via a mobility factor FM :

$$k_{rg}^f = k_{rg}^0 \cdot FM \dots\dots\dots (3.1)$$

$$FM = \frac{1}{1 + fmmob \cdot F_1 \cdot F_2 \cdot F_3 \cdot F_4 \cdot F_5 \cdot F_6 \dots} \dots\dots\dots (3.2)$$

where $fmmob$, the reference gas mobility-reduction factor, is defined as the attainable maximum gas mobility reduction, F_1 through F_6 are functions accounting for the effects of physical factors on gas mobility, e.g. surfactant concentration, water saturation, oil saturation, oil composition, capillary number, salinity and etc. Here we consider three functions: F_2 , F_3 , and F_5 , capturing the effects of water saturation, oil saturation and shear-thinning in the low-quality regime, respectively. The foam model used includes two algorithms for the effect of oil on foam: the wet-foam model and the dryout model.

In the wet-foam model, F_2 represents the effect of water saturation on gas mobility,

$$F_2 = 0.5 + \frac{\arctan(epdry(S_w - fmdry))}{\pi} \dots\dots\dots (3.3)$$

where $epdry$ controls the abruptness of foam collapse as water saturation decreases below the limiting water saturation, $fmdry$, around which foam collapses. If $epdry$ is large, separate sets of parameters affect the high- and low-quality regimes, see, e.g., Cheng et al. (2000). The value of $fmdry$ is usually assumed to be fixed throughout the high-quality regime (Cheng et al. 2000; Boeije and Rossen 2015). This parameter is renamed as $sfdry$ in the dryout model. To avoid confusion, the limiting water saturation is mostly referred to here by its physical denotation, S_w^* .

In the foam model, the effect of oil is restricted by the upper and lower limiting oil saturations, distinguishing the oil saturation above which oil starts harming foam and that above which oil completely destroys foam. Specifically, oil saturation affects foam in the wet-foam model through scaling the reference mobility-reduction factor $fmmob$ via:

$$F_3 = \begin{cases} 1 & S_o \leq floil \\ \left(\frac{fmoil - S_o}{fmoil - floil} \right)^{epoil} & floil < S_o < fmoil \\ 0 & fmoil \leq S_o \leq 1 - S_{wc} - S_{gr} \end{cases} \dots\dots\dots (3.4)$$

where f_{oil} and f_{moil} are oil-related parameters marking the boundaries when oil destabilizes and destroys foam, respectively, and e_{poil} is the oil exponent.

F_5 , capturing shear-thinning behaviour in the low-quality regime, is given by

$$F_5 = \begin{cases} \left(\frac{f_{mcap}}{N_{ca}}\right)^{e_{pcap}} & N_{ca} \geq f_{mcap} \\ 1 & \text{else} \end{cases} \dots\dots\dots (3.5)$$

$$N_{ca} \equiv \frac{k \nabla P}{\sigma_{wg}} \dots\dots\dots (3.6)$$

where f_{mcap} and e_{pcap} are model parameters, and N_{ca} is capillary number, defined as a product of absolute permeability k multiplied by pressure gradient, divided by water-gas surface tension.

In the dryout model, oil affects gas mobility not by scaling f_{mmob} , but by modifying the limiting water saturation S_w^* . F_2 in the dryout model is rewritten as F_7 , given by

$$F_7 = 0.5 + \frac{\arctan(sf_{bet}(S_w - sf_{dry}))}{\pi} \dots\dots\dots (3.7)$$

where sf_{bet} and sf_{dry} play the same roles of ep_{dry} and fm_{dry} in wet-foam model, respectively. Nevertheless, sf_{dry} is not a constant in this model, but instead depends on oil saturation through function G_2 (similar to function F_3 in the wet-foam model):

$$[(1 - sf_{dry}) \cdot G_2 + sf_{dry}] \rightarrow sf_{dry} \dots\dots\dots (3.8)$$

$$G_2 = \begin{cases} 0 & S_o \leq sloil \\ \left(\frac{S_o - sloil}{sfoil - sloil}\right)^{e_{foil}} & sloil < S_o < sfoil \\ 1 & sfoil \leq S_o \leq 1 - S_{wc} - S_{gr} \end{cases} \dots\dots\dots (3.9)$$

where oil-related parameters $sloil$, $sfoil$, e_{foil} correspond to f_{oil} , f_{moil} and e_{poil} in the wet-foam model, respectively.

Tang et al. (2016) show that the wet-foam model represents the effect of oil only on the low-quality regime, while the dryout model captures the effect of oil only on the high-quality regime. However, these results indicate only the effect of oil on foam as represented by this model. The experimental data shown below demonstrate clearly which regimes are affected by oil and serve to check the suitability of the model. The procedures for fitting the model parameters to data are elaborated in Appendix C.

3.1.2 Experimental method

3.1.2.1 Experimental scheme

To examine the effect of oil on local-equilibrium (LE) foam flow in cores, first a series of pure hydrocarbons were screened using bulk-foam tests and coreflood evaluation, so as to select two oil components with a range of effects on foam. In particular, we wanted one component that destabilizes foam slightly and another that substantially destroys foam. The surfactant used is sodium alpha-olefin-sulfonate (AOS) at a concentration of 0.5 wt%, with a salinity of 3wt% NaCl. More details regarding the materials used can be found in Subsection 3.1.2.2 on the Apparatus and Materials. In the bulk-foam test, 5 ml of surfactant solution was mixed in a 10 ml test tube with 1 ml of different pure alkanes, e.g. C₁₆, C₁₄, C₁₂, C₁₀, C₉, C₈ and C₆. These test tubes were kept in an oven at 35°C to check if surfactant precipitates in contact with these alkanes. Foam then is generated by manually shaking these test tubes. The bulk-foam tests here were used to roughly characterize the defoaming potential of a variety of pure alkanes, in terms of surfactant precipitation, initial foam height and foam decay over time. This method can give a quick screening of the detrimental effect of those hydrocarbons examined.

Since foam behaviour in bulk is not always consistent with that in porous media, several candidates potentially meeting our expectations were examined again with corefloods for mobility-reduction factor (*MRF*). *MRF* is defined here as a ratio of pressure drop with foam to that with brine-only injection at the same total superficial velocity:

$$MRF = \frac{\Delta p_{fm}}{\Delta p_{nf}} \dots\dots\dots (3.10)$$

where Δp_{fm} and Δp_{nf} denote pressure drop with and without foam, respectively.

All corefloods in this study were conducted in Bentheimer sandstone at 35°C with a back-pressure fixed at 50 bar. The same core was used to guarantee consistency of experiments. To reuse the core, we cleaned the core by flushing it with, in order, isopropanol, CO₂, and water. Back pressure then is increased and reduced during water flushing to dissolve and remove CO₂ in the system. Two oil components were then selected combining the evaluation results of the bulk-foam tests and the initial screening corefloods. Before carrying out foam corefloods in the presence of oil, a set of experiments without oil were conducted first to identify the two regimes. These two regimes serve as a reference for comparing the effect of oil. During corefloods, instead of monotonically increasing or reducing gas (U_g) or water (U_w) superficial velocity, U_g and U_w were varied in a random sequence to avoid confusing any permeability loss over time with the effect of foam quality. Thereafter, a series of foam corefloods were conducted with oil co-injected concurrently, to examine steady-state interaction of foam and oil in porous media. Specifically, to measure the oil effect quantitatively and ensure steady state, foam was co-injected with oil at a fixed ratio R of oil (U_o) to water (U_w) superficial velocity. The variation in U_w therefore means a proportional change in U_o .

In our experiments, we didn't measure oil or water saturation, so they were estimated through relative-permeability functions. Therefore, it is not practical here to quantify directly foam mobility as a function of oil saturation. Varying the proportion of the two oil components selected allows one to investigate the effect of oil composition on the two regimes central to understanding of foam without oil.

3.1.2.2 Apparatus and materials

The injection system here allows for co-injection of three phases (water, oil, and gas) through two pumps for oil and surfactant solution, respectively, and a gas mass-flow controller, as shown in **Fig. 3.2**. The core-holder is equipped with 5 pressure taps for monitoring pressure drop across each section along the core during corefloods. The gap between the core and the core holder is connected with the inlet line to impose confining pressure. The whole core-holder is placed in a water bath maintained at 35°C. The pressure data are recorded by the data-acquisition system through LabVIEW (Elliott et al., 2007). The back-pressure regulator allows us to carry out experiments under elevated pressure and maintains stable outlet pressure.

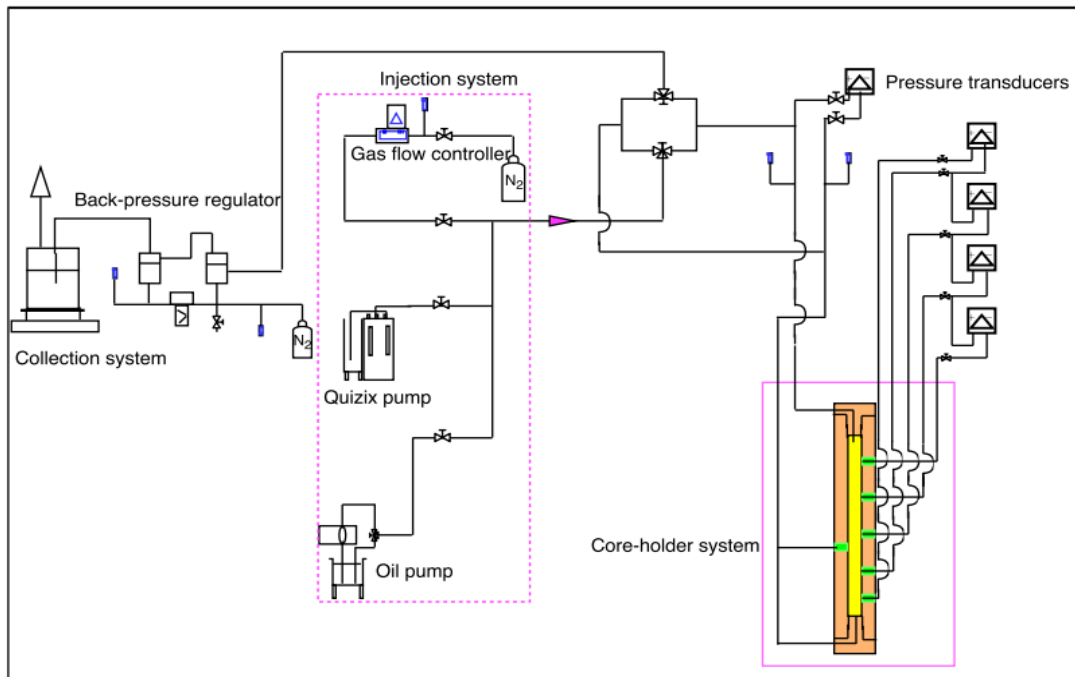


Figure 3.2 A schematic overview of apparatus used for steady-state foam corefloods, allowing for co-injection of oil, water and gas concurrently.

All corefloods conducted here were carried out in a Bentheimer core 4 cm in diameter and 40 cm in length, with an absolute permeability of 1.98 Darcy. The foaming agent used is AOS (sodium C_{14-16} olefin sulfonate) BIOTERGE[®] AS-40K with an activity of 40%, from Stepan company, USA. NaCl is the only salt used to provide salinity, which is 30,000 ppm in all experiments. To screen the oils for experimental study, pure hydrocarbons and oleic acid (OA) are examined, i.e. hexadecane (C_{16}), tetradecane (C_{14}), dodecane (C_{12}), decane (C_{10}), nonane (C_9), octane (C_8) and hexane (C_6). The gas injected is nitrogen. Oleic acid ($C_{18}H_{34}O_2$) with 99% purity was ordered from Honeywell Fluka in the Netherlands. All the alkanes are provided by Sigma-Aldrich, Co. in USA, with a purity of 99% for each.

In laboratory corefloods, a region near the inlet and a region close to the outlet may reflect an entrance or the capillary end effect, respectively. To minimize these effects, all the experimental results reported in the following section are based on data from the third section among the four sections monitored along flow direction. Most of time, when the pressure drops for the two middle sections are approximately equal and stable

with acceptable fluctuations, it is assumed to be a steady state for each measurement. For those injection conditions under which non-uniform state is achieved, we take the data of the second of the middle two sections.

3.2 Results

3.2.1 Oil screening

Comparing foam decay over time with and without oil in the bulk-foam test, in terms of foam height and texture, shows that hexadecane slightly destabilizes foam; after 1010 mins foam height decays by less than half but foam texture is coarse. However, for all the rest of the alkanes examined, foam completely collapsed after 230 mins, and the fewer the carbon atoms on the backbone, the more quickly foam decayed.

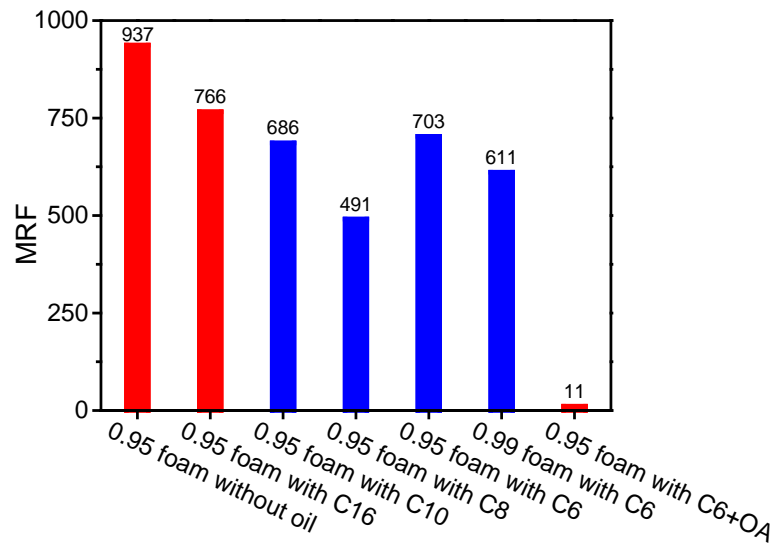


Figure 3.3 Gas mobility-reduction factor (MRF) as a function of oil type. Oil is co-injected with foam at a constant ratio of U_o to U_w of $\frac{1}{4}$ in a Bentheimer core of 1.98 Darcy. Total superficial velocity of U_w and U_g is fixed at 1.5 m/D. Foam quality (0.95 or 0.99) in this case is defined as $f_g = U_g / (U_g + U_w)$. The oil used in the last case consists of 10% OA and 90% C₆.

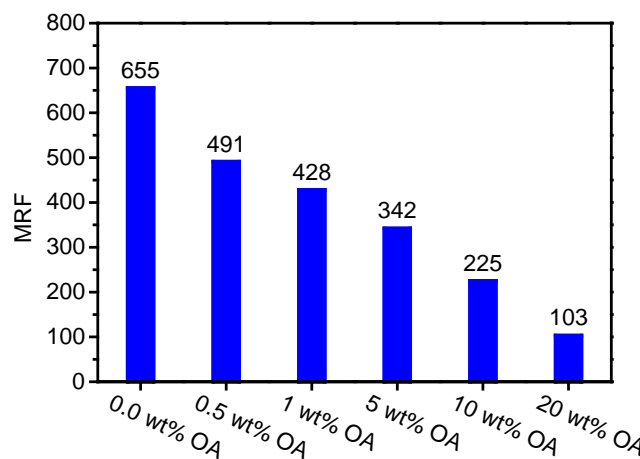


Figure 3.4 The effect of oleic-acid (OA) concentration on foam strength at a foam quality of 0.95 in a Bentheimer core of 1.92 Darcy. Foam quality in this case is defined as $U_g / (U_g + U_w)$. Total superficial velocity of U_w and U_g is fixed at 1.5 m/D. Oil is co-injected with foam at a constant ratio of U_o to U_w of $\frac{1}{4}$. The model oil consists of OA and C₁₆.

Given the concern about inconsistency between foam behaviour in bulk and in rock, C_{16} , C_{10} , C_8 and C_6 were examined again through corefloods in Bentheimer sandstone. The mobility-reduction factor with and without oil in **Fig. 3.3** shows that hexadecane (C_{16}), consistent with the bulk-foam test, is relatively benign to foam stability. However, C_{10} , C_8 and C_6 are not so effective at destroying foam in porous media, though they are detrimental to foam stability in bulk. Oleic acid, however, destroys foam almost completely.

The mobility reduction factor with various oils in **Fig. 3.3** appears to contradict the conclusion that the lighter the oil, the more detrimental it is to foam, in contrast to Andrianov et al. (2011) and Namdar Zanganeh et al. (2011). This issue is not addressed further here. The major intention of **Fig. 3.3** is a quick screening, to determine one oil component which can destroy foam, for the purpose of the following experiments. Taking these results into account, hexadecane and oleic acid were chosen as the two oil components: hexadecane as the one relatively benign to foam stability, and oleic acid as the one destroying foam completely. **Figure 3.4** shows that foam strength decreases greatly with increasing concentration of oleic acid in the model oil. In order to partly destroy foam but still maintain some foam strength, model oils with 10 wt% and 20 wt% OA were investigated. All experiments were conducted in a same core. To avoid interference of oils used before, we conducted experiments first without oil, then with C_{16} , 10% OA and 20%OA in model oil, respectively.

3.2.2 Two foam regimes with and without oil

3.2.2.1 LE foam flow without oil

Figure 3.5 demonstrates that steady-state foam flow in the absence of oil in a Bentheimer core shows two regimes, as expected. The contouring algorithm used is triangle linearization interpolation, which identifies triplets of nearest neighbour data and interpolates $\bar{\nu}p$ linearly within the triangles between those triplets. The high-quality regime appears at foam qualities above approximately 80%. The nearly vertical contours in this regime indicate independence of $\bar{\nu}p$ from U_g . Pressure gradient increases from about 100 to 500-600 psi/ft upon doubling U_w from 0.13 to 0.25 ft/D, indicating strongly shear-thickening rheology in the high-quality regime.

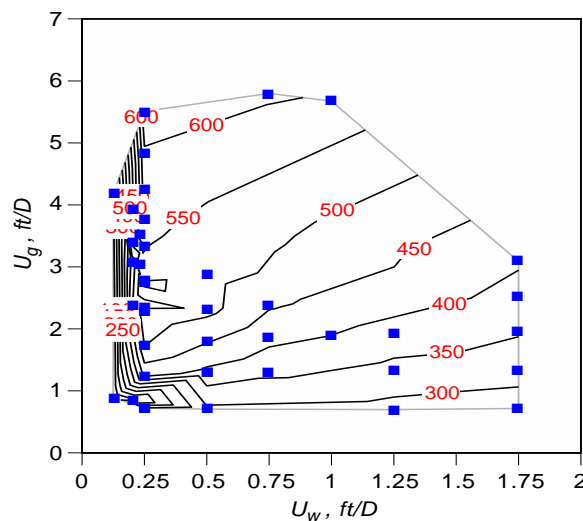


Figure 3.5 Pressure gradient (psi/ft) in the absence of oil, as a function of gas (U_g) and water (U_w) superficial velocities (ft/D) at 35°C in a Benteimer core of 1.98 Darcy. Individual data are indicated by blue symbols. Each filled symbol here represents a steady-state measurement.

However, the $\bar{\nabla}p$ contours in the low-quality regime in **Fig. 3.5**, instead of appearing horizontal as in **Fig. 3.1**, tilt upward to the top right. This means that $\bar{\nabla}p$ in the low-quality regime decreases with increasing U_w at fixed U_g . The studies of de Vries and Wit (1990) and Kim et al. (2005) on CO₂ foam in a variety of porous media suggest similar behavior in the low-quality regime. The study of Hirasaki and Lawson (1985) on foam apparent viscosity in smooth capillaries and the study of Kim et al. on LE CO₂ foam suggest that this behavior may arise from easier flow of bubbles under wetter conditions. Specifically, increasing U_w in the low-quality regime implies an increase in water saturation; there are thicker water films around bubbles, and therefore less flow resistance (less drag on bubble flow). This consequently yields lower $\bar{\nabla}p$ at higher U_w at fixed U_g . More efforts are needed to examine the exact mechanism for upward-tilting $\bar{\nabla}p$ contours in the low-quality regime.

3.2.2.2 LE foam flow with C₁₆

Figure 3.6 shows that steady-state concurrent foam-oil flow (C₁₆ in this case) still produces the two flow regimes as identified in the absence of oil: high- and low-quality regimes. Although hexadecane only slightly destabilizes foam in the bulk-foam tests, apparently both high- and low-quality regimes are affected by the presence of this oil. For the same range of U_g and U_w examined in **Fig. 3.5**, $\bar{\nabla}p$ in the presence of C₁₆ in **Fig. 3.6** is restricted below about 220 psi/ft, nearly three times lower than that without oil (600 psi/ft) in **Fig. 3.5**.

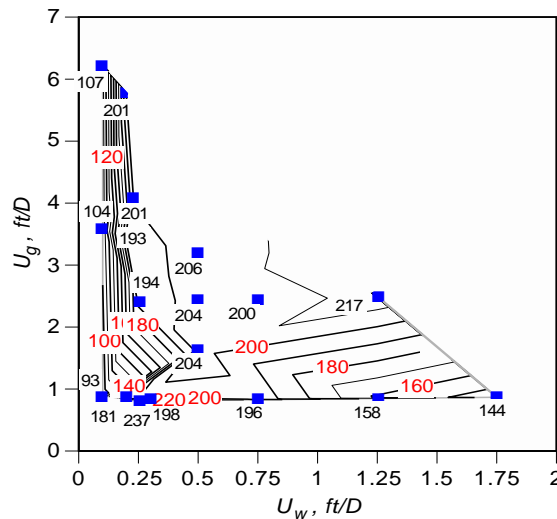


Figure 3.6 Pressure gradient (psi/ft) in the presence of oil, as a function of gas (U_g) and water (U_w) superficial velocities (ft/D) at 35°C in a Benteimer core of 1.98 Darcy. Individual data are indicated by blue symbols. Oil used is hexadecane, co-injected with foam at a fixed ratio of U_o to U_w of R=0.25. Each filled symbol represents a steady-state measurement.

The high-quality regime in **Fig. 3.6** shifts to right compared to **Fig. 3.5**. This suggests that oil reduces foam stability in the high-quality regime by increasing the limiting water saturation (S_w^*) below which foam collapses. The linear relationship between U_w and $\bar{\nabla}p$ in the data at 0.1 and 0.2 ft/D in this regime demonstrates nearly Newtonian rheology, reflecting an approximately constant S_w^* . The low-quality regime in **Fig. 3.6** shifts to lower foam qualities compared with **Fig. 3.5** (approximately below 0.75). $\bar{\nabla}p$ in the low-quality regime in **Fig. 3.6** is reduced by a factor about two relative to that in **Fig. 3.5**, a reduction lesser than in the high-quality regime. Also,

∇p contours in the low-quality regime of **Fig. 3.6**, similar to those in **Fig. 3.5**, also tilt upward with increasing U_w . Since foam in this case is flowing together with oil, the upward-tilting ∇p contours may reflect either easier flow of bubbles under wetter conditions, or the destabilizing effect of oil on foam strength, or a combination of both effects.

The greater decrease in gas-mobility reduction in the high-quality regime than in the low-quality regime reveals that foam in the high-quality regime is more vulnerable to oil. For instance, in the high-quality regime of **Fig. 3.6** with C_{16} , $(U_w, U_g)=(0.2, 2)$ gives a ∇p of 160 psi/ft, 2.5 times lower than the ∇p obtained with the same set of flow rates in **Fig. 3.5** without oil, 400 psi/ft. In the low-quality regime, for $(U_w, U_g)=(1, 1.5)$, the ∇p in **Fig. 3.6** yields out 190 psi/ft, about 1.9 times lower than 360 psi/ft obtained the same set of flow rates in **Fig. 3.5**.

3.2.2.3 LE foam flow with 10 wt% OA in model oil

Introduction of oleic acid, though only 10 wt% in the model oil, plays a significant role on foam behavior and leads to some new behavior. **Figure 3.7** illustrates that only the high-quality regime has been observed for the same range of U_w and U_g as examined in **Fig. 3.5** and **Fig. 3.6**. The generally vertical trend of ∇p contours in the high-quality regime of **Fig. 3.7** suggests that S_w^* is still independent of U_g .

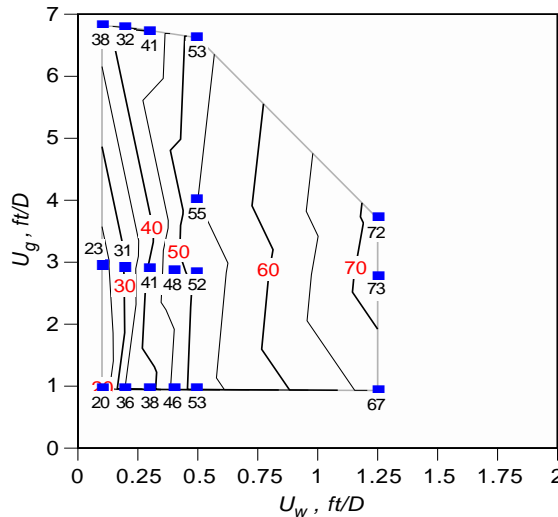


Figure 3.7 Pressure gradient (psi/ft) in the presence of oil, as a function of gas (U_g) and water (U_w) superficial velocities (ft/D) at 35°C in a Benteimer core of 1.98 Darcy. Individual data are indicated by blue symbols. Model oil used consists of 10% oleic acid and 90% hexadecane, co-injected with foam at a fixed ratio of U_o to U_w of $R=0.25$. Each filled symbol represents a steady-state measurement.

The high-quality regime in **Fig. 3.7**, compared to that in **Fig. 3.5** and **Fig. 3.6**, extends to a much greater range of U_w . This suggests that the introduction of OA greatly increases S_w^* , weakening foam to a much larger extent than C_{16} . But the ∇p contours in this regime reveal non-Newtonian behavior: ∇p depends on U_w , but not linearly. Based on Darcy’s Law, the non-linear dependence of ∇p on U_w in the high-quality regime indicates that the S_w^* , usually represented as a constant throughout the high-quality regime in the absence of oil, rises with increasing U_w in the presence of oil. Since oil and foam here are co-injected at a fixed ratio of U_o to U_w , increasing U_w here

also means increasing oil saturation, suggesting a greater destabilizing effect. However, the specific dependence of S_w^* on S_o is not clear yet owing to lack of oil-saturation data during corefloods. The decrease in apparent viscosity with increasing total superficial velocity may reflect either shear-thinning rheology or destabilizing effect of oil on foam.

Fig. 3.7 also illustrates that the high-quality regime in the presence of 10 wt% OA extends down to much lower foam qualities (transition foam quality $f_g^* < 0.44$), compared with **Fig. 3.5** and **Fig. 3.6**. This suggests a greater destabilizing effect of oil on foam than with C_{16} . For instance, $(U_w, U_g)=(0.2, 2)$ in **Fig. 3.7** yields a $\bar{\nu}p$ of 31 psi/ft, nearly 13 times lower than $\bar{\nu}p$ obtained for the same set of flow rates in **Fig. 3.5**.

3.2.2.4 LE foam flow with 20 wt% OA in model oil

Figure 3.8 shows the two foam-flow regimes with 20 wt% OA. The data are extended to lower U_g than with 10 wt% OA in **Fig. 3.7**. Both high- and low-quality regimes show modestly shear-thinning behavior. However, similar to **Fig. 3.7**, the high-quality regime in **Fig. 3.8** shifts to the right and extends to a greater range of U_w . The low-quality regime shrinks to much lower foam qualities (below approximately 0.2). It suggests that the increase in the concentration of more-harmful oil component in an oil mixture destabilizes foam to a greater degree.

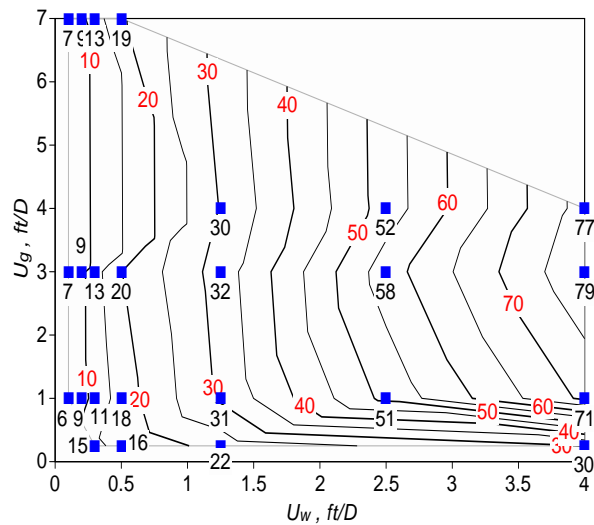


Figure 3.8 Pressure gradient (psi/ft) in the presence of oil, as a function of gas (U_g) and water (U_w) superficial velocities (ft/D) at 35°C in a Benteimer core of 1.98 Darcy. Individual data are indicated by blue symbols. Model oil used consists of 20% oleic acid and 80% hexadecane, co-injected with foam at a fixed ratio of U_o to U_w of $R=0.25$. Each filled symbol represents a steady-state measurement.

The maximum $\bar{\nu}p$ achieved in **Fig. 3.8** is about 13.3 times lower than that without oil in **Fig. 3.5** for same range of flow rates examined, demonstrating again that oil affects both the high-quality and low-quality regimes. The more detrimental effect of oil on foam in **Fig. 3.8** clearly suggests that the high-quality regime bears greater vulnerability to oil. For instance, $\bar{\nu}p$ at $(U_w, U_g)=(2, 0.7)$, in the low-quality regime of **Fig. 3.8**, is approximately 40 psi/ft, about 6.8 times less than that in the absence of oil, 271 psi/ft in **Fig. 3.5**. But $\bar{\nu}p$ in the high-quality

regime of **Fig. 3.8**, e.g. 9 psi/ft at $(U_w, U_g)=(0.2, 2)$, is nearly 40 times less than that in **Fig. 3.5** (400 psi/ft) for the same pair of superficial velocities.

All the experimental conditions are the same in **Fig. 3.7** and **Fig. 3.8** except the oil composition. A 10 wt% increase in OA in the model oil causes approximately a 2-3 times decrease in gas mobility reduction, e.g. 9 psi/ft in **Fig. 3.8** v. 31 psi/ft in **Fig. 3.7** at $(U_w, U_g)=(0.2, 2)$, or 30 psi/ft in **Fig. 3.8** v. 67 psi/ft in **Fig. 3.7** at $(U_w, U_g)=(1.25, 1)$. This suggests that oil composition plays as significant a role as oil saturation on foam stability. The absence of data on oil saturation throughout our experiments makes it difficult to quantitatively compare the effect of oil saturation to that of oil composition on those two regimes. But co-injecting oil and foam at a fixed ratio of U_o to U_w indicates that lower U_w , qualitatively, also means lower oil saturation, suggesting less destabilization of foam.

3.2.3 Fit of model parameters to data

Simulating foam EOR processes in contact with oil confronts many challenges (Farajzadeh et al. 2012; Rossen 2013). One striking challenge among others is which regimes are affected by oil and how oil affects those two regimes. Our experimental data demonstrate that oil affects both regimes but by a different magnitude. Specifically, oil affects the high-quality regime through its effect on limiting water saturation and the low-quality regime through its effect on gas-mobility reduction. Fitting foam model parameters to these data provides a reference for the simulation and prediction of foam performance in the presence of oil. Note that oil saturation is difficult, if not impossible, to control during corefloods. It is not a constant in our experiments of **Figs. 3.6, 3.7** and **3.8**. One must estimate oil saturation using the oil relative-permeability function, which of course introduces some uncertainty.

3.2.3.1 Model fit results

Here, we present a method similar to that of Cheng et al. (2000) to fit model parameters to the data of **Figs. 3.5, 3.6, 3.7**, and **3.8**. In particular, three major functions in the foam model are considered in our model fit to capture the physical effects of water saturation, oil saturation and shear-thinning on the two regimes. Essentially, one needs to fit two key parameters: limiting water saturation S_w^* , dominating the high-quality regime, and reference mobility-reduction factor f_{mob} , controlling the low-quality regime. All foam parameters in this model shift the two regimes by modifying the two key parameters. The parameter $epcap$ in F_5 (**Eq. 3.5**) here is used to capture shear-thinning behavior in the low-quality regime. Detailed fitting procedure applied in this study can be found in Appendix C.

Table 3.1 summarizes the parameter values, with and without accounting for shear-thinning, fitted to the data of **Figs. 3.5, 3.6, 3.7**, and **3.8**, applying the fitting procedure described in the Appendix C. **Figures B-1** and **B-2** illustrate the representative ∇p contours for 300 psi/ft with f_g^* at $(U_w, U_g)=(0.17, 0.75)$ from **Fig. 3.5** and for 160 psi/ft with f_g^* at $(U_w, U_g)=(0.2, 0.9)$ from **Fig. 3.6**, respectively. **Figures B-3** and **B-4** illustrate the contours plotted from **Figs. 3.7** and **3.8**, particularly for fitting S_w^* to each ∇p contour. The mobility-reduction factor for the case with 20% OA in **Fig. B-4** is fitted based on the 30 psi/ft contour with f_g^* at $(U_w, U_g)=(1.17, 0.45)$. The superscript of f_{mob}^* indicates that it excludes shear-thinning, while f_{mob} is the reference mobility-reduction factor adjusted for shear-thinning. When oil is introduced, both f_{mob}^* and f_{mob} incorporate the effects of oil.

Model parameter $epdry/sfbet$ is set to a large value, e.g. 20000, to give an abrupt transition between regimes. The assumption of an abrupt transition is justified in our data as well, as shown in **Figs. B-5** and **B-6** in the Appendix B. The value of $fmcap$ in **Figs. 3.5** and **3.6** is based on the contour for 50 psi/ft, and in **Figs. 3.7** and **3.8** on the contour for 3 psi/ft, to allow shear-thinning to have effect. The model fits to the data of **Figs. 3.6** through **3.8** use the same value of $epcap$ based on the data of **Fig. 3.5** to account for shear-thinning in the low-quality regime. In other words, in our initial fit we assume that the presence of oil doesn't alter the shear-thinning nature of the low-quality regime.

Table 3.1 Overview of fitted parameter values using STARS foam model for all data

Cases	Fitted parameters							
	$fmmob^*$	F_3^*	$fmmob$	F_3	$fmdry /sfdry$	$epdry/sfbet$	$epcap$	$fmcap$
Without oil	$2.26 \cdot 10^5$	–	$5.99 \cdot 10^6$	–	0.146	$2.00 \cdot 10^4$	1.83	$7.50 \cdot 10^{-5}$
C_{16}	$9.73 \cdot 10^4$	0.431	$8.18 \cdot 10^5$	0.137	0.148	$2.00 \cdot 10^4$	1.83	$7.50 \cdot 10^{-5}$
10% OA	Low-quality regime not observed				0.160 at 20 psi/ft	$2.00 \cdot 10^4$	1.83	$4.48 \cdot 10^{-6}$
					0.160 at 30 psi/ft			
					0.162 at 40 psi/ft			
					0.164 at 50 psi/ft			
					0.169 at 60 psi/ft			
0.173 at 70 psi/ft								
20% OA					0.170 at 7 psi/ft	$2.00 \cdot 10^4$	1.83	$4.48 \cdot 10^{-6}$
					0.180 at 10 psi/ft			
					0.183 at 20 psi/ft			
					0.188 at 30 psi/ft			
					0.191 at 40 psi/ft			
					0.193 at 50 psi/ft			
0.194 at 60 psi/ft								
0.194 at 70 psi/ft								

Model fit assumes a large value of $epdry/sfbet$; here, we use a value of $2 \cdot 10^4$.

Figures 3.9 and **3.10** show the model fit in the absence of oil. For experiments in the presence of oil, **Figs. 3.11** through **3.16** are plotted using a combination of the dryout model and wet-foam model to capture, respectively, the effects of oil on the high- and low-quality regimes. The model fit without oil or with oil slightly destabilizing foam, as C_{16} does here, assuming a constant S_w^* throughout the high-quality regime and considering shear-thinning in the low-quality regime, gives good agreement with data. However, when oil that is substantially detrimental to foam is introduced, the model fit with above assumptions doesn't show a good match to data. Instead, a better fit to data is obtained with S_w^* fitted separately to each ∇p contour in the high-quality regime and shear-thinning neglected in the low-quality regime. In other words, the presence of these oils (10 wt% and 20 wt% OA) changes the nature of shear rheology in the low-quality regime.

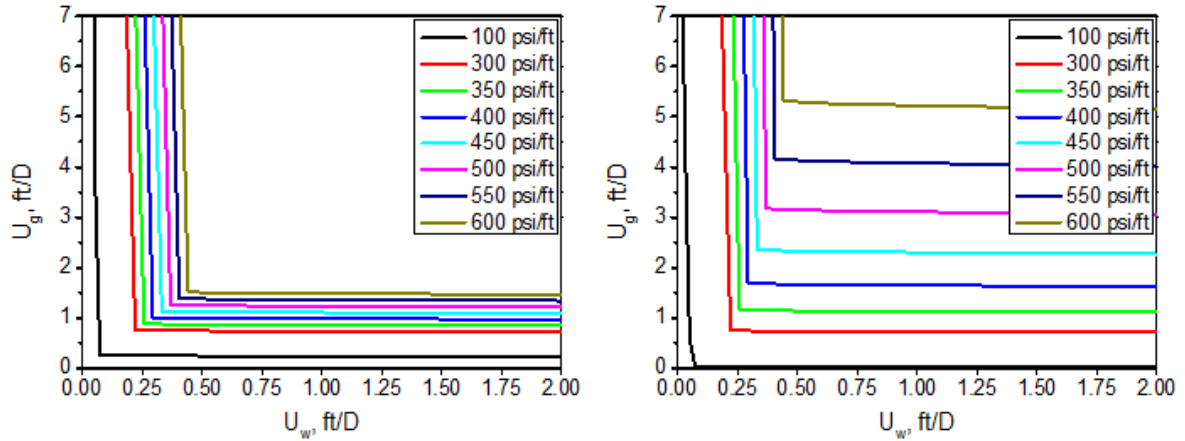


Figure 3.9 (left) Model fit to data of **Fig. 3.5** in the absence of oil, ignoring shear-thinning in the low-quality regime: $fmmob^*=2.26 \cdot 10^5$, $fmdry=0.146$, $epdry=2.00 \cdot 10^4$.

Figure 3.10 (right) Model fit to data of **Fig. 3.5** in the absence of oil, including shear-thinning in the low-quality regime: $fmmob=5.99 \cdot 10^6$, $fmdry=0.146$, $epdry=2.00 \cdot 10^4$, $epcap=1.83$; $fmcap=7.50 \cdot 10^{-5}$.

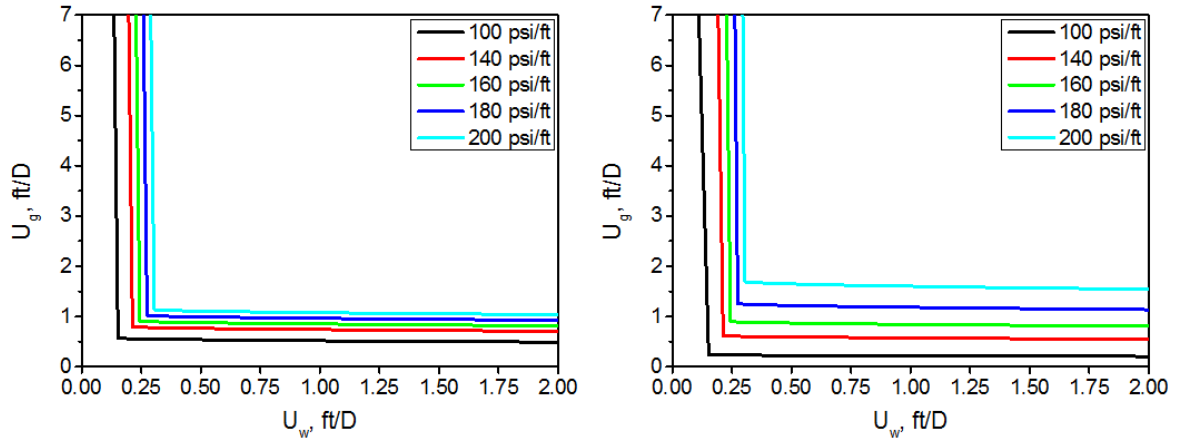


Figure 3.11 (left) Model fit to data of **Fig. 3.6** in the presence of C_{16} , excluding shear-thinning in the low-quality regime: $fmmob^*=9.73 \cdot 10^4$, $sfdry=0.148$, $sfbet=2.00 \cdot 10^4$.

Figure 3.12 (right) Model fit to data of **Fig.3.6** in the presence of C_{16} , including shear-thinning in the low-quality regime: $fmmob=8.18 \cdot 10^5$, $sfdry=0.148$, $sfbet=2.00 \cdot 10^4$, $epcap=1.83$; $fmcap=7.50 \cdot 10^{-5}$.

Specifically, **Figs. 3.9** through **3.12** illustrate that the high-quality regime fitted assuming a constant S_w^* throughout this regime shows a good agreement with the data of **Figs. 3.5** and **3.6**, respectively, although not representing the shear-thickening behaviour in this regime. **Figure 3.9** (without considering shear-thinning in the low-quality regime) and **Figure 3.10** (with shear-thinning) demonstrate that considering shear-thinning in the low-quality regime gives much better match to the data of **Fig. 3.5** in the absence of oil. The same conclusion can also be drawn for model fit to data of **Fig. 3.6** in presence of C_{16} , which is slightly detrimental to foam. However, in both cases, either with or without oil, the fitted results fail to capture the upward-tilting ∇p contours in the low-quality regime, thereby greatly overestimating ∇p in this regime. Therefore, this issue requires improvement of the current models to represent ∇p behaviour in the low-quality regime.

Figure 3.13 shows that when 10 wt% OA is introduced, the high-quality regime fitted using a fixed S_w^* fails to represent the data of **Fig. 3.7**. The assumption of a constant S_w^* throughout the high-quality regime doesn't apply there, in particular when the oil effect is great. Therefore, S_w^* was fitted separately to each ∇p contour in **Fig. B-3**. The resulting model fit in **Fig. 3.14** shows much better agreement with the data than in **Fig. 3.13**, suggesting that S_w^* here is a function either of oil saturation or ∇p . Owing to absence of low-quality-regime data in **Fig. 3.7**, fitted results in this regime in **Figs. 3.13** and **3.14** do not reliably represent the low-quality regime.

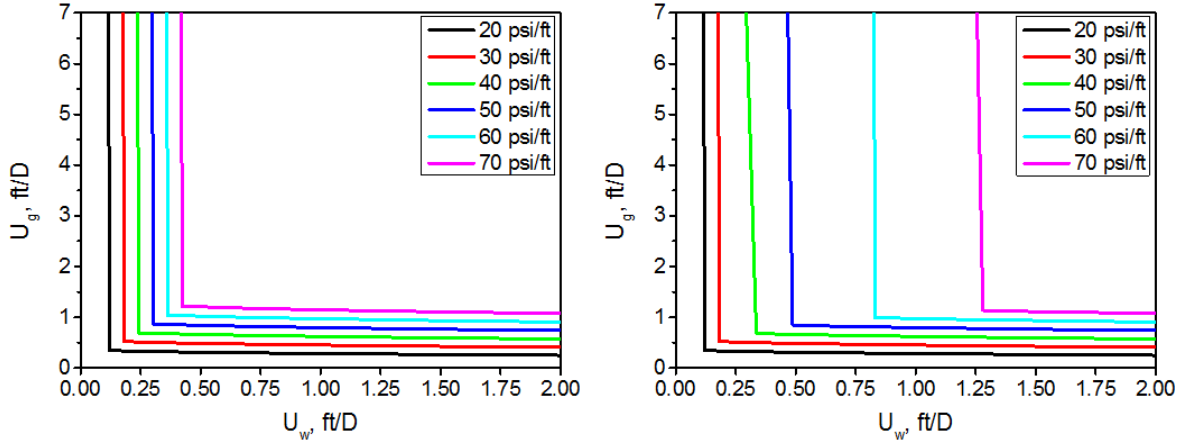


Figure 3.13 (left) Model fit to data of **Fig. 3.7** with 10 wt% OA in model oil based on a representative ∇p contour of 30 psi/ft, excluding shear-thinning in the low-quality regime: $fmmob^*=3.00 \cdot 10^4$, $sfdry=0.160$, $sfbet=2.00 \cdot 10^4$.

Figure 3.14 (right) Model fit to data of **Fig. 3.7** with 10 wt% OA in model oil, excluding shear-thinning in the low-quality regime: $fmmob^*=3.00 \cdot 10^4$, $sfbet=2.00 \cdot 10^4$. **Table 3.1** gives limiting water saturation corresponding to each ∇p contour in the high-quality regime.

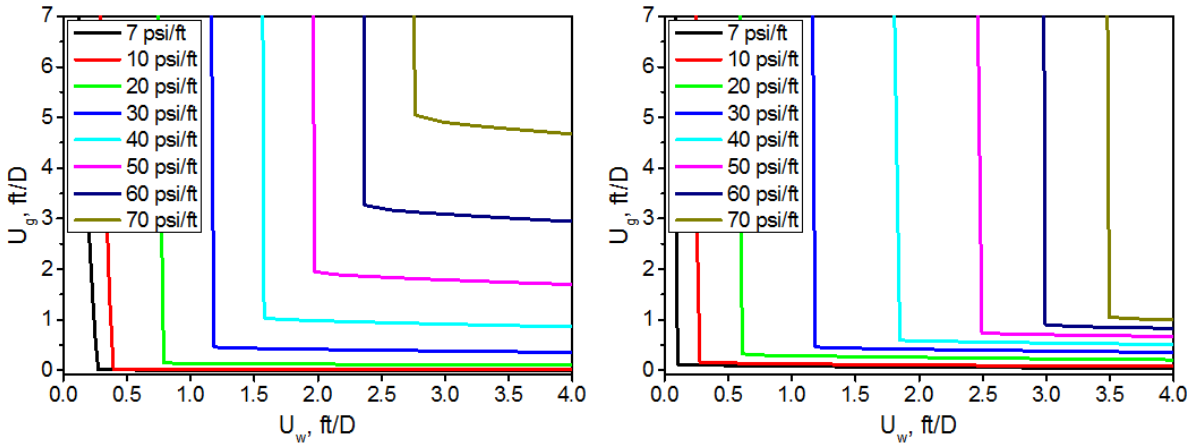


Figure 3.15 (left) Model fit to data of **Fig. 3.8** with 20 wt% OA in model oil based on a representative ∇p contour of 30 psi/ft, assuming shear-thinning in the low-quality regime as fit to data without oil: $fmmob=2.00 \cdot 10^6$, $sfdry=0.188$, $sfbet=2.00 \cdot 10^4$, $epcap=1.83$; $fncap=4.48 \cdot 10^6$.

Figure 3.16 (right) Model fit to data of **Fig. 3.8** with 20 wt% OA in model oil, excluding shear-thinning in the low-quality regime: $fmmob^*=2.96 \cdot 10^4$, $sfbet=2.00 \cdot 10^4$. **Table 3.1** gives the values of limiting water saturation corresponding to each ∇p contour in the high-quality regime.

The model fit in **Fig. 3.15** also assumes a fixed S_w^* , showing again a great mismatch to the high-quality-regime in **Fig. 8**. Nevertheless, **Fig. 3.16**, fitting S_w^* based on each specific $\bar{\nu}p$ contour in **Fig. B-4** agrees well with the data, suggesting again that S_w^* is a function either of $\bar{\nu}p$ or of some other properties, such as oil saturation, that depend on $\bar{\nu}p$. **Figure 3.15** shows that the model fit in the low-quality regime, using the same shear-thinning fitted based on the data without oil, does not match the data of **Fig. 3.8**. Ignoring shear-thinning in this regime, as shown in **Fig. 3.16**, gives much better agreement to the data of **Fig. 3.8** than does **Fig. 3.15**.

3.2.3.2 Attempt to fit oil-related parameters in the model

The model fits illustrated in **Figs. 3.13** through **3.16** suggest that S_w^* varies with $\bar{\nu}p$, U_w , or U_o when OA is present. This implies that for given oil composition S_w^* is a function of oil saturation (S_o) and of $\bar{\nu}p$, U_w , and/or U_o . Comparisons of the effect of oil composition must therefore be made at the same superficial velocities. At the same conditions, our data indicate, OA in the oil destabilizes foam and increases the value of S_w^* .

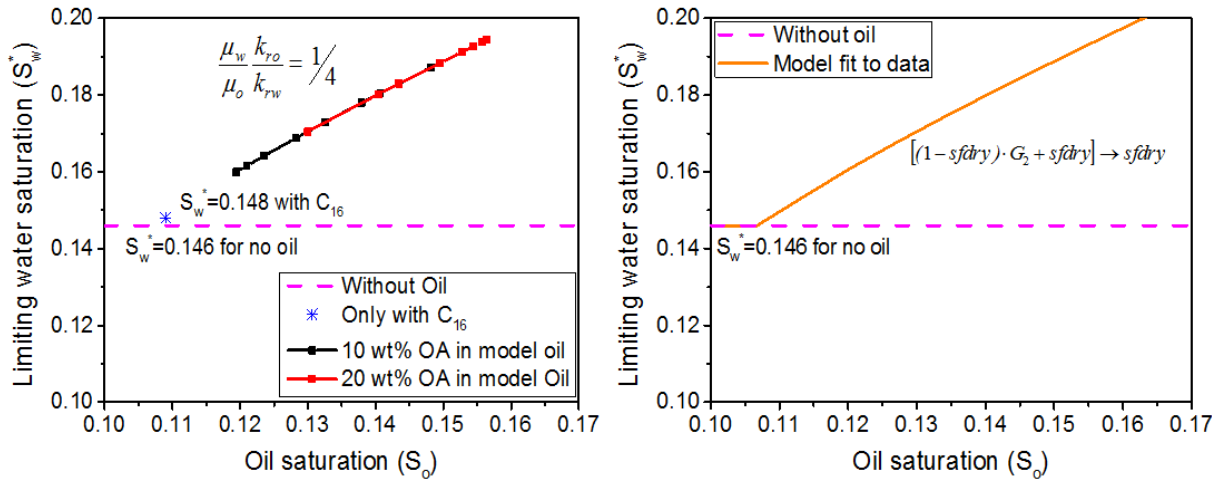


Figure 3.17 (left) The dependence of limiting water saturation (S_w^*) on oil saturation (S_o) based on data of **Figs. 3.7** and **3.8**. S_o on black and red curves is calculated using relative-permeability functions in **Table C-1**.

Figure 3.18 (right) Model fit to **Fig. 3.17** using oil-related parameters in dryout model: $s_{oil}=0.1079$, $s_{foil}=1.4512$, $e_{foil}=0.8645$.

In the foam model in **Eqs. 3.7** to **3.9**, sf_{dry} (representing S_w^*) is a function of S_o . However, the constraint that $U_o/U_w = 1/4$ in our experiments also implies, through the oil- and water-relative-permeability functions, a relation between S_w^* and S_o , since Darcy's law must be satisfied for both phases. **Figure 3.17** shows our model-fitted values of S_w^* and S_o , from **Figs. 3.10**, **3.12**, **3.14** and **3.16**. All the data fit on a single curve, which suggests if one could fit the relation between S_w^* and S_o to this curve one could represent all our results in the current model, without including oil composition, and in addition explaining the apparent non-Newtonian behaviour in the high-quality regime as an indirect reflection of the dependence on oil saturation. In our model fit we assume Corey-type relative-permeability functions for oil and water. However, if the oil- and water-relative-permeability functions are fixed and depend only on S_o and S_w^* , any set of data (S_o , S_w^*) at fixed U_o/U_w must lie on a single curve such as that in **Fig. 3.17**. Thus the trend of the results in **Fig. 3.17** reflects the use of Corey functions and fixed U_o/U_w , not directly the effect of oil on foam.

This conclusion can be demonstrated as follows. **Figure 3.18** shows a model fit to the data using **Eqs. 3.7** to **3.9**, obtained as follows. Using any three sets of (S_o, S_w^*) data in **Fig. 3.17**, the oil-related parameters (s_{oil} , s_{foil} , e_{foil}) in **Eqs. 3.8** and **3.9** can be determined. Fitted results plotted in **Fig. 3.18** give a good match to data in **Fig. 3.17**. The fit is specious, however. **Figure 3.19** shows the behaviour predicted with these parameters, which differs dramatically in the high-quality regime from the data on which the model was based. The reason is as follows. Suppose one could fit the relation $U_o/U_w = 1/4$ in **Fig. 3.17** exactly using a dryout function $S_w^*(S_o)$ in **Eqs. 3.8** and **3.9**. For some superficial velocities (U_{oa}, U_{wa}) in the high-quality regime, let S_{oa} and S_{wa} be the corresponding saturations and $\bar{\nabla}p_a$ the pressure gradient. Consider some multiple of $\bar{\nabla}p_a$, say $\bar{\nabla}p_b = 10 \bar{\nabla}p_a$. Let S_{ob} be the oil saturation with 10 times smaller $k_{ro}(S_o)$ than S_{oa} . The dryout function $S_w^*(S_o)$ gives a value S_{wb} also with 10 times smaller k_{rw} than S_{wa} . The same pair of superficial velocities can be fit to a different pressure gradient - in fact, an infinite number of pressure gradients.

The imperfect fit in **Fig. 3.18** to our results **Fig. 3.17** gives a unique solution for $\bar{\nabla}p$ (**Fig. 3.19**) but one with little relation to the original data. A fit to our data for the high-quality regime must include in addition the effects of oil composition and possibly $\bar{\nabla}p$, U_w , or U_o .

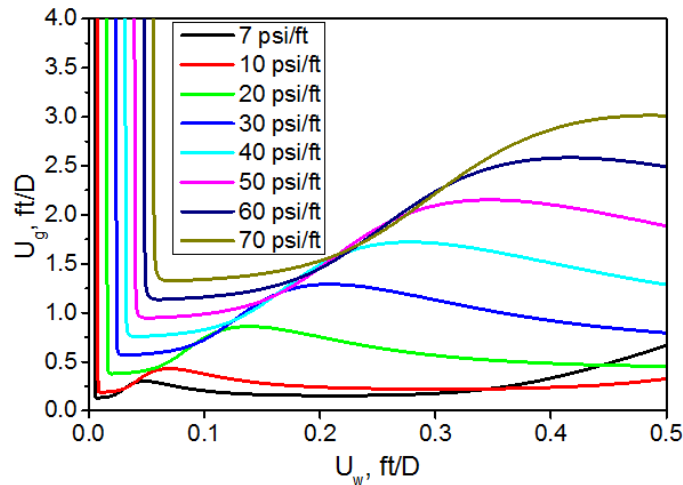


Figure 3.19 Model fit to data of **Fig. 3.8** with 20 wt% OA in model oil, excluding shear-thinning in the low-quality regime: $fmmob^*=2.96 \cdot 10^4$, $sfbet=2.00 \cdot 10^4$, $s_{oil}=0.1079$, $s_{foil}=1.4512$, $e_{foil}=0.8645$. Oil-free limiting water saturation is 0.146 as suggested from **Fig. 3.10**.

3.3 Discussion and remarks

This chapter is a companion study of modeling the effect of oil on foam in Chapter 2 (Tang et al. 2016). The modeling study shows how the effect of oil is represented in the current foam models. To describe the data of steady-state foam flow dynamics with oil, both of wet-foam model and dryout model are necessary to capture the effect of oil on each regime, respectively. The experimental study here provides a practical approach to quantify the effect of oil on steady-state foam behaviour through its effect on the two foam regimes. The method applied for model fitting to the data is simple; each step has a clear physical meaning. This process can give a quick but effective estimation of foam-model parameters for simulation of foam flow through porous media with oil. In a case without adequate data for the two foam regimes, one can use a single foam-quality scan to get similar

parameter values (Cheng et al. 2000). The good match between the fitted results and the data verifies that the model works in representing the foam behaviour with oil, which is a good place to start in simulating foam displacement with oil. Owing to lack of data in oil saturation for each measurement, fitting the oil-related parameters is constrained. Therefore, to relate oil saturation to foam properties, it is recommended to run experiments with oil saturation monitored during corefloods by using visualizing techniques like CT. This study works with a model oil consisting of one component less destructive to foam, and the other one greatly detrimental to foam. It might suggest that the effect of lighter components in crude oil on foam is approximately an interpolation of these two components. Emulsions were observed in the effluent of the experiments with oil. It is unclear how that would affect foam stability in the corefloods. Some studies show that foam injected into a core (co-injection of surfactant solution and gas) with oil takes significantly longer time to approach steady state than without oil. We didn't find this to be the case for our experiments with co-injection of foam and oil. More efforts are still needed to investigate the fundamentals of foam dynamics with oil in porous media, either at steady state or in a dynamic process.

3.4 Conclusions

This study provides an initial approach to simulating foam EOR using steady-state data for flow in the presence of oil.

Experimental data show that the high- and low-quality regimes, central to understanding of foam without oil, also apply in concurrent foam-oil flow. The presence of oil affects foam flow in both regimes, with the high-quality regime more vulnerable to oil. Oil composition plays as significant a role as oil saturation on foam flow.

Specifically, oil, in the high-quality regime, affects foam stability by increasing the limiting water saturation (S_w^*) below which foam collapses. In the low-quality regime, oil lessens gas mobility reduction.

Either with or without oil, in some cases pressure gradient (∇p) decreases with increasing water superficial velocity (U_w) at fixed gas superficial velocity (U_g). This may reflect either easier flow of bubbles under wetter conditions in the absence of oil or an increasing destabilizing effect of oil on foam with increasing U_w and U_o .

Without oil, foam flow in this study shows strongly shear-thinning behaviour in the low-quality regime. This behaviour changes greatly when oil is present. Foam rheology in the high-quality regime in some cases shows Newtonian behavior, but in some others shear-thickening or shear-thinning behaviour.

We present an approach for fitting local-equilibrium implicit-texture foam-model parameters to data for ∇p as a function of U_g and U_w , including shear-thinning in the low-quality regime and the effect of oil on both regimes. To fit the data with oil, both of wet and dryout models are needed simultaneously to represent each regime. Assuming a fixed S_w^* throughout the high-quality regime and including shear-thinning in the low-quality regime with or without oil doesn't give a good match to data, particularly when the oil effect is strong enough. In such cases, one has to fit S_w^* separately to each ∇p contour in the high-quality regime and exclude shear-thinning in the low-quality regime to represent data in both regimes.

Model fits to our data in the high-quality regime suggest that S_w^* is a function of S_o and of ∇p , U_o or U_w . To fit our data, one must include effects of oil composition and possibly ∇p , U_o or U_w . None of current foam simulation models can capture the upward-tilting ∇p contours seen in some cases in the low-quality regime.

3.5 Nomenclature

- $epdry$ = water parameter in foam model (wet-foam model), dimensionless (Eq. 3.3)
- $efoil$ = oil exponent (dryout model), dimensionless (Eq. 3.9)
- $epoil$ = oil exponent (wet-foam model), dimensionless (Eq. 3.4)
- $epcap$ = shear-thinning exponent, dimensionless (Eq. 3.5)
- $fmdry$ = limiting water saturation (wet-foam model), dimensionless (Eq. 3.3)
- $fmmob$ = reference mobility reduction factor, dimensionless (Eq. 3.2)
- $fmoil$ = upper-limiting oil saturation on foam (wet-foam model), dimensionless (Eq. 3.4)
- $floil$ = lower-limiting oil saturation on foam (wet-foam model), dimensionless (Eq. 3.4)
- $fmcap$ = reference capillary number, dimensionless (Eq. 3.5)
- f_g^* = transition foam quality between the two regimes, fraction
- FM = mobility reduction factor, dimensionless (Eq. 3.2)
- F_1 = effect of surfactant concentration on foam, dimensionless (Eq. 3.2)
- F_2 = effect of water saturation on foam, dimensionless (Eq. 3.3)
- F_3 = effect of oil saturation on foam, dimensionless (Eq. 3.4)
- F_4 = effect of gas superficial velocity on foam, dimensionless (Eq. 3.2)
- F_5 = effect of shear-thinning rheology on foam, dimensionless (Eqs. 3.5 and 3.6)
- F_6 = effect of critical capillary number on foam, dimensionless (Eq. 3.2)
- F_7 = effect of water saturation on foam (dryout model), dimensionless (Eq. 3.7)
- G_2 = effect of oil saturation on foam (dryout model), dimensionless (Eq. 3.9)
- k = permeability, m²
- k_{rw}, k_{ro} = water and oil relative permeability, dimensionless
- k_{rg}^0 = foam-free gas relative permeability, dimensionless
- k_{rg}^f = effective gas relative permeability with foam, dimensionless
- MRF = mobility-reduction factor, dimensionless (Eq. 3.10)
- N_{ca} = capillary number, dimensionless
- Δp = pressure drop, Pa
- ∇p = pressure gradient, Pa/m
- $sfdry$ = limiting water saturation, dimensionless (Eq. 3.7)
- $sfbet$ = water parameter in foam model (dryout model), dimensionless (Eq. 3.7)
- $sfoil$ = upper-limiting oil saturation on foam (dryout model), dimensionless (Eq. 3.9)
- $sloil$ = lower-limiting oil saturation on foam (dryout model), dimensionless (Eq. 3.9)
- S_w^* = water saturation at limiting capillary pressure, fraction
- S_w, S_o, S_g = water, oil and gas saturation

- S_{wc} = connate water saturation, fraction
 S_{or} = residual oil saturation, fraction
 S_{gr} = residual gas saturation, fraction
 T = temperature, °C
 U_t = total superficial velocity, m/s
 U_w, U_g, U_o = water, gas and oil superficial velocity, m/s
 μ_w, μ_g, μ_o = water, gas and oil viscosity, Pa s
 σ_{wg} = water/gas surface tension, N/m

Superscripts and subscripts

- a, b = denoting two different states
 f = foam
 fm = in the presence of foam
 nf = in the absence of foam

FRACTIONAL-FLOW MODEL INSIGHTS INTO FOAM-OIL DISPLACEMENT

Summary

Foam is injected into porous media in a variety of fields across enhanced oil recovery, acid well stimulation, aquifer and soil remediation, and CO₂ storage. However, the interaction between foam and an oleic phase in these processes remains a long-standing challenge. We apply three-phase fractional-flow theory and the wave-curve method to find theoretical solutions for the multiphase transport of foam with oil in porous media. Foam is represented through a widely used implicit-texture model.

Physical insights are derived from the theoretical solutions on two key aspects: the dependence of the displacement upon injection (J) and initial (I) conditions and the effects of improved oil-tolerance of the surfactant formulation on the velocities of foam propagation and of the oil bank displaced by foam. The displacement structure is revealed for four representative scenarios, with different combinations of J and I that each allow or kill foam. We also show that numerical simulations where an oil bank has an oil saturation greater than the limiting saturation for foam stability ($f_{m oil}$ in our model) reflect a numerical artifact. This contradiction may arise from the calculation of pressure and pressure gradient using neighbouring grid blocks in a simulation. Enhancing foam tolerance to oil accelerates foam-bank propagation and also achieves greater oil recovery.

4.1 Introduction

The sweep efficiency of gas injection into geological formations, e.g. aquifers or oil reservoirs, is usually very poor, caused by gravity override, viscosity instability and rock heterogeneity (Glass and Yarrington, 2003; Reynolds and Krevor, 2015). Foam in porous media is an aggregation of gas bubbles that are separated by thin aqueous films, called lamellae, stabilized by surfactant (Rossen, 1996). With foam, gas mobility is reduced substantially, i.e. by an order of $10 \sim 10^6$, due to entrapment of gas bubbles and increased capillary resistance to flow (Schramm, 1994; Rossen, 1996). This allows foam to have a broad engineering application in a variety of fields: oil displacement in the petroleum industry (Rossen, 1996; Lake et al., 2014); acid diversion in well stimulation (Zhou and Rossen, 1995); removal of NAPL (Non-Aqueous Phase Liquid) contaminants in soils and aquifers (Estrada et al., 2015; Bertin et al., 2017); and recently, carbon storage in CCUS (Carbon Capture, Utilization and Storage) for mitigating the impact of CO₂ on climate (Bui et al., 2018; Castaneda-Herrera et al., 2018).

One key to success of the applications above is the effectiveness of foam for gas-mobility control in presence of oils or other NAPL's, because they in most cases destabilize foam (Farajzadeh et al., 2012). Fractional-flow theory, aka the Method of Characteristic (MOC), is a powerful analytical tool that can provide crucial physical insights on a displacement (Charbeneau, 1988; LaForce and Johns, 2005; Rossen et al., 2011; You et al., 2015). In addition, fractional-flow theory acts as an important benchmark for numerical simulations, given the numerical challenges in a complex multiphase system such as foam (Rossen, 2013). We apply this theory together with the wave curve method (WCM) (Castañeda et al., 2016) to three-phase flow and find theoretical solutions for foam flow with oil through porous media. In our study, foam in porous media is represented with an implicit-texture (IT) foam model, STARS, that is widely used in the petroleum industry (Computer Modeling Group, 2015). Appendix D gives the details of the IT model that is coupled with a three-phase fractional-flow model for solving mass-conservation equations for three-phase flow.

Prior experimental studies demonstrate that steady-state foam flow through porous media without oil shows two regimes depending on foam quality, f_g – gas volumetric fractional flow in foam (Osterloh and Jante, 1992; Alvarez et al., 2001): the high- and low-quality regimes. Tang et al. (2018) in a recent study find that these two regimes also apply to foam with oil, as illustrated in the steady-state data of **Fig. 4.1a** (with oil) and **Fig. 4.2a** (with oil). Physically, the presence of oil affects both the two regimes; this is implied by the shift of upper-left vertical pressure-gradient ∇p contours in the high-quality regime and lower-right ∇p contours in the low-quality regime in **Fig. 4.2a** relative to **Fig. 4.1a**. Specifically, in the high-quality regime, oil destabilizes foam through its effect on the limiting capillary pressure (Zhou and Rossen, 1995), that corresponds to the limiting water saturation S_w^* around which foam collapses. In the low-quality regime, oil weakens foam through its effect on a reference gas-mobility-reduction factor $fmmob$. (The STARS model does not fit the upward-tilting ∇p contours in the low-quality regime in Fig. 1a (cf. Kim et al., 2005). No currently applied foam simulation model yet accounts for this aspect of foam behavior.)

Figure 4.1b and **Figure 4.2b** are the associated model fit to data without oil (**Fig. 4.1a**) and with oil (**Fig. 4.2a**), respectively, using the IT model. In general, there is a good match between model fit and data, which demonstrates the validity of the IT model for representing foam flow both with and without oil. This agreement between data and the IT model justifies the necessity of understanding the implications of this model for foam flow with oil in geological formations.

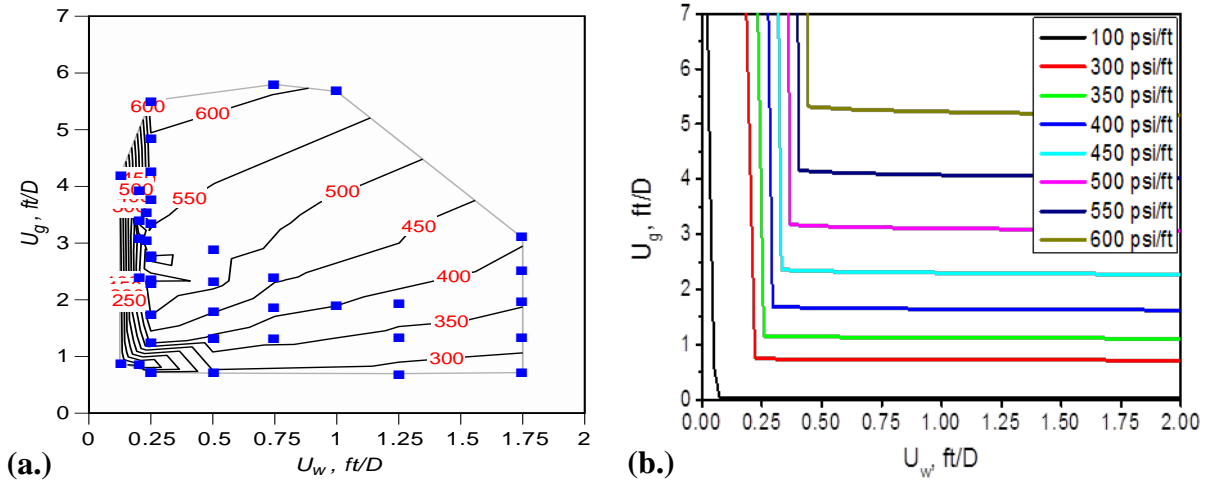


Figure 4.1 Pressure gradient (psi/ft) without oil as a function of gas (u_g) and water (u_w) superficial velocities in a Bentheimer core of 1.98 Darcy: (a) steady-state data (indicated by blue symbols), based on which the contours are plotted; (b) implicit-texture model fit to data of **Fig. 4.1a**. Results from Tang et al. (2018).

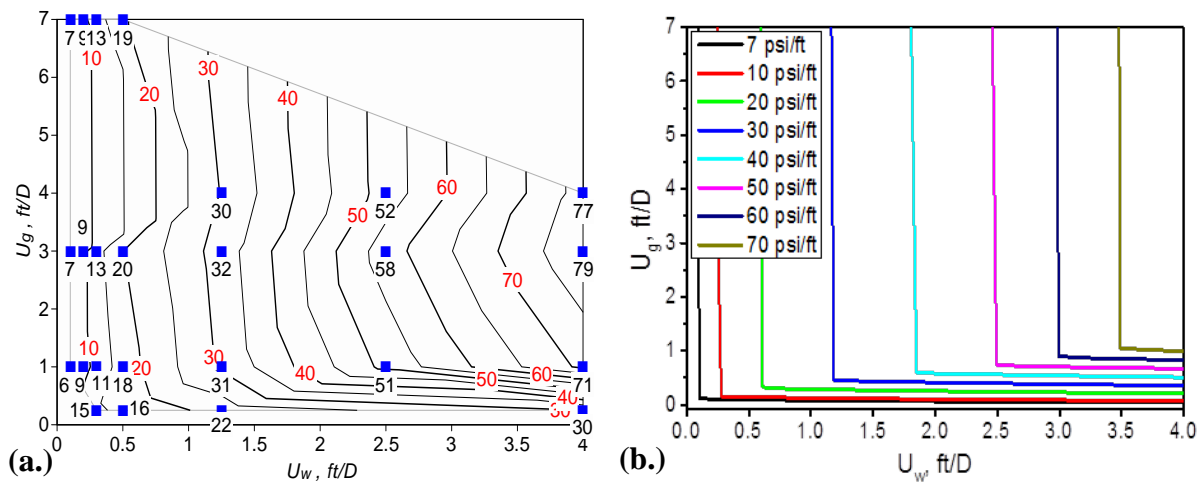


Figure 4.2 Pressure gradient (psi/ft) with oil as a function of gas (u_g) and water (u_w) superficial velocities in a Bentheimer core of 1.98 Darcy: (a) steady-state data (indicated by blue symbols), based on which the contours are plotted; (b) implicit-texture model fit to data of **Fig. 4.2a**. Oil is introduced at a fixed oil/water superficial velocity ratio, 0.25. Results from Tang et al. (2018).

A few field applications have designed foam to collapse in contact with oil, with foam remaining in the oil-free zone to divert subsequently injected agents, e.g. CO_2 , to displace oil (Holm and Garrison, 1988). We assume here that foam is intended to remain stable to oil and, if possible, displace oil directly. In general, we address two key issues concerned with foam displacement: the dependence of the displacement structure (wave type, configuration and fluid mobility) upon initial (I) and injection (J) conditions and the effects of foam tolerance for oil on propagation velocities of foam and of the oil bank. The structure of foam flow with oil is solved for four

representative scenarios with I and J that each either allow or kill foam. The desirability of the displacement structure in each scenario is analysed based on the mobility ratio of the displacing and displaced fluids at the displacement front, foam propagation velocity and oil recovery. Foam stability, especially within an oil bank, is analysed based on theoretical solutions. We then compare the theoretical solutions with a numerical solution in the literature to check the reliability of numerical results. Finally, we show the impact of oil-related factors on foam propagation.

This study is not aimed at fitting or predicting behavior for a particular reservoir, but more generally shows the fundamentals of foam for gas-mobility control and foam displacements with oil in porous media. The methodology and physical insights presented here can be to guide to the interpretation of foam-assisted gas-mobility control and displacements with oil. One can then optimize the design and maximize the benefits of foam processes in its various engineering applications.

4.2 Theoretical background and foam model

4.2.1 Three-phase fractional-flow theory

We show below the governing equations for foam-oil flow through porous media, and the general concepts of three-phase fractional-flow theory and the wave-curve method (WCM). For the more-complete development of this theory, one may refer to Lake et al. (2014), and for the principles of the WCM, to Castañeda et al. (2016) and Liu (1974).

The system of foam flow with oil involves three phases (i.e. water, oil and gas) and interactions between foam and the oleic phase. Mathematically, solving for three-phase flow with all factors considered is a challenge. For the purpose of this study, the system is simplified as follows:

- flow is one dimensional;
- Fractional flows are functions only of local phase saturations and independent of saturation history, spacial phase distribution and flow rates;
- fluids and rock are both incompressible;
- gravity effects can be ignored;
- all phases are immiscible;
- the process is isothermal;
- no dispersive processes are considered (e.g. diffusion, dispersion, and capillary-driven flow);
- local equilibrium is attained immediately;
- all phases have Newtonian rheology;
- surfactant concentration is uniform in the aqueous phase everywhere.

Crucially, in this initial study there is no phase-behavior advantage for foam in displacing oil – no oil-swelling by gaseous components, stripping of oil components into gas, or gas-oil miscibility. In the Corey representation, residual oil saturation to gas is the same as residual to water. Therefore predictions of oil recovery for this process are pessimistic for a gas-injection process that takes advantage of those additional mechanisms. For such a process, mobility control is the key to improving sweep efficiency and delivering gas to zones where these advantages can work.

With the abovementioned assumptions, the system is governed by two independent mass-conservation equations, as follows:

$$\varphi \frac{\partial S_w}{\partial t} + u \frac{\partial f_w}{\partial x} = 0, \dots\dots\dots (4.1)$$

$$\varphi \frac{\partial S_o}{\partial t} + u \frac{\partial f_o}{\partial x} = 0, \dots\dots\dots (4.2)$$

where φ is the porosity of a rock, S_w and S_o are the water and oil saturations, x and t , are the position and time, and u is the total superficial velocity of the three phases. In particular, f_w and f_o are the water and oil fractional flows, defined as:

$$f_j \equiv \frac{u_j}{u}, \dots\dots\dots (4.3)$$

where subscript $j = w, o$ and g denotes water, oil and gas, respectively, and u_j is the Darcy velocity of phase j . f_j indicates the flow potential of phase j , which is a key concept introduced in fractional-flow theory.

Darcy velocity u_j of phase j in **Eq. 4.3** is defined by Darcy's law:

$$u_j = \frac{kk_{rj}}{\mu_j} |\nabla p|, \dots\dots\dots (4.4)$$

where k is the absolute permeability of a medium, k_{rj} is the relative permeability of phase j , μ_j is the viscosity of phase j , $|\nabla p|$ is the magnitude of pressure gradient. k_{rj} of phase j is given by Corey-type relative-permeability model and is assumed to be a function of only its own phase saturation:

$$k_{rj} = k_{rj}^0 \left(\frac{S_{j,a} - S_{jr}}{1 - S_{wc} - S_{or} - S_{gr}} \right)^{n_j}, \dots\dots\dots (4.5)$$

where k_{rj}^0 with superscript 0 is the endpoint relative permeability of phase j , S_{wc} , S_{or} and S_{gr} are the residual saturations of water, oil and gas, $S_{j,a}$ and S_{jr} are the absolute and residual saturation of phase j with n_j being the Corey exponent.

Given that $u = u_w + u_o + u_g$, substituting **Eq. 4.4** into **Eq. 4.3** for phase j transforms f_j to:

$$f_j = \frac{k_{rj} / \mu_j}{k_{rw} / \mu_w + k_{ro} / \mu_o + k_{rg}^f / \mu_g}, \dots\dots\dots (4.6)$$

where (k_{rj} / μ_j) represents the relative mobility of phase j , superscript f denotes the presence of foam and k_{rg}^f is thus the effective gas relative permeability with foam. Through k_{rg}^f , the foam model in Appendix D is coupled with the fractional-flow model in **Eq. 4.6** to represent foam flow with oil. The introduction of foam in **Eq. 4.6** does not change the k_{rw} or k_{ro} functions in **Eq. 4.5**, but only the k_{rg} function, through a mobility-reduction factor FM in **Eq. D-1** (in Appendix D). This assumption that k_{rw} is unaffected by foam is justified by a number of experimental studies and facilitates foam-flow modeling (Rossen, 1996; Schramm, 1994). FM includes F_2 in **Eq.**

D-3 (a function of S_w) and F_3 in **Eq. D-8** (a function of S_o). Therefore, f_j is a function of only saturations (S_w , S_o).

To simplify **Eqs. 4.1** and **4.2**, we introduce dimensionless position x_D and dimensionless time t_D :

$$x_D \equiv \frac{x}{L}, \dots\dots\dots (4.7)$$

$$t_D \equiv \frac{u \cdot t}{(1 - S_{wc} - S_{or} - S_{gr}) L \phi}, \dots\dots\dots (4.8)$$

where L is the reservoir length, and t_D is the number of movable pore volumes injected. S_j , the saturation of phase j , is normalized with respect to the total movable saturations:

$$S_j \equiv \frac{S_{j,a} - S_{jr}}{1 - S_{wc} - S_{or} - S_{gr}}. \dots\dots\dots (4.9)$$

With these dimensionless and normalized variables, the system of **Eqs. 4.1** and **4.2** is simplified to

$$\frac{dS}{dt_D} + \frac{dF}{dx_D} = 0 \dots\dots\dots (4.10)$$

where capitals S and F without superscript or subscript are vectors of $\begin{pmatrix} S_w \\ S_o \end{pmatrix}$ and $\begin{pmatrix} f_w \\ f_o \end{pmatrix}$, respectively.

One major goal here is to solve the system in **Eq. 4.10** for saturations S_w and S_o , as a function of x_D and t_D . Fractional-flow theory states that any S propagates through a permeable medium with a given wave velocity that is a function of S . To solve for $S_w(x_D, t_D)$ and $S_o(x_D, t_D)$, one needs to solve for wave velocities for all saturations that appear in a displacement. The velocity of S is given by derivatives of fractional flows with respect to saturations (Lake et al., 2014):

$$\eta(S) \equiv \frac{dx_D}{dt_D} = \frac{dF}{dS}. \dots\dots\dots (4.11)$$

The derivatives in **Eq. 4.11** are solved through RPN (n-dimensional Riemann Problem), a program developed in the Group of Fluid Dynamics at IMPA (Instituto Nacional de Matemática Pura e Aplicada, in Brazil), which implements the WCM.

The WCM produces two major solutions for a displacement (Azevedo et al., 2010; Castañeda et al., 2016): a composition path that connects injection state J to initial state I , and associated wave velocities of the saturations along the path. $S_w(x_D, t_D)$ and $S_o(x_D, t_D)$ in a displacement are illustrated on a saturation profile as a function of position at any given time.

A complete composition path is solved by constructing two families of wave curves: a forward slow wave curve starting from J , and a backward fast wave curve initiating from I . These two families of wave curves usually

cross, resulting in an intermediate state IJ at the intersection. A complete path follows the path from J to IJ , and then to I . Shock waves along a path are solved through the Rankine-Hugoniot locus, based on a mass balance across the shock:

$$F(S) - F(S_I) = \sigma(S - S_I) \dots\dots\dots (4.12)$$

where S_I with subscript I denotes the saturations at the initial state I , and σ is the shock velocity from S_I to S .

4.2.2 Foam model

The IT model STARS includes two algorithms to represent the effect of oil on foam, i.e. the “wet-foam” algorithm for the effect of oil on the low-quality regime and the “dry-out” algorithm for the effect of oil on the high-quality regime (Tang et al., 2019). The wet-foam model (in Appendix D) is implemented in this initial study, but we believe results using the dry-out model would be similar.

Foam in the IT model modifies gas mobility by reducing gas relative permeability k_{rg} in Eq. 4.5 through a mobility-reduction factor FM as in Eq. D-1. FM accounts for the effects of a series of physical factors on foam stability and strength, e.g. surfactant concentration, water saturation, oil saturation, shear-thinning rheology, and salinity. FM in our analysis includes a reference-mobility-reduction factor $fmmob$ and two key functions, F_2 in Eq. D-3 for the effect of S_w and F_3 in Eq. D-8 for the effect of S_o .

The arctangent function for F_2 in Eq. D-3 is approximated here by a polynomial function in Eq. D-7, to facilitate the calculation of derivatives of fractional flows in Eq. 4.11. Parameter $fmdry$ in Eq. D-3 or D-7 represents the limiting water saturation S_w^* around which foam collapses; the abruptness of the collapse depends on an adjustable parameter $epdry$. F_3 describes the effect of oil on foam with two limits in S_o , i.e. the upper-limiting oil saturation $fmoil$ above which foam is killed completely and the lower-limiting oil saturation $floil$ below which oil has no impact. For S_o between $fmoil$ and $floil$, oil has a non-linear effect on foam as described in Eq. D-8.

Table D-1 in Appendix D summarizes the model parameter values. We use a value for $fmmob$ less than that obtained in the lab (Boeije and Rossen, 2015; Cheng et al., 2000), to account for the decrease in gas-mobility reduction due to field complexities, e.g. adverse wettability, high salinity or high temperature. A large value for $epdry$ is assumed, which corresponds to an abrupt foam collapses at S_w around S_w^* .

Figure 4.3 plots $(1/FM)$ in Eq. D-2 as a function of (S_w, S_o) in ternary saturation space, with F_2 (Eq. D-7) and F_3 (Eq. D-8) included. Figure 4.3 illustrates a foam-property map that is characterized by the values of $(1/FM)$ shown using the color bar; a larger value of $(1/FM)$ indicates larger gas-mobility reduction and thus stronger foam. The plot of $(1/FM)$ splits the ternary diagram into two regions: the foam region with $(1/FM) > 1$, indicated by the colored lower-left patch, and the no-foam region with $(1/FM) =$ or ~ 1 , indicated by the white portion of the ternary diagram. The foam region comprises two portions: full-strength foam for $S_o < floil$ and $S_w > (S_w^* + \varepsilon)$, where $\varepsilon = [1/(0.2 \times epdry)]$ (Eq. D-5) and partially-destabilized foam for $floil < S_o < fmoil$ or $(S_w^* - \varepsilon) \leq S_w \leq (S_w^* + \varepsilon)$. This study assumes that $floil = S_{or}$, so full-strength foam is not shown in Fig. 4.3.

Foam properties in **Fig. 4.3** correspond to the two flow regimes as in **Figs. 4.1** and **4.2**. Along directions parallel to gas-oil binary, for $S_w < S_w^* - \varepsilon$, $(1/FM) = 1$ since foam cannot be maintained due to conditions that are too dry. With S_w increasing from $(S_w^* - \varepsilon)$ to $(S_w^* + \varepsilon)$, $(1/FM)$ rises suddenly and abruptly, indicating that foam reduces gas mobility significantly. Foam in this narrow range of water saturations corresponds to the high-quality regime in **Figs. 4.1** and **4.2**. For $(S_w^* + \varepsilon) < S_w$, strong foam is present, related to the low-quality regime in **Figs. 4.1** and **4.2**. The transition between the two regimes corresponds to a transition zone in **Fig. 4.3** within the narrow interval $(S_w^* - \varepsilon) \leq S_w \leq (S_w^* + \varepsilon)$. Given that $\varepsilon \sim [1/(0.2 \times epdry)]$ is very small, corresponding to a very sharp transition, the transition zone is not visible here.

Parallel to gas-water binary, for $S_o \leq floil$, F_3 in **Eq. D-8** is equal to unity, meaning that oil has no impact on foam stability. In the interval $floil < S_o < fmoil$, F_3 drops as S_o increases, causing a decrease in $(1/FM)$ and thus in gas-mobility reduction. With S_o greater than $fmoil$, $F_3 = 0$ and $(1/FM) = 1$; foam is destroyed completely because of high S_o .

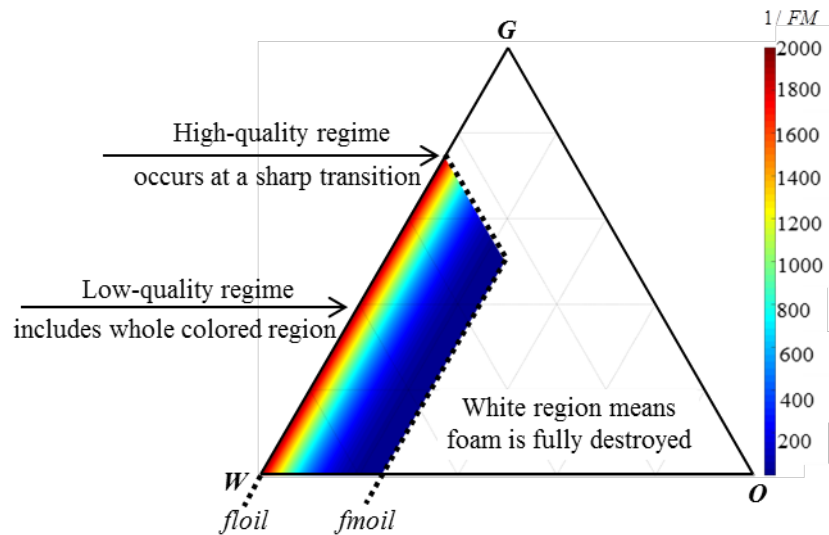


Figure 4.3 Foam properties as a function of (S_w, S_o) in ternary saturation space, characterized by the values of gas-mobility-reduction factor $(1/FM)$ (**Eq. D-2** in Appendix D). The model parameters are given in **Table D-1**. The three vertices G, O, and W represent the saturations of gas, oil or water at residual saturation of the other two phases, respectively. Thus this and subsequent plots do not display residual phase saturations.

4.3 Results and discussion

Table 4.1 summarizes the saturations of J and I in all cases presented. These cases are grouped in four representative scenarios based on J and I , with subscripts fm and nf denoting conditions inside or outside the foam region in **Fig. 4.3**, respectively. For J_{nf} foam cannot be maintained because it is too dry, whereas at I_{nf} foam is killed completely, a result of S_o greater than the upper limit $fmoil$ for stable foam. These examples illustrate a variety of applications of foam with different initial states and injection strategies.

Case 1 of each scenario in **Table 4.1** is the base case to illustrate the displacement structure. Case 2 in Scenario 3 and Case 2 in Scenario 4 are solved to analyze foam stability within an oil bank and at the foam-bank front, respectively, upon foam injection (for J allowing foam). In Scenario 3, the effect of foam tolerance to oil (reflected by f_{moil} and f_{loil}) on foam-bank propagation is analysed through Cases 1~ 3. Similar analysis of foam-bank propagation is conducted for Scenario 4.

Table 4.1 A summary of cases presented for the fractional-flow analysis of foam flow with oil in four representative scenarios varying J and I .

Scenarios		Injection conditions $J = (S_w, S_o)$	Initial conditions $I = (S_w, S_o)$	Foam model parameters
Scenario 1 (J_{nf} to I_{nf})	Case 1	$J = (0.2, 0)$	$I = (0.1875, 0.8125)$	Refer to Table A-1
Scenario 2 (J_{nf} to I_{fm})	Case 1	$J = (0.2, 0)$	$I = (0.7750, 0.2250)$	Refer to Table A-1
Scenario 3 (J_{fm} to I_{fm})	Case 1	$J = (0.3125, 0)$	$I = (0.7750, 0.2250)$	$f_{moil} = 0.25, f_{loil} = 0$, others from Table A-1
	Case 2	$J = (0.3125, 0)$	$I = (0.7750, 0.2250)$	$f_{moil} = 0.5, f_{loil} = 0$, others from Table A-1
	Case 3	$J = (0.3125, 0)$	$I = (0.7750, 0.2250)$	$f_{moil} = 0.5, f_{loil} = 0.2$, others from Table A-1
Scenario 4 (J_{fm} to I_{nf})	Case 1	$J = (0.3125, 0)$	$I = (0.1875, 0.8125)$	$f_{moil} = 0.25, f_{loil} = 0$, others from Table A-1
	Case 2	$J = (0.3125, 0)$	$I = (0.1875, 0.8125)$	$f_{moil} = 0.5, f_{loil} = 0$, others from Table A-1
	Case 3	$J = (0.3125, 0)$	$I = (0.1875, 0.8125)$	$f_{moil} = 0.5, f_{loil} = 0.2$, others from Table A-1

Note all saturations and parameters f_{moil} and f_{loil} listed are normalized for residual saturations through **Eq. 4.9**.

4.3.1 Structure of foam displacement with oil

4.3.1.1 Scenario 1 for J_{nf} displacing I_{nf}

Figure 4.4 shows the composition path for Case 1 of Scenario 1 in ternary saturation space, where both J_{nf} and I_{nf} are outside the foam region in **Fig. 4.3**. S_w at J_{nf} is too low (too dry) to give foam, and S_o at I_{nf} is too high for foam to be stable. In this and subsequent illustrations, the wave type and configuration along a path from J to I are indicated by solid and dashed lines that represent spreading waves and shocks, respectively. Spreading waves comprise saturations that appear in a displacement, whereas saturations within shocks are not observed.

As illustrated in **Fig. 4.4**, the path starting from J_{nf} includes a spreading wave followed by a shock. Thereafter, it exhibits a second spreading wave connected by a second shock to I_{nf} . The whole path bypasses the foam region, suggesting there is no foam occurring at all.

Figure 4.5 displays the wave velocities (on the top axis) of saturations along the path in **Fig. 4.4**, and saturation profiles for water, oil and gas at time $t_D = 0.05$ PVI. At time $t_D = 0.05$, the positions of all saturations on the bottom axis of **Fig. 4.5** are obtained by multiplying $t_D = 0.05$ with their associated wave velocities. The boxed

numbers labelled on the top specify the total relative mobility λ_{total} at that position with unit $(1/cp)$, defined as follows:

$$\lambda_{total} = k_{rw}/\mu_w + k_{ro}/\mu_o + k_{rg}^f/\mu_g \dots\dots\dots (4.13)$$

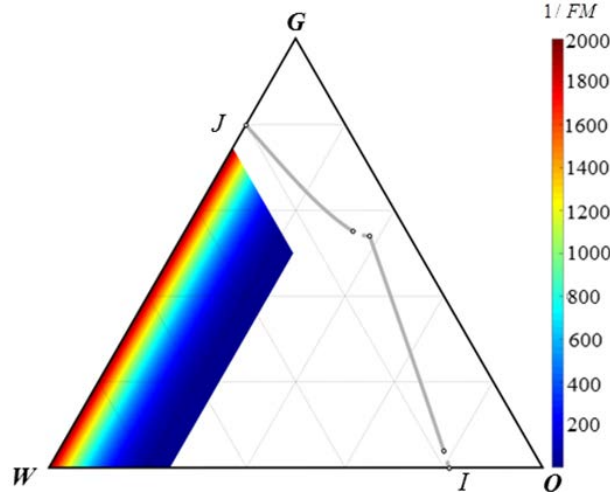


Figure 4.4 Composition path for case 1 of Scenario 1 in **Table 4.1** in ternary saturation space, where injection (J_{nf}) and initial (I_{nf}) conditions are both outside the foam region. In this and subsequent plots, The three vertices G, O, and W represent the saturations of gas, oil or water at residual saturation of the other two phases, respectively. Thus, the residual saturations for the three phases are not shown here. A solid line marks a spreading wave, with a dashed line denoting a shock.

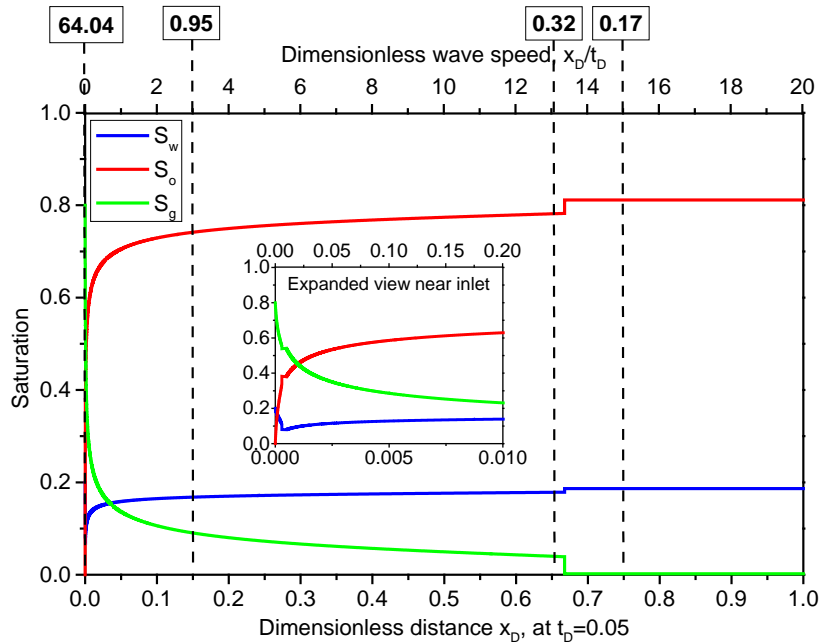


Figure 4.5 Wave velocities of saturations (on the top axis) and saturation profiles as a function of position (on the bottom axis) at time $t_D = 0.05$ PVI (Pore Volume Injection) along the path in **Fig. 4.4**. Boxed numbers labelled on the top are the total relative mobility λ_{total} (**Eq. 4.13**) at that position, with units $(1/cp)$.

Figure 4.5 illustrates that the green profile pushes forward the red profile, with the blue profile nearly flat, suggesting that gas is (slowly) displacing oil in Scenario 1. The expanded view shows that oil at saturation ~ 0.1

is displaced by gas with a dimensionless velocity $(x_D / t_D) = 0.001$; this is equivalent to more than 1000 PVI required to displace oil to this saturation. The extremely slow oil displacement results from the fact that without foam gas is much more mobile than oil and water. In addition, λ_{total} increases throughout the displacement. In two or three dimensions fingering would be expected, further worsening the displacement. The structure illustrated in **Figs. 4.4** and **4.5** is thus not desirable.

4.3.1.2 Scenario 2 for J_{nf} displacing I_{fm}

Figure 4.6 illustrates the composition path for case 1 of Scenario 2 in **Table 4.1**, where J_{nf} is outside but I_{fm} inside the foam region. This scenario represents the displacement in situations where J_{nf} is too dry to maintain foam whereas foam is developed some distance from the injection well. This might correspond to a SAG process with a single gas slug injected following a single surfactant slug.

The composition path in **Fig. 4.6** consists of three spreading waves and two shocks, as indicated by the solid and dashed lines. Starting from J_{nf} , the path has two spreading waves outside the foam region and then enters into the foam region with a shock. Then, along the foam boundary at $S_o = f_{moil}$, there is a third spreading wave connected by a second shock to I_{fm} ; this suggests that foam is present only downstream and substantially weakened by oil in this scenario.

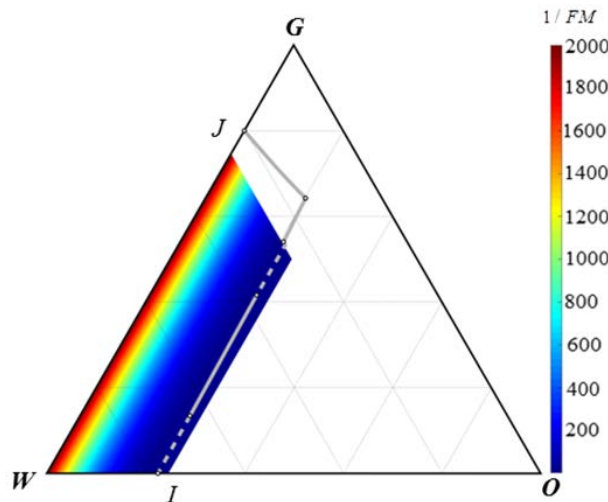


Figure 4.6 Composition path for Case 1 of Scenario 2 in **Table 4.1** in ternary saturation space, with injection condition J_{nf} outside but initial condition I_{fm} just inside the foam region. The three vertices G, O, and W represent the saturations of gas, oil or water at residual saturation of the other two phases, respectively. A solid line denotes a spreading wave, with a dashed line representing a shock.

Figure 4.7 displays the wave velocities of saturations (on the top axis) and saturations profiles at time $t_D = 0.2$ PVI for water, oil and gas along the path in **Fig. 4.6**. As seen from saturation profiles, gas displaces water forward with a velocity of 4.12, but hardly displaces oil at all. S_o with saturation 0.1 is displaced by gas with a velocity of 0.002, equivalent to more than 500 PVI required to drive oil saturation to this value throughout the displacement. The slow oil displacement results from high total relative mobility λ_{total} . As in Scenario 1 mobility increases with time and fingering would be expected in 2D or 3D. The structure of Scenario 2 is not desirable

either. The presence of foam downstream, though substantially destabilized by oil, does slow down gas propagation somewhat; the foam-front velocity is 4.12 in Scenario 2 in **Fig. 4.7**, compared to 13.35 in Scenario 1 in **Fig. 4.5**.

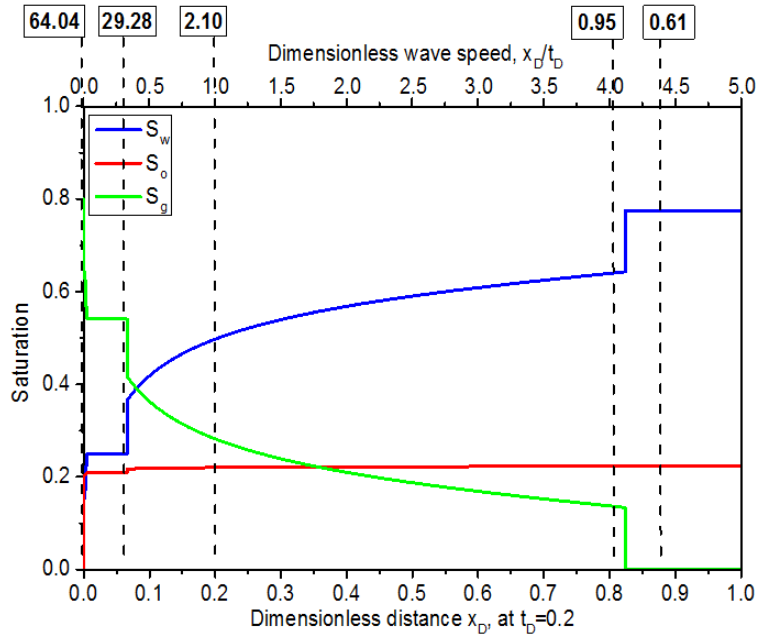


Figure 4.7 Wave velocities of saturations (on the top axis) and saturation profiles as a function of position (on the bottom axis) at time $t_D = 0.2$ PVI along the path in **Fig. 4.6**. Boxed numbers labelled on the top are the total relative mobility λ_{total} (Eq. 4.13) at that position, with units ($1/cp$).

4.3.1.3 Scenario 3 for J_{fm} displacing I_{fm}

Figure 4.8 presents the composition path for Case 1 of Scenario 3 in **Table 4.1**, where J_{fm} and I_{fm} both are inside the foam region. Most field applications correspond to this scenario, e.g. co-injection of surfactant solution and gas where foam is developed starting from the well, or SAG (Surfactant-Alternating-Gas) where the alternating slugs mingle some distance from the injection well.

The displacement in Scenario 3 shown in **Fig. 4.8**, starting from J_{fm} , compares a spreading wave, an abrupt shock, a second short spreading wave and eventually a second shock to I_{fm} . In contrast to Scenarios 1 and 2, in Scenario 3 with J_{fm} and I_{fm} the whole path is located within the foam region, meaning that water is sufficient to main foam and oil does not kill foam along the entire displacement.

Figure 4.9 shows the velocities of saturations (on the top axis) and saturation profiles at time $t_D = 0.2$ PVI for water, oil and gas along the path in **Fig. 4.8**. Near the entrance, the gas profile stays above the oil and water profiles, suggesting that foam displaces oil there. S_o with saturation 0.03 is displaced with a velocity of 0.08, equivalent to 12.5 PVI to recover nearly all oil, much more efficient than 1000 or 500 PVI required in Scenarios 1 or 2 (but still not practical for field application). In addition, lower-mobility fluids displace higher-mobility fluids throughout the displacement; this suggests successful mobility control and improved sweep efficiency in 2D or 3D.

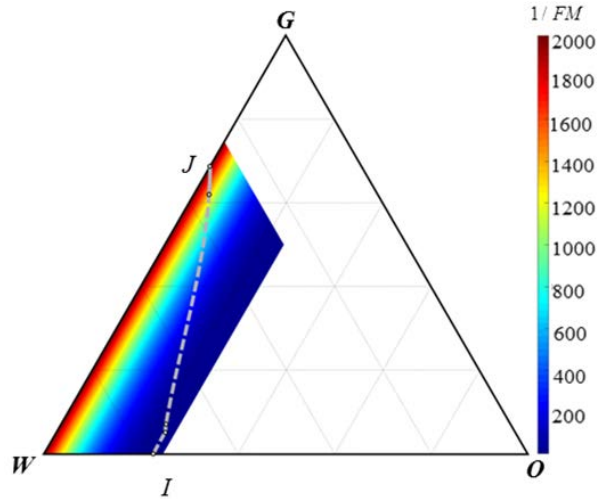


Figure 4.8 Composition path for Case 1 of Scenario 3 in **Table 4.1** in ternary saturation space, with injection (J_{fm}) and initial (I_{fm}) conditions both inside the foam region. The three vertices G, O, and W represent the saturations of gas, oil or water at residual saturation of the other two phases, respectively. A solid line denotes a spreading wave, with a dashed line representing a shock.

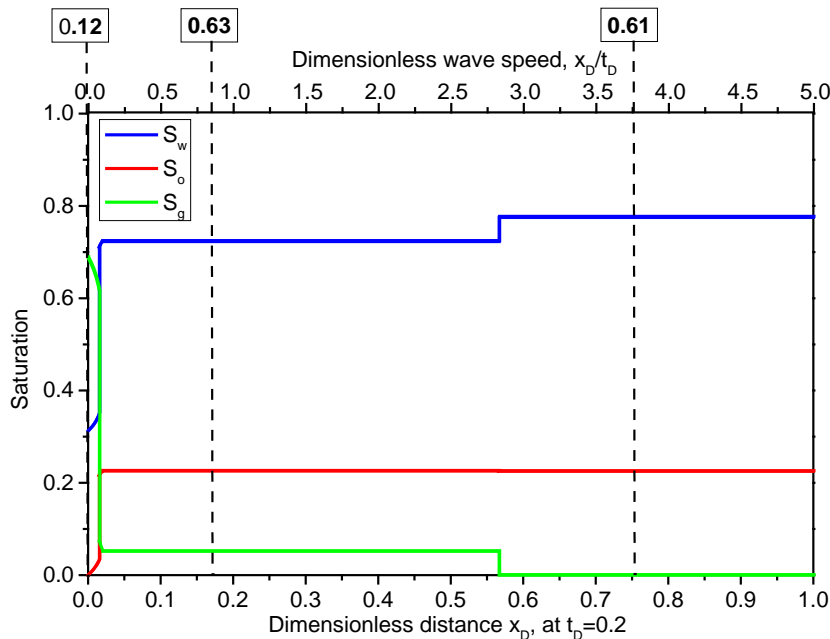


Figure 4.9 Wave velocities of saturations (on the top axis) and saturation profiles as a function of position (on the bottom axis) at time $t_D = 0.2$ PVI along the path in **Fig. 4.8**. Boxed numbers labelled on the top are the total relative mobility λ_{total} (**Eq. 4.13**) at that position, with units ($1/cp$).

4.3.1.4 Scenario 4 for J_{fm} displacing I_{nf}

Figure 4.10 illustrates the composition path for Case 1 of Scenario 4 in **Table 4.1**, where J_{fm} is inside but I_{nf} outside the foam region. The path from J_{fm} to I_{nf} illustrated in **Fig. 4.10** comprises a spreading wave, shock, spreading wave, shock, and shock (nearly invisible). The path from J_{fm} until some point on the second spreading wave is located within the foam region, which then crosses the foam boundary at $S_o = fmoil$ with a sharp inflection.

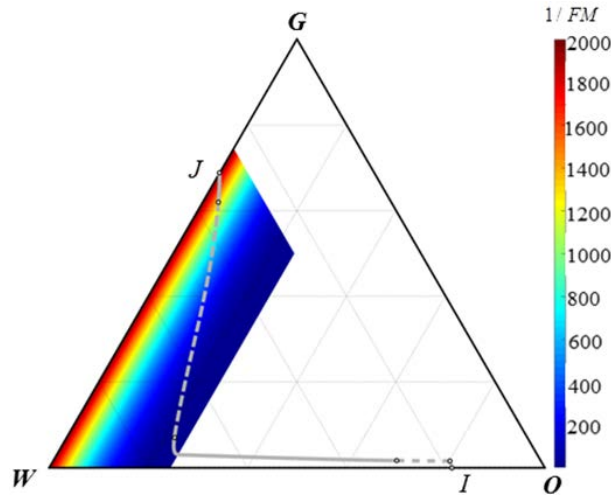


Figure 4.10 Composition path for Case 1 of Scenario 4 in **Table 4.1** in ternary saturation space, with J_{fm} inside but I_{nf} outside the foam region. The three vertices G, O, and W represent the saturations of gas, oil or water at residual saturation of the other two phases, respectively. A solid line denotes a spreading wave, with a dashed line representing a shock.

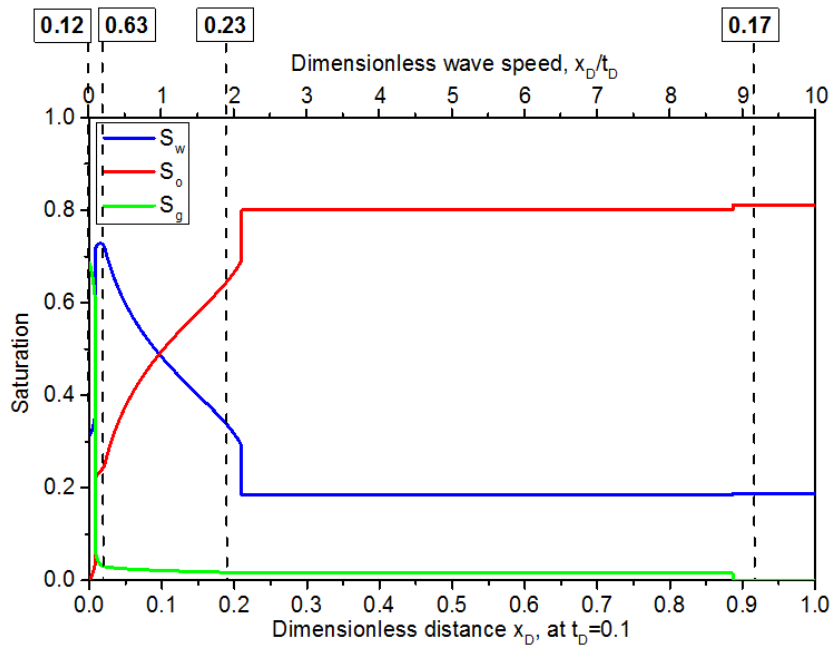


Figure 4.11 Wave velocities of saturations (on the top axis) and saturation profiles as a function of position (on the bottom axis) at time $t_D = 0.1$ PVI along the path in **Fig. 4.10**. Boxed numbers labelled on the top are the total relative mobility λ_{total} (**Eq. 4.13**) at that position, with units $(1/cp)$.

Figure 4.11 shows the associated wave velocities of saturations (on the top axis) and saturations profiles at time $t_D = 0.1$ PVI for water, oil and gas along the path in **Fig. 4.10**. Foam starting from the well displaces nearly all oil (to a saturation of 0.03) with a velocity of ~ 0.08 , equivalent to 12.5 PVI required to displace nearly all oil. Note that ahead of the foam region, it is thus water that displaces oil. It is thus waterflooding that reduces S_o below f_{moil} and allows a stable foam bank to form. As shown at the top of **Fig. 4.11**, foam, with $\lambda_{total} \sim 0.12$ $(1/cp)$, stably displaces the water-bank ahead of it, with $\lambda_{total} \sim 0.63$ $(1/cp)$. The waterflood might be subject to

fingering, however, which suggests that in 2D or 3D a higher oil saturation might remain behind to inhibit the foam bank.

4.3.2 Foam formulations with improved tolerance to oil

We present here an analysis of displacements from Scenarios 3 and 4 with a surfactant formulation more tolerant to oil, reflected in a larger value of f_{moil} .

4.3.2.1 Scenario 3 with J_{fm} displacing I_{fm}

Figure 4.12 illustrates the composition path for Case 2 of Scenario 3 with parameter f_{moil} double of that in Case 1 in **Table 4.1**. **Figure 4.13** shows the wave velocities of saturations (on the top axis) and saturation profiles at time $t_D = 1$ PVI for water, oil and gas, corresponding to the path in **Fig. 4.12**. Relative to Case 1, in **Fig. 4.8**, the increase in f_{moil} extends the foam region in **Fig. 4.12**, reflecting foam more stable to oil. The whole path from J_{fm} to I_{fm} is still located within the foam region. The velocity of the foam bank is three times that of the case in **Fig. 8**.

Figure 4.13 illustrates that an oil bank is created ahead of the foam bank. S_o in the oil bank nowhere exceeds the upper limit f_{moil} for stable foam. Oil within the oil bank weakens but does not kill foam completely. The uniform state in the oil bank corresponds to the intermediate state IJ in **Fig. 4.12**, which is the intersection of the forward slow path from J and backward fast path from I solved in the WCM (Liu, 1974; Castañeda et al., 2016). Accordingly, IJ , and the whole path, lie within the foam region. The generality of this finding (S_o in the oil bank $< f_{moil}$) is demonstrated by the following argument.

Suppose that foam injection creates an oil bank in Scenario 3, with J_{fm} to I_{fm} and that within this oil bank, S_o exceeds its upper limit for stable foam, f_{moil} . Immediately behind the oil bank, foam is present and water fractional flow f_w is significantly high, because foam reduces gas mobility substantially. Within the oil bank, gas mobility is high and S_o is high, with the result that $f_w \sim 0$. Nevertheless, S_w increases from the foam bank to the oil bank. The decrease in f_w and increase in S_w implies negative velocity for the foam front (as seen from **Eq. 4.11**). However, all velocities in a forward displacement must be positive. This negative velocity for water violates the wave-velocity compatibility required for a physical displacement (Lake et al., 2014).

A similar contradiction can also be seen shown at the front of the oil bank. Suppose within the oil bank $S_o > f_{moil}$, and ahead of the oil bank $S_o < f_{moil}$. Within the oil bank, where foam is killed and gas mobility is high, f_o is much lower than ahead of the oil bank, where, if gas is present, mobility is reduced by foam. Oil fractional flow is lower in the oil bank than ahead of it, but S_o is greater. A similar argument can be made regarding the gas phase. Within the oil bank, f_g is much greater than that inside the foam bank, where its mobility is reduced. But S_g is greater in the foam bank. Again, the implication is a negative velocity. The initial assumption that the oil bank can have $S_o > f_{moil}$ thus implies negative velocities, demonstrating that in a scenario with J_{fm} displacing I_{fm} , if there is an oil bank, $S_o < f_{moil}$ within the oil bank.

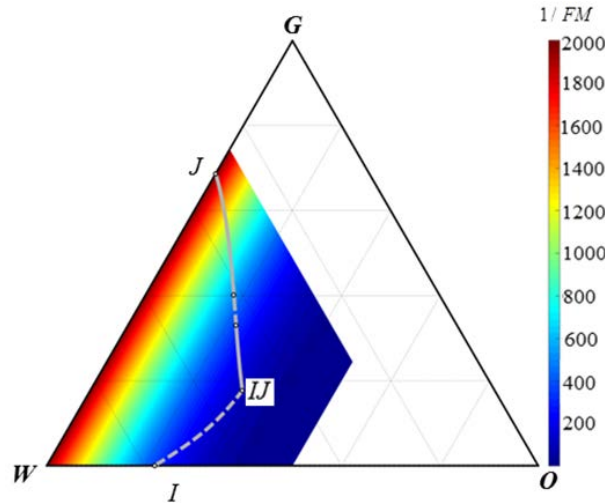


Figure 4.12 Composition path for Case 2 of Scenario 3 in **Table 4.1** in ternary saturation space, with J_{fm} and I_{fm} both inside the foam region. Parameter f_{moil} is increased to 0.5 relative to Case 1 in **Fig. 4.8**. The three vertices G, O, and W represent the saturations of gas, oil or water at residual saturation of the other two phases, respectively. A solid line denotes a spreading wave, with a dashed line representing a shock.

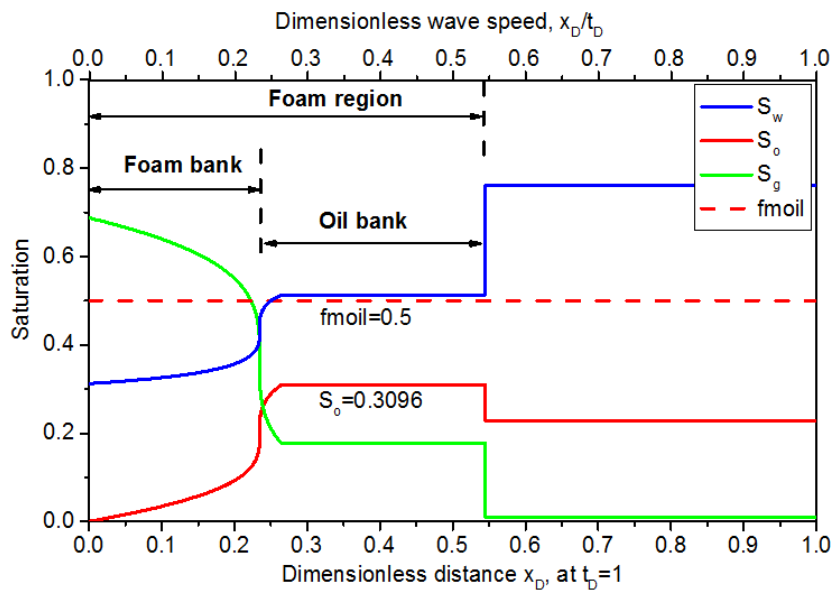


Figure 4.13 Wave velocities of saturations (on the top axis) and saturation profiles as a function of position (on the bottom axis) at time $t_D = 1$ PVI for water oil and gas, corresponding to the path in **Fig. 4.12**. Note that $S_o < f_{moil}$ within the oil bank.

4.3.2.2 Scenario 4 with J_{fm} displacing I_{nf}

Figure 4.14 exhibits the composition path for Case 2 of Scenario 4 with parameter f_{moil} double of that in Case 1 in **Table 4.1**. **Figure 4.15** shows the wave velocities of saturations (on the top axis) and saturation profiles at time $t_D = 0.25$ PVI for water, oil and gas, corresponding to the path in **Fig. 4.14**. The increase in f_{moil} again extends the foam region in **Fig. 4.14**, relative to Case 1 in **Fig. 4.10**, but in the cases presented (**Figs. 4.10** and **4.14**), modifying f_{moil} does not change the wave type or configuration along the displacement path. The velocity of the oil bank is about three times greater than in **Fig. 10**, however.

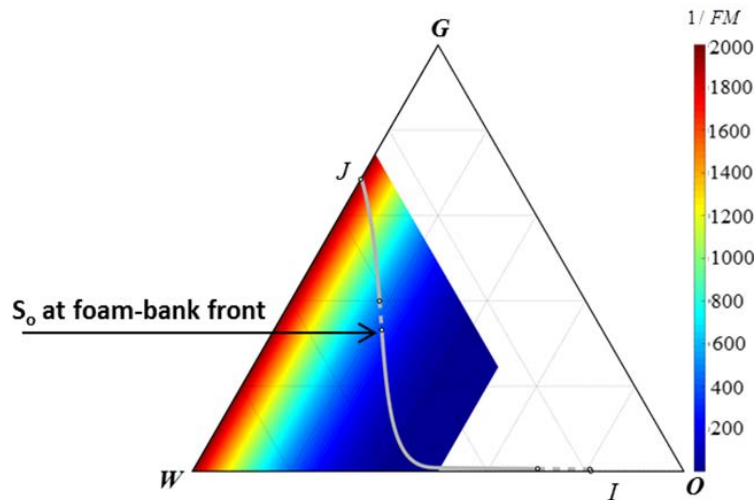


Figure 4.14 Composition path for Case 2 of Scenario 4 in **Table 4.1** in ternary saturation space, with J_{fm} inside but I_{nf} outside the foam region. Parameter f_{moil} is increased to 0.5 relative to Case 1 in **Fig. 4.10**. The three vertices G, O, and W represent the saturations of gas, oil or water at residual saturation of the other two phases, respectively. A solid line denotes a spreading wave, with a dashed line representing a shock.

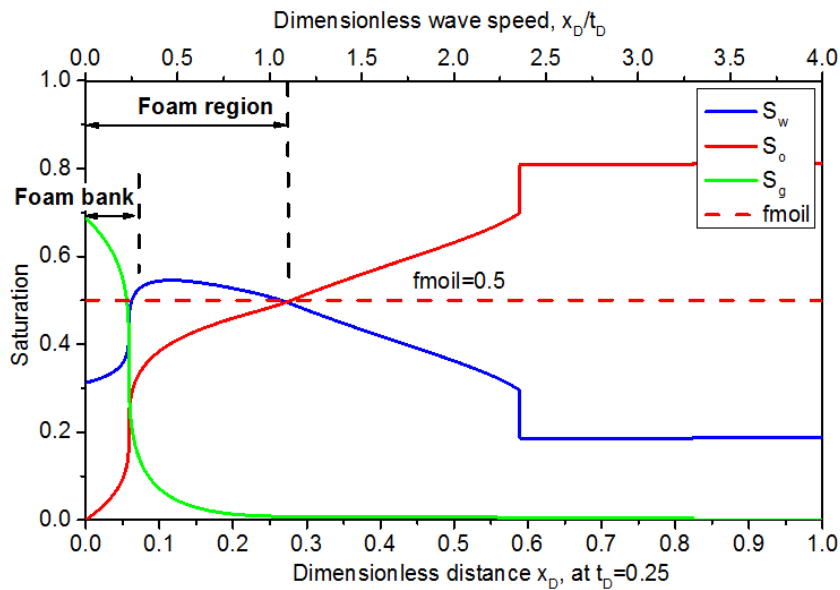


Figure 4.15 Wave velocities of saturations (on the top axis) and saturation profiles as a function of position (on the bottom axis) at time $t_D = 0.25$ PVI (Pore Volume Injection) along the path in **Fig. 4.14**. Note that $S_o < f_{moil}$ immediately ahead of foam bank.

Figure 4.15 shows that S_o immediately in front of the foam bank is again less than f_{moil} ; S_o is reduced below f_{moil} by waterflood ahead of the foam bank. This value of S_o is related to the endpoint of the first shock (as labelled in **Fig. 4.14**), which resides inside the foam region. A foam displacement is also possible with initial state I_{nf} that does not allow stable foam, though it relies on a waterflood ahead of foam to reduce oil saturation ahead of the foam.

4.3.2.3 Numerical artifact in foam simulation with oil

Numerical simulations of foam flow with oil faces various numerical challenges (Rossen, 2013), in particular because gas mobility changes abruptly depending on whether foam is present. Comparing the theoretical and numerical solutions for foam displacements with oil pinpoints a potential artifact in standard finite-difference simulation. The possible reason for that artifact is as follows.

Figure 4.16 shows the numerical simulation results for 1D immiscible foam flow with oil from Liu et al. (2011) using the same IT model approximation as in this paper. J and I in the simulation of Liu et al. are both in the foam region, as in Scenario 3 in our analysis. However, in contradiction with solutions presented above, Fig. 4.16 shows a value of S_o within the oil bank greater than f_{moil} .

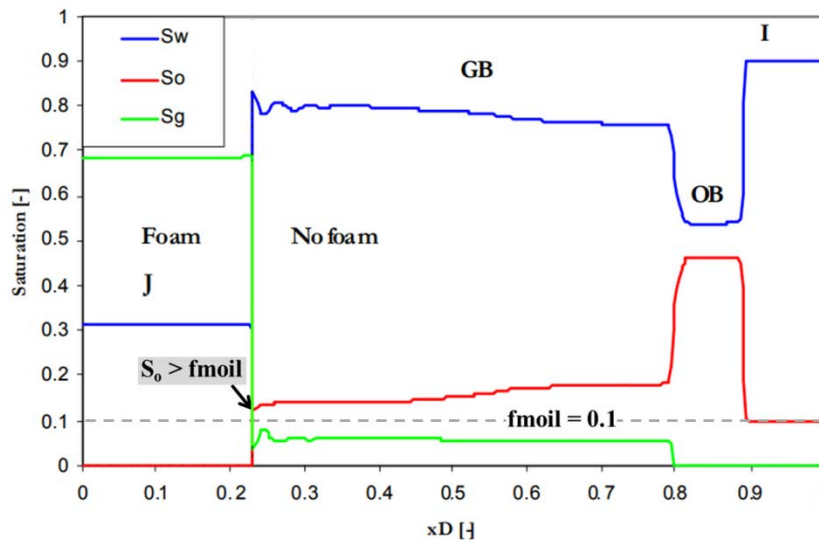


Figure 4.16 Numerical results for 1D immiscible foam displacement with oil, adapted from Liu et al. (2011). Parameter f_{moil} used is 0.1 (implied by the dashed line). S_o within the oil bank is much greater than f_{moil} .

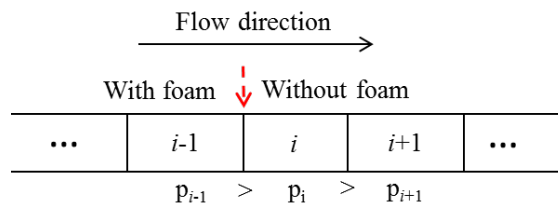


Figure 4.17 Schematic of pressure calculation using neighboring grid blocks in finite-difference simulation. The interface between grids $(i - 1)$ and i corresponds to the foam displacement front in Fig. 4.16.

The propagation of foam with $S_o > f_{moil}$ ahead may be a result of calculation of pressure p or pressure gradient ∇p using neighboring grid blocks. As schematically illustrated in Fig. 4.17, the foam-displacement front in Fig. 4.16 corresponds to the interface between grid blocks i and $(i - 1)$. The pressure gradient in grid block i that regulates the flow out of this grid should be small, in the absence of foam. It is this pressure gradient that (slowly) displaces oil from grid block i . In the numerical simulation, the pressure in grid block i is calculated using pressures in the neighboring grid $(i - 1)$ with foam and grid $(i + 1)$. Pressure in grid $(i - 1)$ with foam should

be much greater than that in grid i without foam. This causes an otherwise small pressure in grid i (without foam) greatly overestimated. The pressure gradient that regulates the flow of oil out of grid i is therefore greatly overestimated relative to its actual value in the absence of foam. When S_o in grid i is reduced (by the artificially inflated pressure gradient) to a value less than f_{moil} , foam advances to grid block i , misleadingly implying that foam can efficiently displace oil ahead of it with $S_o > f_{moil}$.

This numerical artifact would persist at any spatial resolution. One could argue that the simulation accurately represents the effects of the transition between a zone of no foam in the oil bank and foam behind it. In the MOC, the transition zone at a shock is represented as a travelling wave, which is an ongoing area of research in three-phase MOC. In two-phase fractional-flow theory, however, the traveling wave imposes additional constraints, but does not relax the velocity constraint on the overall displacement (see, e.g., Ashoori et al., 2011). Thus the prohibition against foam displacing an oil bank with $S_o > f_{moil}$ is expected to remain.

4.3.3 Foam-bank propagation with oil

We analyze here the impacts of the oil-related foam model parameters in the model on foam-bank propagation in Scenarios 3 and 4.

Figure 4.18 shows the saturation velocities (on the top axis) and saturation profiles (on the bottom axis) at 1 PVI for gas (upper figure) and oil (lower figure), respectively, in Scenario 3 with respect to foam-oil parameters f_{moil} and f_{loil} . In this scenario foam displaces an initial oil saturation that allows foam. Similarly, **Fig. 4.19** illustrates the same parameters on foam-bank propagation with Cases 1, 2 and 3 in Scenario 4 in **Table 4.1**. In this case foam displaces an initial saturation that does not allow foam.

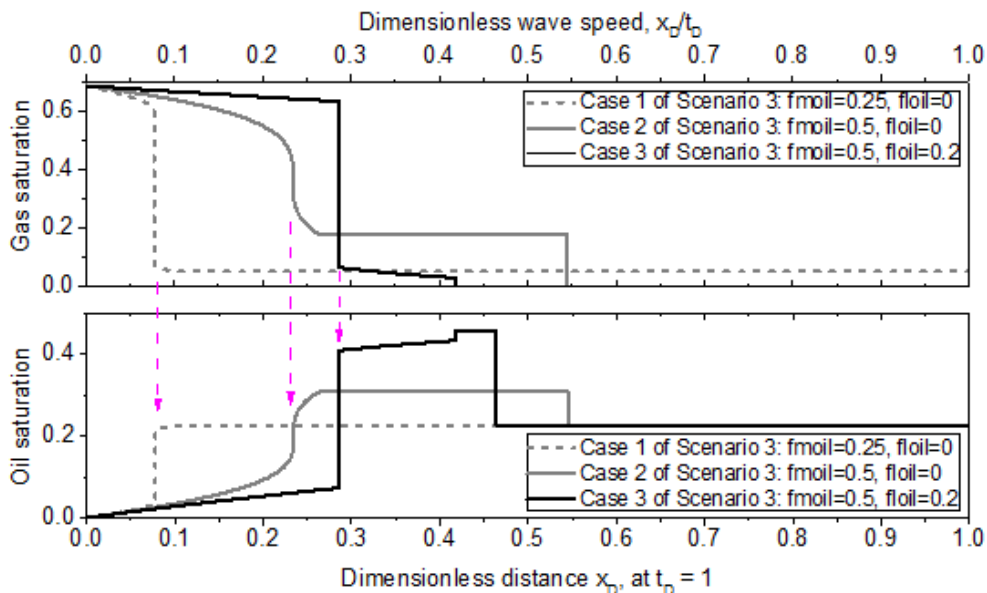


Figure 4.18 Wave velocities of saturations (on the top axis) and saturation profiles (on the bottom axis) at 1 PVI for gas (upper figure) and oil (lower figure), respectively, in Cases 1, 2 and 3 of Scenario 3 in **Table 4.1**. The arrows indicate the front of the foam bank in each case.

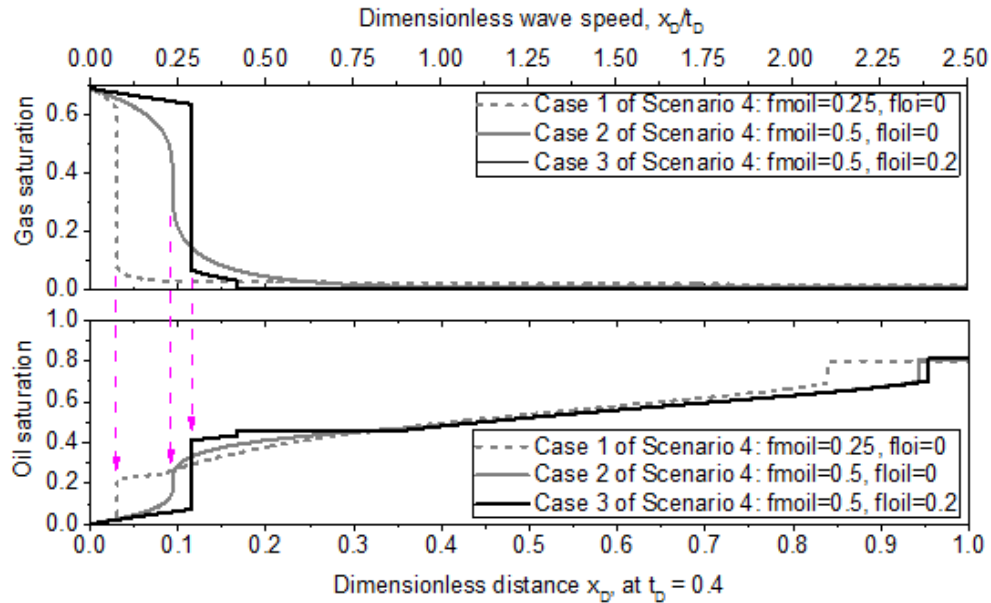


Figure 4.19 Wave velocities of saturations (on the top axis) and saturation profiles (on the bottom axis) at 0.4 PVI for gas (upper figure) and oil (lower figure), respectively, in Cases 1, 2 and 3 of Scenario 4 in **Table 4.1**. The arrows indicate the front of the foam bank in each case.

The gas-saturation profiles in **Figs. 4.18** and **4.19** both suggest that increasing f_{moil} or f_{loil} (i.e., designing a surfactant formulation less sensitive to oil) accelerates propagation of the foam-bank. It also raises oil saturation within the oil bank, though it slows the initial breakthrough of the oil bank somewhat. On the whole, it accelerates the production of most of the oil.

Figures 4.18 and **4.19** show that the foam bank propagates with nearly same velocity (x_D/t_D), i.e. 0.078, 0.234 or 0.287, for the same oil tolerance but different initial conditions. This solution suggests the propagation velocity of the foam bank may not be subject to initial condition that allows or kills foam, but rather mainly to foam properties at the injection conditions.

4.4 Conclusions

We present a fractional-flow analysis of foam flow with oil, with the theoretical solutions solved through the wave curve method (WCM). Physical insights on two key aspects of foam displacement with oil are revealed: the dependence of the displacement upon injection (J) and initial (I) conditions and the effects of improved oil-tolerance of the surfactant formulation on the velocities of foam propagation and of the oil bank. We also show that numerical simulations indicating an oil bank with oil saturation greater than the limiting saturation for foam stability (f_{moil} in our model) reflect a numerical artifact.

Among the cases we examine, only foam injected with sufficient water for foam stability (i.e. injection state J allowing foam) gives a displacement structure that is desirable, featuring low-mobility fluids upstream chasing high-mobility fluids downstream. This structure may represent the displacement following co-injection of surfactant solution and gas, or SAG (Surfactant-Alternating-Gas) some distance from the well where slugs have

mingled. Our results suggest that a SAG process with a single gas slug following surfactant would not be successful, at least for the foam properties considered here.

Our examples, along with an analysis of saturation velocities, show that oil saturation (S_o) within an oil bank (if created and displaced by foam) is never greater than the upper limit for stable foam, f_{moil} . This is also true for initial state I with S_o greater than f_{moil} , though waterflooding ahead of foam may reduce S_o ahead of foam below f_{moil} . This argument is justified through a consideration of the wave velocities of saturations implied by such a displacement.

Enhancing the tolerance of foam to oil accelerates propagation of the foam bank and displaces oil more effectively ahead of the foam bank. In addition, in the cases presented, foam-bank propagation is not subject to initial conditions but only to foam properties at injection conditions.

This approach, applied with model parameters fitting a given application, as well as these findings can guide the interpretation of foam behavior and more-complex numerical simulations in a variety of engineering applications: oil displacement in the petroleum industry, removal of NAPL (Non-aqueous Phase Liquid) contaminants removal in aquifers and soils, and carbon storage in CCUS (Carbon Capture, Utilization and Storage).

FRACTIONAL-FLOW THEORY OF FOAM-OIL DISPLACEMENT WITH MULTIPLE STATES

Summary

Understanding the interplay of foam and non-aqueous phases in porous media is key to improving the design of foam for enhanced oil recovery and remediation of aquifers and soils. A widely used implicit-texture foam model predicts phenomena analogous to cusp catastrophe theory: the surface describing foam apparent viscosity as a function of fractional flows folds on itself. Thus there are multiple steady states fitting the same injection condition J defined by the injected fractional flows. Numerical simulations suggest the stable injection state among multiple steady states but do not explain the reason.

We address the issue of multiple steady states from the perspective of wave propagation, using three-phase fractional-flow theory. The wave-curve method is applied to solve the two conservation equations for composition paths and wave speeds in 1D foam flow with oil. There is a composition path from each possible injection state J to the initial state I satisfying the conservation equations. The stable displacement is the one with wave speeds (characteristic velocities) all positive along the path from J to I . In all cases presented, two of the paths feature negative wave velocity at J ; such a solution does not correspond to the physical injection conditions. A stable displacement is achieved by either the upper, strong-foam state or lower, collapsed-foam state, but never the intermediate, unstable state. Which state makes the displacement depends on the initial state of a reservoir. A boundary curve is defined that captures the dependence of the choice of the displacing state on initial condition.

5.1 Introduction

Catastrophe theory, initially founded by Thom in 1960s and further developed by Zeeman in 1970s, is a branch of bifurcation theory for dynamical systems and of singularity theory in geometry (Thom & Zeeman 1974; Zeeman 1977; Arnold et al. 1999; Wiggins 2013). The cusp catastrophe, among the seven elementary catastrophes described by Zeeman (1977), is schematically illustrated in **Figs. 5.1** and **5.2**. The theory cusp catastrophe states that equilibrium behavior controlled by two independent quantities forms a smooth surface folding on itself. Theoretically, all states between the two edges of the fold in **Fig. 5.1** are unstable and cannot be observed in nature. At each edge of the fold, the system makes a sudden and dramatic jump between the two states, illustrated in **Fig. 5.2**, upon a small change of the controls.

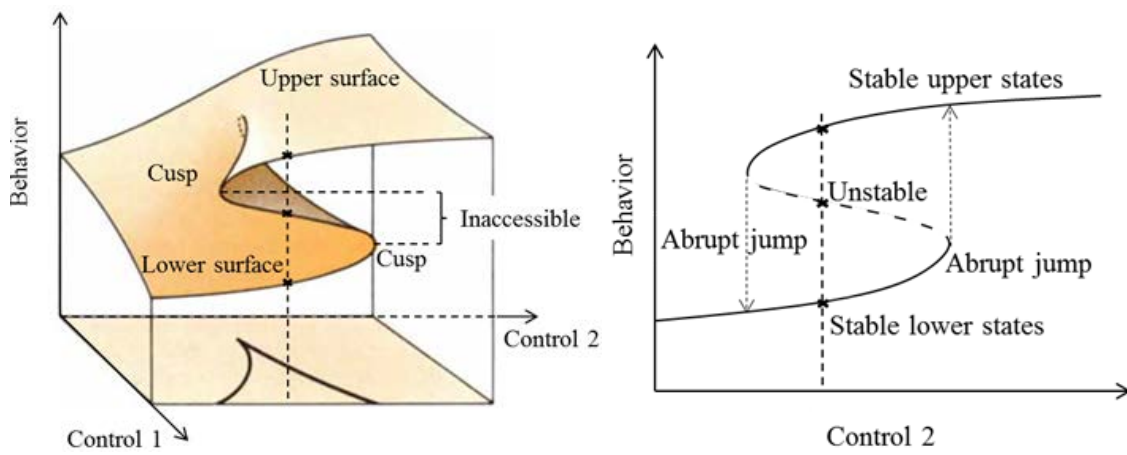


Figure 5.1 (Left) Illustration of the cusp catastrophe: a smooth surface describes behavior at equilibrium as a function of two independent controls; adapted from Zeeman (1977).

Figure 5.2 (Right) Equilibrium behavior with control 1 fixed on the front plane of **Fig. 5.1**. Dotted line shows a case of multiple steady states corresponding to the same values of both controls.

In principle, any event meeting the conditions of the theory would exhibit behavior similar to that in **Fig. 5.1** and **2**. This is found in many models in physics and engineering, i.e. in wave propagation, minimum surface area, nonlinear oscillations and elasticity (Van der Waals, 1910; Holmes & Rand, 1976; Golubitsky & Keyfitz, 1980; Guckenheimer, 1986; Kravtsov & Orlov, 1990). Some theoretical predictions have been verified experimentally or in practice, with others not yet observed. Recent studies of Tang et al. (2019) as shown in Chapter 2 find similar phenomena for foam flow with oil in porous media. Specifically, the widely used foam simulation model STARS (Computer Modeling Group, 2015) predicts, for some combinations of oil, water and gas fractional flows, three different sets of saturations. Chapter 3 in this study (Tang et al., 2018) shows that this model gives realistic representation of steady-state foam behavior with oil. Either this simulator or a foam model similar to that in the simulator has been used to represent a variety of coreflood studies and field applications of foam (Chalbaud et al., 2002; Spirov et al., 2012; Ma et al., 2013; Norris et al., 2014; Sharma et al., 2017; Rognmo et al., 2018; Alcorn et al., 2018). Thus it is essential to understand the model's behaviour, including how it represents displacements with multiple possible displacing states. The study here presents physical insights into these phenomena and their implications for the dynamics of oil displacement by foam.

Numerous processes involve foam flow through porous media, e.g. oil displacement in reservoirs (Rossen 1996; Kavscek et al. 1997; Liu et al. 2010), removal of NAPL (Non-Aqueous Phase Liquid) contaminants in aquifers and soils (Johnson et al. 2001; Jeong & Corapcioglu 2005; Kao et al. 2008; Geistlinger et al. 2009) and CO₂ storage (Juanes et al. 2006; Iglauer et al. 2011a; 2011b). Foam is not a separate phase, but a dispersion of gas in liquid such that gas bubbles are separated by interconnected liquid films, called lamellae. The applications above mainly rely on the fact that foam can reduce gas mobility considerably by trapping gas bubbles via those lamellae (Rossen 1996). Most oils are detrimental to foam, and this affects significantly the effectiveness of foam for gas mobility control. The interaction between foam and oil is complex and is not yet fully understood (Farajzadeh et al. 2012).

Currently, there exist two groups of models describing foam dynamics in porous media: population-balance models (Kavscek et al. 1995; Kam & Rossen 2003) and implicit-texture (IT) models (Cheng et al. 2000; Computer Modeling Group 2015). The two groups of models capture different physics involving foam generation and destruction as well as foam behavior at steady state (Lotfollahi et al. 2016).

Population-balance foam models capture the dynamics of foam generation and destruction through a dynamic calculation of bubble density (number of bubbles per unit volume). In the absence of oil, the model of Kam and Rossen (2003) predicts behavior analogous to the cusp catastrophe of **Fig. 5.2**, where the pressure gradient ∇p is plotted as a function of gas (u_g) and water (u_w) superficial velocities (Kam and Rossen 2003; Afsharpoor et al. 2010). This behavior has been experimentally confirmed in foam corefloods in two ways: first, by showing a sudden jump in ∇p upon a small increase in superficial velocity, and thereafter a hysteresis with the velocity decreasing; second, in experiments with ∇p fixed, by revealing the entire S-shaped curve illustrated in **Fig. 5.2** (Gauglitz et al. 2002). Nevertheless, few current population-balance models represent the effect of oil on foam. The model of Myers & Radke (2000) accounts for the effect of oil by reducing the bubble-generation rate in that oil occupies part of the pore space and reduces the number of sites where lamellae could be created. This model does not capture the impact of oil on foam stability (e.g. oil condition for foam collapse). Ma et al. (2018) in a recent study attempt to represent the effect of oil by increasing the bubble destruction rate in a population-balance model. In separate ways, that model would be expected to alter the low- and high-quality foam regimes, respectively, in a way similar to that of the model described below. The details of behavior of their model and the validity of the model to represent foam flow with oil is not yet experimentally justified.

Implicit-texture (IT) models assume local equilibrium, meaning that foam everywhere immediately reaches a state, where bubble generation rate matches the destruction rate. Foam texture, i.e. bubble size, is not represented explicitly in IT models, but is reflected implicitly through a gas mobility-reduction factor. The IT foam model in the STARS simulator defines gas mobility in foam as a function of water (S_w) and oil (S_o) saturations (i.e., fraction of pore volume occupied by water or oil). The approximations of local equilibrium and implicit texture simplify the analysis of foam flow dynamics, in particular in a complex interaction with oil. The model and parameters used below is based on a fit of model parameters to foam behavior without oil (Cheng et al., 2000), and is consistent with foam behavior with oil reported by Tang et al. (2018).

The STARS foam model as discussed in Chapter 2 (Tang et al., 2016) suggests the behavior illustrated in **Figs. 5.1** and **5.2**, for steady-state foam flow with oil. The behavior was evaluated through foam apparent viscosity μ_{app} , i.e. the inverse of total relative mobility (see *Foam Model* section below for its specific definition). With oil, μ_{app} predicted by the model, when plotted on a ternary diagram of oil, water and gas fractional flows, appears as a surface folding on itself. **Fig. 5.3** illustrates this behavior in terms of ∇p as a function of fractional flows, with more details given in the *Foam Model* section in terms of μ_{app} . The folded region means that the same injection condition J , with a given set of fractional flows, corresponds to three possible foam states in terms of saturations. The middle state is intrinsically unstable and therefore not seen in nature. The existence of multiple states has not been directly confirmed in the laboratory, but it is physically plausible and consistent with observations of foam behavior (Tang et al., 2018). At the same injection rates, a strong foam, with large μ_{app} and ∇p , could displace oil and maintain oil saturation low, while a collapsed-foam state with low μ_{app} and ∇p might leave oil saturation high and foam unstable. This raises an essential question concerning the effectiveness of foam displacements: which of the multiple foam states, with different μ_{app} and ∇p , all fitting to a same set of injected fractional flows, actually occurs in a given displacement?

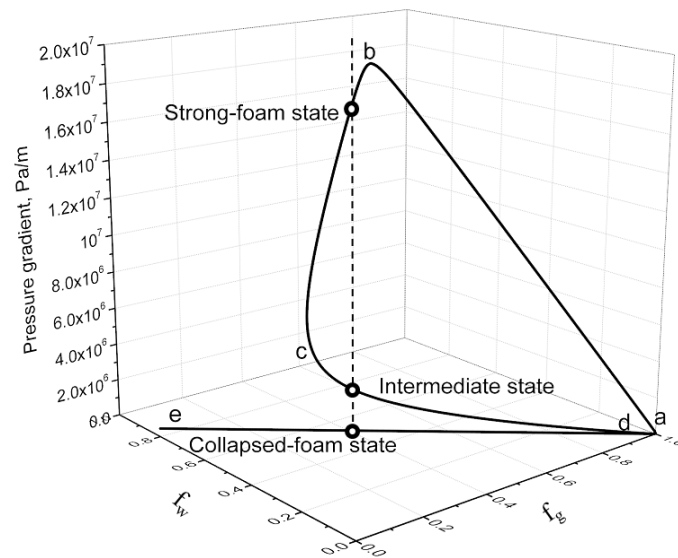


Figure 5.3 Pressure gradient ∇p as a function of water (f_w) and gas (f_g) fractional flows at total superficial velocity $u_t = 3.53 \times 10^{-5}$ m/s, predicted by the wet-foam representation in Appendix E with a fixed ratio of $(f_o/f_w)=0.25$; adapted from Tang et al. (2016). The trace follows a sequence: a, b, c, d and e. The dashed line indicates a case of multiple foam states fitting same set of fractional flows, caused by the portion of the curve between c and d folding towards the lower right corner. Model parameters used for the illustration are referred to **Table E-1** in Appendix E.

Tang et al. (2016) performed simple 1D numerical simulations with fixed injection rates corresponding to cases with multiple possible states. Their simulation results suggest a displacement by either the upper state, with large μ_{app} , or the lower state, with small μ_{app} , but never the (unstable) one in the middle. These observations are

consistent with catastrophe theory. However, a numerical simulation does not explain why a particular (strong or weak) foam is seen in the displacement.

We here present an analysis of a displacement with multiple possible injection states fitting same injected fractional flows, using an analytical approach, the wave curve method (WCM) for three-phase flow. The WCM is also referred to, in petroleum engineering, as fractional-flow theory or the method of characteristics (MOC). Fractional-flow theory excludes the numerical artifacts that can afflict foam simulation (Rossen 2013).

A CAD (Computer Assisted Design) package, RPN (n-dimensional Riemann Problem) that applies the WCM has been developed in the group of fluid dynamics at IMPA (Instituto Nacional de Matemática Pura e Aplicada) in Brazil (Azevedo et al. 2010; Castañeda et al. 2016). This program efficiently determines Riemann solutions for 1D three-phase flow, including the complications of foam. The Riemann solutions provide a mathematical criterion that distinguishes states observed or not observed in the displacement. Using this tool, we explore the dependence of the displacement on initial condition.

The significance of our findings for field applications is discussed below. Some suggestions are provided for the direct experimental verification of multiple steady states through foam corefloods in laboratory.

5.2 Theory and mathematical approach

5.2.1 Three-phase fractional-flow theory

The core of fractional-flow theory concerns modeling transport of fluids in porous media, specifically, by solving for phase saturations as a function of position x and time t (Lake et al. 2014). The solutions are usually illustrated as a saturation profile as a function of position at a given time or saturation history at a given position.

In a system of foam flow with oil, the presence of three phases means there are two independent variables to be determined, water (S_w) and oil (S_o) saturations as a function of (x, t) . Gas saturation is $S_g = (1 - S_w - S_o)$. For the purpose of our study, we have made the following assumptions:

- 1D flow,
- fractional flows are only functions of local phase saturations,
- incompressible fluids and rock,
- gravity can be ignored,
- no mass exchange between phases (immiscible phases),
- isothermal process,
- no dispersive processes (diffusion, dispersion, or capillary-driven flow),
- immediate attainment of local-equilibrium behavior,
- Newtonian rheology for all phases,
- uniform concentration of surfactant in the aqueous phase throughout the medium, which implies that either adsorption is insignificant or it has already been satisfied.

The system is governed by two mass-conservation equations for $x > 0$ and $t > 0$:

$$\varphi \frac{\partial S_w}{\partial t} + u \frac{\partial f_w}{\partial x} = 0, \dots\dots\dots (5.1)$$

$$\varphi \frac{\partial S_o}{\partial t} + u \frac{\partial f_o}{\partial x} = 0, \dots\dots\dots (5.2)$$

where φ is porosity, a rock property (a volume fraction of rock that is pore space) and u is the total superficial velocity of the three phases; i.e. $u \equiv u_w + u_o + u_g$. f_w and f_o in **Eqs. 5.1** and **5.2** are the fractional flows of water and oil, defined as the fraction of phase volumetric flux to the total volumetric flux:

$$f_j \equiv \frac{u_j}{u}, \dots\dots\dots (5.3)$$

where subscript $j = w, o$ or g represents water, oil or gas, respectively.

Superficial velocity u_j of phase j is determined by Darcy's law:

$$u_j = \frac{kk_{rj}}{\mu_j} |\nabla p|, \dots\dots\dots (5.4)$$

where k is the absolute permeability of the porous medium, μ_w , μ_o and μ_g are the water, oil and gas viscosities, $|\nabla p|$ is the absolute magnitude of pressure gradient, and k_{rj} is the relative permeability of phase j . The ratio of (k_{rj}/μ_j) is referred to as the relative mobility of phase j .

Substituting **Eq. 5.4** into **Eq. 5.3** yields:

$$f_j = \frac{k_{rj}/\mu_j}{k_{rw}/\mu_w + k_{ro}/\mu_o + k_{rg}^f/\mu_g}, \dots\dots\dots (5.5)$$

where superscript f in k_{rg}^f indicates the presence of foam. We assume that presence of foam does not alter the relative-permeability function for water or oil, but only that for gas. This is supported by a number of experimental observations and greatly simplifies the physics and modeling of foam flow in porous media (Rossen 1996; Schramm 1994).

In the STARS foam model (see Appendix E for specific algorithms), k_{rg}^f is defined as k_{rg} , i.e. gas relative permeability without foam, reduced by a mobility-reduction factor FM (Computer Modeling Group 2015). The scaling factor FM , given in **Eq. E-2** in Appendix E, is a function of a series of physical factors affecting foam stability and degree of gas-mobility reduction by foam. Two major factors in FM concerning water and oil saturations are included in this study, meaning that FM is a function only of saturations.

The commonly used models for k_{rj} include Stone I and II (Stone 1970; 1973) and the Corey model. In a case of three-phase flow, k_{rj} of the intermediate-wetting phase in Stone I and II is related to that of the other two phases based on channel-flow theory, rather than a unique function of its own saturation. Foam alters gas mobility so drastically that Stone's models can give unphysical results with foam, e.g. positive relative permeability at zero

oil saturation. For simplicity, therefore, we use a Corey-type relative-permeability model, where foam-free k_{rj} of phase j is a function of S_j alone:

$$k_{rj} = k_{rj}^0 \left(\frac{S_j - S_{jr}}{1 - S_{wc} - S_{or} - S_{gr}} \right)^{n_j}, \dots\dots\dots (5.6)$$

where k_{rj}^0 is the endpoint relative permeability, n_j is the Corey exponent that reflects wettability, and S_{wc} , S_{or} and S_{gr} represent the residual saturations of each phase. **Equation E-2** in Appendix E for FM , with F_2 and F_3 included, combined with **Eq. 5.6** for k_{rj} , suggest that fractional flow f_j in **Eq. 5.5** is a function only of saturations.

To simplify **Eqs. 5.1** and **5.2**, dimensionless position, x_D and dimensionless time, t_D are introduced:

$$x_D \equiv \frac{x}{L}, \dots\dots\dots (5.7)$$

$$t_D \equiv \frac{u \cdot t}{(1 - S_{wc} - S_{gr} - S_{or}) L \phi}, \dots\dots\dots (5.8)$$

where L is the 1D reservoir length, and t_D is the number of movable pore volumes injected, with movable pore volume scaled by $(1 - S_{wc} - S_{gr} - S_{or})$. **Equations 5.1** and **5.2** then are simplified to:

$$\frac{\partial S}{\partial t_D} + \frac{\partial F}{\partial x_D} = 0, \dots\dots\dots (5.9)$$

where S and F are both vectors, i.e. $s = \begin{pmatrix} S_w \\ S_o \end{pmatrix}$ and $F = \begin{pmatrix} f_w \\ f_o \end{pmatrix}$.

Fractional-flow theory interprets a displacement process in terms of wave propagation (Buckley and Leverett, 1942; Wooding and Morel-Seytoux, 1976; Charbeneau, 1988; Avraam and Payatakes, 1995; Lake et al., 2014; Reynolds and Krevor; 2015). In principle, all saturations between J and I along a composition path exist at the origin at $t_D = 0$. Upon injection, water, oil and gas propagate starting from the origin with given wave speeds as a function of saturations. Solving for the saturation profile and history is then equivalent to solving for waves speeds, $\eta(S)$:

$$\eta(S) \equiv \frac{x_D}{t_D}. \dots\dots\dots (5.10)$$

Substituting $\eta(S)$ into **Eq. 5.9**, and using chain rule of differentiation, the system is rearranged to (Lake et al. 2014):

$$[J(S) - \eta I^*] dS = 0, \dots\dots\dots (5.11)$$

where I^* denotes the 2-by-2 identity matrix, with an asterisk to distinguish it from the initial state, I . $J(S)$ is the Jacobian matrix:

$$J(S) = \begin{pmatrix} J_{ww}(S) & J_{wo}(S) \\ J_{ow}(S) & J_{oo}(S) \end{pmatrix}, \dots\dots\dots (5.12)$$

where $J_{ij}(S) = \partial f_i / \partial S_j$ with i and $j = w, o$ and g denoting water, oil and gas, respectively.

Mathematically, $\eta(S)$ to be solved is the eigenvalue of the Jacobian matrix $J(S)$. A physical problem of solving for wave speeds, $\eta(S)$, is eventually converted to a mathematical problem concerning eigenvalues of the Jacobian matrix in **Eq. 5.12** (Lax 1957; Liu 1974; Castañeda et al. 2016; Castañeda 2018).

5.2.2 Wave-curve method

The wave-curve method (WCM) implemented in the RPN solves the system described by **Eq. 5.9** for two major outputs: a composition path from J to I that provides S along the path, and the associated wave speed for each value of S . The two types of solutions together define the structure of a displacement. From the saturations and wave speeds arising from $x_D = t_D = 0$, the saturation profile can be determined at any time, and the saturation history at any location. A number of studies of multi-phase flow in porous media, concerning a hyperbolic system of conservation laws, provide a detailed description of the method (Azevedo et al. 2010; Castañeda et al. 2016; Castañeda 2018). This section briefly explains the general principles of the WCM applied in the RPN program (Liu 1974; Smoller 2012), especially to distinguish the Riemann problem that the WCM solves from that of physical displacements.

Generally, the composition path for J displacing I is determined by constructing two families of wave curves via the WCM, as illustrated in **Fig. 5.4**: a forward slow-wave curve and a backward fast-wave curve. The forward slow wave curve starts from J ; the smaller eigenvalue of $J(S)$ in **Eq. 5.12** at each saturation is assigned in the WCM as the characteristic speed at saturation S . The corresponding eigenvector gives the direction of saturation change from current saturation to the next saturation. At this saturation the eigenvalues of $J(S)$ in **Eq. 5.12** are again calculated and the process continues until the entire slow path is determined.

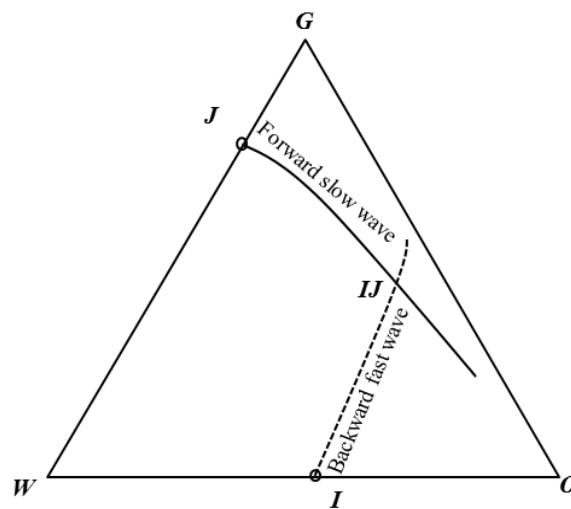


Figure 5.4 Simplified schematic of wave curve construction in the RPN program using the wave-curve method (WCM). The three vertices G, O, and W represent the saturation of gas, oil and water, respectively, where only that phase flows: i.e., at residual saturation of the other two phases. Thus residual phase saturations are not

shown on this, or subsequent, plots. The slow wave curve is constructed in the forward direction starting from J , and the fast wave curve, in the backward direction initiating from I .

Saturations within a shock, if it occurs, are unphysical and do not appear on a saturation profile. That leads to a discontinuity in saturations, meaning that the shock speed cannot be resolved through $J(S)$ comprising derivatives that are a function of saturations. The shock and its speed σ that reach I are then determined by constructing a Rankine-Hugoniot (RH) locus via the RH condition (Azevedo et al. 2010; Castañeda et al. 2016):

$$F(S) - F(S_I) = \sigma(S - S_I), \dots\dots\dots (5.13)$$

where S_I represent phase saturations at I . The RH condition is derived from a mass balance across a shock. This condition as in **Eq. 5.13** defines all possible states that may reach I via a shock, seen from the dashed line in **Fig. 5.4**, referred to as the backward fast-wave curve.

The two families of wave curves as illustrated in **Fig. 5.4** cross at some point denoted as IJ , at which the slow speed is less than the fast wave speed. The spreading wave velocities of saturations along the forward slow-wave curve increase in the forward direction starting from J . The shock velocities of points, along the backward fast-wave curve, decrease in the backward direction initiating from I to IJ . The whole path, from J to IJ and then to I , is thus guaranteed to meet the compatibility of monotonically increasing wave velocity. This result hinges on the nonlinearity of relative-permeability functions. In the simplified case of linear relative-permeability functions, shocks (**Eq. 5.13**) occur along the same curve as spreading waves (**Eq. 5.11**), but this is not the case in general (Namdar Zanganeh et al. 2011; Lake et al. 2014).

To avoid confusion in mathematical and engineering terminologies, we clarify that all the states that connect J to I (solved through the two families of wave curves), as shown in **Fig. 5.4** and subsequent illustrations, are referred to as a composition path. Saturation points on a spreading-wave curve are physical, which can be observed in a displacement. The two endpoints of a shock wave (i.e. intersection state IJ and initial state I in **Fig. 5.4**) are physical and can also be observed, whereas the other saturation points between these two states within the shock are unphysical, which cannot be observed.

Note that the WCM in the RPN has a different problem definition than a coreflood with specified injection rates of phases. In a coreflood, at $t_D = 0$, initial state I is defined as follows:

$$\begin{cases} S(x_D, 0) = I & 0 < x_D \leq 1 \\ S(x_D, 0) = J & x_D = 0 \end{cases} \dots\dots\dots (5.14)$$

Upon injection, initial state I , present for $0 < x_D \leq 1$ is displaced forward by injection state J starting at $x_D = 0$ with specified fractional flows of phases, as schematically illustrated in **Fig. 5.5**.

Strictly, the WCM does not specifically solve for a physical displacement of I for $0 < x_D \leq 1$ by J at $x_D = 0$. Instead, as shown in **Fig. 5.6**, it solves for an initial state with I present for $x_D > 0$ and J for $x_D \leq 0$:

$$\begin{cases} S(x_D, 0) = I & x_D > 0 \\ S(x_D, 0) = J & x_D \leq 0 \end{cases} \dots\dots\dots (5.15)$$

where S is a vector of saturations in a case of three-phase flow. Starting at time $t_D = 0$, injection of state J (from $x_D \ll 0$) begins, and the state evolves. The analysis below shows that this distinction is crucial to determining the correct displacing state J among multiple possible injection states. In particular, only a composition path with all positive wave velocities can represent a physical displacement by J at $x_D = 0$.

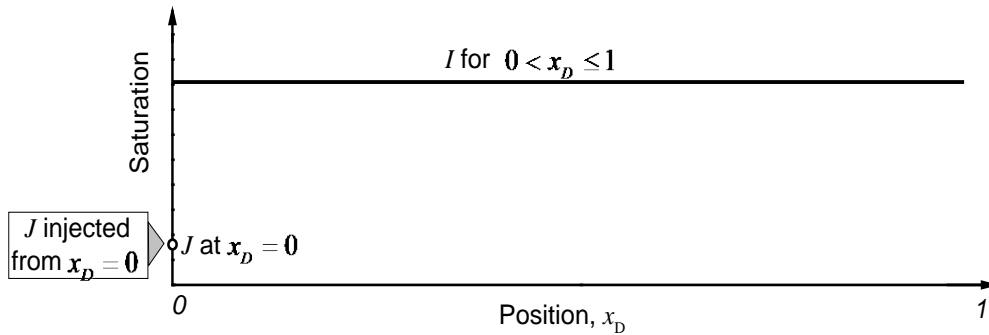


Figure 5.5 Schematic of problem definition for a coreflood. Injection state J , originating from $x_D = 0$ with given fractional flows of phases, displaces initial state I present for $0 < x_D \leq 1$.

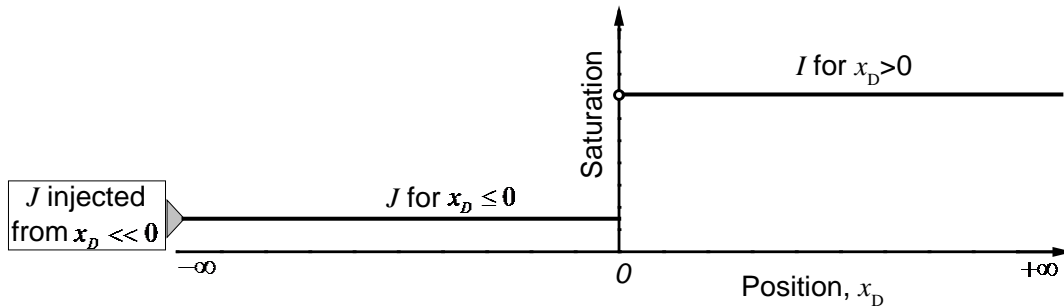


Figure 5.6 Schematic of problem definition for a displacement solved in the wave-curve method. Injection state J , from $x_D \ll 0$, drives an initial state of I for $x_D > 0$ and J for $x_D \leq 0$.

5.3 Foam model

A key to the success of foam-related applications is the physical stability and strength of foam with oil. We here apply the widely used IT foam model in the STARS simulator (Computer Modeling Group 2015; Cheng et al. 2000). It includes two algorithms describing the effect of oil on foam properties: the wet-foam representation and the dry-out representation. Appendix E gives the wet-foam representation that describes impacts of a series of physical factors on foam properties, i.e. surfactant concentration, water saturation, oil saturation, salinity, shear-thinning rheology and capillary number. Two major functions as in **Eqs. E-3** and **E-4** are included in this study to quantify the effect of S_w and S_o on foam properties. The dry-out representation can also predict multiple steady states (Tang et al. 2016), but we do not employ it here.

The model parameters we used are based on a detailed fit of coreflood data for foam without oil (Cheng et al., 2000; Alvarez et al., 2001) and are consistent with coreflood data on foam with oil (Tang et al., 2018).

5.3.1 Foam representation on ternary diagram

In corefloods, the mobility reduction in gas by foam is measured through pressure drop or pressure gradient. In modeling, this is evaluated via a mobility-reduction factor FM (Eq. E-2 in Appendix E) as a function of S_w and S_o . Through the factor FM , foam modifies gas mobility by reducing gas relative permeability. A larger value of $(1/FM)$ indicates greater reduction to gas mobility and thus stronger foam. The model parameters used as given in Table E-1 in Appendix E indicate a very strong foam, with an abrupt collapse of foam at S_w near the limiting water saturation, $fmdry$ (physically denoted as S_w^*).

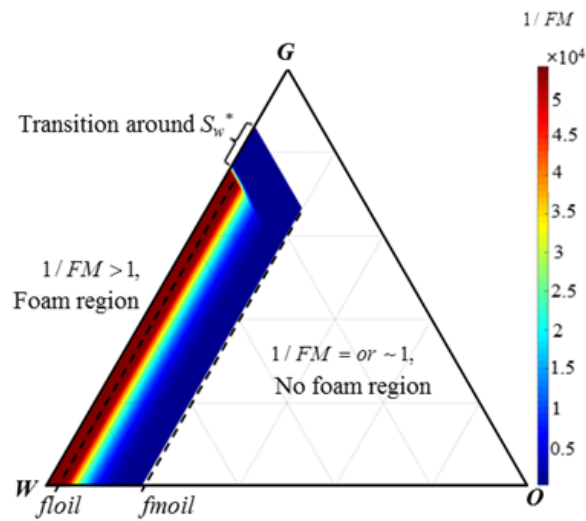


Figure 5.7 Foam-property map in ternary saturation space, visualized through gas-mobility-reduction factor ($1/FM$) defined by the wet-foam representation. Model parameters are in Table E-1 in Appendix E.

Figure 5.7 plots $(1/FM)$ in Eq. E-2 in ternary saturation space as defined in the wet-foam representation, where function F_2 in Eq. E-3, for the effect of S_w , and F_3 in Eq. E-4, for the effect of S_o , are considered. Generally, the factor $(1/FM)$ splits the ternary saturation space into three regions: a full-strength foam region, a partially-destabilized foam region and a no-foam region. The region with foam either at full strength or partially destabilized has $(1/FM) > 1$; this region resides at the lower-left corner of the ternary diagram. The remaining, white region, with $(1/FM) \sim 1$, indicates absence of foam.

The absence of foam indicated by the white region in Fig. 5.7 arises mainly from two reasons related to foam stability and strength. Foam stability is controlled by the limiting capillary pressure, which corresponds to a limiting water saturation S_w^* (Khatib et al., 1988; Rossen and Zhou, 1995). Along a direction parallel to the G–O binary, for S_w lower than S_w^* , foam collapses. The abruptness of collapse depends on an adjustable parameter $epdry$ in Eq. E-3, the value of which is large in this study as justified in coreflood measurements (Kim et al. 2005; Boeije & Rossen 2015; Tang et al. 2018). Specifically, for $S_w < (S_w^* - \varepsilon)$ F_2 in Eq. E-3 is nearly zero,

setting the inverse of factor FM in **Eq. E-1** close to unity. There is nearly no reduction in k_{rg}^f due to absence of foam in this range of S_w . As S_w rises, a transition zone in the interval $(S_w^* - \varepsilon) < S_w < (S_w^* + \varepsilon)$ seen in **Fig. 5.7** is marked by an abrupt increase in $(1/FM)$. This zone corresponds to an abrupt drop in k_{rg}^f around S_w^* in **Fig. E-1** in Appendix E. For $S_w > (S_w^* + \varepsilon)$, foam is at full strength in the absence of oil.

In the other direction, parallel to the G–W binary, increasing S_o weakens foam via **Eq. E-4**, leading to a larger value of FM and thus less gas-mobility reduction. The effect of S_o in **Eq. E-4** is bounded by two limits, an upper-limiting oil saturation f_{moil} and lower-limiting oil saturation f_{loil} . Specifically, for $S_o < f_{loil}$, oil-saturation-dependent function F_3 in **Eq. E-4** equals unity, meaning that oil has no detrimental impact on foam. For S_o between f_{loil} and f_{moil} , oil shows a nonlinear effect, indicated by the color gradient in **Fig. 5.7**. When $S_o > f_{moil}$, F_3 is zero, with $(1/FM)=1$; foam is killed completely. This corresponds to the sudden rise of k_{rg}^f around S_w , roughly 0.45 along the bottom axis of **Fig. E-1** in Appendix E. The full-strength foam results from combined effects of S_w and S_o , specifically for $S_w > (S_w^* + \varepsilon)$ and $S_o < f_{loil}$.

5.3.2 Multiple steady states in foam model

Experimental observations show that most oils destabilize foam (Rossen 1996; Farajzadeh et al. 2012). The widely used IT foam model shown in Appendix E suggests a cusp catastrophe as in **Figs. 5.1** and **5.2**, leading to multiple foam states. Tang et al. (2016) provide a detailed analysis of the occurrence of the multiple foam states. These phenomena are briefly described here for the purpose of our study.

The foam properties as shown in **Fig. 5.7** are usually evaluated through foam apparent viscosity μ_{app} . A larger value of μ_{app} indicates stronger foam. Treating multiphase flow in foam flow with oil as a pseudo-single phase and applying Darcy’s law gives the definition of apparent viscosity of total flow, μ_{app} :

$$\mu_{app} \equiv \frac{k \nabla p}{u}, \dots\dots\dots (5.16)$$

where u represents the total superficial velocity. With $u = u_w + u_o + u_g$, solving for ∇p for three-phase flow (**Eq. 5.4**) and substituting into **Eq. 5.16** returns μ_{app} as a function of (S_w, S_o) :

$$\mu_{app} = \frac{1}{k_{rw}/\mu_w + k_{ro}/\mu_o + k_{rg}^f/\mu_g}, \dots\dots\dots (5.17)$$

where the denominator $(k_{rw}/\mu_w + k_{ro}/\mu_o + k_{rg}^f/\mu_g)$ is the total relative mobility. Since fractional flows f_j for each phase defined in **Eq. 5.5** are also functions only of (S_w, S_o) , μ_{app} is then correlated to f_g, f_o and f_w through (S_w, S_o) .

Figure 5.8 plots μ_{app} as a function of f_g, f_o and f_w , using the wet-foam representation in Appendix E. On a ternary diagram of fractional flows, the shape of foam apparent viscosity μ_{app} forms a surface. The curves on

the surface are plotted for μ_{app} at various fixed ratios (f_o/f_w), which is equivalent to fixing (u_o/u_w). The blue curve, along the $f_g - f_w$ binary, shows the changing trend of μ_{app} without oil. As a group, the curves illustrate the shape of the surface.

A key feature illustrated in **Fig. 5.8** is that the surface folds back towards $f_g = 1$ in the middle, due to the destabilizing effect of oil on foam as explained by Tang et al. (2016). In the folded region, a set of fractional flows f_g, f_o and f_w corresponds to three possible foam states: a strong foam state with large μ_{app} on the upper surface, a collapsed-foam state with very small μ_{app} at the bottom nearly flat surface, and the intermediate state on the folding surface. Projection of the folded region onto the ternary diagram gives the dashed line, beyond which foam does not exist, either due to low S_w or high S_o . As briefly mentioned in the Introduction, the key issue we answer in the following section is which of the multiple possible foam states is the displacing state to oil for injection with fractional flows in the folded region. The displacing state controls the success of a foam process, since different states have very different mobilities.

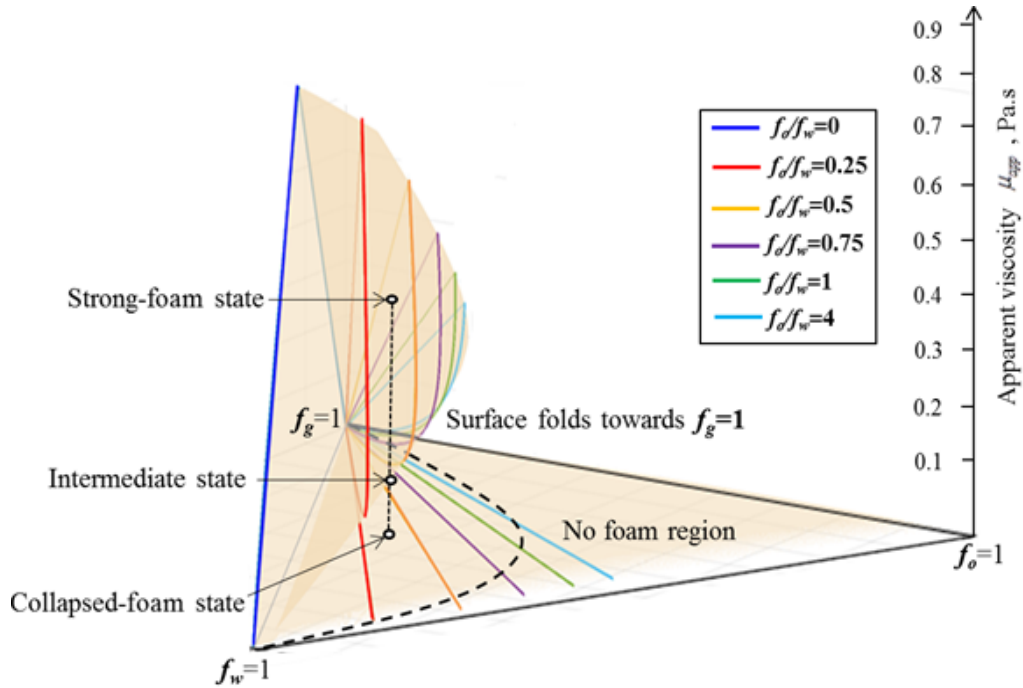


Figure 5.8 A surface describing foam apparent viscosity μ_{app} as a function of f_w, f_o and f_g , predicted by the wet-foam representation in Appendix E. The three vertices represent 100% f_w, f_o and f_g , respectively. The curves on the surface are plotted with various fixed ratios (f_o/f_w). The dashed line on the plane of ternary diagram illustrates projection of the surface. The vertical dashed line indicates a case of multiple foam states fitting a same set of fractional flows: an upper strong-foam state, intermediate state and lower collapsed-foam state.

5.4 Displacing state among multiple steady states

For a number of engineering applications described by a cusp catastrophe, the final state achieved in the folded region depends on the initial state (Holmes & Rand 1976; Golubitsky & Keyfitz 1980; Guckenheimer 1986;

Kravtsov & Orlov 1990). For a given set of injected fractional flows, we define two types of initial conditions I_1 , i.e. unfavorable (I_1) or favorable (I_2) to displacement by stable foam.

Figure 5.9 gives an example of a set of multiple foam states J_1 , J_2 and J_3 , all fitting the same injected fractional flows, and two types of initial states I_1 and I_2 . There are thus six composition paths, from each of J_1 , J_2 , and J_3 , to each of I_1 , and I_2 , respectively. The issue is which path represents the solution for the given injected fractional flows and each initial condition. **Table 5.1** summarizes the saturations of each possible injection state, J_1 , J_2 , and J_3 , and of the two types of initial conditions, I_1 and I_2 in **Fig. 5.9**. All the parameters needed in the construction of composition paths are taken from **Table E-1** in Appendix E.

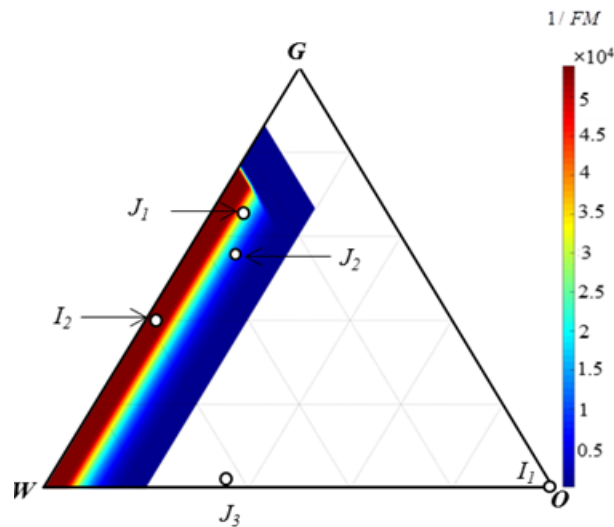


Figure 5.9 Illustration of a displacement with multiple possible displacing states represented by J_1 (upper state – low mobility), J_2 (middle state), and J_3 (lower state – high mobility) corresponding to the same injected fractional flows. I_1 and I_2 represent two initial conditions, unfavourable and favourable for displacement by stable foam (upper state), respectively. The colored patch indicates the foam region. Saturations are given in **Table 5.1**.

Table 5.1 A summary of cases presented for the analysis of multiple possible displacing states fitting the same injected fractional flows.

Scenarios		Injection conditions $J = (S_w, S_o)$		Initial conditions $I = (S_w, S_o)$	Remark
Scenario 1	Case 1	$J_1=(0.26998, 0.05404)$	Strong foam state	$I_1=(0, 1)$, outside stable foam region	J_1, J_2 and J_3 , all fit the same set of (f_w, f_o, f_g)
	Case 2	$J_2=(0.36382, 0.10110)$	Intermediate state		
	Case 3	$J_3=(0.65210, 0.34435)$	Collapsed foam state		
Scenario 2	Case 1	$J_1=(0.26998, 0.05404)$	Strong foam state	$I_2=(0.6, 0.01)$, inside stable foam region	
	Case 2	$J_2=(0.36382, 0.10110)$	Intermediate state		
	Case 3	$J_3=(0.65210, 0.34435)$	Collapsed-foam state		

Note that all saturations listed here are normalized for residual saturations through **Eq. E-5** in Appendix E.

Note that I_1 and I_2 in **Fig. 5.9** were selected outside and inside the foam region, mainly to illustrate the impact of the initial state on the choice of the displacing state among J_1 and J_2 and J_3 . However, the fundamental division of I in ternary saturation space, for the choice of the displacing state among the given set of J_1, J_2 and J_3 , is not necessarily the boundary of the foam region. The dependence of the displacing state on the initial state is captured through a boundary curve shown below.

5.4.1 Initial state outside foam region

The two major outputs in Riemann solutions solved by the WCM – composition paths and wave speeds – provide physical insights that unravel the occurrence and features of a displacement, i.e. wave type, configuration and propagation. We analyze Scenario 1 in **Table 5.1** first, with the initial state I_1 outside the foam region, based on the Riemann solutions of cases 1, 2 and 3 with J_1, J_2 and J_3 as the injection state, respectively.

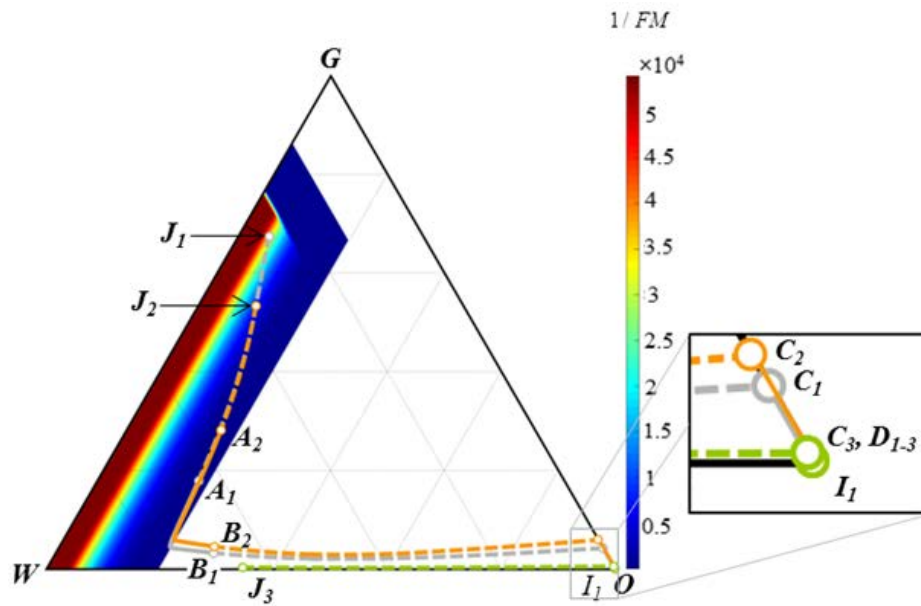


Figure 5.10 Three composition paths in ternary saturation space constructed from each of J_1, J_2 , and J_3 , respectively, to I_1 , which resides outside the foam region. The respective tracks of the three paths are denoted by: $J_1 - A_1 - B_1 - C_1 - D_1 - I_1$; $J_2 - A_2 - B_2 - C_2 - D_2 - I_1$; $J_3 - C_3 - D_3 - I_1$. The three saturation points at J_1, J_2 , and J_3 represent three foam states, all fitting the same (f_w, f_o, f_g) . A solid curve represents a spreading wave and a dashed curve represents a shock.

Figure 5.10 shows the three composition paths from each of J_1, J_2 , and J_3 to I_1 . Though J_2 might be intrinsically unstable as suggested by catastrophe theory, one could still theoretically construct a composition path from J_2 to I_1 . Tracks of the three paths from J to I on **Fig. 5.10** follow, respectively: $J_1 - A_1 - B_1 - C_1 - D_1 - I_1$; $J_2 - A_2 - B_2 - C_2 - D_2 - I_1$; $J_3 - C_3 - D_3 - I_1$. Each path comprises two groups of wave curves, i.e. the forward slow-wave group from J and backward fast-wave group from I as schematically illustrated in **Fig. 5.4**. These two groups of wave curves in a path are distinguished by the intersection state IJ , that corresponds to the point C_1 in J_1 path, C_2 in J_2 path and C_3 in J_3 path, respectively. Along each path in **Fig. 5.10**, the portion from J to IJ represents the slow-wave group, and the rest portion from IJ to I corresponds to the fast-wave group.

The specific structure of the three paths in **Fig. 5.10** is indicated by dashed and solid curves that represent the shock and spreading waves, respectively. The labelled letters A_k , B_k , C_k and D_k ($k = 1, 2$ and 3) indicate the transitions along each path from a shock to a spreading wave or the reverse. The paths from J_1 and J_2 to I_1 exhibit similar wave type and configuration. Both paths start from the injection state with a shock (from $J_1 - A_1$ along the path from J_1 or $J_2 - A_2$ along path from J_2) followed by a spreading wave (from $A_1 - B_1$ or $A_2 - B_2$). Thereafter, there occurs a second shock (from $B_1 - C_1$ or $B_2 - C_2$), that is connected to a second spreading wave (from $C_1 - D_1$ or $C_2 - D_2$) which eventually reaches I_1 with a shock wave, i.e. from D_1 to I_1 or D_2 to I_1 . Both paths feature a sharp inflection across the foam boundary at $S_o = fmoil$. This arises from foam collapse that yields an abrupt rise in gas mobility. Capturing this sharp inflection in calculations requires very fine resolution in saturation steps. The path from J_3 (with very small gas fractional flow as given in **Table 5.1**), at which foam is fully collapsed, starts with a shock from J_3 to C_3 . A nearly invisible spreading wave in **Fig. 5.10** connects C_3 to D_3 , which shocks to I_1 .

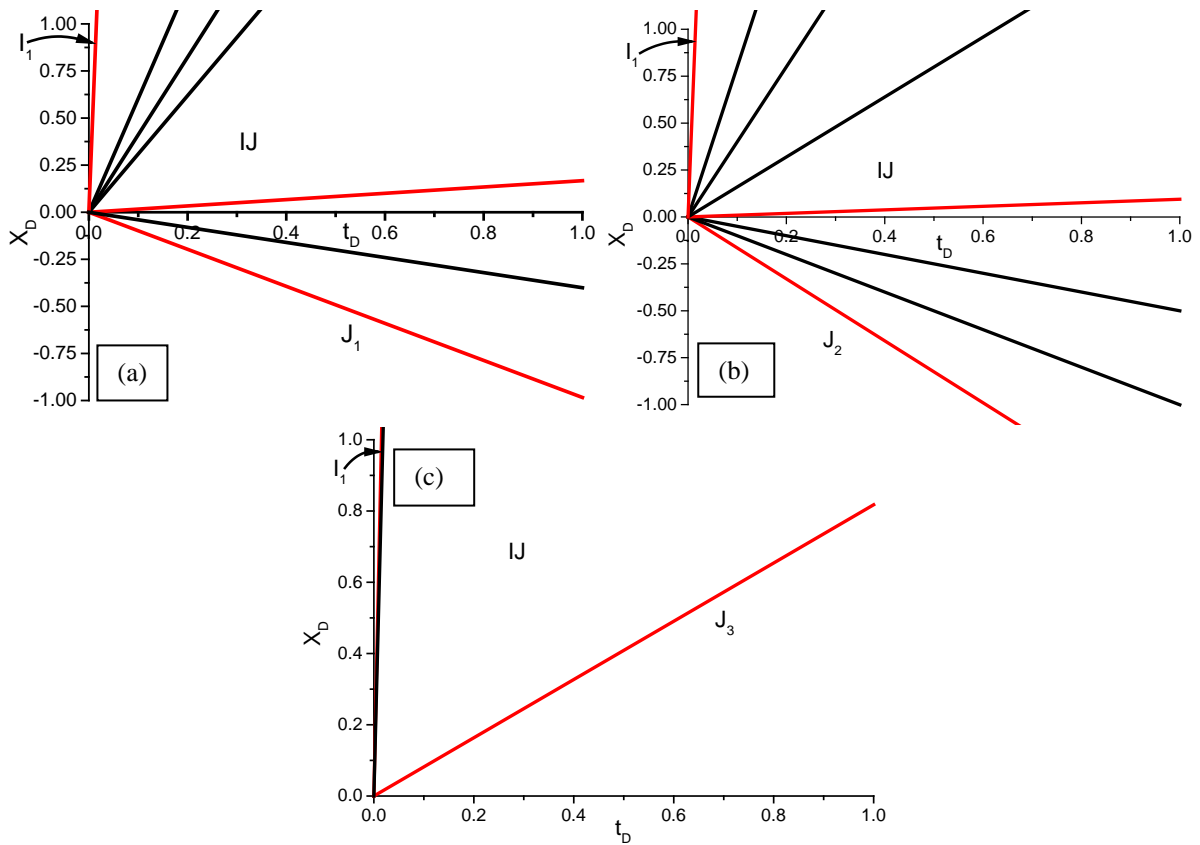


Figure 5.11 Trajectories of the associated wave speeds as a function of saturations along each path from J_1 , J_2 and J_3 to I_1 in **Fig. 5.10** in dimensionless x_D vs. t_D space. A red trajectory marks a shock, with black lines representing characteristics within spreading waves. Only the path from J_3 gives wave speeds that are all positive.

Figures 5.11 (a), (b) and (c) illustrate trajectories of the associated wave speeds as a function of saturations along each path from J_1 , J_2 and J_3 to I_1 in dimensionless x_D vs. t_D space. Fractional-flow theory states that, as implied by **Eq. 5.10** (Lake et al. 2014), the slope of each trajectory line in **Fig. 5.11** is the constant wave speed of

a given feature (shock, characteristic, etc.). A red trajectory corresponds to a shock wave, as denoted by a dashed curve in **Fig. 5.10**. Black lines in **Fig. 5.11** represent characteristics within spreading waves. I , J and IJ mark constant-state regions, with IJ being the intersection state at C_1 , C_2 or C_3 as illustrated in **Fig. 5.4**. The existence of the constant-state region at IJ is a major difference between two- and three-phase flows in porous media.

Comparing the wave speeds in **Figs. 5.11, (a), (b)** and **(c)** shows that the paths from each of J_1 and J_2 to I_1 pass through the bottom quadrant, reflecting negative wave speeds. In a physical displacement, the injected fractional flows $F(J)$ are maintained fixed at $x_D = 0$ as shown in **Fig. 5.5**. However, for both paths starting from J_1 and J_2 as in **Figs. 5.11 (a)** and **(b)**, the fractional flows at $x_D = 0$ with $t_D > 0$ deviate from those at J_1 or J_2 , due to the negative wave velocities. The appearance of negative wave velocities then rules out a foam state being the displacing state in a physically acceptable displacement.

Only the path from J_3 in **Fig. 5.11 (c)** yields wave speeds all positive, that corresponds to the physical injection condition in **Fig. 5.5**. J_3 , among the multiple possible foam states, is thus the displacing state in scenario 1 that displaces initial state I_1 outside the foam region.

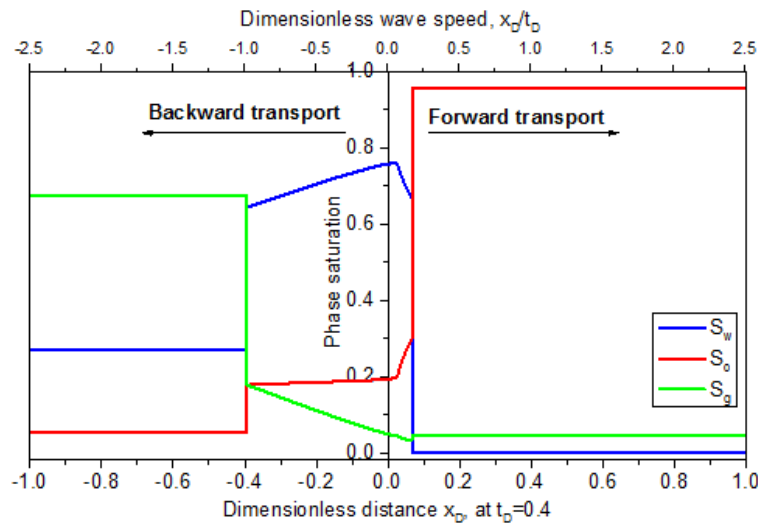


Figure 5.12 Wave speeds (on the top axis) and saturation profiles (on the bottom axis) for water, oil and gas along the path from J_1 to I_1 in **Figs. 5.10** and **5.11(a)**.

To illustrate the physical meaning of negative velocities in transport, we illustrate the Riemann solutions in terms of saturation profiles using the path from J_1 in **Fig. 5.10**. **Figure 5.12** displays the associated wave speeds from **Fig. 5.11 (a)** as a function of saturations (on the top axis), and also saturations as a function of position at fixed time ($t_D = 0.4$) on the bottom axis. Upon injection, those saturations with positive velocities in **Fig. 5.12** move forward from $x_D = 0$, whereas those with negative velocities propagate backward. For $t_D > 0$, the state at $x_D = 0$ is not J_1 ; thus the Riemann solution for a displacement with negative wave velocity is physically unacceptable.

5.4.2 Initial state inside foam region

A similar stability analysis is performed for Scenario 2 for the same set of foam states, J_1 , J_2 and J_3 , but with a different initial state I_2 , now inside the foam region.

Figure 5.13 illustrates the three composition paths from each of J_1 , J_2 and J_3 to I_2 , which are solved again based on the definition of **Eq. 5.15**. The structures of the three paths are indicated by their associated tracks: $J_1 - M_1 - I_2$; $J_2 - M_2 - I_2$; $J_3 - M_3 - I_2$. Specifically, the intersection state IJ that splits the slow- and fast-wave groups in the paths corresponds to the points M_1 , M_2 and M_3 on **Fig. 5.13**; these three points are located very close to each other, as seen in the left expanded view of **Fig. 5.13**, and all belong to the Hugoniot locus of I_2 . The paths from J_1 and J_3 to I_2 follow a similar structure, both starting with a slow shock (from $J_1 - M_1$ or $J_3 - M_3$) and then reaching I_2 with a fast shock (from $M_1 - I_2$ or $M_3 - I_2$). The path from J_2 follows first a spreading wave from $J_2 - M_2$, and thereafter a shock from M_2 to I_2 .

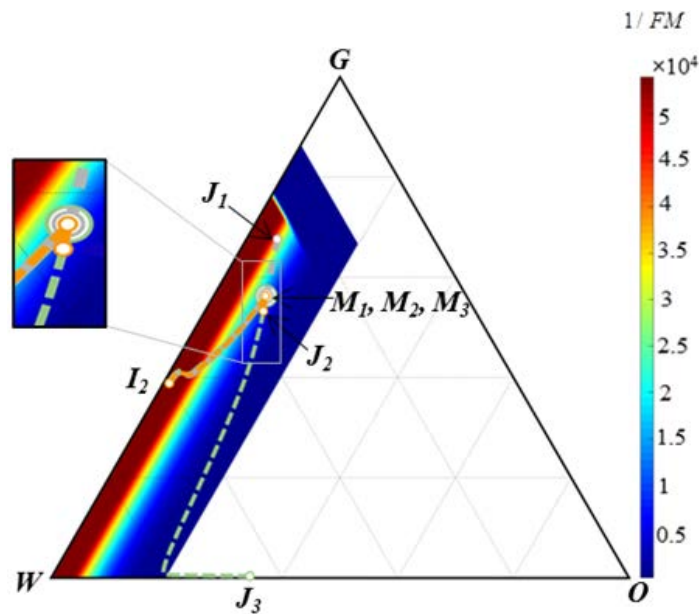


Figure 5.13 Three composition paths in ternary saturation space constructed from each of J_1 , J_2 , and J_3 , respectively, to I_2 located inside the foam region. The track of each path is: $J_1 - M_1 - I_2$; $J_2 - M_2 - I_2$; $J_3 - M_3 - I_2$. The phase saturations at J_1 , J_2 , and J_3 are the same as those in **Fig. 5.10**, fitting the same (f_w, f_o, f_g) . A solid curve represents a spreading wave and a dashed curve marks a shock.

Figures 5.14 (a), (b) and (c) show trajectories of the associated wave speeds as a function of saturations along each path from J_1 , J_2 and J_3 to I_2 in dimensionless x_d vs. t_d space. Only the path from J_1 to I_2 in the three paths has exclusively trajectories residing in upper quadrant, i.e., only positive wave speeds. Therefore, only the strong-foam state, J_1 , among the multiple possible injection states, is the physically true displacing state to the initial state I_2 . J_2 is not the displacing state in either scenario. The choice of the displacing state, among the multiple possible injection states, shows a dependence on initial state. In the following subsection, we show the nature of the dependence of the occurrence of J_1 or J_3 on initial state.

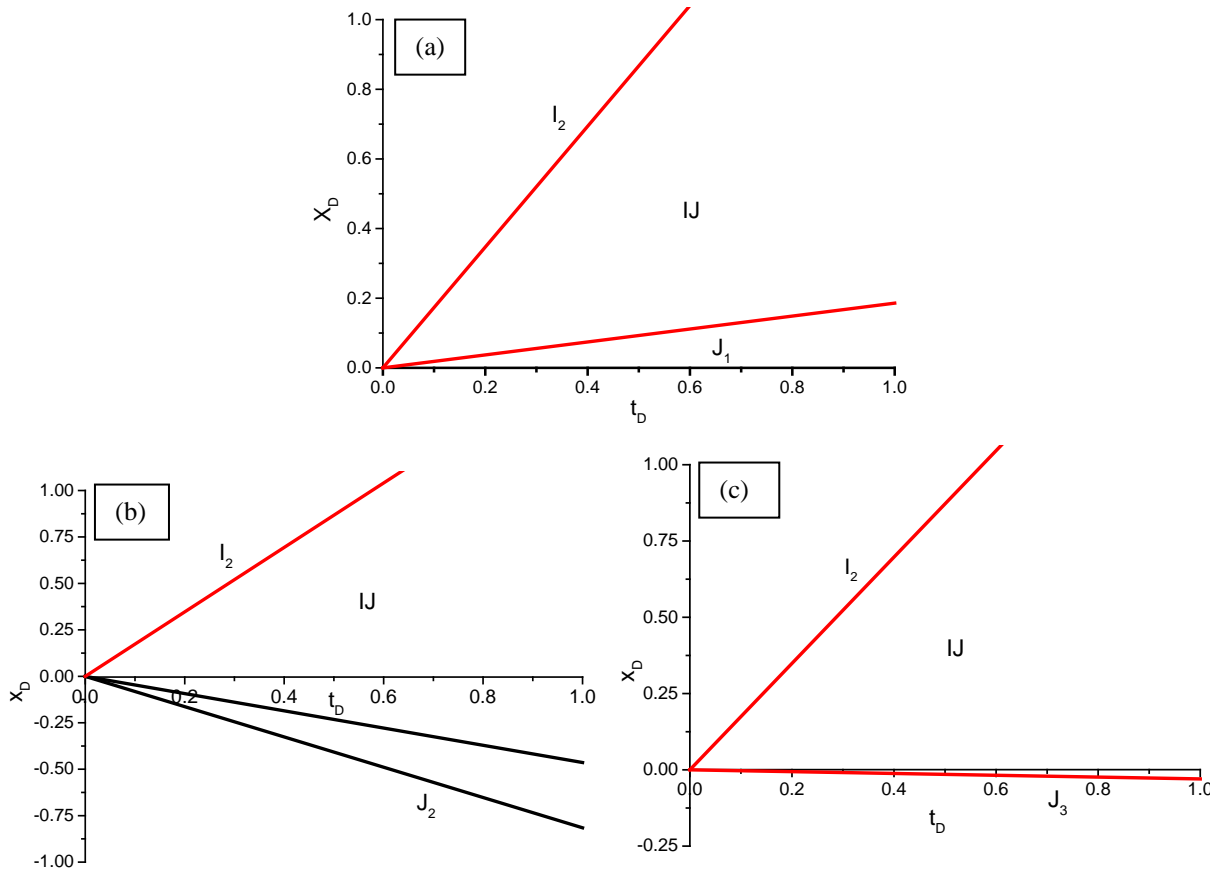


Figure 5.14 Trajectories of the associated wave speed as a function of saturations along each path from J_1 , J_2 , and J_3 to I_2 in **Fig. 5.13** in dimensionless x_D vs. t_D space. A red trajectory marks a shock, with black lines representing characteristics within spreading waves. Only the path from J_1 gives only positive wave speeds.

5.4.3 Boundary curve for the dependence of the nature of the displacement on I

To determine which of J_1 or J_3 is the displacing state to any initial state in ternary saturation space, it is tedious and impractical to go through the calculations as in **Figs. 5.11** and **5.14** for every I . It is then necessary to capture the universal dependence of the choice of the displacing state on initial state in whole ternary saturation space. This is especially crucial to improving the prediction and control of foam displacement with a given initial state in a reservoir, in particular with J corresponding to multiple possible injection states.

Intuitively, for an initial state I_2 inside the foam region, with low S_o favorable for stable foam, it makes sense that strong-foam state J_1 , with large μ_{app} and $\bar{V}p$, would make the displacement. By the same logic, an initial state I_1 outside the foam region, where high S_o that kills foam, would be displaced by the collapsed-foam state J_3 with low μ_{app} and $\bar{V}p$.

However, the location of I inside or outside the foam region is not decisive for the displacement by J_1 or J_3 . Instead, ternary saturation space is divided by a “boundary curve” (defined through the intermediate state J_2) that determines which of J_1 or J_3 makes the physically acceptable displacement. Mathematically, the boundary curve

is developed in terms of a forward fast-wave curve starting from J_2 . Specifically, in the cases presented in this study, its definition is given by the following two conditions:

$$\begin{cases} f_w(S) - f_w(J_2) = \sigma [S_w - S_w(J_2)] \\ f_o(S) - f_o(J_2) = \sigma [S_o - S_o(J_2)] \end{cases}, \dots\dots\dots (5.18)$$

$$\lambda_f(J_2) > \sigma > \lambda_{s,f}(S), \dots\dots\dots (5.19)$$

where $\sigma \in R_0^+$, S is a vector of saturations, and subscripts f and s denote the fast and slow eigenvalues of Jacobian matrix in Eq. 5.12, respectively. Equation 5.18 is the expanded form of Rankine-Hugoniot condition in Eq. 5.13. This condition gives all states S along the forward Rankine-Hugoniot locus starting from J_2 . Equation 5.19, as stated in Lax theory (Lax 1957), defines the 2-Lax shocks starting from J_2 . $\lambda_f(J_2)$ in Eq. 5.19 is positive, guaranteeing that all admissible 2-Lax shocks from J_2 have positive wave speeds σ . These two conditions therefore in Eqs. 5.18 and 5.19 represent a collection of admissible local 2-Lax shocks starting from J_2 , illustrated as the boundary curve in Fig. 5.15.

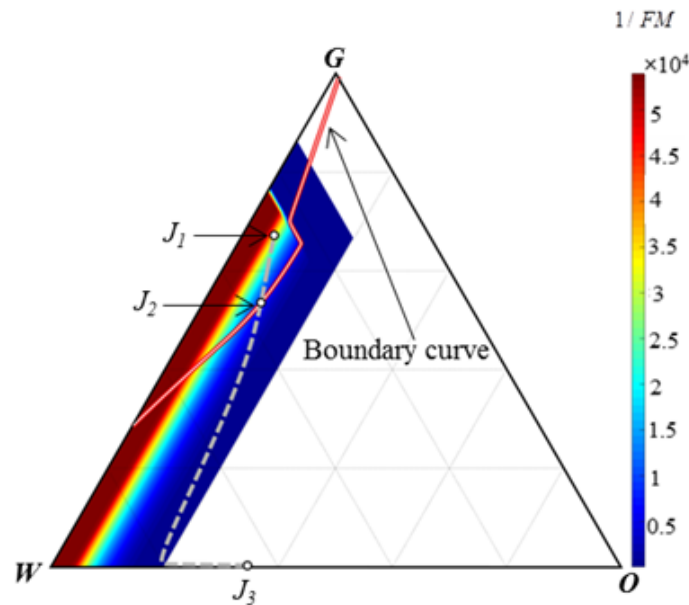


Figure 5.15 Boundary curve defined through the intermediate state J_2 by Eqs. 5.18 and 5.19, that captures the dependence of the nature of the displacement on initial state I .

Ternary saturation space as shown in Fig. 5.15 is split into two regions: the region above the boundary curve, where state J_1 resides, and the region below the boundary curve, where state J_3 is located. For any I in the upper region, the strong foam state J_1 is the displacing state that gives a path with wave speeds all positive. In contrast, for any I in the lower region, the collapsed-foam state J_3 makes the physically acceptable displacement.

For an I exactly on the boundary curve in Fig. 5.15, one could not distinguish which of J_1 , J_2 or J_3 makes the displacement, since all paths from J_1 , J_2 and J_3 are physically admissible in theory. The path from J_2 is connected to I by an admissible 2-Lax shock. Given that J_1 , J_2 and J_3 all fit the same injected fractional flows, the path from J_1 or J_3 would jump first to J_2 with zero velocity and then follow the same track as the path from J_2 to I (Castañeda & Furtado 2016). However, any perturbation that takes I off the boundary curve would always results

in negative velocities along any sort of path from J_2 , which is physically unacceptable. A physically acceptable displacement would then shift to either J_1 or J_3 , depending on the location of I with respect to the boundary curve.

5.5 Discussion

5.5.1 Significance for field applications

Foam for enhanced oil recovery is of course never co-injected with oil. Nevertheless, geological formations and fluids have many complexities (Lake et al. 2014): geological heterogeneity, fractures, unfavourable mobility ratios of displacing to displaced fluids, gravity segregation, etc. Part of the oil may remain in place due to limited displacement and sweep efficiency after initial gas injection. Since foam enhances greatly the sweep and displacement efficiency of gas injection, it is likely that injected foam flows with oil starting near the wellbore. Direct applications of foam to removing DNAPL contaminants in aquifers and soils would also involve co-current foam flow with fluids that may affect foam stability. All these situations may have multiple possible foam states fitting the same injected fractional flows for most process designs. If a displacing phase is a collapsed-foam state, that means a failure of foam application. The theory and findings presented in this study may assist in predicting the displacing state for given initial conditions. One can then optimize the design of foam processes to ensure their success in engineering applications.

In a simplified one-dimensional model for foam processes in a homogeneous medium, the injected foam lies along the water-gas binary of the phase diagram and the initial state below and to the right. If gas has not previously been injected, the initial state is on the water-oil binary. The foam performance with the particular model parameters we implemented is not sufficiently effective for such a process. Only an initial state I in the small upper-left region in **Fig. 5.15** would be displaced by the strong foam state J_1 . The poor performance arises in part from the values of the oil parameter f_{oil} selected, close to S_{or} . This implies that most physically realizable oil saturation destabilizes foam somewhat. In addition, in the cases examined foam collapses completely at a modest oil saturation above f_{moil} .

In contrast, experimental observations and field pilots demonstrate that foam can show very good performance in displacing oil (Simjoo et al. 2012; Tang et al. 2018). Thus the parameters used here for illustration do not by any means represent all foam processes with all oils. By selecting surfactants that enhance foam tolerance to oil, i.e. with f_{oil} well above S_{or} and a large value of f_{moil} , a foam process more resistant to oil could be modelled by techniques similar to those here. Further efforts are needed to explore the displacement behavior with greater tolerance of foam to oil, so that one can represent cases of oil displacement by stronger foam and maximize the benefit of foam applications.

5.5.2 Experimental verification of multiple steady states

Here we suggest two ways to confirm the multiple steady states predicted for foam flow with oil using laboratory corefloods. First, one could do a displacement, under different initial conditions, with an injection condition (fixed fluxes) that corresponds to multiple steady states. The core would be initialized either at a high S_o such as I_2 , or a low S_o like I_1 . Foam apparent viscosity or pressure gradient (∇p) across the core achieved at steady state may well depend on the initial conditions. Different foam states achieved for the same injection condition would

reflect the existence of multiple steady states, i.e. J_1 and J_3 . Second, one could fix ∇p and f_g across the core. A series of measurements at steady state with increasing ∇p might give a folding curve similar to **Fig. 5.2**. Both approaches face challenges. Collecting foam model parameters and relative-permeability curves that fit a specific situation is time-consuming and difficult in the presence of oil. Core-scale artifacts (entrance region for foam generation, capillary end effect) can distort coreflood measurements, even at steady state. Moreover, as noted in the wave speeds reported above, the time to reach steady state can be long, especially in the cases of displacement by a weak or collapsed foam.

5.6 Conclusions

The implicit-texture foam model discussed here predicts multiple steady states for foam flow with oil: an upper strong-foam state J_1 , intermediate state J_2 and lower collapsed-foam state J_3 , with different apparent viscosities but all fitting the same set of fractional flows. A displacement could then correspond to more than one possible injection state for the same injected fractional flows. Our study shows how to determine which state makes the displacement and the dependence of the nature of the displacement on initial condition, using three-phase fractional-flow theory and the wave-curve method.

The wave-curve method (WCM) for three-phase flow in porous media has a different problem definition than a coreflood with specified injection rates. In a coreflood, injection state J is fixed at, $x_D = 0$ displacing forward initial state I , which is present for $0 < x_D \leq 1$. In the WCM, J is injected from $x_D \ll 0$, with initial state I present for $x_D > 0$ and J for $x_D \leq 0$.

The distinction between the problem definitions in the WCM and a coreflood, makes the WCM capable of identifying the unique displacing state among multiple possible injection states J_1 , J_2 and J_3 . A composition path, from each of J_1 , J_2 and J_3 to initial state I , can be constructed in the WCM, satisfying the conservation equations. Only the path with only positive velocities, in the solutions solved by the WCM, corresponds to a physical injection by J maintained at $x_D = 0$. Any composition path featuring negative velocities does not correspond to this physical injection condition.

A stable displacement could be made by either the upper strong-foam state J_1 or the lower collapsed-foam state J_3 , but never the intermediate, intrinsically unstable state J_2 . The choice of the displacing state shows a dependence on initial state. We define a boundary curve through the unstable intermediate state J_2 in ternary saturation space, that captures the dependence of the nature of the displacement on initial state I . For any I in the region where the upper state J_1 resides, the strong foam state J_1 makes the displacement. For any I located in the region where the lower state J_3 lies, it corresponds to a stable displacement by the collapsed-foam state J_3 .

The significance and implications of the findings for field applications are discussed. We also give suggestions for the verification of multiple steady states in foam flow with oil through corefloods in laboratory.

CT COREFLOOD STUDY OF TRANSIENT FOAM FLOW WITH OIL

Summary

We present a CT coreflood study of foam flow with two representative oils: hexadecane C_{16} (benign to foam) and a mixture of 80 wt% C_{16} and 20 wt% oleic acid (OA) (very harmful to foam). The purpose is to understand the transient dynamics of foam, both generated in-situ and pre-generated, as a function of oil saturation and type. Foam dynamics with oil (generation and propagation) are quantified through sectional pressure-drop measurements. Dual-energy CT imaging monitors phase saturation distributions during the corefloods. With C_{16} , injection with and without pre-generation of foam exhibits similar transient behavior: strong foam moves quickly from upstream to downstream and creates an oil bank. In contrast, with 20 wt% OA, pre-generation of foam gives very different results from co-injection, suggesting that harmful oils affect foam generation and propagation differently. Without pre-generation, initial strong-foam generation is very difficult even at residual oil saturation of just 0.1; the generation finally starts from the outlet (a likely result of the capillary-end effect). This strong-foam state propagates backwards against flow and very slowly. The cause of backward propagation is unclear yet. However, pre-generated foam shows two stages of propagation, both from the inlet to outlet. First, weak foam displaces most of the oil, followed by a propagation of stronger foam at lower oil saturation. Implicit-texture foam models for enhanced oil recovery cannot distinguish the different results between the two types of foam injection with very harmful oils. This is because these models do not distinguish between pre-generation and co-injection of gas and surfactant solution.

6.1 Introduction

Injection of gases (e.g., CO₂, steam, N₂ or hydrocarbon gases) is nowadays a mature enhanced oil recovery (EOR) technology (Van Bergen et al., 2004; Zuloaga et al., 2017; Baghernezhad et al., 2019). Nevertheless, gas injection EOR is in general subject to poor sweep efficiency (Orr, 2007). Foam in porous media possesses unique microstructure (bubbles separated by interconnected thin films) and reduces considerably gas mobility (Kovscek and Radke, 1993; Rossen, 1996). These features give foam injection into geological formations broad engineering applications, e.g. remediation of aquifers or soils (Hayes, 2001; Hirasaki et al., 1997) and Carbon Capture, Utilization and Storage (Alcorn et al., 2018; Bui et al., 2018; Ren and Duncan, 2019). In the petroleum industry, both laboratory studies and field pilots identify foam as a promising technology in assisting gas injection EOR (Andrianov et al., 2011; Carpenter, 2018; Patil et al., 2018; Rossen, 1996). The application of foam for EOR mainly rests on the fact that the dramatic gas-mobility reduction caused by foam results in a remarkable increase in the sweep efficiency of gas injection and thus an increase in oil recovery. Key to the success of foam EOR is the effectiveness of foam for gas-mobility control, which is evaluated in terms of foam stability and strength (reflected through its apparent viscosity – the inverse of total relative mobility of phases).

Foam-oil displacement in reservoirs is a complex process in which the effectiveness of foam is subject to many physical factors, e.g. water saturation, salinity, oil saturation and composition, pressure, temperature, surfactant type and concentration, rock properties, etc. (Rossen, 1996; Rossen, 2013). The impact of oil among these factors is most prominent, since oil left behind in place after prior flooding is out of one's control and subsequent foam injection in most cases is unavoidably in contact with oils most of which destabilize foam (Farajzadeh et al., 2012). However, the quantitative correlation between foam stability and oil-related factors (e.g. oil saturation S_o and composition) have remained a long-standing challenge, in particular in transient displacements (Farajzadeh et al., 2012). This gap in knowledge restricts our understanding to foam-oil interactions in geological formations and, more importantly, the reliable design of a foam EOR project.

Foam flow without oil at steady-state shows two regimes as a function of foam quality (i.e., gas volumetric fractional flow in foam) (Osterloh and Jante, 1992; Alvarez et al., 2001): high- and low-quality regimes. Tang et al. (2016; 2018) have quantified the effect of several model oils on foam through their effects on the two foam regimes. Their data demonstrate that the two regimes for steady-state foam flow without oil also apply to foam with oil, with the high-quality regime more sensitive to oil. In addition, they find in their data fitting that the two foam regimes with oil can be captured by a widely used implicit-texture foam model in STARS simulator (Computer Modeling Group, 2015). These two regimes are often used as a starting point for deeper exploration of subsurface foam dynamics. In particular, the two regimes provide a basis for estimating foam model parameters in simulating foam EOR processes on the field scale (see, e.g., Boeije and Rossen, 2015; Rossen and Boeije, 2015). However, there is a knowledge gap concerning the transient dynamics of foam flow with oil and the confidence of using foam properties estimated from steady-state data to simulate dynamic behavior.

Many prior studies investigate transient foam flow with oil that is immobile, i.e. foam injection at residual oil saturation S_{or} (Myers and Radke, 2000; Jensen and Friedmann, 1987; Schramm and Novosad, 1990; Raterman, 1989). The S_{or} was achieved by pre-flushing an oil-saturated core with water and / or surfactant and assumed to

be unchanged by foam injection. As S_o was not measured directly in these studies, S_{or} may be lower to foam than to water or surfactant, given the highly increased pressure gradient with foam. Ignoring the change in S_{or} may thus cause misinterpretation of the correlation between foam dynamics and S_o .

Recent studies explore the transient behavior of foam flow with oil using CT scanning to monitor phase distributions during corefloods (Simjoo et al., 2013; Janssen et al., 2019). For simplicity, foam or liquid phase was regarded as a single phase in CT imaging. Foam stability without oil is controlled by limiting capillary pressure, which corresponds to a limiting water saturation S_w^* , the water saturation below which foam collapses abruptly (Zhou and Rossen, 1995; Cheng et al., 2000). Tang et al. (2018) in their experimental study find that oil destabilizes foam by increasing S_w^* . Nevertheless, specific water saturation or oil saturation or both is unknown when treating foam or liquid phase as a single phase. One loses insights on the correlation between S_o and foam stability (i.e. featured by S_w^*). More recently, Janssen et al. (2019) measure three-phase saturations to investigate the creation of an oil bank during foam injection. Model oil examined in their study is hexadecane, much less harmful to foam stability than some crude oils in reservoirs.

We present a CT coreflood study of foam displacement with two representative model oils: one benign to foam stability and the other very harmful to foam stability. A major purpose is to understand the transient dynamics of foam, both pre-generated and generated in situ by co-injection of surfactant solution and gas, as a function of oil (including oil type and oil saturation). We measure both transient and steady-state sectional pressure drops vs. time to infer foam properties and dynamics, e.g. strength, generation and propagation. The real-time three-phase distributions along a core are monitored using dual-energy CT scanning. We then relate quantitatively foam properties and dynamics to phase distributions (in particular, oil type and saturation). At the end, we discuss the implications of the experimental findings to the engineering applications and simulations of foam EOR.

6.2 Experimental design

6.2.1 Materials and apparatus

6.2.1.1 Materials

For the purpose of the study, two representative model oils are examined: hexadecane (C_{16}) of 99% purity supplied by Sigma-Aldrich, and a mixture of 80 wt% C_{16} and 20 wt% oleic acid (OA) of a purity 99% provided by Honeywell Fluka. Their effects on steady-state foam flow have been shown in Chapter 3 (Tang et al., 2018): C_{16} is relatively benign to foam stability whereas the mixture with 20 wt% OA greatly destabilizes foam. Here we use these two model oils to examine the detrimental effects of oil on transient dynamics of in-situ-generated and pre-generated foam during EOR processes.

The gas phase for foam generation is pure nitrogen (N_2) with a purity of 99.98%. Foaming agent is BIO-TERGE AS-40K AOS (C_{14-16} alpha-olefin-sulfonate), delivered with an activity of 40%, that is used directly as received from the provider Stepan company in USA. Surfactant solution is prepared using deionized water. Surfactant concentration we use is 0.5 wt% AOS in the solution with a salinity of 3 wt% sodium chloride (Merck). Below, aqueous surfactant solution is referred to as the water phase.

The core sample is Bentheimer sandstone. **Table 6.1** lists the physical properties of the Bentheimer core sample used in our experiments. To avoid the complexity of property changes in core samples and facilitate the comparison of experimental results, we conduct all the measurements in the same core. Isopropanol of 99.9% purity (C₃H₈O, Emplura) is used to kill foam in cleaning the core.

Table 6.1 Physical properties of Bentheimer core used in foam flow experiments

Properties	Quantities
Length (cm)	40 ± 0.1
Diameter (cm)	4 ± 0.1
Pore volume (cm ³)	110.5
Porosity (%)	22 ± 0.1
Absolute permeability to brine (Darcy)	2.82 ± 0.1

6.2.1.2 CT coreflood apparatus

Figure 6.1 shows a schematic of the CT coreflood apparatus constructed for foam flow experiments with oil. As one follows the flow path starting from the left side, water and oil are each injected using a Vindum pump (VP-12K, Vindum Engineering, Inc.). The pump can work smoothly up to 12, 000 psi (827.4 bar) and delivers oscillation-free flow rates ranging from 0. 0001 – 29 cm³/min. Two pistons in the pump allow continuous injection of water or oil as needed rates. Gas is provided by a 200 bar N₂ cylinder, and its injection is controlled through a Bronkhorst gas mass-flow controller (F-111B), with a rate ranging from 0.16 – 160 cm³/min (at standard pressure *P* and temperature *T* conditions). The fluids are then injected into a core sample (i.e., Bentheimer sandstone), which is held by a PEEK (polyether-ether-ketone) coreholder. The core surface is sealed with a glue of ~ 0.2 cm, to prevent the bypass of fluids from the side of the core.

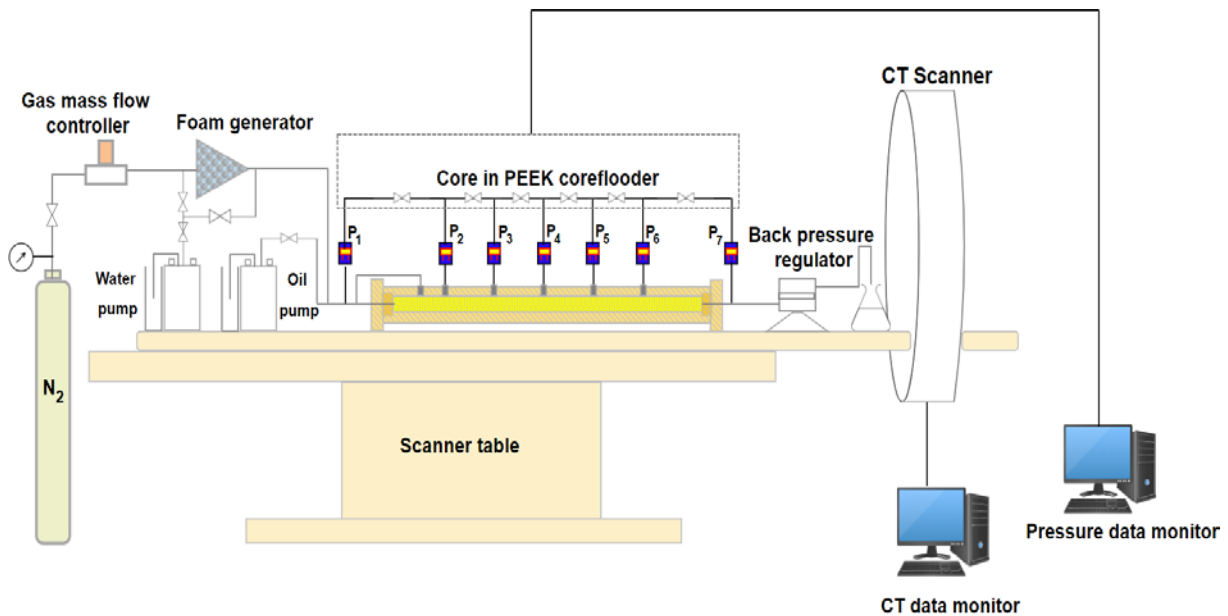


Figure 6.1 Schematic of CT coreflood apparatus for foam-oil flow experiments.

A back-pressure regulator is placed downstream of the coreholder to maintain P at the core outlet at 50 bar. Confining pressure, at the upstream injection pressure, is imposed by connecting the injection line to the narrow chamber between the coreholder and core sample, which is filled with water.

The whole coreflood apparatus is placed on the CT scanner table, the top portion of which is movable in both forward and backward directions. The pressure monitor records pressure drops across six sections along the core through pressure transducers (i.e. P_{1-7}), with the first and last section of length 6.6 cm, and the four sections in the middle each of 6.7 cm. These transducers are connected to the Bentheimer core through the coreholder using PEEK tubes. The CT data monitor records CT measurements for phase distributions. The specifications of CT measurements and foam-flow experimental procedures are given in subsequent sections, with determination of phase distributions from CT images delineated in Appendix F.

6.2.2 CT measurements

The key parameter measured through CT scanner is the linear attenuation coefficient, μ_{CT} given by

$$I_{CT} = I_{CT,0} \left(\exp^{-\mu_{CT}x} \right), \dots\dots\dots (6.1)$$

where $I_{CT,0}$ is the original intensity of photons in X-ray source, I_{CT} is the intensity of photons transmitted across a material of distance x , \exp denotes natural exponential, and μ_{CT} is the linear attenuation coefficient.

μ_{CT} in the CT scanner used is linearly transformed to Hounsfield (HU) unit scale, the value of which is referred to as CT number, given as follows:

$$CT = 1000 \times \frac{\mu_{CT} - \mu_{CT,water}}{\mu_{CT,water} - \mu_{CT,air}}, \dots\dots\dots (6.2)$$

where $\mu_{CT,water}$ and $\mu_{CT,air}$ are respectively linear attenuation coefficients of water and air.

CT scans in this study are taken perpendicular to flow direction and start from core outlet. Each slice scanned is 2 mm in thickness, with a resolution of 512-by-512 pixels. A single scan of the whole core comprises 204 slices, with two extra slices at each end of the core, and takes in total 27 seconds. CT numbers in foam flow with oil are a function of saturations of three phases, i.e. water saturation S_w , oil saturation S_o and gas saturation S_g . To solve for S_w , S_o and S_g through measured CT numbers, one needs dual energies, each of which gives a series of independent CT numbers as a function of e.g. S_w and S_o . S_g is equal to $(1 - S_w - S_o)$.

To distinguish water from oil, a common practice is to dope either water or oil or both to enlarge the contrast in CT number between the two phases. 140-kv and 80-kv beams are employed here and in this study. **Figure 6.2** shows CT numbers of water doped by KI (potassium iodide) and oil doped by IDD (iododecane) in bulk, relative to cases without dopant. We find that doping oil phase alone with 20 wt% IDD gives a greater contrast between CT attenuations (HU) of water and oil than doping water or both phases, e.g., 31 for water vs. 1012 for oil with 140 kv and 56 for water vs. 2386 for oil with 80 kv (seen from **Fig. 6.2**). Specifically, the CT attenuation ratio of 140 kv / 80 kv for water (e.g., $31/56 = 0.55$) is different from that for doped oil (e.g., $1012/2386 = 0.42$). Therefore, the two energy beams yield two independent CT numbers (each as a function of S_w , S_o and S_g) in a

single voxel. Steady-state coreflood tests by co-injecting gas, water and oil doped with 20 wt% IDD did not show noticeable difference in pressure gradient ∇P relative to that without oil dopant; this demonstrates the addition of IDD does not significantly affect foam behavior. We choose to dope the oleic phase with 20 wt% IDD in our CT foam coreflood experiments.

In the CT images we present below, solid red, green and blue represent 100%, 50% and 0% saturations of the given phase, respectively.

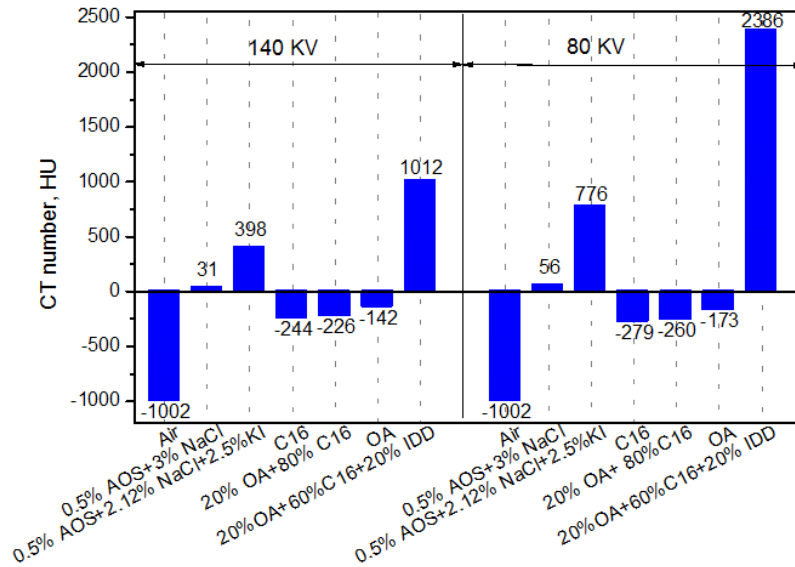


Figure 6.2 CT numbers of water and oil in bulk with and without dopant at a temperature of 21°C and pressure of 1 bar, in Hounsfield units (HU). IDD (iodododecane) is dopant for oil and KI (Potassium iodide), for surfactant solution. C₁₆ and OA denote the model oils, hexadecane and oleic acid, and AOS is the surfactant used.

6.2.3 Experimental procedures

All the foam-oil flow experiments are conducted in the CT room at ~ 21°C. For three-phase saturation measurements using dual energies, one needs to follow a particular experimental sequence as follows. The specific formulas for calculating porosity and phase saturations based on measured CT numbers are described in Appendix F.

Step 1. Core sample preparation. Drill a Bentheimer core of sizes listed in Table 1. Apply a layer of glue to the radial surface of the core to prevent bypass of fluids along its side. Cut the glued core to fit the size of coreholder. Dry the core in an oven at 60°C for 48 hours. Insert the core into the coreholder and close the coreholder. Connect the coreholder to the rest of the setup and conduct gas-leakage test to ensure no leakage at elevated pressure. The following measurements are all with the back-pressure fixed at 50 bar.

Step 2. CT scan of dry core (CT_{dry}). Conduct a CT scan of the dry core before introducing any liquids.

Step 3. CT scan of wet core (CT_{wet}) and permeability test. Conduct a CT scan of a 100% brine-saturated core, and measure the absolute permeability K of the core to brine.

- Step 4. CT scan of the core at connate water saturation S_{wc} to oil flood ($CT_{S_{wc}}$). Flush the brine-saturated core in Step 3 with 4 PV oil until S_{wc} and take a CT scan. Our measured value of S_{wc} is comparable to SCAL (Special Core Analysis) data in Bentheimer sandstone, i.e. 0.14 – 0.18 (Andrianov et al., 2012).
- Step 5. CT scan of the core at S_{orw} (waterflood residual oil saturation) ($CT_{S_{orw}}$). Flush the core at S_{wc} in step 4 with 4 PV brine until S_{orw} and take a scan. The oil saturation at 4 PV injection of brine is confirmed to be at waterflood residual oil saturation S_{orw} by 15 PV injection.
- Step 6. Injection of 1 PV surfactant solution to satisfy surfactant adsorption before foam injection. Because this is not an ultralow IFT surfactant, no oil is produced during this step.
- Step 7. Pressure-drop (ΔP) measurements and CT scan of the core during foam injection. Following step 6, inject foam into the core at S_{orw} , in one of two ways, i.e. either by co-injection of surfactant solution and gas or by direct injection of pre-generated foam. Upon injection, measure sectional ΔP vs. time and take CT scans according to foam responses that are reflected by the measured ΔP .
- Step 8. CT scan of the core at final steady state.
- Step 9. Cleaning of the core sample, following the procedures as follows:
- Kill foam from previous experiments using 4 PV isopropanol.
 - Flush the core with CO₂ for 5 hours. Most isopropanol is displaced out and the rest is volatilized by CO₂, to guarantee no interference of isopropanol to following foam measurements.
 - Clean CO₂ with brine injection. Most CO₂ is displaced and the rest is dissolved in brine through enhancing and releasing back pressure of 50 bar several times during flush.
 - Check the cleaning, by measuring core permeability K to brine. If K deviates significantly from the original value, one could repeat the steps 1 – 3 above. In our measurements, K after cleaning is within $\pm 7\%$ original permeability.
- Step 10. Preparation of next experiment. Since the same core is used in additional experiments, steps 2 to 4 give the reference CT scans that can be applied to three-phase saturation measurements in all subsequent experiments. Thus, in each new experiment, we prepare the core and satisfy surfactant adsorption following steps 3 to 6 (without needing to take CT scans, except for step 5 to determine initial state S_{orw}), and then start foam injection and CT scans from Step 7.

Table 6.2 An overview of experimental conditions in foam-oil flow experiments

Experiment	Oil type	Injection condition			Initial condition (S_{orw})	Back pressure, (bar)	Remarks
		f_g	$u_t = u_g + u_w$ (ft/day)	Foam injection			
EXP-01	Hexadecane (C ₁₆)	91%	4.58	In-situ-generated foam	0.46 ± 0.02	25	Simjoo and Zitha (2013)
EXP-02		70%	4.58	Pre-generated foam	0.41 ± 0.02	50	–
EXP-03	Mixture of 80wt% C ₁₆ + 20wt% OA	70%	4.58	In-situ-generated foam	0.39 ± 0.02	50	–
EXP-04		70%	4.58	Pre-generated foam	0.45 ± 0.02	50	–

OA denotes oleic acid, f_g (i.e., gas fractional flow in foam) is the injected foam quality.

6.3 Results and discussion

Table 6.2 gives an overview of the injection and initial conditions in each foam-oil flow experiment we conduct. In general, the experimental results we present include data on sectional ΔP along a core, saturations profiles and CT images. The data on ΔP quantify foam properties and reflect foam generation and propagation. Phase distributions obtained in CT measurements provide complementary data.

6.3.1 Model oil – C₁₆

6.3.1.1 In-situ-generated foam

Studies on foam flow with less-harmful oils, e.g. C₁₆, have been reported in the literature (Simjoo and Zitha, 2013; Janssen et al., 2018; Amirmoshiri et al., 2018). For comparison with foam flow with harmful oils, we refer to the results of Simjoo and Zitha (2013) to illustrate the transient dynamics of in-situ-generated foam flow with C₁₆.

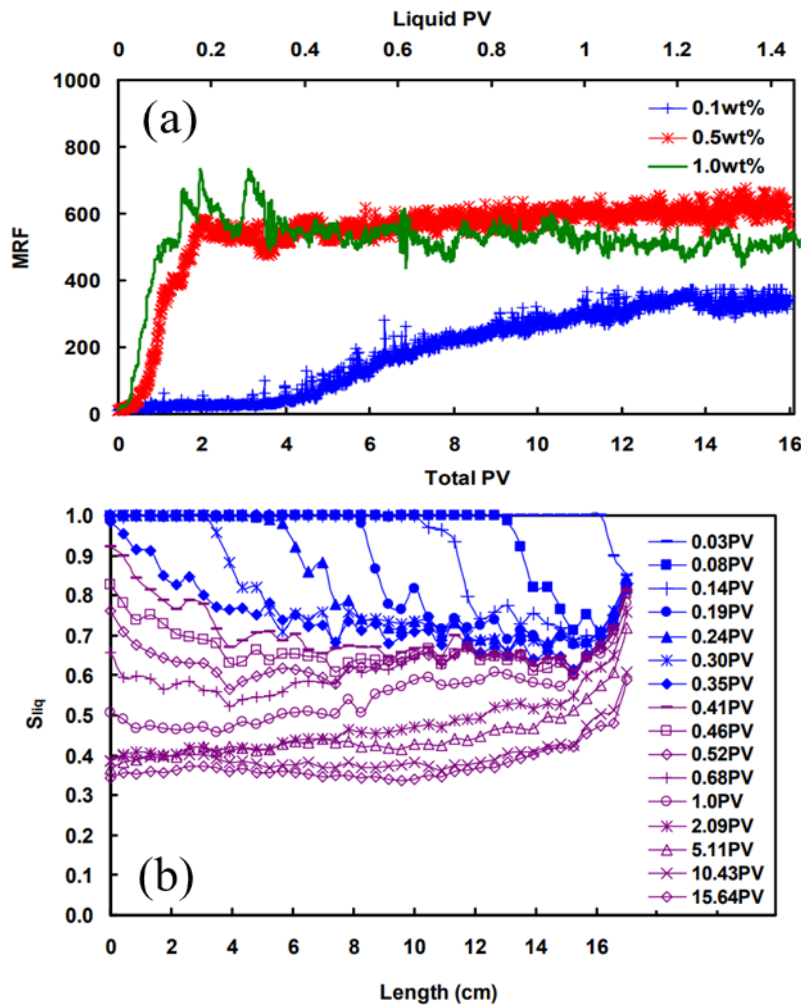


Figure 6.3 Data from Simjoo and Zitha (2013) on foam displacement with model oil C₁₆ in a Bentheimer core initially at S_{orw} : (a) MRF (mobility-reduction factor); (b) liquid-saturation profile vs. position for the case with 0.5 wt% surfactant concentration. The right side corresponds to the core inlet. The injection and initial conditions are listed under EXP-01 in **Table 6.2**.

Figure 6.3a, from Simjoo and Zitha (2013), shows MRF (mobility reduction factor) upon co-injection of surfactant solution and gas into a core at waterflood residual saturation of C_{16} . They define MRF as the ratio of overall pressure drop with foam to that of brine flowing at 100% water saturation. **Fig. 6.3b** is the liquid-saturation (water plus oil) profile for the case with a surfactant concentration of 0.5 wt%. The rapid increase in MRF for this surfactant concentration demonstrates that with oil benign to foam stability, strong foam could be generated immediately upon co-injection of gas and surfactant solution. Nevertheless, 2 PV injection are needed for strong foam to propagate through the core, suggesting a delay in foam propagation relative to injection. In other words, strong foam propagates with a dimensionless velocity (pore volumes occupied divided by pore volumes injected) less than unity. We refer this phenomenon as the “retarding effect”, which is caused by breaking of bubbles at the foam front.

Comparing **Figs. 6.3a and 6.3b** shows that the increase in MRF corresponds to the forward propagation of an oil bank to the outlet within the first 2 PV injection. Strong foam propagates forward, from upstream to downstream.

Note that at steady state (e.g. 15.64 PV in **Fig. 6.3a**), liquid saturation remains greater near the inlet, thought to be an ‘entrance effect’ in foam injection. Water and oil are plotted together in the CT images of Simjoo and Zitha. It is difficult in their data to relate MRF to oil saturation or determine if an oil bank is created by foam.

6.3.1.2 Pre-generated foam

In our own experiment in the presence of C_{16} , pre-generated foam exhibits transient behavior very similar to that with in-situ-generated foam as in **Fig. 6.3**. **Figure 6.4** presents sectional pressure-drop (dp) history during injection of pre-generated foam into a core with C_{16} at S_{orw} . Upon injection, strong foam propagates in forward direction through the core over about 1.5 PV injection; this is comparable to the 2 PV injection (PVI) required with in-situ-generated foam in **Fig. 6.3a**. This is followed by an apparent refinement of foam texture, with sectional pressure drops at steady state increased by $\sim 42\%$. This refinement appears to take place simultaneously throughout the core. Similar refinement is also seen in the results of Simjoo and Zitha as in **Figs. 6.3a and 6.3b**, after foam breakthrough at about 0.4 PV.

The similar transient dynamics of foam, whether in-situ-generated or pre-generated, demonstrates that C_{16} has similar effects on foam generation and propagation. The same transient foam behavior might be expected for crude oil with components less-harmful to foam stability, such as heavy oils.

Figure 6.5 shows the three-phase saturation profiles as a function of dimensionless position and associated CT images (at the top) at different pore volumes injected, that correspond to the experiment in **Fig. 6.4**. **Figure 6.5a** shows that foam in the forward propagation creates an oil bank with $S_o \sim 0.8$ at the displacement front. Nearly 50% OOIP (Oil Originally In Place) is produced through the oil bank by the initial foam propagation, with an additional 25% OOIP produced by the refined foam, leaving 25% OOIP in place (**Fig. 6.5c**).

$S_g \sim 0$ ahead of foam front seen from gas saturation profiles and CT images in **Figs. 6.5a and 6.5b** suggests that foam effectively prevents gas from escaping in displacing some less-harmful oils. S_g remains at ~ 0.7 at steady

state (shown in **Fig. 6.5c**) including both mobilizing and trapped gas bubbles, but it is unclear of the proportion of each. The original water phase does not play a significant role in oil displacement but mainly displaced out by the oil bank rather than foam.

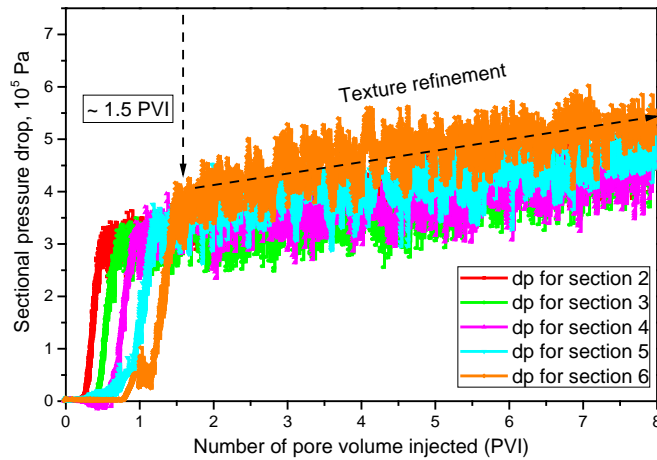


Figure 6.4 Sectional pressure drops vs. pore volumes injected upon injection of pre-generated foam into a Bentheimer core at S_{orw} with C_{16} . dp denotes sectional pressure drop, with sections 1 ~ 6 numbered from core inlet to outlet. The injection and initial conditions are listed under EXP-02 in **Table 6.2**.

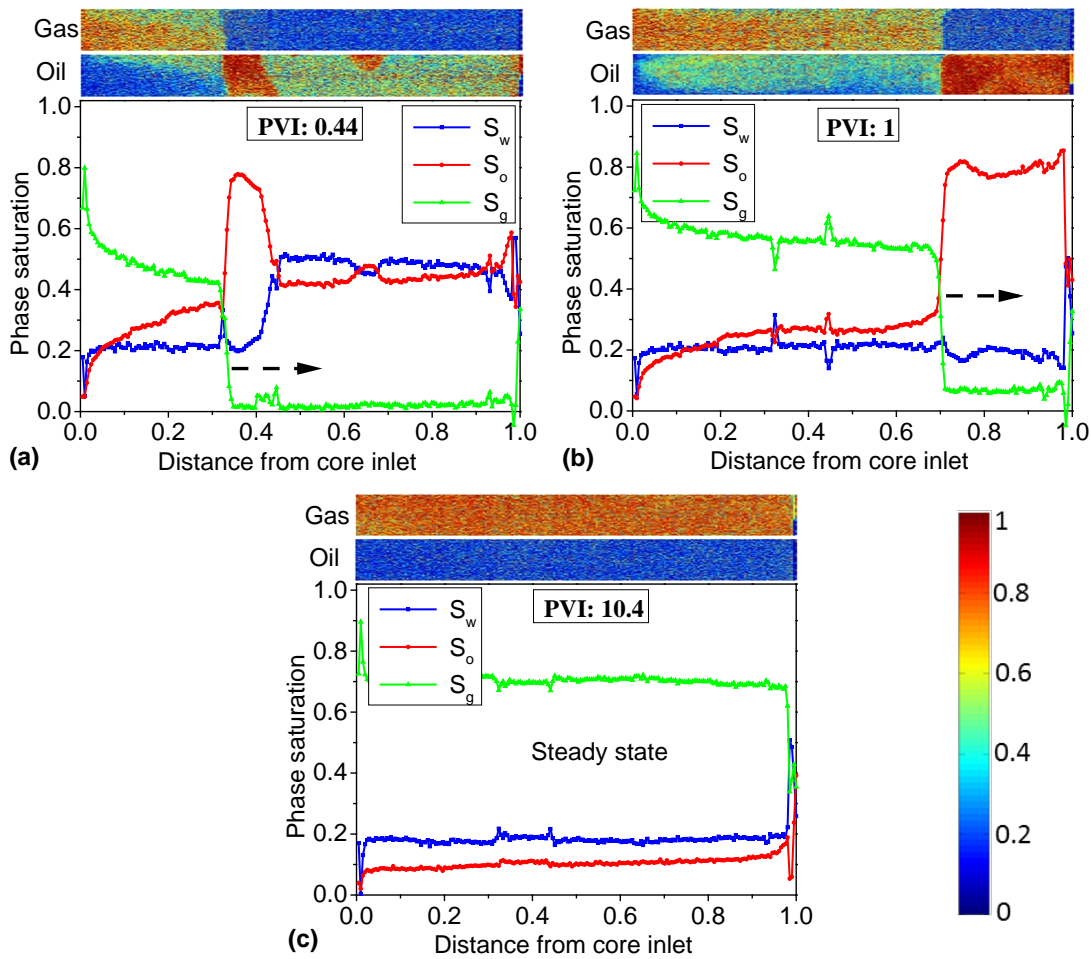


Figure 6.5 Phase saturation profiles vs. dimensionless position and CT scan images (on top) for gas and oil, corresponding to the foam experiment of **Fig. 6.4** at different times: (a) 0.44 PVI; (b) 1 PVI; (c) 10.4 PVI. Foam is injected from position zero. Arrows indicate the direction of foam propagation.

6.3.2 Model oil – mixture of 80 wt% C₁₆ and 20 wt% OA

In contrast with less-harmful oils such as C₁₆, with the model oil containing 20 wt% OA, foam generated in situ upon co-injection of phases behaves very differently from pre-generated foam. The results we show below may represent transient foam behavior in reservoirs with crude oils that destabilize foam.

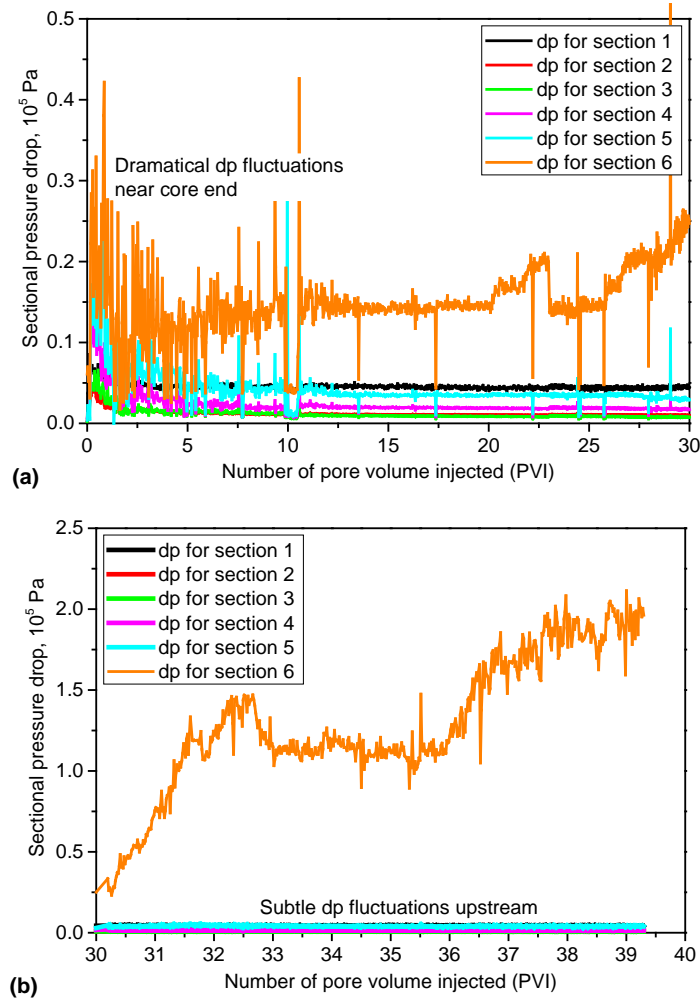


Figure 6.6 Sectional pressure drops vs. PVI upon co-injection of gas and surfactant solution into a Bentheimer core at S_{orw} , with model oil comprising 80 wt% C₁₆ and 20 wt% OA: **(a)** 0 – 30 PVI; **(b)** 30 – 40 PVI. dp denotes sectional pressure drop, with sections 1 ~ 6 numbered from core inlet to outlet. The injection and initial conditions are listed under EXP-03 in **Table 6.2**.

6.3.2.1 In-situ-generated foam

Figure 6.6 displays the sectional pressure-drop history upon co-injection of phases to develop in-situ foam into Bentheimer core at S_{orw} . In this case the model oil contains 20 wt% OA; **Fig. 6.6b** on the bottom is continuation of **Fig. 6.6a** at later times. As seen from **Figs. 6.6a** and **6.6b**, sectional pressure drops along the core do not show a significant increase except for that in the last section. Generation of strong foam begins near the core outlet. From about 25 to 40 PVI, the last sectional pressure drop keeps on rising but the others upstream remain nearly unchanged. We ended experiment before seeing significant upstream propagation through the rest of the core (Apaydin and Kovscek, 2001; Nguyen et al., 2009). The initiation of strong-foam generation near the core outlet

is thought to be triggered by capillary-end effect, i.e. that capillary pressure sharply reduces to zero at the outflow face of the core (Apyadin and Kovscek, 2001). Similar behavior is reported by Shah et al. (2018), where foam is generated due to capillary effects as flow crosses a low-to-high permeability boundary. Nevertheless, capillary-end effect that occurs on a lab scale is still of uncertain relevance to the field scale.

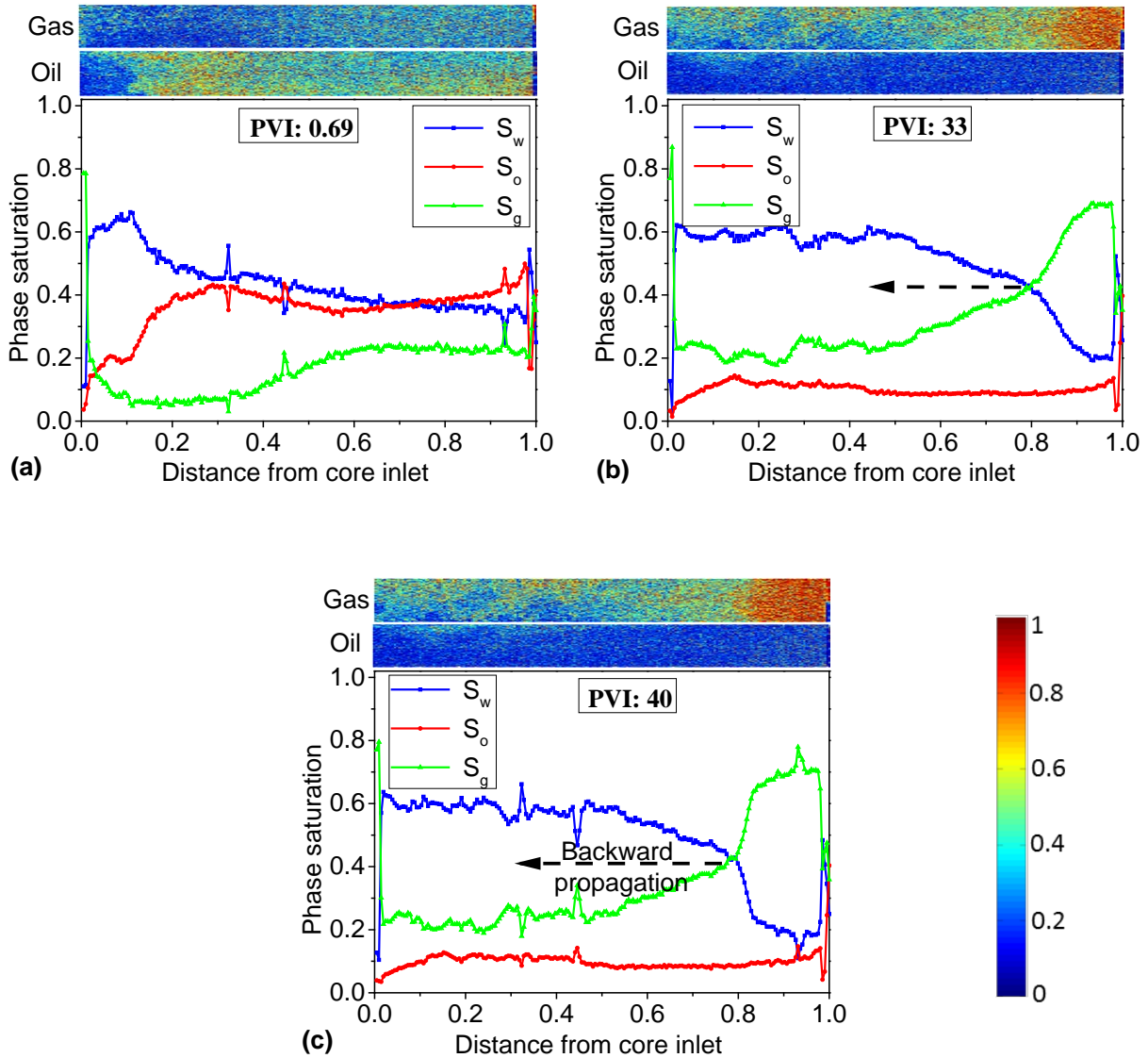


Figure 6.7 Phase saturation profiles vs. dimensionless position and CT scan images (on top) for gas and oil, corresponding to the foam experiment of **Fig. 6.6** at different times: (a) 0.69 PVI; (b) 33 PVI; (c) 40 PVI. Foam is injected from position zero. Arrows mark the direction of foam propagation.

Figure 6.7 gives the three-phase saturation profiles and CT images for gas and oil phases at different times for the experiment in **Fig. 6.6**. Saturation profiles in **Fig. 6.7a** suggest that prior to 0.69 PVI gas breakthrough has occurred, without displacing much oil or forming strong foam. In the second scan, taken at 33 PVI (**Fig. 6.7b**), the high gas saturation near the core outlet is consistent with the presence of strong foam there indicated in **Fig. 6.6b**. At the outflow face of the core in **Fig. 6.7b**, both water and oil saturations rise sharply whereas gas saturation drops sharply, which is an indication of capillary-end effect; this supports the preceding argument in **Fig. 6.6** of strong-foam generation triggered by this effect.

The gas and water saturation profiles near dimensionless position 0.8 in **Figs. 6.7b** and **Fig. 6.7c** suggest very slow backward propagation of strong foam. The backward propagation is also reported in the study of Apaydin and Kavscek (2001) and of Nguyen et al. (2009). From its propagation distance over 7 PVI between **Figs. 6.7b** and **6.7c**, the foam front propagates roughly with a dimensionless velocity ~ 0.0014 . Thus, about 560 PVI would be needed for foam to propagate upstream through the core. With 33 PVI (in **Fig. 6.7b**), residual oil saturation is relatively uniform along the core and about 0.1, but foam generation still does not occur except at the core outlet. Very detrimental oils even with small quantities can significantly restrain initial foam generation.

6.3.2.2 Pre-generated foam

Figure 6.8 presents the sectional pressure-drop history upon direct injection of pre-generated foam into a Bentheimer core at S_{orw} with 20 wt% OA in the model oil. The evolution of sectional pressure drops suggests two stages of foam propagation: primary and secondary propagation. These two stages of propagation both start from the core inlet and march towards to the core outlet, as implied by the sequential increase in the sectional pressure drops from sections 2 – 6. Foam strength in sections 2 to 6 at 7.3 PVI in the secondary propagation increases respectively by a factor 5.2, 7, 8.35, 9.8 and 15.17 in the various sections, relative to the strength at 2.6 PVI during primary propagation.

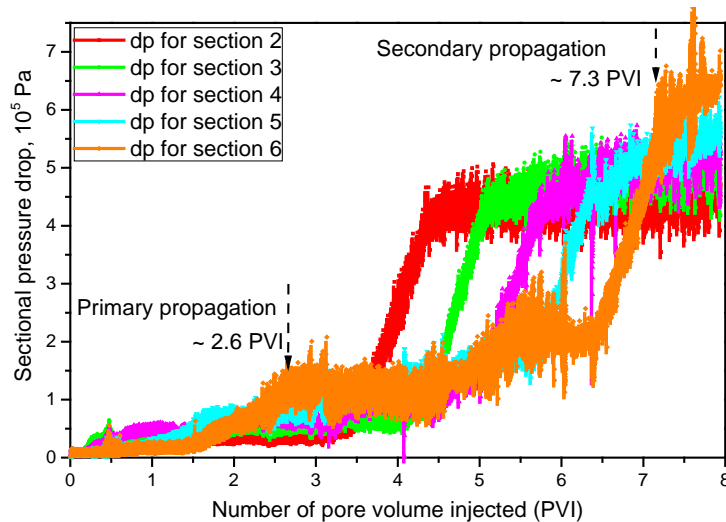


Figure 6.8 Sectional pressure drops vs. PVI upon injection of pre-generated foam into a Bentheimer core at S_{orw} with model oil comprising 80 wt% C_{16} and 20 wt% OA. dp denotes sectional pressure drop, with sections 1 ~ 6 numbered from core inlet to outlet. The injection and initial conditions are listed under EXP-04 in **Table 6.2**.

Primary propagation through section 6 takes 2.6 PVI, as seen in **Fig. 6.8**. The pressure drop for the first section was not recorded due to a limitation of the apparatus, so it is difficult to determine the starting time of the secondary propagation. It requires in total more than 4.3 PVI as it enters section 2. The cause of the secondary propagation of stronger foam is still unclear slower than the primary propagation (with weaker foam).

Figure 6.9 shows the associated phase-saturation profiles and CT images for gas and oil at different times for the experiment of **Fig. 6.8**. The measured saturations and CT images in **Figs. 6.9a** and **6.9b** show that most oil (~ 74% OOIP) is displaced by the primary weak foam, followed by the secondary strong foam that displaces a small quantity of oil (~ 3.8% OOIP). Gas distribution appears to be heterogeneous through the first 1.57 PVI, as seen from the gas CT images. **Figure 6.9b** suggests the secondary propagation has started before the primary propagation reaches the core outlet. Upon injection, an ultimate residual oil saturation of about 0.1 (i.e. 22.2% OOIP) remains in place (**Fig. 6.9c**).

In the region between the primary and secondary propagation fronts shown in **Fig. 6.9b**, although water saturation is relatively high, no strong foam is observed. Evidently, as suggested in **Figs. 6.6** and **6.7**, the presence of detrimental oils even at residual oil saturation about 0.1 inhibits the generation of stronger foam. This suggests that in the presence of harmful crude oils, foam generation in absence of oil, either in the near-well region or in the wellbore, may be needed to ensure the long-distance foam propagation in reservoirs; generating foam in the presence of residual oil may be very difficult.

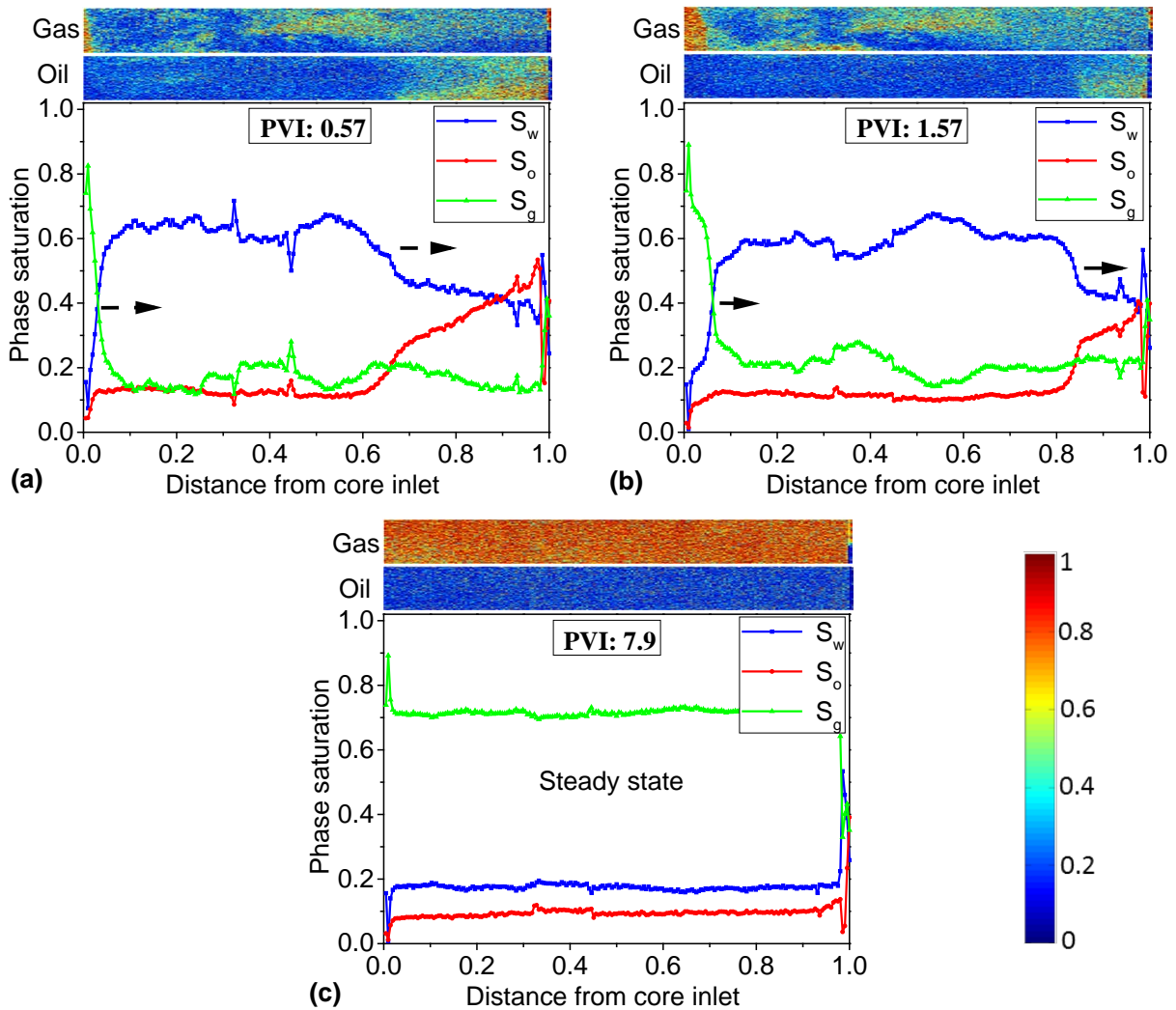


Figure 6.9 Phase saturation profiles vs. dimensionless position and CT scan images (on top) for gas and oil, corresponding to the foam experiment of **Fig. 6.8**: (a) 0.57 PVI; (b) 1.57 PVI; (c) 7.9 PVI. Foam is injected from position zero. Arrows indicate the foam propagation direction.

6.3.3 Implications for foam EOR and modeling

6.3.3.1 Implications for applications of foam EOR

Statistic reported by Manrique et al. (2010) indicate that 377 out of 1507 worldwide EOR projects implement gas injection. In principle, those EOR projects that utilize gas injection are also applicable for foam injection, through which the sweep efficiency can be significantly enhanced and so does oil recovery. To ensure successful engineering applications of foam EOR, one must take into account the foam-oil interactions, in particular the stability of foam with oil in targeted reservoirs.

The experimental investigation we present provides crucial insights on two major aspects concerned with foam EOR: selection of candidate oil reservoirs and project design. Rock and fluid properties originally in an oil reservoir are out of one's control. Oils in different reservoirs have different components and thus different destabilizing effects to foam stability (Farajzadeh et al., 2012). Foam EOR works more suitably for reservoirs with less-harmful oils, e.g. unconventional heavy oils (Bagheri, 2017). To mitigate the poor injectivity of pre-generated foam, co-injection of surfactant solution and gas or SAG (surfactant-alternating-gas) may successfully make in-situ foam (Gong et al., 2019) in the presence of less-harmful oils and displace it efficiently.

For those reservoirs with oils greatly detrimental to foam stability, co-injection of phases or SAG may have risks of failing in foam generation in situ, that would lead to failure of foam EOR. The injection of foam pre-formed on surface may give a good performance in improving oil production, but raise concerns about injectivity. In these situations, to develop in-situ foam with either co-injection of phases or SAG to displace oil, one needs to find surfactants or combinations of surfactants to enhance the tolerance of foam to oil. Experimental studies demonstrate that permeability contrast from low to high can assist in foam generation in the absence of oil (Falls et al., 1988; Tanzil et al., 2000; Shah et al., 2018). If it is demonstrated to work in the presence of oil, another option could be to choose those oil reservoirs with large heterogeneity to apply foam EOR (Renkema and Rossen, 2007).

All of our experiments are conducted in water-wet conditions. A number of recent foam EOR field pilots are carried out in carbonate reservoirs (Alcorn et al., 2018; Carpenter, 2018), which are usually oil wet. Sanchez and Hazlett concludes (1992) that foam cannot be generated in oil-wet formations with oil present, and that foam can be generated in oil-wet conditions without oil only when the formation wettability is altered by surfactant to water-wet. More efforts are needed to confirm the generality of their conclusions and understand the transient foam behavior (generation and propagation) in oil-wet reservoirs.

6.3.3.2 Implications for modeling of foam flow with oil

Foam EOR models reported in the literature in general fall into two groups: population-balance models (Kovscek et al., 1995; Kam, 2008) and implicit-texture (IT) models (Cheng et al., 2000; Computer Modeling Group, 2015; Tang et al., 2018). Population-balance models are at early stage of development in incorporating the effect of oil on foam (Myers & Radke, 2000; Ma et al., 2018). Most numerical simulations of foam EOR processes are conducted with implicit-texture models.

A widely used IT foam model, representative of current IT models, is the one in STARS simulator (Computer Modeling Group, 2015). Foam in the IT model modifies gas mobility through using a mobility reduction factor FM to reduce gas relative permeability (Tang et al., 2018), as follows:

$$k_{rg}^f = k_{rg}^{nf} \cdot FM, \dots\dots\dots (6.3)$$

$$FM = FM(S_w, S_o), \dots\dots\dots (6.4)$$

where k_{rg}^f and k_{rg}^{nf} represent gas relative permeability with and without foam, respectively, and FM is a function of only saturations S_w and S_o . The representation of foam in **Eqs. 6.3** and **6.4** assumes “local equilibrium (LE)” meaning that foam properties, characterized by the factor $FM(S_w, S_o)$, immediately reach its final state everywhere and anytime.

Current simulations assume the LE assumption applies for all cases regardless of oil type and the way of foam injection, and use directly foam-simulation parameters estimated from steady-state data to predict dynamic foam displacements with oil. Our experimental observations with less-harmful oils such as C_{16} and other prior studies without oil (Persoff et al., 1991; Kovsky et al., 2010) support the validity of the IT model.

However, IT foam models cannot distinguish the different results for co-injection of phases and direct injection of pre-generated foam as seen in **Figs. 6.6** and **6.8**. The reason is fundamental: without accounting for foam texture, the two cases would be simulated with identical injection conditions. It is possible that an IT model could represent either the case of co-injection or pre-generation on its own, but not both with the same parameters. This issue needs further exploration.

6.4 Conclusions

Foam interaction with oil in geological formations remains a long-standing challenge in the process of foam enhanced oil recovery (EOR). We conduct a dual-energy CT coreflood study of foam flow with two representative model oils on the lab scale, where foam response and oil displacement is reflected by the sectional pressure drops and phase distributions. The results provide initial insights for deeper exploration of foam-oil displacement and interactions on field scales.

The generation and propagation of foam is subject to the destabilizing effects of oil on foam stability and depends in part on the injection strategy. With less-harmful oils, e.g. C_{16} , foam generated in situ upon co-injection of surfactant solution and gas shows transient dynamics similar to that with direct injection of pre-generated foam;. This suggests that less-harmful oils have similar effects on foam generation and propagation. Analogous behavior could be expected for foam flow with heavy oils in general with compositions relatively benign to foam.

In contrast to less-harmful oils, very detrimental oils (e.g. with 20 wt% oleic acid in our study) impose very different effects on the conditions for foam generation and propagation, as implied by the completely different behavior between the two ways of foam injection. (1.) Foam generation in situ is very difficult with harmful oils in place, even at low oil saturation. The initial generation of strong foam starts at the core outlet (thought to be a

result of the capillary end effect) and propagates upstream. (2.) Pre-generated foam shows two stages of propagation, both from core inlet to outlet. The primary propagation comprises weak foam that displaces most oil, followed by the secondary propagation of stronger foam.

Implicit-texture foam models for EOR simulation cannot distinguish the very different behavior between pre-generated and in-situ-generated foam with very harmful oils. It is possible that such a model could represent one process or the other. Further investigations are on this issue and to improve the prediction of foam EOR.

NEW CAPILLARY NUMBER DEFINITION FOR MICROMODELS

Summary

Mobilization or trapping of fluids in porous media, fundamentally, is a result of a force competition. Numerous studies investigate mobilization efficiency using the capillary number (N_{ca}), which represents a ratio of driving force for mobilization, i.e. pressure or hydrostatic effects of gravity, to capillary resistance. The conventional definitions of N_{ca} were initially proposed for 3D porous media, yet many experimental studies use these definitions for 2D networks. Experimental observations and theoretical analysis show that the conventional N_{ca} definitions do not work for 2D networks given the very different flow geometries between 2D and 3D networks.

A new capillary number (N_{ca}) definition is proposed for 2D etched micromodels. We derive the new definition from a force balance on a nonwetting ganglion trapped by capillarity. It incorporates the impact of pore microstructure on mobilization. The geometrical factors introduced can be estimated directly from image analysis of the pore network etched in the micromodel, without conducting flow experiments. The improved fit of the new N_{ca} to published data supports its validity. The new definition yields a consistent trend in the capillary-desaturation curve (CDC). The conventional N_{ca} definitions proposed for porous rock give a large scatter in the CDC for data in micromodels. This is due to the different type of flow in micromodels, as 2D networks, relative to 3D geological porous media. In particular, permeability is dominated by channel depth in micromodels with shallow depth of etching, and generally there is no simultaneous multiphase flow under capillary-dominated conditions. Applying the conventional definitions to results in micromodels may lead to misleading conclusions for fluid transport in geological formations.

The new N_{ca} definition, as an indicator for mobilization, may be applied to microfluidic studies of a variety of processes across the fields of groundwater, energy and climate: removal of NAPL (Non-Aqueous Phase Liquid) contaminants from aquifers and soils; enhanced recovery of oil in reservoirs; or trapping efficiency of CO₂ in CCUS (Carbon Capture, Utilization and Storage).

7.1 Introduction

The transport of fluids in porous media, on the macroscopic scale, is captured by permeability and relative-permeability functions. One key focus of fluid transport in porous media, either in practical applications or in lab and theoretical studies, is the mobilization or trapping efficiency of the nonwetting phase. For instance, numerous efforts have been made to enhance the recovery of oil in a reservoir (Lake et al., 2014), or to maximize the removal of NAPL (Non-Aqueous Phase Liquid) in contaminated ground water and soil (Johnson et al., 2001; Jeong & Corapcioglu, 2005; Kao et al, 2008; Geistlinger et a., 2009). Other recent studies have attempted to increase the entrapment efficiency of CO₂ in CCUS (Carbon Capture, Utilization and Storage), to relieve the impact of CO₂ on global climate (Juanes et al., 2006; Iglauer et al., 2011a, 2011b). The correlation between nonwetting-phase saturation (S_{nw}) and capillary number (N_{ca}), initially realized by Bethel and Calhoun (1953), has long been widely used to analyse the mobilization of nonwetting phase in geological formations. The plot of S_{nw} against N_{ca} is usually referred to as the capillary-desaturation curve (CDC). This type of curve, in combination with other curves, i.e., of relative permeability and capillary pressure (Green & Willhite, 1998; Lake et al., 2014), are thought to be among the most fundamental curves in understanding the dynamics of fluid transport in geological formations. The usefulness of the CDC depends on demonstrating a consistent relationship between S_{nw} and N_{ca} , regardless of all the complexities in rock and fluid properties, including pore geometry and ganglion-length distribution. This consistency makes the capillary number an important indicator for the mobilization or trapping efficiency of the nonwetting phase in the processes discussed above.

The conventional N_{ca} definitions were all originally proposed for 3D porous rock. These definitions have been applied to 2D pore networks, ignoring the fact that the flow is very different between the two types of porous media. Our study aims at proposing a new mobilization condition for the nonwetting phase in 2D pore networks, in particular micromodels. The new criterion is not intended to equate microfluidics to 3D porous media. If one attempts to extrapolate microfluidic experimental results to interpret behavior in 3D porous media, the conventional N_{ca} definitions can lead to incorrect conclusions for fluid transport.

Several capillary-number definitions for geological porous rock have been reported in the literature. Generally, most of the definitions fall into two major simplified forms, either in terms of velocity (Foster, 1973; Green & Willhite, 1998) or macroscopic pressure gradient (Brownell & Katz, 1947), as in **Eqs. 7.1** and **7.2**:

$$N_{ca} = \frac{v\mu}{\sigma} \dots\dots\dots (7.1)$$

$$N_{ca} = \frac{k|\nabla p|}{\sigma} \dots\dots\dots (7.2)$$

where v and μ are the interstitial velocity and viscosity of the displacing fluid, respectively, σ interfacial tension (IFT) between the displacing and displaced fluids, k permeability, and $|\nabla p|$ the magnitude of macroscopic pressure gradient. All the other definitions are based on the two major forms above. Moore and Slobod (1955), in their analysis using a pore-doublet model, introduced $(\cos \theta)$ into the denominator of **Eq. 7.1** to account for wettability. Abrams (1975) modified the definition in **Eq. 7.1**, using the interstitial velocity of displacing phase and taking the viscosities of both phases into account. Some definitions adjusted the form of **Eq.**

7.2 by including $(\cos \theta)$ into the denominator (Dombrowski & Brownell, 1954; Reed & Healy, 1977). Pennell et al. (1996) used the permeability to the displacing phase in **Eq. 7.2** rather than absolute permeability, which, in addition, introduces the relative permeability. Since the relative permeability varies with S_{nw} , the value of which in turn depends on N_{ca} , the definition in **Eq. 7.2** involving the relative permeability is impractical for implementation in numerical simulations (Sheng, 2010).

The most commonly used definition of capillary number is in **Eq. 7.1**. That in **Eq. 7.2** is based on a simplified force balance. Through the relation $v\mu = (kk_{rw} \nabla p) / \phi$, based on Darcy's Law, the first definition in **Eq. 7.1** is related to that in **Eq. 7.2** via:

$$(N_{ca})_2 = \frac{(N_{ca})_1}{(k_{rw} / \phi)} \dots\dots\dots (7.3)$$

where subscripts 1 and 2 denote the definitions in **Eqs. 7.1** and **7.2**, respectively, and k_{rw} represents the relative permeability to the wetting (continuous) phase. The definition in **Eq. 7.2** is, we think, more directly related to the physics of mobilization. It can be derived from a force balance on a trapped nonwetting ganglion, with the crucial assumption that pore length and pore-throat width each scale with the square root of permeability (Sheng, 2010).

Numerous studies have attempted to understand the physics behind the CDC in more detail. For instance, Yeganeh et al. (2016) investigated the relation between S_{nw} and N_{ca} through the ganglion-length distribution and a critical ganglion length that is inversely related to N_{ca} (Larson et al., 1977). A variety of other expressions exist that describe the effect of fluid properties on mobilization (Al-Shalabi et al., 2014; Bethel & Calhoun, 1953; Franklin, 1994; Pope et al., 2000; Rodríguez de Castro et al., 2015).

On a microscopic scale, the transport of fluids in porous media depends on the geometry and topology of the network of pore throats and bodies (Chatzis et al., 1983; Ross & Kovscek, 2002). However, the link between permeability and pore geometry is not the same for all porous media. In particular, permeability in shallow-etched micromodels is dominated by the channel depth, rather than the geometrical factors that control trapping, e.g. pore-throat width and pore-body diameter, as in porous rock. In addition, it has long been known (Chatzis & Dullien, 1977; Wilkinson, 1984; Mohanty et al., 1987) that simultaneous multiple phase flow under capillary-dominated conditions is a feature of 3D pore networks, but not true in general for 2D networks. Thus the distribution of residual nonwetting phase is expected to be very different.

Equation 7.1 indicates an immediate problem in applying a definition of N_{ca} that involves relative permeability to both 3D pore networks and micromodels. Since 2D pore networks usually do not allow simultaneous, capillary-dominated multiphase flow, one important implication is that the relative-permeability functions for microfluidic devices are markedly different from those for rock. In the case of water displacing oil in a water-wet micromodel, the onset of trapping of oil marks the beginning of water flowing as a continuous phase, which is a condition where $k_{rw} \sim 0$. This is because the two phases cannot percolate each other in a displacement (Chatzis & Dullien, 1977; Wilkinson, 1984; Mohanty et al., 1987). The oil phase first becomes discontinuous at the same

point where water becomes continuous across the medium. This is also true for rectangular channels where wetting phase cannot move simultaneously together with nonwetting phase through thick films connecting water surrounding adjacent pillars. The reason is that the condition for connecting the wetting phase around pillars is also the condition for snap off that blocks throat to nonwetting phase (Rossen, 2003). The relative-permeability curves cross at zero relative permeability rather than above as in rock (Rossen & Kumar, 1992). Thus k_{rw} factor in a micromodel is very different than that in rock. The value of N_{ca} in **Eq. 7.2** must be much larger for micromodels than that in **Eq. 7.1** under the same conditions, by a factor different from that for geological porous media. Thus one is especially likely to misinterpret mobilization in micromodels, based on the value of N_{ca} defined in **Eq. 7.1**. For instance, capillary numbers around 10^{-5} as defined by **Eq. 7.1** correspond to considerable mobilization in micromodels, e.g., S_{nw} of about 10~15% (Geistlinger et al., 2015; Buchgraber et al., 2012). This greatly overestimates mobilization implied by similar capillary numbers in geological porous media.

Microfluidic devices are particularly useful in revealing the fundamentals of transport of fluids in porous media, in that flow processes and phase-interaction dynamics can be observed directly. To describe mobilization in micromodels, we propose in this study a new definition of capillary number, taking into account the pore geometry of 2D microfluidic networks.

AlQuaimi and Rossen (2017) recently proposed a mobilization condition for the nonwetting phase in rough-walled fractures, from a force balance on a trapped ganglion. Here we derive a new N_{ca} definition for micromodels using a method similar to theirs. The geometrical factors controlling capillary trapping in micromodels differ fundamentally from those in fractures. In a fracture, aperture-depth variation along a flow path dominates the capillary pressure between nonwetting and wetting phases. In micromodels, where aperture depth is usually uniform, capillary pressure is controlled by the widths of pore throats and pores, perpendicular to the etching. The validity of the new definition is then tested using published data obtained in a variety of micromodels varying in the pore geometry. The introduction pore microstructure in the new definition overcomes the large scatter in the CDC that occurs with the conventional definitions.

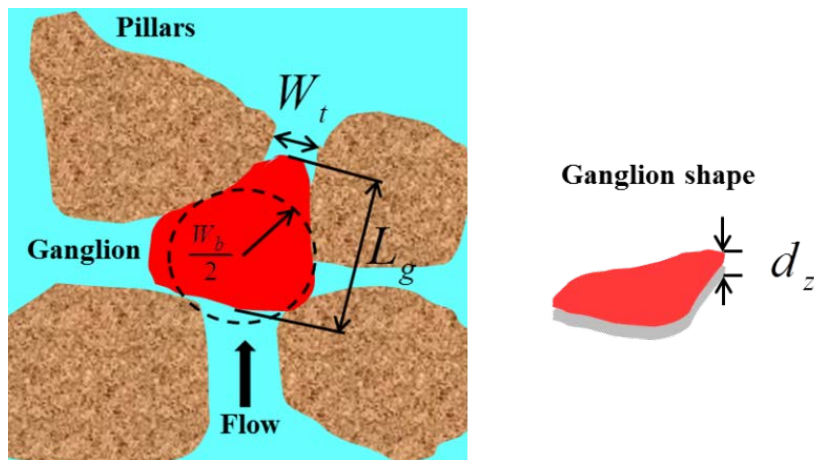


Figure 7.1 Representation of a nonwetting ganglion trapped by capillarity in a micromodel: **left**, top view of a horizontally mounted micromodel; **right**, 3D view of the ganglion shaped by the pore space with relatively shallow etching, where the ganglion is shown as flat due to uniform channel depth.

7.2 New capillary number definition

In this section, we present the derivation of the new N_{ca} definition for micromodels, starting with a force balance on a trapped nonwetting ganglion illustrated in **Fig. 7.1**. We then illustrate how to estimate all the parameters needed in the new definition.

7.2.1 Derivation from a force balance

The residual non-aqueous phase at the end of a displacement consists of discrete blobs trapped behind pore throats. Our study focuses on the mobilization of the nonwetting phase as schematically illustrated in **Fig. 7.1**.

The nonwetting ganglion trapped in **Fig. 7.1** is subject to the following forces: pressure, gravity, and capillary resistance. The mobilization of the ganglion in **Fig. 7.1** is thus a competition of pressure/gravitational force, sometimes called viscous force, and capillary resistance (Larson et al., 1977).

We define a dimensionless factor N_{ca} , as a ratio of viscous force, F_v , to capillary resistance, F_c :

$$N_{ca} = \frac{F_v}{F_c} \dots\dots\dots (7.4)$$

At the onset of mobilization, the leading edge of the ganglion resides in the pore throat, and the trailing edge in the pore body. Such a configuration yields different curvatures at the leading and trailing edges, leading to capillary resistance to the mobilization. The capillary pressure across any interface is described by the Laplace equation:

$$P_c = \sigma \left(\frac{1}{r_1} + \frac{1}{r_2} \right), \dots\dots\dots (7.5)$$

where σ is the interfacial tension, r_1 and r_2 the principle radii of curvature of the interface.

Lenormand et al. (1983) derived the capillary pressure across an interface in a rectangular channel:

$$P_c \cong 2\sigma \left(\frac{1}{x} + \frac{1}{y} \right), \dots\dots\dots (7.6)$$

where x and y represent the height and width of the rectangular cross-section. The capillary-pressure difference, Δp_c , across the curved interfaces at the leading and trailing edges of the ganglion is then given by:

$$F_c = \Delta p_c = \sigma \left(\frac{2 \cos \theta}{W_t} - \frac{2 \cos \theta}{W_b} \right), \dots\dots\dots (7.7)$$

where θ is the contact angle, and W_t and W_b the pore-throat width and pore-body diameter (as viewed from above) as shown in **Fig. 7.1**, respectively. The channel depth, d_z , is uniform and thus drops out in **Eq. 7.7**.

The viscous force, F_v , across a trapped ganglion of length L_g as in **Fig. 7.1** is given by:

$$F_v \cong |\nabla \Phi| L_g, \dots\dots\dots (7.8)$$

where $|\nabla\Phi|$ is the magnitude of the macroscopic flow-potential gradient, the combined effects of pressure p and gravity. For the remainder of this derivation, for simplicity we assume the flow is horizontal, and $|\nabla\Phi|=|\nabla p|$.

We assume for simplicity that both the ganglion length L_g and its distribution scale with L_p , the length of a pore (roughly identical to pore-body diameter W_b in the networks considered). For the experiments analysed here (**Figure G-1** in Appendix G), the characteristic ganglion length L_g at residual state at the end of a displacement is a factor of about 1.1 ~ 1.4 of W_b . Then we substitute L_p for L_g in the remainder of the derivation.

The viscous force F_v required to mobilize a ganglion of length L_p has to overcome the capillary resistance F_c :

$$F_v > F_c, \text{ or } |\nabla p| \cdot L_p > \sigma \left(\frac{2 \cos \theta}{W_t} - \frac{2 \cos \theta}{W_b} \right). \dots\dots\dots (7.9)$$

The left side of **Eq. 7.9** divided by the right side yields a criterion for the mobilization in terms of the dimensionless capillary number N_{ca} :

$$N_{ca} \equiv \frac{F_v}{F_c} = \left(\frac{|\nabla p|}{\sigma \cos \theta} \right) \left[\frac{L_p W_t}{2 \left(1 - \frac{W_t}{W_b} \right)} \right] > 1. \dots\dots\dots (7.10)$$

The second term in brackets describes the impact of the geometric characteristics of the pore network on the displacement of residual nonwetting phase. Since all the parameters involved in the bracketed term are related to the geometry of the micromodel, the second term in **Eq. 7.10** should be a constant for a given micromodel, independent of fluid properties. Note that our derivation is based on a ganglion one pore in length. Ganglia several pores long would be mobilized at N_{ca} somewhat smaller than unity. More fundamentally, the derivation assumes that the distribution of ganglion lengths for all micromodels scales with the length of a single pore. This assumption facilitates the calculation of the new N_{ca} in **Eq. 7.10** based only on microfluidic geometry, without needing to perform flow experiments in advance.

7.2.2 Comparison of the new and conventional N_{ca}

Nearly all publications concerning the CDC for micromodels apply the conventional N_{ca} definitions. To reveal the relation between the new definition for micromodels and the conventional definition for porous rock, and for the convenience of re-examining published data from micromodels, we derive a conversion factor between the two definitions.

Mathematically, the conversion is done via introducing permeability k into the new definition in **Eq. 7.10**. Physically, this requires one to relate k to the pore geometry of a micromodel. Since the link between the permeability and pore microstructure is complex, we estimated k of a micromodel by comparison to a smooth slit. Specifically, the permeability, k_s , of a smooth slit of aperture d_z is given by (Tsang, 1992; van Golf-Racht, 1982; Zimmerman & Bodvarsson, 1996):

$$k_s = \frac{d_z^2}{12}, \dots\dots\dots (7.11)$$

where subscript s denotes the slit, and d_z represents the aperture of the slit.

Channel depth d_z is usually a fixed constant for a given micromodel. Permeability in a micromodel, k is reduced first by the porosity, because only the pores can conduct flow. For a simple reference case of wide, shallow, straight, smooth channels, permeability would be $[(d_z^2/12) \cdot \varphi]$, where φ is the porosity. If the etching depth is comparable to the channel width, or the channel network geometry is more complex, then k would be reduced by more than φ . This remaining reduction in estimated permeability we incorporate into an adjustable factor ζ :

$$k = \left(\frac{d_z^2}{12}\right) \cdot (\varphi\zeta), \dots\dots\dots (7.12)$$

where ζ is a factor incorporating several effects, as is geometric tortuosity for 3D porous media (Doyen, 1988; Ghanbarian et al., 2013). We use this factor here only to allow us to relate the new definition of N_{ca} to the conventional definition based on permeability, to illustrate their difference.

Introducing the relation defined by **Eq. 7.12** into the second bracketed term in **Eq. 7.10** yields:

$$\begin{aligned} \frac{L_p W_t}{2 \left(1 - \frac{W_t}{W_b}\right)} &= \left(\frac{d_z^2}{12} \varphi\zeta\right) \left(\frac{1}{\frac{d_z^2}{12} \varphi\zeta}\right) \frac{L_p W_t}{2 \left(1 - \frac{W_t}{W_b}\right)} \\ &= k \cdot \left[\left(\frac{12}{2}\right) \left(\frac{W_t}{d_z}\right)^2 \left(\frac{L_p}{W_t}\right) \frac{1}{\left(1 - \frac{W_t}{W_b}\right)} (\varphi\zeta) \right] \dots\dots\dots (7.13) \end{aligned}$$

Replacing the bracketed term in **Eq. 7.10** with the right side of **Eq. 7.13** and grouping all the geometrical factors together produces an expression for the new N_{ca} equivalent to that in **Eq. 7.10**:

$$N_{ca} = \left(\frac{k |\nabla p|}{\sigma \cos \theta}\right) \left[\left(\frac{12}{2}\right) \left(\frac{W_t}{d_z}\right)^2 \left(\frac{L_p}{W_t}\right) \frac{1}{\left(1 - \frac{W_t}{W_b}\right)} (\varphi\zeta) \right] \dots\dots\dots (7.14)$$

where the first term in parentheses is the conventional definition in **Eq. 7.2**. The second part, in brackets, describes the impact of pore microstructure.

We define the second bracketed term in **Eq. 7.14** as the geometric term G:

$$G \equiv \left(\frac{12}{2}\right) \left(\frac{W_t}{d_z}\right)^2 \left(\frac{L_p}{W_t}\right) \frac{1}{\left(1 - \frac{W_t}{W_b}\right)} (\varphi\zeta) \dots\dots\dots (7.15)$$

The factors in G can be estimated from image analysis of a micromodel and a value for permeability. The value of G is fixed for a specific micromodel. After knowing G , one can convert the new and conventional definitions.

7.2.3 Calculation of parameters in the new N_{ca}

The parameters needed for the calculation of the new N_{ca} (Eq. 7.10) include pressure gradient ∇P , interfacial tension σ , contact angle θ , characteristic pore-throat width W_t , characteristic pore-body diameter W_b , and pore length L_p (Table 7.1 below). The geometrical factors, W_t , W_b and L_p , can be obtained via image analysis of a micromodel. One can calculate the new N_{ca} in Eq. 7.10 after acquiring the parameters summarized in Table 7.1.

Table 7.1 Summary of Parameters Needed for Calculation of the New N_{ca}

	Model parameters	Remarks
Geometrical factors	Characteristic pore-throat width, W_t	Average of pore-throat distribution
	Characteristic pore-body diameter, W_b	Average of pore-body distribution
	Pore length, L_p	Roughly identical to W_b in the networks considered here
Fluid and media properties	Wettability, indicated by contact angle, θ	Measured in lab
	Interfacial tension between phases, σ	Measured in lab
Flow data	Pressure gradient, ∇P	Measured via flow experiments

7.3 Test of the new N_{ca} definition

This section illustrates first the major issues concerning the direct application of the conventional N_{ca} definitions to analyse mobilization in micromodels (Fig. 7.2). The validity of the new N_{ca} definition is then verified using the same data (Fig. 7.3).

Data from published experiments that represent a variety of micromodels differing in their pore geometry are used to test this model. Table 7.2 summarizes all the key parameters depicting the network geometry and properties of micromodels used in these studies. These include, in particular, the geometric factors characterizing the microstructure of pore throats and pore bodies, and pore length. The values of the geometric parameters in Table 7.2 are either given in the publications or estimated from image analysis of the micromodel (Jeong et al., 2003; Ibrahim, 2009; Yeganeh et al., 2016). The values of ζ are calculated via Eq. 7.12 based on k provided in the respective studies in Table 7.2, which then gives the values of G defined in Eq. 7.15. Based on the conversion in Eq. 7.14, one can then translate the conventional N_{ca} to the new N_{ca} , to check the effectiveness of the new definition. The studies of Jones et al. (2018) and of Kawale et al. (2017) do not provide two-phase flow data, but allow geometric analysis of the micromodels. We present the values of G for these cases, to illustrate the expected impact of pore geometry if the CDC were measured with these micromodels.

Relatively few experimental studies provide the experimental details needed to estimate N_{ca} using Eq. 7.10, i.e., permeability, pore geometry, wettability and pressure gradient.

Table 7.2 An Overview of Micromodel Parameters collected from Microfluidic Studies in the Publications

Published studies	Micromodel geometrical factors					Micromodel properties		Adjustable factor ζ	Values of G
	$W_i, \mu m$	$W_b, \mu m$	$L_p, \mu m$	$d_s, \mu m$	$k, \mu m^2$	ϕ			
Kawale et al., 2017	Aligned squares	217	307	307	120	204	0.69	0.246	558
	Staggered squares	109	415	415	120	180	0.71	0.211	169
	Aligned circles	162	338	338	120	214	0.71	0.251	246
Jones et al., 2018	Staggered circles	162	338	338	12	179	0.71	0.210	293
		13	60	60	5	0.72	0.71	0.488	691
		152	326	326	130	17	0.27	0.045	2741
Jeong et al., 2003	Model A								
Jeong et al., 2003	Model B	130	272	272	130	22.5	0.28	0.057	1505
		64	210	210	150	20	0.50	0.022	483
Ibrahim, 2009									
Yeganeh et al., 2016	Case 1	86	156	156	110	362	0.59	0.614	41
	Case 2	86	155	155	110	362	0.59	0.614	41

The capillary-desaturation curves shown in **Fig. 7.2** were collected from a variety of microfluidic studies (Ibrahim, 2009; Jeong and Corapcioglu, 2003, 2005; Yeganeh et al., 2016). Different conventional N_{ca} definitions were applied in these studies. For instance, Jeong and Corapcioglu (2003) used a definition similar to **Eq. 7.1**, but including contact angle and ignoring porosity, given by:

$$N_{ca} = \frac{q\mu_a}{\sigma \cos \theta} = \frac{kk_{rw} |\nabla p|}{\sigma \cos \theta} \dots\dots\dots (7.16)$$

where q and μ_a represent in their study the superficial velocity and viscosity of the displacing fluid, and k and k_{rw} the absolute and relative permeability, respectively.

The studies of Ibrahim (2009) and Yeganeh et al. (2016) employed the following definition:

$$N_{ca} = \frac{v\mu}{\sigma \cos \theta} \dots\dots\dots (7.17)$$

This definition is a factor $(1/\phi)$ times of that in **Eq. 7.16**. We converted all the data, for the convenience of comparison, to the definition in **Eq. 7.16** in **Fig. 7.2**.

The parameters, θ , σ and ∇p , are either taken or estimated from the publications. The key to the calculation of the new N_{ca} is the determination of the second bracketed term in **Eq. 7.10**. We estimated all the parameters in this term from image analysis of the micromodel based on pictures in the original publications. The characteristic pore-throat width, W_t , and pore-body length, L_p , are estimated by taking the average of their respective distributions. The channel depth, d_z , is given in the publications.

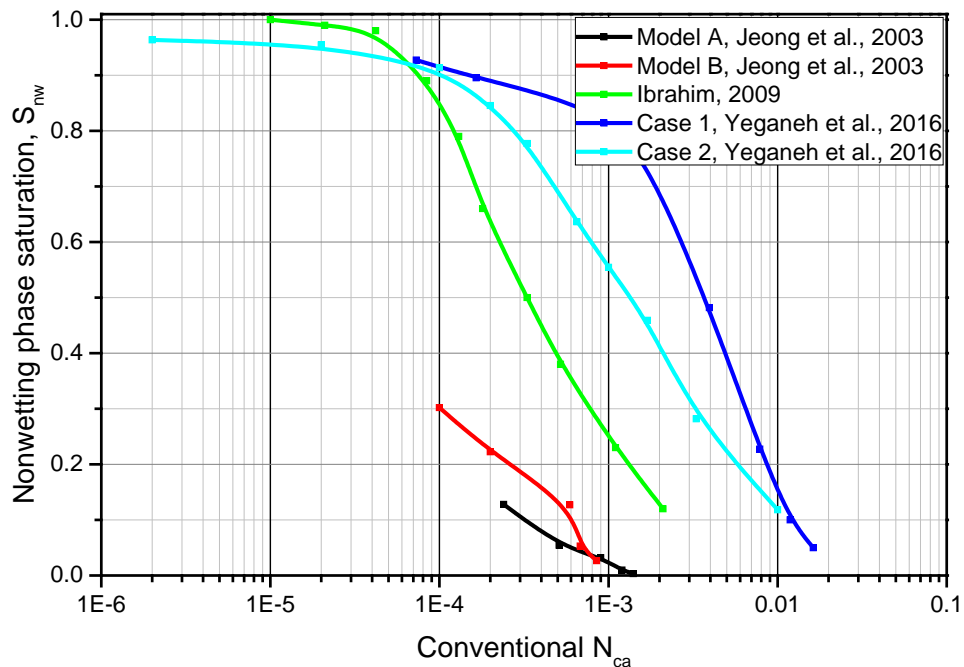


Figure 7.2 Capillary-desaturation curves using the conventional capillary number N_{ca} definitions. All the data shown here are adapted from data in publications. Note that the CDC for micromodels results using the conventional definitions shows a large scatter, suggesting system-dependence.

Figure 7.2 shows the capillary-desaturation curves based on data from five microfluidic devices in three studies, using the conventional definition of N_{ca} in **Eq. 7.16**. The data diverge by almost two orders of magnitude. The large scatter in **Fig. 7.2** suggests that the CDC using the N_{ca} in terms of $v\mu$ or $u\mu$ is system-dependent. Thus, neither of the two definitions in **Eqs. 7.16** and **7.17** works for micromodels.

The same data in **Fig. 7.2** were then replotted in **Fig. 7.3** using the new definition in **Eq. 7.10**. Calculating the new N_{ca} requires ∇p , which was not reported in the studies of **Fig. 7.2**. These are the only studies where we can find the data we need. **Equation 7.14**, by incorporating Darcy’s velocity, is equivalently rearranged to:

$$N_{ca} = \left(\frac{u\mu}{\sigma \cos \theta} \right) \frac{1}{k_{rw}} \left[\left(\frac{12}{2} \right) \left(\frac{W_t}{d_z} \right)^2 \left(\frac{L_p}{W_r} \right) \frac{1}{\left(1 - \frac{W_r}{W_b} \right) (\phi \zeta)} \right] \dots \dots \dots (7.18)$$

Through **Eq. 7.18**, one can translate the values of conventional N_{ca} from **Eq. 7.16** in **Fig. 7.2** to the new N_{ca} . The quantities in the large brackets can be determined from image analysis of the micromodels, except for ζ which is calculated here from measured k through **Eq. 7.12**. We do not know the value of k_{rw} in these studies, or how it varies with S_{nw} . In **Fig. 7.3** we assume a value of 1 so as to examine the shape of the new model using the published data in **Fig. 7.2**. The simplification implies that the values of N_{ca} in **Fig. 7.3** should be somewhat larger than shown.

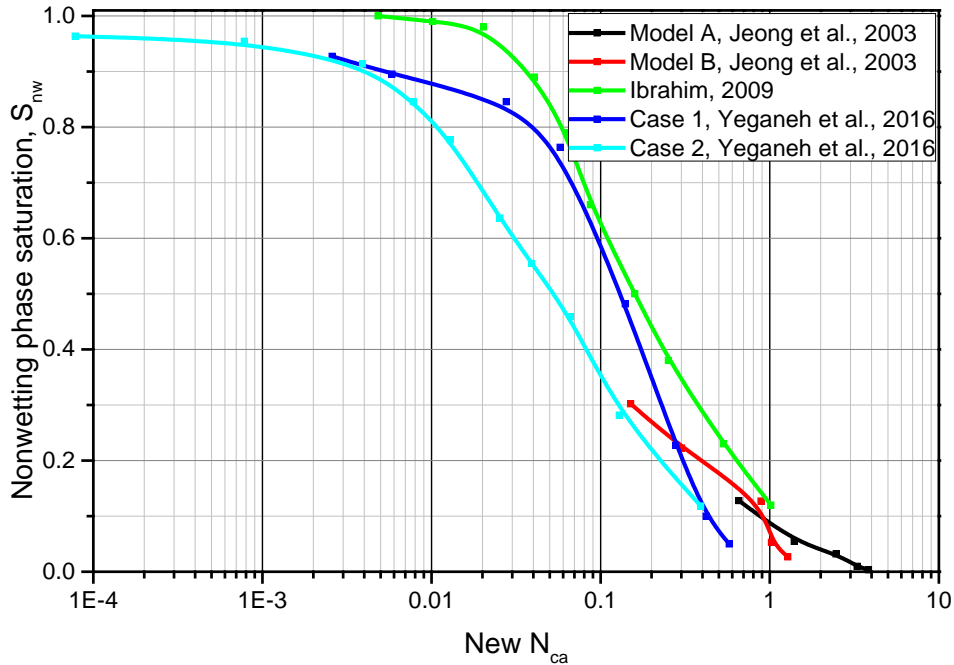


Figure 7.3 Capillary-desaturation curves using the new capillary number N_{ca} definition in **Eq. 7.10**, using data in **Fig. 7.2**.

Figure 7.3 shows that the new N_{ca} definition gives a much better match to the data in micromodels, in spite of the unknown factor k_{rw} and the simplifying assumption concerning the ganglion length distribution. The

improved fit of the new N_{ca} to data confirms its validity by yielding a consistent trend in the CDC. As the k_{rw} factor was ignored in the translation of conventional in **Fig. 7.2** to new N_{ca} in **Fig. 7.3**, the true CDC may move to the right somewhat from **Fig. 7.3**, though allowing for ganglia longer than a pore would tend to move it back to the left. The consistent trend in the CDC demonstrates the validity of the new N_{ca} for evaluating mobilization or trapping of the nonwetting phase in microfluidic studies. In addition, the values of new N_{ca} in **Fig. 7.3** are tens to thousands of times greater than those in **Fig. 7.2**, as implied by the values of G in **Table 7.2**. These confirm the overestimation of the conventional CDC using the definitions in **Eqs. 7.1** and **7.2** for mobilization in micromodels.

The complications concerning ζ are glossed over in the conventional N_{ca} definitions in **Eqs. 7.1** and **7.2** as well. Nonetheless, they work remarkably well, yielding a consistent trend in the CDC for geological porous media. Here we discuss k , k_{rw} and ζ in relating the two definitions using **Eq. 7.14** or **Eq. 7.18** only to illustrate the difference between the new and conventional definitions. The new N_{ca} model we suggest in **Eq. 7.10** does not include k , k_{rw} or ζ .

7.4 Discussion

It is the dependence of the new N_{ca} on pore geometry as described in the bracketed term in **Eq. 7.18** that shifts the separate CDC's in **Fig. 7.2** to converge to **Fig. 7.3**. The large values of G (**Table 7.2**) explain the reason why the value of N_{ca} needed to mobilize the nonwetting phase in micromodels using the conventional definition is much less than that in rock (Buchgraber et al., 2012; Geistlinger et al., 2015). The conventional definition is misleading, when using micromodel results to interpret displacements in porous rock.

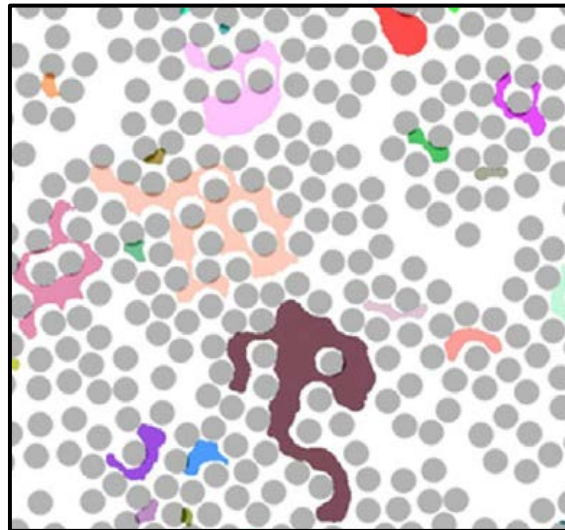


Figure 7.4 Distribution of trapped ganglia in a highly heterogeneous network, adapted from Geistlinger et al. (2015). Gray circles represent pillars on the way, shaping flow channels, and colored clusters represent trapped gas ganglia.

All the data we examined were obtained in fairly homogeneous or slightly heterogeneous networks (**Figure G-1** in Appendix G). The assumption of ganglion length scaling with one pore in length is consistent with

experimental observations for these micromodels. For very heterogeneous networks, the distribution of ganglion length is complex, as illustrated in **Fig. 7.4**, adapted from Geinstinger et al. (2015). To apply the new definition in such a context, one may need to capture the distribution of L_g to describe the mobilization effectively, since the distribution of ganglia affects the capillary resistance significantly. Some studies (Iglauer et al., 2010; Iglauer et al., 2011a, 2011b) show that the distribution of L_g for a range of N_{ca} values near the onset of mobilization follows a universal power law predicted from percolation theory.

Figure 7.3 shows that the mobilization starts for values of the new N_{ca} less than one. The derivation is based on a trapped ganglion a single pore long. In a displacement process, the distribution of ganglion lengths includes many ganglia several pores in length. The viscous force required to mobilize those ganglia is much less than that for a ganglion filling a single pore; they are mobilized at $N_{ca} < 1$. The new definition of N_{ca} in **Eq. 7.10** in principle reflects the maximum effort required to mobilize an isolated trapped ganglion. Also accounting for the factor k_{rw} in **Eq. 7.18** would increase the values of new N_{ca} .

The CDC gives the correlation between S_{nw} and N_{ca} , which is an analysis done after the experiment. To predict the mobilization or trapping in terms of a dimensionless N_{ca} , a physical model is then needed to describe the relation of S_{nw} as a function of N_{ca} . This can enhance our understanding about the fundamentals of CDC. Furthermore, it is useful for optimizing an operation designed to maximize the mobilization efficiency in oil recovery, removal efficiency of NAPL in contaminated ground water and soils, or the trapping efficiency of CO_2 in CCUS.

7.5 Conclusions

Mobilization of residual nonwetting phase in 2D micromodels is very different from that in 3D geological porous media. Consequently, the conventional N_{ca} definitions proposed for 3D pore networks do not apply to micromodel results. Direct application to micromodel results without accounting for the difference in pore geometry may lead to incorrect conclusions for fluid transport in geological formations.

A new capillary number (N_{ca}) definition, derived from the force balance on a nonwetting ganglion trapped by capillarity, is proposed for micromodels.

The new definition incorporates the impact of pore geometry on mobilization. The geometrical factors introduced can be estimated from image analysis of the network of a micromodel, without performing flow experiments. The improved fit of the new N_{ca} to published data supports its validity by yielding a consistent trend in CDC, suggesting the crucial role that pore geometry plays in mobilization.

The new N_{ca} definition works better than the conventional definitions for the evaluation of mobilization or trapping efficiency of nonwetting phase in microfluidics in a variety of processes: removal of NAPL contaminants in soils and aquifers, displacement of oil in petroleum industry and trapping of CO_2 in CCUS (Carbon Capture, Utilization and Storage).

A conversion factor between the new and conventional N_{ca} definitions is provided, to compare the difference and facilitate re-examining published data in micromodels.

Further experimental studies are needed to demonstrate the validity of a CDC based on the new N_{ca} definition for a wider range of microfluidic network geometries.

7.6 Nomenclature

- d_z = channel depth of a micromodel, m
 F_c = capillary force, Pa
 F_v = viscous force, Pa
 G = geometric factor for micromodels, dimensionless
 k = absolute permeability, m²
 k_s = permeability of a smooth slit of aperture d_z , m²
 k_{rw} = relative permeability of wetting phase, dimensionless
 L_g = length of a trapped ganglion, m
 L_p = length of one pore, m
 N_{ca} = capillary number, dimensionless
 P_c = capillary pressure, Pa
 $|\nabla p|$ = magnitude of macroscopic pressure gradient, pa/m
 Δp_c = capillary-pressure difference over curved interface of a ganglion, Pa
 q = superficial velocity, m/s
 r_1, r_2 = principle radii of curvature, m
 μ, μ_a = viscosity of displacing fluid, pa.s
 u, v = superficial and interstitial velocity of displacing fluid, m/s
 x, y = width and height of cross-section of a rectangular duct, m
 W_b = characteristic pore-body diameter, m
 W_t = characteristic pore-throat width, m
 σ = interfacial tension over an interface, N/m
 ϕ = porosity, a fraction
 $|\nabla\Phi|$ = magnitude of macroscopic flow-potential gradient, pa/m
 θ = contact angle, dimensionless as measured in radians
 ζ = adjustable factor to relate permeability and geometry, dimensionless

Subscripts and superscripts

- b** = pore body
c = capillarity
g = ganglion
t = pore throat
v = viscous force

z = channel depth

CONCLUSIONS AND RECOMMENDATIONS

8.1 Contributions of the study to foam EOR

The study in this thesis seeks to understand foam flow dynamics with oil in porous media, either at steady-state or in a transient state, through lab measurements and associated modeling of behavior. Here we review the major contributions of the study to foam EOR, with the detailed conclusions summarized in the next subsection:

- The two flow regimes for foam without oil also apply to foam with oil. This can be a starting point for deeper exploration of foam-oil flow in geological formations.
- The IT foam models with the local-equilibrium approximation can represent the two foam regimes with oil. Depending on the detrimental effects of oil on foam, one needs to combine both wet-foam and dry-out algorithms in the model to capture the behavior in both regimes.
- Fractional-flow modeling of transient foam flow with oil using the IT models, though with a number of simplifications, can provide physical insights regarding foam displacement with oil in geological formation. In particular, foam never banks up in the displacement front to an oil saturation greater than the upper limit for stable foam. Simulation results contradict the theoretical solutions, which may suggest an artifact in the simulation.
- Co-current foam-oil flow starting some distance from the injection well may lead to multiple possible foam states with different mobilities fitting the same injection condition. A displacement by the collapsed-foam state means a failure of foam EOR process. Fractional-flow theory together with the wave-curve method is a practical approach that determines the unique displacing state and its dependence on initial conditions. One can then enhance the chance of a displacement by a strong-foam state through controlling foam properties for the given reservoir conditions.
- Conventional capillary-number definitions do not work for 2D micromodels, given that the flow between 2D and 3D networks is very different because of different pore geometries. Direct application of the conventional definitions to micromodels can mislead the interpretation of the mobilization in microfluidics. We propose a new capillary-number definition for micromodels, the validity of which is confirmed by published data in the literature.

8.2 Summary of conclusions

The thesis examines various aspects of steady-state and transient foam-oil dynamics during EOR processes, from both theory and measurements: representation of the oil effect in the widely used IT foam model STARS; experimental demonstration of steady-state foam-flow regimes with oil and validation of the IT model in representing the data; fractional-flow insights into 1D transient foam-oil dynamics; theoretical determination of the physically acceptable displacing state among multiple possible injection states and the nature of its

dependence on the initial state; transient foam dynamics as a function of oil type and oil saturation; definition of a new capillary-number in 2D microfluidics and validation as a criterion for non-wetting phase mobilization. The major conclusions from the journal articles of which the thesis is composed are summarized as follows.

8.2.1 Implicit-texture modeling of the effect of oil on foam

We examine the widely used IT foam model STARS for how oil shifts the two steady-state foam regimes in the two algorithms: respectively wet-foam and dry-out algorithms. A special phenomenon – multiple steady states – is predicted in both algorithms, a finding reminiscent of catastrophe theory. Simple 1D numerical simulations are conducted to determine the stability of these steady states and the influence of initial state on the final state achieved in a foam displacement. We conclude:

- The wet-foam algorithm represents the effect of oil only on the low-quality regime, without direct effect on the high-quality regime; the dry-out algorithm delineates the effect of oil only on the high-quality regime, without direct impact on the low-quality regime.
- Both wet-foam and dry-out algorithms predict multiple steady states. Some fractional flows or superficial velocities of phases correspond to multiple foam states, i.e., the upper strong-foam state with high apparent viscosity (μ_{app}) and pressure gradient (∇p), intermediate state, and lower collapsed-foam state with low apparent viscosity and pressure gradient.
- Numerical stability analysis through simple 1D simulations indicates that the upper, strong-foam state and lower, collapsed-foam state are stable, but the intermediate state is intrinsically unstable. The formation of and displacement by the strong- or collapsed-foam state depends on initial state in a reservoir.

8.2.2 Steady-State foam-flow regimes with oil

We conduct steady-state foam corefloods with oil, to demonstrate the applicability of the two regimes for foam without oil to foam with oil. We then fit the IT model to the steady-state data with and without oil, using either the wet-foam algorithm or dry-out algorithm, or a combination of the two algorithms. The validity of the IT model in reproducing the data is demonstrated, which also helps interpret the foam-oil interaction mechanism in each regime. The main findings are as follows:

- The two regimes for foam without oil also apply to foam with oil. Oil affects both the two regimes, with a greater impact on the high-quality regime. More detrimental oils yield a larger contrast between its impact on the high- and low-quality regimes.
- The IT model shows a good match to the data with oil, except for failing to capture the upward-tilting pressure-gradient contours in the low-quality regime. This demonstrates the validity of the model in representing steady-state foam flow with oil.
- With oil containing 10% or 20% oleic acid, greatly detrimental to foam, one needs to combine wet-foam and dry-out algorithms in the modeling, to represent the behavior in both regimes.
- Fundamentally, the good match in modeling and data reveals that oil destabilizes foam in the high-quality regime by increasing the limiting water saturation, the water saturation below which foam collapses abruptly; and that oil weakens foam in the low-quality regime via reducing the mobility-reduction factor to gas phase.

8.2.3 Fractional-flow model insights into transient foam flow with oil

We present a fractional-flow analysis of foam flow with oil, with the theoretical solutions solved through the wave curve method (WCM). Physical insights on two key aspects of foam displacement with oil are revealed: the dependence of the displacement upon injection (J) and injection (I) conditions and the effects of improved oil-tolerance of the surfactant formulation on the velocities of foam propagation and of the oil bank. We also show that numerical simulations with an oil bank of oil saturation greater than the limiting saturation for foam stability (f_{moil} in our model) reflect a numerical artifact. We reach the following conclusions:

- Among the cases we examine, only foam injected with sufficient water for foam stability (i.e. injection state J allowing foam) is the displacement structure desirable, featuring low-mobility fluids upstream chasing high-mobility fluids downstream. This structure may represent the displacement following co-injection of surfactant solution and gas, or SAG (Surfactant-Alternating-Gas) some distance from the well where slugs have mingled. Our results suggest that a SAG process with a single gas slug following surfactant would not be successful, at least for the foam considered here.
- Our examples, along with an analysis of saturation velocities, show that oil saturation (S_o) within an oil bank (if created and pushed by foam) is never greater than the upper limit for stable foam, f_{moil} . This is also true for initial state I with S_o greater than f_{moil} , though waterflooding ahead of foam may reduce S_o ahead of foam below f_{moil} . This argument is justified through a consideration of the wave velocities of saturations implied by such a displacement.
- Enhancing the tolerance of foam to oil accelerates propagation of the foam bank and displaces oil more effectively ahead of the foam bank. In addition, in the cases presented, foam-bank propagation is not subject to initial conditions but only to foam properties at injection conditions.
- This approach, applied with model parameters fitting a given application, as well as these findings can guide the interpretation of foam behavior and more-complex numerical simulations in a variety of engineering applications: oil displacement in the petroleum industry, removal of NAPL (Non-aqueous Phase Liquid) contaminants removal in aquifers and soils, and carbon storage in CCUS (Carbon Capture, Utilization and Storage).

8.2.4 Fractional-flow theory of foam-oil displacement with multiple states

The multiple steady states predicted by the IT model raise an important issue in foam EOR: some injection conditions correspond to multiple possible injection states (i.e. multiple foam states with different apparent viscosity). We demonstrate that the wave-curve method used in three-phase fractional-flow theory is capable of identifying the unique displacing state among the multiple steady states. The choice of the displacing state shows a dependence on initial state, the nature of which is captured in our study. Specifically, the following conclusions are drawn:

- The WCM solves a problem with different constraints than physical corefloods with specified injection rates of phases. In a coreflood, starting at $t_D = 0$, injection state J is injected at position $x_D = 0$ and displaces initial state I present for $0 < x_D \leq 1$. In the WCM, J at $t_D = 0$ is injected from $x_D \ll 0$ and drives an initial state that comprises J present for $x_D \leq 0$ and I for $x_D > 0$.

- The distinction between the problem definitions in the WCM and physical corefloods makes the WCM capable of identifying the unique displacing state among multiple possible injection states. Specifically, in the fractional-flow solutions solved by the WCM, a physically-acceptable displacement path possesses only positive wave velocities along the whole composition path. A path with negative wave velocities does not fit the physical injection conditions (in particular, with J maintained at $x_D = 0$ upon injection).
- The occurrence of the physically-acceptable displacing state among multiple steady states shows a dependence on initial state. The nature of the dependence is captured by a “boundary curve” that is defined through the intermediate middle state in ternary saturation space. For I above the boundary curve where the strong-foam state resides, the strong-foam state makes the displacement; for I below the boundary curve, the collapsed-foam state makes the displacement. When I is on the boundary curve, depending on perturbations to I , the physically-acceptable path shifts either to the strong-foam state or collapsed-foam state, but never the intermediate state.
- In practice, foam is never co-injected with oil, but co-current foam-oil flow may occur starting some distance from the well, leading to multiple possible steady states away from the well. The findings here could help predict the displacing state and optimize the design of foam displacement by the strong state.

8.2.5 CT coreflood study of transient foam flow with oil

Most prior studies do not have direct information on oil saturation during foam corefloods. Through CT foam corefloods with oil, we seek to understand quantitatively the correlation between transient dynamics of foam (both in-situ generated and pre-generated) and oil type and saturation. Two representative model oils are used, i.e. C_{16} (benign to foam) and an oil mixture with 80% C_{16} and 20% oleic acid (OA), (greatly detrimental to foam), whose effects on steady-state foam flow were examined in Chapter 3. The CT measurements give phase distributions, in particular oil-saturation distributions, and provide supplementary data on foam dynamics reflected through sectional pressure-drop measurements. We analyze the suitability of current IT models in representing transient foam dynamics with oil according to our experimental observations. Our conclusions are as follows:

- Transient foam flow with less-harmful oil (e.g. C_{16}) shows analogous dynamics for both co-injection of surfactant solution and gas to generate foam in situ and direct injection of pre-generated foam. In both ways of foam injection, strong foam evolves forward from upstream to downstream, similar to that for foam without oil. The foam effectively displaces oil and creates an oil bank at the displacement front.
- A greatly detrimental oil has significantly different effects on the conditions for foam generation and propagation. This is demonstrated by our experimental observations that with the model oil containing 20% OA, in-situ generated foam behaves very differently from pre-generated foam. In particular, upon co-injection of surfactant solution and gas, in-situ foam generation is very difficult and eventually starts at the outlet (thought to be caused by capillary-end effect on the lab scale). In contrast, pre-generated foam shows two stages of propagation. Upon direct injection of foam, weak foam evolves and displaces most oil first, followed by a slow piston-like propagation of much stronger foam.
- The considerably different dynamics of in-situ-generated and pre-generated foam with oil shows that some dynamics are missed in the IT models. The IT models can represent the transient dynamics of

both in-situ generated and pre-generated foam without oil or with oil less harmful (e.g. C_{16}). With greatly harmful oil, the IT model cannot represent both results for pre-generated foam and in-situ-generated foam with the same set of parameters, because it does not explicitly represent the presence or absence of foam as distinct from local saturations. Further efforts are needed to improve the predictability of the IT model for foam EOR with oil.

8.2.6 New N_{ca} definition for micromodels

A new capillary-number (N_{ca}) model is proposed for 2D pore networks, e.g. 2D micromodels, to evaluate the mobilization of non-wetting phase in microfluidics. The validity of the new model is supported by the data from the literature. We reach the following conclusions:

- The conventional capillary-number definitions originally proposed for 3D geological porous media do not work for 2D micromodels. This problem arises from the fact that the flow in 2D pore networks is very different from that in 3D formations. In particular, in 2D pore networks, permeability is controlled in general by channel depth rather than the geometrical factors that control trapping. In addition, there is no simultaneous multiphase flow in 2D networks, as is a typical feature for 3D pore networks. Direct application of the conventional N_{ca} to micromodel results may mislead the interpretation of the mobilization results.
- A new capillary-number (N_{ca}) definition is proposed based on a force balance on a ganglion trapped in a single pore by capillarity. The new definition accounts for the impact of pore microstructure (e.g. pore throats and pore bodies) on non-wetting phase mobilization in microfluidics. The geometrical factors involved in the new model can be estimated directly from an image analysis of the micromodels, without needing to conduct flow experiments.
- The new N_{ca} model is validated by yielding a single trend on the capillary-desaturation curve (i.e. non-wetting phase saturation vs. N_{ca}) for micromodels, using the published two-phase flow data.

8.3 Recommendations for further research

The effectiveness of foam for gas-mobility control with oil dictates whether a foam EOR process can succeed. With oil, all aspects concerned with foam in porous media become more complex. This thesis contributes to efforts in quantitatively understanding the foam dynamics with oil in geological formations for the purpose of EOR. A number of issues still need further efforts to fill in the knowledge gap in theory and mechanisms of foam-oil interactions in porous media. Based on the findings and insights of the thesis, we give some recommendations for further research, in particular on aspects of implicit-texture modeling and deeper exploration of foam-oil dynamics.

8.3.1 Further research on implicit-texture foam modeling

The experimental observations and model fit to data with oil pinpoint some issues with the current the implicit-texture foam models. To effectively model foam EOR processes, the IT models need to be improved in the accurate representation of the effect of oil (including both oil saturation and oil composition), estimation of oil related factors, and local equilibrium approximation. Specifically, the following aspects need further research:

- In our experimental investigation of steady-state foam-flow with oil in Chapter 3, the lack of data on oil saturation S_o restricts the estimation of oil-related factors in IT foam-oil modeling. A practical approach needs to be proposed to estimate the oil factors indirectly based on data without direct information on S_o . As an alternative CT steady-state foam coreflood with oil can be conducted to directly capture S_o in each steady-state measurement. The use of CT can also help check the uncertainty in the oil saturations estimated from pressure data using a Corey-type oil-relative permeability function.
- In our data in Chapter 3 on the two regimes without oil or with oil less detrimental to foam, i.e. C_{16} , the pressure-gradient ∇p contours in the low-quality regime tilt upward. The current IT models need to be improved to capture this upward-tilting trend; otherwise, the low-quality regime cannot be represented quantitatively.
- In the CT foam coreflood with oil conducted in Chapter 6, for oils greatly detrimental to foam (i.e. with 20% oleic acid), in-situ foam generation by co-injection of surfactant solution and gas is very difficult even at uniform residual oil saturation. This suggests that the IT models which do not represent foam texture explicitly cannot simultaneously represent all cases with some oils. One needs to improve the IT model, to represent the dynamics of, e.g., in-situ generated foam in these cases.
- Prior numerical simulations implement directly foam-simulation parameters that are estimated from steady-state data, to simulate foam-oil displacement in reservoirs as a guide for practice. However, the reliability of using steady-state foam properties to predict transient behavior needs to be verified first at a lab scale.

8.3.2 Further research on foam dynamics with oil

Coreflood measurements have an unavoidable limitation that flow processes and surface phenomenon cannot be seen directly. The mechanisms of foam-oil interactions need further investigation. For deeper exploration through lab measurements, we recommend the following:

- Microfluidic investigations, during which the process can be visualized directly, may help to explore the interaction mechanisms between foam and oil on the pore scale. In addition, experimental observations in our corefloods in Chapter 3 or 6 indicate the formation of emulsions. Microfluidic studies may provide insights on the formation of emulsions and their impact on foam stability and flow.
- Our steady-state data with oil in Chapter 3 show that oil makes foam flow easier in the low-quality regime. In porous rocks, bubble sizes are thought to be close to pore sizes (Alvarez et al., 2001). This argument is expected to be also true for foam with oil. Then, further efforts are needed to understand what makes the flow easier with oil in the low-quality regime. This might be because, e.g., the drag force is reduced when bubbles cross pore throats and bodies with oil present; or that oil reduces the number of trapped bubbles; or other reasons that need to be investigated.
- Throughout this study, oil is not miscible with gas. Thus, oil affects foam mainly through its interaction with aqueous lamellae. For gas, e.g. CO_2 , that is miscible with oil, oil interacts with both aqueous lamellae and the gas phase. Current knowledge in miscible foam with oil at both steady state and transient state needs to be improved.
- Finally, the research in this thesis is carried out for one-dimensional foam flow with oil. With multiple dimensions, additional physics, e.g. gravity or fingering, are involved. The impact of oil on foam in

CONCLUSIONS AND RECOMMENDATIONS

multiple dimensions needs further investigation, especially its impact on lamellae creation, long-distance foam propagation and gravity override of gas in foam.

BIBLIOGRAPHY

- Abrams, A. (1975). The Influence of Fluid Viscosity, Interfacial Tension, and Flow Velocity on Residual Oil Saturation Left by Waterflood. *SPE-5050-PA*.
- Aveyard, R., Binks, B.P., Fletcher, P. D. I., Peck, T. G., & Rutherford, C. E. (1994). Aspects of Aqueous Foam Stability in the Presence of Hydrocarbon Oils and Solid Particles. *Advances in Colloid and Interface Science* 48 (April):93–120.
- Avraam, D., & Payatakes, A. (1995). Flow Regimes and Relative Permeabilities during Steady-State Two-Phase Flow in Porous Media. *Journal of Fluid Mechanics*, 293, 207–236.
- Arnold, V. I., Kazarinoff, N., Afrajmovich, V. S., Il'yashenko, Y. S., & Shil'nikov, L. P. (1999). *Dynamical Systems V: Bifurcation Theory and Catastrophe Theory*. Springer Berlin Heidelberg.
- Alvarez, J.M., Rivas, H.J., & Rossen, W.R. (2001). Unified Model for Steady-State Foam Behavior at High and Low Foam Qualities. *SPE J.* 6 (3):325-333.
- Apaydin, O. G., & Kovscek, A. R. (2001). Surfactant Concentration and End Effects on Foam Flow in Porous Media. *Transport in porous media*, 43(3), 511-536.
- Gauglitz, P. A., Friedmann, F., Kam, S. I., & Rossen, W. R. (2002). Foam Generation in Homogeneous Porous Media. *Chemical Engineering Science*, 57(19), 4037-4052.
- Ashoori, E., van der Heijden, T., & Rossen, W. (2010). Fractional-flow Theory of Foam Displacements with Oil. *SPE journal*, 15(02), 260-273.
- Azevedo, A. V., de Souza, A. J., Furtado, F., Marchesin, D., & Plohr, B. (2010). The Solution by the Wave Curve Method of Three-Phase Flow in Virgin Reservoirs. *Transport in Porous Media*, 83(1), 99–125.
- Afsharpoor, A., Lee, G. S., & Kam, S. I. (2010). Mechanistic Simulation of Continuous Gas Injection Period during Surfactant-Alternating-Gas (SAG) Processes Using Foam Catastrophe Theory. *Chemical Engineering Science*, 65(11), 3615–3631.
- Azevedo, A. V., de Souza, A. J., Furtado, F., Marchesin, D., & Plohr, B. (2010). The Solution by the Wave Curve Method of Three-phase Flow in Virgin Reservoirs. *Transport in Porous Media*, 83(1), 99–125.
- Andrianov, A., Farajzadeh, R., Nick, M. M., Talanana, M., & Zitha, P. L. J. (2011). Immiscible Foam for Enhancing Oil Recovery: Bulk and Porous Media Experiments. In *SPE-143578-MS*. SPE: Society of Petroleum Engineers.
- Ashoori, E., Marchesin, D., & Rossen, W. R. (2011). Roles of Transient and Local Equilibrium Foam Behavior in Porous Media: Traveling Wave. *Colloids and Surfaces A: Physicochemical and Engineering Aspects*, 377(1-3), 228-242.
- Andrianov, A., Farajzadeh, R., Mahmoodi Nick, M., Talanana, M., & Zitha, P. L. (2012). Immiscible Foam for Enhancing Oil Recovery: Bulk and Porous media Experiments. *Industrial & Engineering Chemistry Research*, 51(5), 2214-2226.
- Al-Shalabi, E., Sepehrnoori, K., Pope, G., & Mohanty, K. (2014). A Fundamental Model for Predicting Oil Recovery Due to Low Salinity Water Injection in Carbonate Rocks. Presented at the SPE Energy

BIBLIOGRAPHY

- Resources Conference, Society of Petroleum Engineers.
- Al Ayesh, A. H., Salazar, R., Farajzadeh, R., Vincent-Bonnieu, S., & Rossen, W. R. (2017). Foam Diversion in Heterogeneous Reservoirs: Effect of Permeability and Injection Method. *SPE Journal*, 22(05), 1-402.
- AlQuaimi, B., & Rossen, W. (2017). New Capillary Number Definition for Displacement of Residual Nonwetting Phase in Natural Fractures. *Geophysical Research Letters*.
- Al Sumaiti, A., Shaik, A. R., Mathew, E. S., & Al Ameri, W. (2017). Tuning Foam Parameters for Mobility Control using CO₂ Foam: Field Application to Maximize Oil Recovery from a High Temperature High Salinity Layered Carbonate Reservoir. *Energy & Fuels*, 31(5), 4637–4654.
- Amirmoshiri, M., Zeng, Y., Chen, Z., Singer, P. M., Puerto, M. C., Grier, H., ... & Hirasaki, G. J. (2018). Probing the Effect of Oil Type and Saturation on Foam Flow in Porous Media: Core-Flooding and Nuclear Magnetic Resonance (NMR) Imaging. *Energy & Fuels*, 32(11), 11177–11189.
- Alcorn, Z. P., Fredriksen, S. B., Sharma, M., Rognmo, A. U., Føyen, T. L., Fernø, M. A., & Graue, A. (2018). An Integrated CO₂ Foam EOR Pilot Program with Combined CCUS in an Onshore Texas Heterogeneous Carbonate Field. In *SPE Improved Oil Recovery Conference*. Society of Petroleum Engineers.
- AlQuaimi, B. I., & Rossen, W. R. (2018). Foam Generation and Rheology in a Variety of Model Fractures. *Energy & Fuels*.
- Buckley, S. E., & Leverett, M. C. (1942). Mechanism of Fluid Displacement in Sands. *SPE-942107-G*, 146(1), 107–116. <https://doi.org/10.2118/942107-G>.
- Brownell, L. E., & Katz, D. L. (1947). Flow of Fluids through Porous Media. 2. Simultaneous Flow of 2 Homogeneous Phases. *Chemical Engineering Progress*, 43(11), 601–612.
- Bethel, F. T., & Calhoun, J. C. (1953). Capillary Desaturation in Unconsolidated Beads. *SPE-953197-G*. <https://doi.org/10.2118/953197-G>.
- Bernard, G. G., & Jacobs, W. L. (1965). Effect of Foam on Trapped Gas Saturation and on Permeability of Porous Media to Water. *Society of Petroleum Engineers Journal*, 5(04), 295-300.
- Bergeron, V., Fagan, M. E., & Radke, C. J. (1993). Generalized Entering Coefficients: A Criterion for Foam Stability against Oil in Porous Media. *Langmuir* 9 (7):1704–13.
- Basheva, E. S., Ganchev, D., Denkov, N. D. Kasuga, k., Satoh, N., & Tsujii, K. (2000). Role of Betaine as Foam Booster in the Presence of Silicone Oil Drops. *Langmuir* 16 (3): 1000–1013.
- Buchgraber, M., Kovscek, A. R., & Castanier, L. M. (2012). A Study of Microscale Gas Trapping Using Etched Silicon Micromodels. *Transport in Porous Media*, 95(3), 647–668.
- Blunt, M. J., Bijeljic, B., Dong, H., Gharbi, O., Iglauer, S., Mostaghimi, P., ... & Pentland, C. (2013). Pore-scale Imaging and Modelling. *Advances in Water Resources*, 51, 197-216.
- Boeije, C. S., & Rossen, W. (2015). Fitting Foam-simulation-model Parameters to Data: I. Coinjection of Gas and Liquid. *SPE-174544-PA*. <https://doi.org/10.2118/174544-PA>
- Bertin, H., Estrada, E. D. C., & Atteia, O. (2017). Foam Placement for Soil Remediation. *Environmental Chemistry*, 14(5), 338–343.
- Bagheri, S. R. (2017). Experimental and Simulation Study of the Steam–Foam Process. Part 2: The Effect of Oil on Foam Generation. *Energy & Fuels*, 31(3), 2687–2696.
- Bui, M., Adjiman, C. S., Bardow, A., Anthony, E. J., Boston, A., Brown, S., ... & Hackett, L. A. (2018). Carbon

BIBLIOGRAPHY

- capture and storage (CCS): the way forward. *Energy & Environmental Science*, 11(5), 1062–1176.
- Baghernezhad, D., Siavashi, M., & Nakhaee, A. (2019). Optimal Scenario Design of Steam-assisted Gravity Drainage to Enhance Oil Recovery with Temperature and Rate Control. *Energy*, 166, 610–623.
- Bergeron, V., Fagan, M. E., and Radke, C. J. (1993). Generalized Entering Coefficients: A Criterion for Foam Stability against Oil in Porous Media. *Langmuir* 9 (7):1704–13. doi: 10.1021/la00031a017.
- Dombrowski, H., & Brownell, L. (1954). Residual Equilibrium Saturation of Porous Media. *Industrial & Engineering Chemistry*, 46(6), 1207–1219.
- Chatzis, I., & Dullien, F. A. L. (1977). Modelling Pore Structure By 2-D And 3-D Networks With Application to Sandstones. *PETSOC-77-01-09*.
- Chatzis, I., Morrow, N. R., & Lim, H. T. (1983). Magnitude and Detailed Structure of Residual Oil Saturation. *SPE-10681-PA*. <https://doi.org/10.2118/10681-PA>.
- Charbeneau, R. J. (1988). Multicomponent exchange and subsurface solute transport: Characteristics, coherence, and the Riemann problem. *Water Resources Research*, 24(1), 57–64.
- Doyen, P. M. (1988). Permeability, Conductivity, and Pore Geometry of Sandstone. *Journal of Geophysical Research: Solid Earth*, 93(B7), 7729–7740.
- Christensen, J. R., Stenby, E. H., & Skauge, A. (1998). Review of WAG Field Experience. In *International Petroleum Conference and Exhibition of Mexico*. Society of Petroleum Engineers.
- Cheng, L., Reme, A. B., Shan, D., Coombe, D. A., & Rossen, W. R. (2000). Simulating Foam Processes at High and Low Foam Qualities. (2000) *SPE-59287-MS*. *SPE: Society of Petroleum Engineers*. <https://doi.org/10.2118/59287-MS>.
- Chalbaud, C. A., Moreno, R. A., & Alvarez, J. M. (2002). Simulating Foam Process for a Venezuelan Pilot Test. Society of Petroleum Engineers. doi:10.2118/77699-MS.
- Conn, C. A., Ma, K., Hirasaki, G. J., & Biswal, S. L. (2014). Visualizing Oil Displacement with Foam in a Microfluidic Device with Permeability Contrast. *Lab on a Chip*, 14(20), 3968–3977.
- Computer Modeling Group (Calgary, Alberta, Canada), *STARS User's Guide*, Version 2015. See also *GEM User's Guide*.
- Castañeda, P., Abreu, E., Furtado, F., & Marchesin, D. (2016). On a Universal Structure for Immiscible Three-Phase Flow in Virgin Reservoirs. *Computational Geosciences*, 20(1), 171–185.
- Castañeda, P., & Furtado, F. (2016). The Role of Sonic Shocks between Two-and Three-Phase States in Porous Media. *Bulletin of the Brazilian Mathematical Society, New Series*, 47(1), 227–240.
- Castañeda, P. (2018). Explicit Construction of Effective Flux Functions for Riemann Solutions. In: Klingenberg C., Westdickenberg M. (eds) *Theory, Numerics and Applications of Hyperbolic Problems I. HYP 2016*. (pp. 273–284). Presented at the *XVI International Conference on Hyperbolic Problems: Theory, Numerics, Applications*, Springer.
- Castaneda-Herrera, C. A., Stevens, G. W., & Haese, R. R. (2018). Review of CO₂ Leakage Mitigation and Remediation Technologies. *Geological Carbon Storage: Subsurface Seals and Caprock Integrity*, 238, 327.
- Carpenter, C. (2018). Integrated CO₂-Foam Pilot in a Heterogeneous Carbonate Field. *SPE-0718-0072-JPT*, 70(7), 72–74. <https://doi.org/10.2118/0718-0072-JPT>.
- Cavalcante Filho, J. S. de A., Delshad, M., & Sepehrnoori, K. (2018). Estimation of Foam-Flow Parameters for

BIBLIOGRAPHY

- Local Equilibrium Methods by Use of Steady-State Flow Experiments and Optimization Algorithms. SPE-179597-PA. doi.org/10.2118/179597-PA.
- de Vries, A. S., & Wit, K. (1990). Rheology of Gas/Water Foam in the Quality Range Relevant to Steam Foam. SPE-18075-PA. https://doi.org/10.2118/18075-PA.
- Dalland, M., Hanssen, J. E., & Kristiansen, T. S. (1994). Oil Interaction with Foams under Static and Flowing Conditions in Porous Media. *Colloids and Surfaces A: Physicochemical and Engineering Aspects* 82 (2):129–40.
- Elliott, C., Vijayakumar, V., Zink, W., & Hansen, R. (2007). National Instruments LabVIEW: a Programming Environment for Laboratory Automation and Measurement. *JALA: Journal of the Association for Laboratory Automation*, 12(1), 17–24.
- Estrada, E. D. C., Bertin, H., & Atteia, O. (2015). Experimental Study of Foam Flow in Sand Columns: Surfactant Choice and Resistance Factor Measurement. *Transport in Porous Media*, 108(2), 335–354.
- Eftekhari, A. A., & R. Farajzadeh. (2017). Effect of Foam on Liquid Phase Mobility in Porous Media. *Scientific Reports* 7 (March):43870.
- Foster, W. R. (1973). A Low-Tension Waterflooding Process. SPE-3803-PA. https://doi.org/10.2118/3803-PA
- Falls, A. H., Hirasaki, G. J., Patzek, T. W., Gauglitz, D. A., Miller, D. D., & Ratulowski, T. (1988). Development of a Mechanistic Foam Simulator: The Population Balance and Generation by Snap-Off. SPE-14961-PA, August. doi: 10.2118/14961-PA.
- Frye, G. C., & Berg, J. C. (1989). Antifoam Action by Solid Particles. *Journal of Colloid and Interface Science* 127 (1):222–38.
- Fisher, A.W., Foulser, R. W. S., & Goodyear, S. G. (1990). Mathematical Modeling of Foam Flooding. In SPE-20195-MS. SPE: Society of Petroleum Engineers. doi: 10.2118/20195-MS.
- Friedmann, F., Chen, W. H. & Gauglitz, P.A. (1991). Experimental and Simulation Study of High-Temperature Foam Displacement in Porous Media. SPE-17357-PA, February. doi: 10.2118/17357-PA.
- Franklin, M. (1994). Scale-up of Miscible Flood Processes for Heterogeneous Reservoirs, Petroleum Engineering Department, Stanford University.
- Farajzadeh, R., Andrianov, A., Krastev, R., Hirasaki, G. J., & Rossen, W. R. (2012). Foam–oil Interaction in Porous Media: Implications for Foam Assisted Enhanced Oil Recovery. *Advances in Colloid and Interface Science*, 183–184, 1–13.
- Farajzadeh, R., Lotfollahi, M., Eftekhari, A. A., Rossen, W. R., & Hirasaki, G. J. H. (2015). Effect of Permeability on Implicit-Texture Foam Model Parameters and the Limiting Capillary Pressure. *Energy & Fuels*, 29(5), 3011–3018.
- Farajzadeh, R., Eftekhari, A. A., Hajibeygi, H., Kahrobaei, S., Van der Meer, J. M., Vincent-Bonnieu, S., & Rossen, W. R. (2016). Simulation of Instabilities and Fingering in Surfactant Alternating Gas (SAG) Foam Enhanced Oil Recovery. *Journal of Natural Gas Science and Engineering*, 34, 1191-1204.
- Golubitsky, M., & Keyfitz, B. L. (1980). A Qualitative Study of the Steady-State Solutions for a Continuous Flow Stirred Tank Chemical Reactor. *SIAM Journal on Mathematical Analysis*, 11(2), 316–339.
- Guckenheimer, J. (1986). Multiple Bifurcation Problems for Chemical Reactors. *Physica D: Nonlinear Phenomena*, 20(1), 1–20.

BIBLIOGRAPHY

- Gauglitz, P.A., Friedmann, F., Kam, S. I, & Rossen, W.R. (2002). Foam Generation in Homogeneous Porous Media. *Chem. Eng. Sci.* 57(19), 4037-4052.
- Garrett, P. R. (1979). The Effect of Polytetrafluoroethylene Particles on the Foamability of Aqueous Surfactant Solutions. *Journal of Colloid and Interface Science* 69 (1):107–21.
- Green, D. W., & Willhite, G. P. (1998). *Enhanced Oil Recovery* (Vol. 6). Henry L. Doherty Memorial Fund of AIME, Society of Petroleum Engineers Richardson, TX.
- Gauglitz, A. P., Friedmann, F., Kam, S. I. and Rossen, W. R. (2002). Foam Generation in Homogeneous Porous Media. *Chemical Engineering Science* 57 (19):4037–52.
- Glass, R. J., & Yarrington, L. (2003). Mechanistic Modeling of Gingering, Nonmonotonicity, Fragmentation, and Pulsation within Gravity/buoyant Destabilized Two-phase/Unsaturated Flow. *Water Resources Research*, 39(3).
- Geistlinger Helmut, Lazik Detlef, Krauss Gunnar, & Vogel Hans-Jörg. (2009). Pore-Scale and Continuum Modeling of Gas Flow Pattern Obtained by High-Resolution Optical Bench-Scale Experiments. *Water Resources Research*, 45(4).
- Ghanbarian, B., Hunt, A. G., Ewing, R. P., & Sahimi, M. (2013). Tortuosity in porous media: a critical review. *Soil Science Society of America Journal*, 77(5), 1461–1477.
- Geistlinger, H., Ataei-Dadavi, I., Mohammadian, S., & Vogel, H.-J. (2015). The Impact of Pore Structure and Surface Roughness on Capillary Trapping for 2-D and 3-D Porous Media: Comparison with Percolation Theory. *Water Resources Research*, 51(11), 9094–9111.
- Gong, J., Vincent-Bonnieu, S., Kamarul Bahrim, R. Z., Groenenboom, J., Farajzadeh, R., & Rossen, W. R. (2018). Modelling of Liquid Injectivity in Surfactant-Alternating-Gas Foam Enhanced Oil Recovery. In *SPE EOR Conference at Oil and Gas West Asia*. Society of Petroleum Engineers.
- Gong, J., Vincent-Bonnieu, S., Bahrim, K., Zhafri, R., Mamat, C., Bakri, C. A. N., ... & Rossen, W. R. (2019). Modeling of Liquid Injectivity in Surfactant-Alternating-Gas Foam Enhanced Oil Recovery. *SPE Journal*.
- Harkins, W. D., and Feldman, A. (1922). Films: the Spreading of Liquids and the Spreading Coefficient. *Journal of the American Chemical Society* 44 (12):2665–85.
- Holm, L. W. (1968). The Mechanism of Gas and Liquid Flow Through Porous Media in the Presence of Foam. *Society of Petroleum Engineers Journal*, 8(04), 359-369.
- Holmes, P., & Rand, D. (1976). The Bifurcations of Duffing's Equation: An Application of Catastrophe Theory. *Journal of Sound and Vibration*, 44(2), 237–253.
- Hirasaki, G., Miller, C., Szafranski, R., Lawson, J., & Akiya, N. (1997). Surfactant/foam Process for Aquifer Remediation. Presented at the International symposium on oilfield chemistry, Society of Petroleum Engineers.
- Hagoort, J. (1980). Oil recovery by Gravity Drainage. *Society of Petroleum Engineers Journal*, 20(03), 139-150.
- Hirasaki, G. J., & Lawson, J. B. (1985). Mechanisms of Foam Flow in Porous Media: Apparent Viscosity in Smooth Capillaries. *SPE-12129-PA*, April. doi: 10.2118/12129-PA.
- Hahn, P. S., Ramamohan, T. R., & Slattery, J. C. (1985). Mobility Control in the Displacement of Residual Oil by an Unstable Foam. *AIChE Journal*, 31(6), 1029–1035.
- Holm, L., & Garrison, W. H. (1988). CO₂ Diversion with Foam in an Immiscible CO₂ Field Project. *SPE*

BIBLIOGRAPHY

- Reservoir Engineering*, 3(1), 112–118.
- Hiraski, G. J. (1989). The Steam-Foam Process. *Journal of Petroleum Technology*, 41(05), 449-456.
- Hirasaki, G. J., Miller, C. A., Szafranski, R., Tanzil, D., Lawson, J. B., Meinardus, H., ... & Wade, W. H. (1997). Field Demonstration of the Surfactant/Foam Process for Aquifer Remediation. In *SPE Annual Technical Conference and Exhibition*. Society of Petroleum Engineers.
- Hayes, T. D. (2001). Foam Transport Process for In-situ Remediation of Contaminated Soils.
- Hayes, Thomas D. (2001). "Foam Transport Process for In-situ Remediation of Contaminated Soils." U.S. Patent 6,210,955.
- Hussain, A. A. A., Amin, A., Vincent-Bonnieu, S., Farajzadeh, R., Andrianov, A., Hamid, P. A., & Rossen, W. R. (2017). Effect of Oil on Gravity Segregation in SAG Foam Flooding. In *IOR 2017-19th European Symposium on Improved Oil Recovery*.
- Islam, M. R., & Farouq Ali, S. M.. (1988). Numerical Simulation Of Foam Flow In Porous Media. In *PETSOC-88-39-04. PETSOC: Petroleum Society of Canada*. doi: 10.2118/88-39-04.
- Ibrahim, A. S. (2009). Investigation of the Mobilization of Residual Oil Using Micromodels. Presented at the SPE Annual Technical Conference and Exhibition, *Society of Petroleum Engineers*, SPE-129515-STU.
- Iglauer, S., Favretto, S., Spinelli, G., Schena, G., & Blunt, M. J. (2010). X-ray Tomography Measurements of Power-Law Cluster Size Distributions for the Nonwetting Phase in Sandstones. *Physical Review E*, 82(5), 56315.
- Iglauer, S., Wülling, W., Pentland, C. H., Al-Mansoori, S. K., & Blunt, M. J. (2011a). Capillary-Trapping Capacity of Sandstones and Sandpacks. *SPE Journal*, 16(04), 778-783.
- Iglauer S., Paluszny, A., Pentland, C. H., & Blunt, M. J. (2011b). Residual CO₂ Imaged with X-ray Micro-Tomography. *Geophysical Research Letters*, 38(21).
- Jensen, J. A., & Friedmann, F. (1987). Physical and Chemical Effects of an Oil Phase on the Propagation of Foam in Porous Media. In *SPE-16375-MS* (p. 14). SPE: Society of Petroleum Engineers. <https://doi.org/10.2118/16375-MS>.
- Jeong, S.-W., & Corapcioglu, M. Y. (2005). Force Analysis and Visualization of NAPL Removal during Surfactant-Related Floods in a Porous Medium. *Journal of Hazardous Materials*, 126(1), 8–13. <https://doi.org/10.1016/j.jhazmat.2005.06.015>.
- Janssen, M. T. G., Zitha, P. L. J., & Pilus, R. M. (2018). Oil Recovery by Alkaline-Surfactant-Foam ASF Flooding: Effect of Drive Foam Quality on Oil Bank Propagation. In *SPE-190235-MS* (p. 32). SPE: Society of Petroleum Engineers. <https://doi.org/10.2118/190235-MS>.
- International Energy Agency (2018). World Energy Outlook 2018. <https://www.iea.org/weo/>.
- Johnson, P. C., Johnson, R. L., Bruce, C. L., & Leeson, A. (2001). Advances in In Situ Air Sparging/Biosparging. *Bioremediation Journal*, 5(4), 251–266.
- Jeong, S.-W., & Corapcioglu, M. Y. (2003). A Micromodel Analysis of Factors Influencing NAPL Removal by Surfactant Foam Flooding. *Journal of Contaminant Hydrology*, 60(1–2), 77–96.
- Jeong, S.-W., & Corapcioglu, M. Y. (2005). Force Analysis and Visualization of NAPL Removal During Surfactant-Related Floods in a Porous Medium. *Journal of Hazardous Materials*, 126(1), 8–13.
- Juanes R., Spiteri E. J., Orr F. M., & Blunt M. J. (2006). Impact of Relative Permeability Hysteresis on Geological CO₂ Storage. *Water Resources Research*, 42(12).

BIBLIOGRAPHY

- Jones, S. A., Getrouw, N., & Vincent-Bonnieu, S. (2018). Foam Flow in a Model Porous Medium: I. The Effect of Foam Coarsening. *Soft matter*, 14(18), 3490-3496.
- Janssen, M. T. G., Pilus, R. M., & Zitha, P. L. J. (2019). A Comparative Study of Gas Flooding and Foam-Assisted Chemical Flooding in Bentheimer Sandstones. *Transport in Porous Media*.
- Khatib, Z. I., Hirasaki, G. J., and Falls, A. H. (1988). Effects of Capillary Pressure on Coalescence and Phase Mobilities in Foams Flowing Through Porous Media. *SPE reservoir engineering*, 3(03), 919-926.
- Kular, G. S., Lowe, K., and Coombe, D. (1989). Foam Application in an Oil Sands Steamflood Process. In *SPE-19690-MS. SPE: Society of Petroleum Engineers*. doi: 10.2118/SPE-19690-MS.
- Kravtsov, Y. A., & Orlov, Y. I. (1990). Geometrical Optics of Inhomogeneous Media: Springer Series on Wave Phenomena. *Springer-Verlag New York, Inc.*
- Kovscek, A. R., & Radke, C. J. (1993). Fundamentals of Foam Transport in Porous Media (No. DOE/BC-93000174). *Lawrence Berkeley Lab., CA (United States)*.
- Kovscek, A. R., Patzek, T. W., & Radke, C. J. (1995). A Mechanistic Population Balance Model for Transient and Steady-state Foam Flow in Boise Sandstone. *Chemical Engineering Science*, 50(23), 3783-3799.
- Kovscek, A. R., Tadeusz, W. P., & Radke, C. J. (1997). Mechanistic Foam Flow Simulation in Heterogeneous and Multidimensional Porous Media. *SPE Journal*, 2(4), 511-526.
- Kharabaf, H., & Yortsos, Y. C. (1998). A Pore-network Model for Foam Formation and Propagation in Porous Media. *SPE Journal*, 3(01), 42-53.
- Kruglyakov, P. M., & Vilkova, N. G. (1999). The Relation between Stability of Asymmetric Films of the Liquid/liquid/gas Type, Spreading Coefficient and Surface Pressure. *Colloids and Surfaces A: Physicochemical and Engineering Aspects* 156 (1):475-87.
- Kam, S. I., & Rossen, W. R. (2003). A Model for Foam Generation in Homogeneous Media. *SPE-87334-PA*. <https://doi.org/10.2118/87334-PA>
- Kim, J., Dong, Y., and Rossen, W. R.. (2005). Steady-State Flow Behavior of CO₂ Foam. *SPE-89351-PA*, December. doi: 10.2118/89351-PA.
- Kam, S. I., Nguyen, Q. P., Li, Q., & Rossen, W. R. (2007). Dynamic Simulations with an Improved Model for Foam Generation. *SPE Journal*, 12(01), 35-48.
- Kao, C. M., Chen, C. Y., Chen, S. C., Chien, H. Y., & Chen, Y. L. (2008). Application of in Situ Biosparging to Remediate a Petroleum-Hydrocarbon Spill Site: Field and Microbial Evaluation. *Chemosphere*, 70(8), 1492-1499.
- Kam, S. I. (2008). Improved Mechanistic Foam Simulation with Foam Catastrophe Theory. *Colloids and Surfaces A: Physicochemical and Engineering Aspects*, 318(1), 62-77.
- Kovscek, A. R., Chen, Q., & Gerritsen, M. (2010). Modeling Foam Displacement with the Local-equilibrium Approximation: Theory and Experimental Verification. *SPE Journal*, 15(1), 171-183.
- Kawale, D., Marques, E., Zitha, P. L., Kreutzer, M. T., Rossen, W. R., & Boukany, P. E. (2017). Elastic Instabilities during the Flow of Hydrolyzed Polyacrylamide Solution in Porous Media: Effect of Pore-Shape and Salt. *Soft Matter*, 13(4), 765-775.
- Kapetas, L., Vincent-Bonnieu, S., Farajzadeh, R. Eftekhari, A. A., Mohd Shafian, S. R. Kamarul Bahrim, R. Z., & Rossen, W. R. (2017). Effect of Permeability on Foam-Model Parameters: An Integrated Approach

BIBLIOGRAPHY

- from Core-Flood Experiments through to Foam Diversion Calculations. *Colloids and Surfaces A: Physicochemical and Engineering Aspects* 530 (Supplement C):172–80.
- Lax, P. D. (1957). Hyperbolic Systems of Conservation Laws II. *Communications on Pure and Applied Mathematics*, 10(4), 537–566.
- Liu, T. P. (1974). The Riemann Problem for General 2×2 Conservation Laws. *Transactions of the American Mathematical Society*, 199, 89–112.
- Larson, R., Scriven, L., & Davis, H. (1977). Percolation Theory of Residual Phases in Porous Media. *Nature*, 268(5619), 409.
- Lenormand, R., Zarcone, C., & Sarr, A. (1983). Mechanisms of the Displacement of One Fluid by Another in a Network of Capillary Ducts. *Journal of Fluid Mechanics*, 135, 337–353.
- Law, D. H., Yang, Z., and Stone, T. W. (1992). Effect of the Presence of Oil on Foam Performance: A Field Simulation Study. *SPE-18421-PA*, May. doi: 10.2118/18421-PA.
- LaForce, T., & Johns, R. T. (2005). Analytical Solutions for Surfactant-Enhanced Remediation of Nonaqueous Phase Liquids. *Water Resources Research*, 41(10).
- Li, R. F., Yan, W., Liu, S., Hirasaki, G., & Miller, C. A. (2010). Foam Mobility Control for Surfactant Enhanced Oil Recovery. *SPE Journal*, 15(4), 928–942.
- Liu, M., Andrianov, A., & Rossen, W. R. (2011). Sweep Efficiency in CO₂ Foam Simulations with Oil. Presented at the IOR 2011-16th European Symposium on Improved Oil Recovery.
- Lake, L. W., Johns, R. T., Rossen, W. R., & Pope, G. (2014). Fundamentals of Enhanced Oil Recovery. *Richard, Texas: Society of Petroleum Engineers*.
- Lotfollahi, M., Farajzadeh, R., Delshad, M., Varavei, A., & Rossen, W. R. (2016). Comparison of Implicit-texture and Population-balance Foam Models. *Journal of Natural Gas Science and Engineering*, 31, 184-197.
- Lotfollahi, M., Kim, I., Beygi, M. R., Worthen, A. J., Huh, C., Johnston, K. P., ... DiCarlo, D. A. (2016). Experimental Studies and Modeling of Foam Hysteresis in Porous Media. In *SPE-179664-MS*. SPE: Society of Petroleum Engineers.
- Moore, T. F., & Slobod, R. L. (1955). Displacement of Oil by Water-Effect of Wettability, Rate, and Viscosity on Recovery. In *SPE-502-G*. SPE: Society of Petroleum Engineers. <https://doi.org/10.2118/502-G>.
- Mohanty, K. K., Davis, H. T., & Scriven, L. E. (1987). Physics of Oil Entrapment in Water-Wet Rock. *SPE-9406-PA*.
- Mohammadi, S., Coombe, D., & Stevenson, V. (1993). Test of Steam-foam Process for Mobility Control in South Casper Creek Reservoir. *Journal of Canadian Petroleum Technology*, 32(10), 49–54.
- Mannhardt, K., Novosad, J. J., and Schramm, L. L. (1998). Foam/Oil Interactions at Reservoir Conditions. In *SPE-39681-MS*. SPE: Society of Petroleum Engineers.
- Ma, K., Lopez-Salinas, J. L., Puerto, M. C., Miller, C. A., Biswal, S. L., & Hirasaki, G. J. (2013). Estimation of Parameters for the Simulation of Foam Flow through Porous Media. Part 1: the Dry-Out Effect. *Energy & fuels*, 27(5), 2363-2375.
- Myers, T. J., and Radke C. J. (2000). Transient Foam Displacement in the Presence of Residual Oil: Experiment and Simulation Using a Population-Balance Model. *Industrial & Engineering Chemistry Research* 39 (8): 2725–41.

BIBLIOGRAPHY

- Manrique, E. J., Thomas, C. P., Ravikiran, R., Izadi Kamouei, M., Lantz, M., Romero, J. L., & Alvarado, V. (2010). EOR: Current Status and Opportunities. In *SPE-130113-MS* (p. 21). SPE: Society of Petroleum Engineers.
- Ma, K., Lopez-Salinas, J., Puerto, M. C., Miller, C. A., Biswal, S. L., and Hirasaki, G. J. (2013). "Estimation of Parameters for the Simulation of Foam Flow through Porous Media. Part 1: The Dry-Out Effect." *Energy & Fuels* 27 (5):2363–75.
- Ma, K., Ren, G., Mateen, K., Morel, D., and Cordelier, P. (2015). Modeling Techniques for Foam Flow in Porous Media. *SPE-169104-PA*, June.
- Ma, K., Mateen, K., Ren, G., Luo, H., Bourdarot, G., & Morel, D. (2018). Mechanistic Modeling of Foam Flow Through Porous Media in the Presence of Oil: Review of Foam-Oil Interactions and an Improved Bubble Population-Balance Model. Presented at the SPE Annual Technical Conference and Exhibition, Society of Petroleum Engineers.
- Nguyen, Q. P., Rossen, W. R., Zitha, P. L. J., & Currie, P. K. (2009). "Determination of Gas Trapping With Foam Using X-Ray Computed Tomography and Effluent Analysis". Society of Petroleum Engineers.
- Namdar Zanganeh, M., Kam, S. I., LaForce, T., & Rossen, W. R. (2011). The Method of Characteristics Applied to Oil Displacement by Foam. *SPE-121580-PA*.
- Norris, S. O., Scherlin, J. M., Mukherjee, J., Vanderwaal, P., Abbas, S., & Nguyen, Q. P. (2014). CO₂ Foam Pilot in Salt Creek Field, Natrona County, WY: Phase II: Diagnostic Testing and Initial Results. Society of Petroleum Engineers.
- Orr, J. F., & Taber, J. J. (1984). Use of Carbon Dioxide in Enhanced Oil Recovery. *Science*, 224(4649), 563-569.
- Osterloh, W. T., & Jante, M. J., Jr. (1992). Effects of Gas and Liquid Velocity on Steady-State Foam Flow at High Temperature. In *SPE-24179-MS*. SPE: Society of Petroleum Engineers.
- Orr, F. M. (2007). *Theory of Gas Injection Processes* (Vol. 5). Tie-Line Publications Copenhagen.
- Oil and Gas Journal. 2010. Oil and Gas EOR Survey. 108(36).
- Pope, G. A. (1980). The Application of Fractional Flow Theory to Enhanced Oil Recovery. *Society of Petroleum Engineers Journal*, 20(03), 191-205.
- Patzek, T. W., and Myhill, N. A. (1989). Simulation of the Bishop Steam Foam Pilot. In *SPE-18786-MS*. SPE: Society of Petroleum Engineers.
- Persoff, P., Radke, C. J., Pruess, K., Benson, S. M., & Witherspoon, P. A. (1991). A Laboratory Investigation of Foam Flow in Sandstone at Elevated Pressure. *SPE-18781-PA*.
- Pennell, K. D., Pope, G. A., & Abriola, L. M. (1996). Influence of Viscous and Buoyancy Forces on the Mobilization of Residual Tetrachloroethylene during Surfactant Flushing. *Environmental Science & Technology*, 30(4), 1328–1335.
- Pope, G., Wu, W., Narayanaswamy, G., Delshad, M., Sharma, M., & Wang, P. (2000). Modeling Relative Permeability Effects in Gas-Condensate Reservoirs with a New Trapping Model. *SPE Reservoir Evaluation & Engineering*, 3(2), 171–178.
- Purohit, P. K., & Bhattacharya, K. (2003). Dynamics of Strings Made of Phase-Transforming Materials. *Journal of the Mechanics and Physics of Solids*, 51(3), 393–424.
- Pavel, S., Rudyk, S., and Khan, A. (2012). Foam Assisted WAG: Snorre Revisit with New Foam Screening Model. In *SPE-150829-MS*. SPE: Society of Petroleum Engineers.

BIBLIOGRAPHY

- Patil, P. D., Knight, T., Katiyar, A., Vanderwal, P., Scherlin, J., Rozowski, P., ... Nguyen, Q. P. (2018). CO₂ Foam Field Pilot Test in Sandstone Reservoir: Complete Analysis of Foam Pilot Response. In *SPE-190312-MS* (p. 14). SPE: Society of Petroleum Engineers.
- Patil, P. D., Knight, T., Katiyar, A., Vanderwal, P., Scherlin, J., Rozowski, P., ... Nguyen, Q. P. (2018). CO₂ Foam Field Pilot Test in Sandstone Reservoir: Complete Analysis of Foam Pilot Response. Society of Petroleum Engineers.
- Reed, R. L., & Healy, R. N. (1977). Some Physicochemical Aspects of Microemulsion Flooding: a Review In *Improved Oil Recovery by Surfactant and Polymer Flooding* (pp. 383–437). Elsevier.
- Raterman, K. T. (1989). An Investigation of Oil Destabilization of Nitrogen Foams in Porous Media. In *SPE-19692-MS* (p. 11). SPE: Society of Petroleum Engineers.
- Rossen, W.R. & Gauglitz, P.A. (1990). Percolation Theory of Creation and Mobilization of Foams in Porous Media. *AIChE J.* 36, 1176-1188.
- Rossen, W. R., & Kumar, A. T. A. (1992). Single- and Two-Phase Flow in Natural Fractures. In *SPE-24915-MS*. SPE: Society of Petroleum Engineers.
- Rossen, W.R. & Zhou, Z.H. (1995). Modeling Foam Mobility at the Limiting Capillary Pressure. *SPE Adv. Technol.* 3, 146-152.
- Rossen, W. R. (1996). Foams in Enhanced Oil Recovery. In *Foams: Theory, Measurements, and Applications*, 413–64. Marcel Dekker.
- Rossen, W. R., & Wang, M. (1997). Modeling Foams for Acid Diversion. In *SPE-38200-MS*. SPE: Society of Petroleum Engineers.
- Reme, A. B. (1999). Parameter Fitting and Calibration Study with a Commercial Foam Simulator. PhD thesis, Norwegian University of Science and Technology.
- Rossen, W. R., & Wang, M. W. (1999). Modeling Foams for Acid Diversion. *SPE Journal*, 4(02), 92-100.
- Rossen, W., Zeilinger, S., Shi, J., & Lim, M. (1999). Simplified Mechanistic Simulation of Foam Processes in Porous Media. *SPE Journal*, 4(3), 279–287.
- Ross, C. M., & Kavscek, A. R. (2002). Pore Microstructure and Fluid Distribution in a Diatomaceous Reservoir. In *SPE-75190-MS*. SPE: Society of Petroleum Engineers.
- Rong, J. G. (2002). Experimental Evaluation of Foam in Environmental Remediation. PhD thesis at University of Texas at Austin, USA.
- Rossen, W. R. (2003). A Critical Review of Roof Snap-off as a Mechanism of Steady-state Foam Generation in Homogeneous Porous Media. *Colloids and Surfaces A: Physicochemical and Engineering Aspects*, 225(1–3), 1–24.
- Renkema, W., & Rossen, W. (2007). Success of SAG Foam Processes in Heterogeneous Reservoirs. Presented at the IPTC 2007: International Petroleum Technology Conference.
- Rossen, W. R., Venkatraman, A., Johns, R. T., Kibodeaux, K. R., Lai, H., & Tehrani, N. M. (2011). Fractional Flow Theory Applicable to Non-Newtonian Behavior in EOR Processes. *Transport in Porous Media*, 89(2), 213–236.
- Rossen, W.R. (2013). Numerical Challenges in Foam Simulation: A Review. In *SPE-166232-MS*. SPE: Society of Petroleum Engineers.
- Reynolds, C., & Krevor, S. (2015). Characterizing Flow Behavior for Gas Injection: Relative Permeability of

BIBLIOGRAPHY

- CO₂-brine and N₂-water in Heterogeneous Rocks. *Water Resources Research*, 51(12), 9464–9489.
- Rossen, W.R. and Boeije, C. S., "Fitting Foam-simulation-model Parameters to Data: II. Surfactant-alternating-gas Foam Applications," *SPE Reservoir Evaluation and Engineering*, 18(2), 273-283 (2015).
- Rodríguez de Castro, A., Shokri, N., Karadimitriou, N., Oostrom, M., & Joekar-Niasar, V. (2015). Experimental Study on Nonmonotonicity of Capillary Desaturation Curves in a 2D pore network. *Water Resources Research*, 51(10), 8517–8528.
- Rognmo, A. U., Fredriksen, S. B., Alcorn, Z. P., Sharma, M., Føyen, T., Eide, Ø., ... & Fernø, M. (2018). Pore-to-Core EOR Upscaling for CO₂-foam for CCUS. In *SPE Europec featured at 80th EAGE Conference and Exhibition*. Society of Petroleum Engineers.
- Ren, B., & Duncan, I. J. (2019). Reservoir Simulation of Carbon Storage Associated with CO₂ EOR in Residual Oil Zones, San Andres formation of West Texas, Permian Basin, USA. *Energy*, 167, 391-401.
- Stone, H. (1970). Probability model for Estimating Three-Phase Relative Permeability. *Journal of Petroleum Technology*, 22(2), 214–218.
- Stone, H. (1973). Estimation of Three-Phase Relative Permeability and Residual Oil Data. *Journal of Canadian Petroleum Technology*, 12(4).
- Stahl, C. R., Gibson, M. A., & Knudsen, C. W. (1987). U.S. Patent No. 4,694,907..
- Stahl, Charles R., Michael A. Gibson, & Christian W. Knudsen (1987). "Thermally-enhanced oil recovery method and apparatus." Washington, DC: U.S. Patent 4,694,907.
- Schramm, L. L., & Novosad, J. J. (1990). Micro-Visualization of Foam Interactions with a Crude Oil. *Colloids and Surfaces* 46 (1):21–43.
- Schramm, L. L., & Novosad, J. J. (1992). The Destabilization of Foams for Improved Oil Recovery by Crude Oils: Effect of the Nature of the Oil." *Enhanced Oil Recovery* 7 (1):77–90.
- Sanchez, J., & Hazlett, R. (1992). Foam Flow through an Oil-wet Porous Medium: a Laboratory Study. *SPE Reservoir Engineering*, 7(1), 91–97.
- Schramm, L. L. (1994). Foams: Fundamentals and Applications in the Petroleum Industry. In Comstock M. Joan (Ed.) (Vol. 242, pp. i–vii). *American Chemical Society*.
- Schramm, L.L. & Wassmuth, F. (1994). Foams: Basic Principles. Foams: Fundamentals and Applications in the Petroleum Industry, L.L. Schramm ed., 3-45. Washington, DC: *Advances in Chemistry Series* 242, American Chemical Soc.
- Shen, C., Nguyen, Q. P., Huh, C., & Rossen, W. R. (2006). Does Polymer Stabilize Foam in Porous Media? In *SPE-99796-MS. SPE: Society of Petroleum Engineers*.
- Sheng, J. (2010). *Modern Chemical Enhanced Oil Recovery: Theory and Practice*. Gulf Professional Publishing.
- Smoller, J. (2012). Shock Waves and Reaction-Diffusion Equations (Vol. 258). *Springer Science & Business Media*.
- Shah, D. O. (Ed.). (2012). Improved Oil Recovery by Surfactant and Polymer Flooding. Elsevier.
- Spirov, P., Rudyk, S., & Khan, A. (2012). Foam Assisted WAG, Snorre Revisit with New Foam Screening Model. Society of Petroleum Engineers.
- Simjoo, M., & Zitha, P. L. J. (2013). Effects of Oil on Foam Generation and Propagation in Porous Media. In *SPE-165271-MS. SPE: Society of Petroleum Engineers*.

BIBLIOGRAPHY

- Simjoo, M., Dong, Y., Andrianov, A., Talanana, M., & Zitha, P. (2013). CT Scan Study of Immiscible Foam Flow in Porous Media for Enhancing Oil Recovery. *Industrial & Engineering Chemistry Research*, 52(18), 6221–6233.
- Sharma, M., Alcorn, Z. P., Fredriksen, S., Fernø, M., & Graue, A. (2017). Numerical Modelling Study for Designing CO₂-Foam Field Pilot. In *IOR 2017-19th European Symposium on Improved Oil Recovery*.
- Shah, S. Y., Wolf, K.-H., Pilus, R. M., & Rossen, W. R. (2018). Foam Generation by Capillary Snap-off in Flow across a Sharp Permeability Transition. Presented at the *SPE Improved Oil Recovery Conference, Society of Petroleum Engineers*.
- Schramm, L. L., & Novosad, J. J. (1990). Micro-visualization of Foam Interactions with a Crude Oil. *Colloids and Surfaces*, 46(1), 21–43.
- Shah, S. Y., Wolf, K.-H., Pilus, R. M., & Rossen, W. R. (2018). Foam Generation by Capillary Snap-Off in Flow Across a Sharp Permeability Transition. Presented at the SPE Improved Oil Recovery Conference, Society of Petroleum Engineers.
- Thom, R., & Zeeman, E. (1974). Catastrophe Theory: its Present State and Future Perspectives. *Dynamical Systems-Warwick*, (468), 366.
- Tsang, Y. (1992). Usage of “Equivalent Apertures” for Rock Fractures as Derived from Hydraulic and Tracer Tests. *Water Resources Research*, 28(5), 1451–1455.
- Tanzil, D., Hirasaki, G. J., & Miller, C. A. (2000). Mobility of Foam in Heterogeneous Media: Flow Parallel and Perpendicular to Stratification. In *SPE Annual Technical Conference and Exhibition*. Society of Petroleum Engineers.
- Tang, G. Q., & Kovscek, A. R. (2006). Trapped Gas Fraction during Steady-state Foam Flow. *Transport in porous media*, 65(2), 287-307.
- Tang, J., Ansari, M. N. & Rossen, W. R. (2016). Modeling the Effect of Oil on Foam for EOR. *XV ECMOR EAGE*, Amsterdam, the Netherlands.
- Tang, J., Vincent-Bonnieu, S., & Rossen, W. R. (2017). Effect of Oil on Steady-State Foam Flow Regimes in Porous Media. *EAGE IOR*, Stavanger, Norway.
- Tang, J., Vincent-Bonnieu, S., & Rossen, W. (2018). Experimental Investigation of the Effect of Oil on Steady-state Foam Flow in Porous Media. *SPE Journal*.
- Tang, J., Ansari, M. N., & Rossen, W. R. (2019). Quantitative Modeling of the Effect of Oil on Foam for Enhanced Oil Recovery. *SPE Journal*.
- U.S. Department of Energy (2016). Enhanced Oil Recovery. At <https://www.energy.gov/fe/science-innovation/oil-gas-research/enhanced-oil-recovery>.
- Van der Waals, J. D. (1910). The equation of state for gases and liquids. *Nobel lectures in Physics*, 1, 254.
- van Golf-Racht, T. D. (1982). *Fundamentals of Fractured Reservoir Engineering* (Vol. 12). Elsevier.
- Van Bergen, F., Gale, J., Damen, K., & Wildenborg, A. (2004). Worldwide Selection of Early Opportunities for CO₂-Enhanced Oil Recovery and CO₂-enhanced Coal Bed Methane Production. *Energy*, 29(9–10), 1611–1621.
- Wooding, R., & Morel-Seytoux, H. J. (1976). Multiphase Fluid Flow through Porous Media. *Annual Review of Fluid Mechanics*, 8(1), 233–274.
- Wilkinson, D. (1984). Percolation Model of Immiscible Displacement in the Presence of Buoyancy Forces. *Phys.*

BIBLIOGRAPHY

- Rev. A*, 30(1), 520–531.
- Weaire, D. L., & Hutzler, S. (2001). *The physics of foams*. Oxford University Press.
- Wiggins, S. (2013). *Global Bifurcations and Chaos: Analytical Methods*. Springer New York.
- Xu, Q., & Rossen, W. R. (2003). Effective Viscosity of Foam in Periodically Constricted Tubes. *Colloids and Surfaces A: Physicochemical and Engineering Aspects* 216 (1):175–94.
- You, K., DiCarlo, D., & Flemings, P. B. (2015). Quantifying Hydrate Solidification Front Advancing Using Method of Characteristics. *Journal of Geophysical Research: Solid Earth*, 120(10), 6681–6697.
- Yeganeh, M., Hegner, J., Lewandowski, E., Mohan, A., Lake, L. W., Cherney, D., ... & Jaishankar, A. (2016). Capillary Desaturation Curve Fundamentals. Presented at the SPE Improved Oil Recovery Conference, SPE-179574-MS.
- Zeeman, E. C. (1977). *Catastrophe Theory: Selected Papers, 1972–1977*. Addison-Wesley.
- Zhou, Z. H., & Rossen, W. R. (1994). Applying Fractional-Flow Theory to Foams for Diversion in Matrix Acidization. *SPE Production & Facilities*, 9(01), 29-35.
- Zhou, Z., & Rossen, W. R. (1995). Applying Fractional-flow Theory to Foam Processes at the “Limiting Capillary Pressure.” *SPE Advanced Technology Series*, 3(1), 154–162.
- Zimmerman, R. W., & Bodvarsson, G. S. (1996). Hydraulic Conductivity of Rock Fractures. *Transport in Porous Media*, 23(1), 1–30.
- Zeng, Y., Muthuswamy, A., Ma, K., Wang, L., Farajzadeh, R., Puerto, M., & Hirasaki, G. J. (2016). Insights on Foam Transport from a Texture-Implicit Local-Equilibrium Model with an Improved Parameter Estimation Algorithm. *Industrial & Engineering Chemistry Research*, 55(28), 7819–7829.
- Zuloaga, P., Yu, W., Miao, J., & Sepehrnoori, K. (2017). Performance Evaluation of CO₂ Huff-n-Puff and Continuous CO₂ Injection in Tight Oil Reservoirs. *Energy*, 134, 181–192.

IMPLICI-TEXTURE FOAM MODEL – STARS

The widely used STARS foam model (Computer Modeling Group, 2015) includes two algorithms to represent the influence of oil on foam: the wet-foam model and dry-out model. More details pertaining these two models are provided here.

Wet-foam model

In this model, it is assumed that the presence of foam affects the relative permeability of gas, but not those for water or oil. In the model, foam modifies the foam-free relative permeability of gas k_{rg}^0 by multiplying a mobility factor, FM :

$$k_{rg}^f = k_{rg}^0 \cdot FM, \dots\dots\dots (A-1)$$

where k_{rg}^f is the effective gas relative permeability with foam. A smaller value of FM indicates stronger foam, while FM equal to 1 means no foam exists.

Mobility factor FM is given by **Eq. A-2**; it depends on a series of functions, F_1, F_2, F_3 , etc., reflecting the dependence of foam on surfactant concentration, water saturation, oil saturation, capillary number, oil composition and salinity, respectively (Cheng et al., 2000; Computer Modeling Group, 2015):

$$FM = \frac{1}{1 + fmmob \cdot F_1 \cdot F_2 \cdot F_3 \cdot F_4 \cdot F_5 \cdot F_6 \dots}, \dots\dots\dots (A-2)$$

where parameter $fmmob$ is the reference mobility reduction factor in a situation where all conditions yield maximum foam strength. The factors F_i are given different subscripts in different references.

We consider the water-saturation-dependent function F_2 and the oil-dependent function F_3 given by:

$$F_2 = 0.5 + \frac{\arctan(epdry(S_w - fmdry))}{\pi}, \dots\dots\dots (A-3)$$

$$F_3 = \begin{cases} 1 & S_o \leq floil \\ \left(\frac{fmoil - S_o}{fmoil - floil} \right)^{epoil} & floil < S_o < fmoil \\ 0 & fmoil \leq S_o \leq 1 - S_{wc} - S_{gr} \end{cases} \dots\dots\dots (A-4)$$

An abrupt transition between the low- and high-quality regimes corresponds to a large value of *epdry*. **Table A-1** gives the definitions of the parameters in **Eqs. A-3** and **A-4**. We use Corey relations for the foam-free relative permeabilities for water, oil and gas:

$$k_{rw} = k_{rw}^o \left(\frac{S_w - S_{wc}}{1 - S_{wc} - S_{or} - S_{gr}} \right)^{n_w} \dots\dots\dots (A-5)$$

$$k_{ro} = k_{ro}^o \left(\frac{S_o - S_{or}}{1 - S_{wc} - S_{or} - S_{gr}} \right)^{n_o} \dots\dots\dots (A-6)$$

$$k_{rg} = k_{rg}^o \left(\frac{S_g - S_{gr}}{1 - S_{wc} - S_{or} - S_{gr}} \right)^{n_g} \dots\dots\dots (A-7)$$

where k_{rw}^o , k_{ro}^o and k_{rg}^o are each the end-point relative permeability and n_w , n_o and n_g the Corey exponent for the given phase. The larger the Corey exponent of a given phase, the more wetting it is to rock.

Table A-1 An overview of foam-simulation-parameter definitions

Parameters	Definition
<i>fmmob</i>	Reference-mobility-reduction factor corresponding to maximum foam strength
<i>fmdry</i>	Limiting water saturation, around which foam collapses, for wet-foam and dry-out models, respectively. The value of <i>sfdry</i> is not a fixed constant but is instead a function of oil saturation.
<i>epdry</i>	Parameter determining how abruptly gas mobility changes for water saturation near <i>fmdry</i> or <i>sfdry</i> for wet-foam and dry-out models, respectively.
<i>fmoil</i>	Upper-limiting oil saturation, greater than which foam collapses completely for wet-foam and dry-out models, respectively.
<i>floil</i>	Lower-limiting oil saturation, lower than which oil has no detrimental effect on foam for wet-foam and dry-out models, respectively.
<i>epoil</i>	Exponent for oil effect for wet-foam and dry-out models, respectively.

Table A-2 An overview of STARS foam model parameters used

Foam model parameters			Corey-relation parameters								
<i>fmmob</i>	<i>fmdry/sfdry</i>	<i>epdry/sfbet</i>	k_{rw}^o	k_{ro}^o	k_{rg}^o	n_w	n_o	n_g	S_{wc}	S_{or}	S_{gr}
54000	0.316	6000	0.20	0.50	0.94	4.2	2.0	1.3	0.2	0.1	0.2
Rock & fluids properties											
D_w	D_o	D_g	k (D)	ϕ	$\mu_w (Pa \cdot s)$	$\mu_o (Pa \cdot s)$	$\mu_g (Pa \cdot s)$				
3	3	3	1.3	0.3	7.00E-04	5.00E-03	2.07E-05				

Table A-2 summarizes all the model parameter values examined except for the oil-related parameters specified in each figure in the text. The same parameter values are used throughout Chapter 2 unless otherwise specified.

Dry-out model

The form of the dry-out model is similar to the wet-foam model, except that the limiting water saturation is no longer a constant. Here, we consider the dry-out and wet-foam models for oil and foam separately, while they can be used together in the STARS model. Therefore, here for the dry-out model FM is given by

$$FM = \frac{1}{1 + fmmob \cdot F_7} \dots\dots\dots (A-8)$$

where F_7 is a water-saturation-dependent function.

$$F_7 = 0.5 + \frac{\arctan(sfbet(S_w - sfdry))}{\pi} \dots\dots\dots (A-9)$$

Parameters $sfbet$ and $sfdry$ play the roles of $epdry$ and $fmdry$ in the wet-foam model, respectively, but limiting water saturation $sfdry$ in the dry-out model is scaled by a series of functions accounting for the impacts of surfactant concentration, oil saturation, salinity and capillary number, represented respectively with symbols G_1 , G_2 , G_3 and G_4 . Here we consider only the effect of oil saturation, reflected in G_2 , and given by

$$G_2 = \begin{cases} 0 & S_o \leq sloil \\ \left(\frac{S_o - sloil}{sfoil - sloil} \right)^{efoil} & sloil < S_o < sfoil \\ 1 & sfoil \leq S_o \leq 1 - S_{wc} - S_{gr} \end{cases} \dots\dots\dots (A-10)$$

where the upper-limiting oil saturation $sfoil$ and lower-limiting oil saturation $sloil$ play similar roles to $fmoil$ and $floil$, respectively, in the wet-foam model. The original, oil-free value of the limiting water saturation $sfdry$ is then rescaled by

$$[(1 - sfdry) \cdot G_2 + sfdry] \rightarrow sfdry \dots\dots\dots (A-11)$$

If S_o is less than $sloil$, $G_2 = 0$ and oil has no detrimental effect on foam. The limiting water saturation, $sfdry$, is then equal to its oil-free value. If S_o is larger than $sfoil$, $G_2 = 1$ and $sfdry = 1$. If the transition between regimes is abrupt ($sfbet$ sufficiently large), foam collapses completely at all water saturations. For S_o between these two values, G_2 lies in between 0 and 1, and $sfdry$ takes a value between its oil-free value and 1.

Substituting the limiting water saturation as modified by **Eqs. A-10** and **A-11** into **Eq. A-9** allows one to obtain the mobility factor FM accounting for the effects of oil and water saturations. The Corey relations for foam-free relative permeabilities and the same model parameters as in **Table A-2** are applied in the dry-out model, also with oil-related parameters specified in each figure in the text.

STEADY-STATE DATA ADAPTED FOR MODEL FIT

Following the method of Cheng et al. (2000), we use a contour of fixed $\bar{V}p$ passing through the low- and high-quality regimes to fit S_w^* and $fmmob^*$. The following plots show the contours used in each case. See Appendix C for details of the fitting procedure.

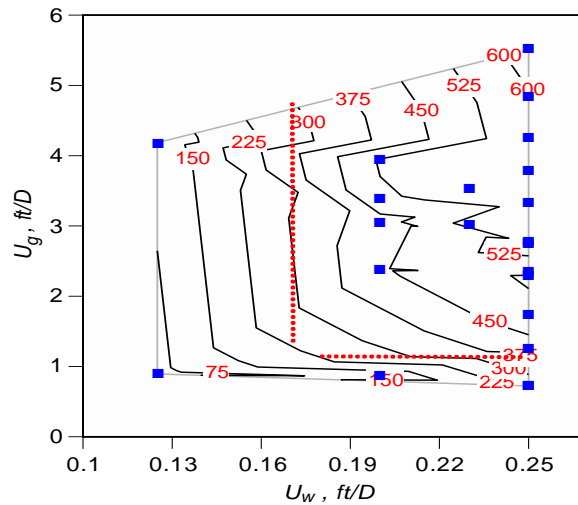


Figure B-1 Expanded view of Fig. 3.5, with representative contour at 300 psi/ft (red dotted lines) used in fitting model to data.

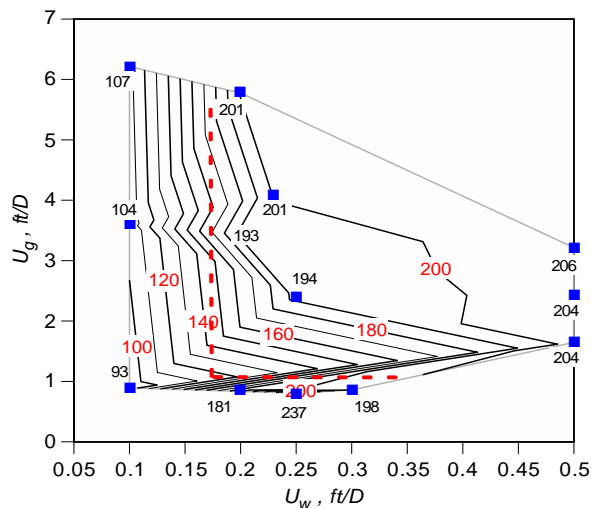


Figure B-2 Expanded view of Fig. 3.6, with representative contour at 160 psi/ft (red dotted lines) used in fitting model to data.

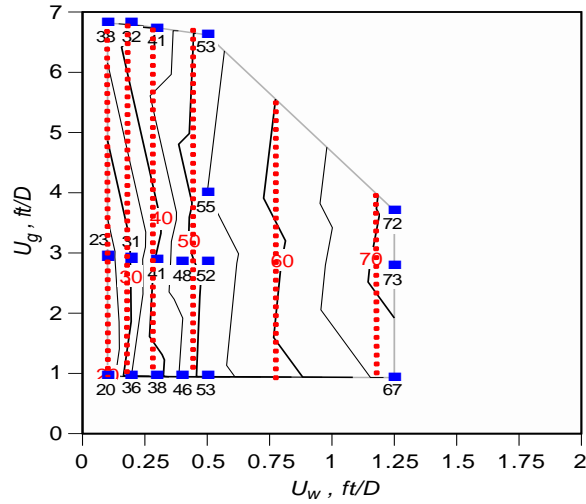


Figure B-3 Contours of fixed $\bar{\nu}_p$ from **Fig. 3.7** used in fitting model to data. Each red dotted line represents a specific $\bar{\nu}_p$ contour across the high-quality-regime data.

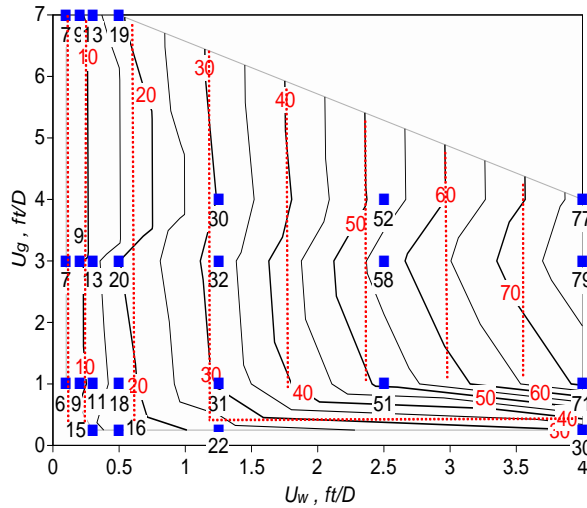


Figure B-4. Contours of fixed $\bar{\nu}_p$ from **Fig. 3.8** used in fitting model to data. Each red dotted line represents a specific $\bar{\nu}_p$ contour across the data in each regime.

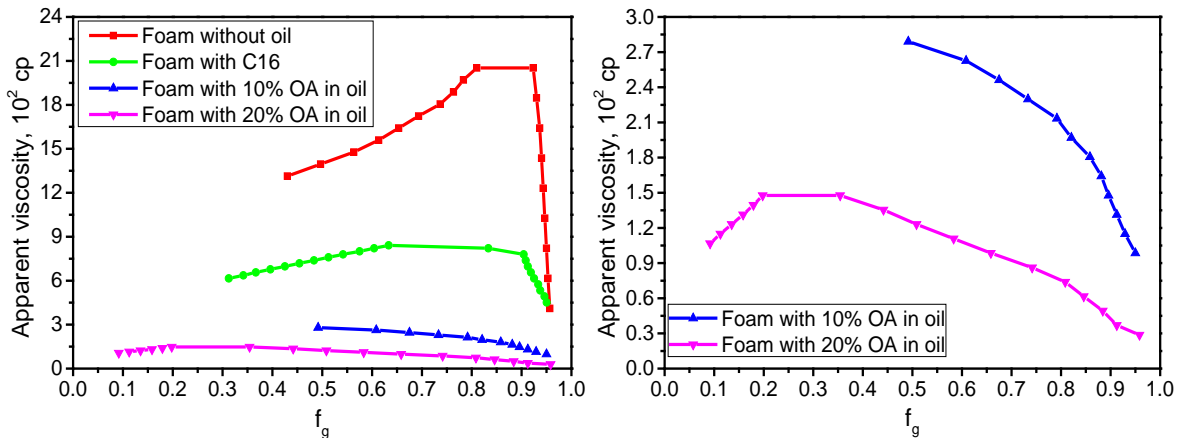


Figure B-5 (Left). Comparison of oil-type effect on local-equilibrium foam strength in terms of single foam-quality scan. The data are adapted from **Figs. 3.5, 3.6, 3.7** and **3.8** by making a diagonal line at fixed $U_i=3$ ft/D.

Figure B-6 (Right). An expanded view of **Fig. B-5** for illustration of foam-quality transition with oleic acid in model oil.

APPENDIX C

FOAM-SIMULATION-PARAMETER FITTING METHOD

The functions examined in the foam model include the following parameters: $fmmob$, $fmdry$ ($sfdry$), $epdry$ ($sfbet$), $epcap$, $fncap$, $fmoil$ ($sfoil$), $fmoil$ ($sfoil$), and $epoil$ ($efoil$). However, owing to absence of oil-saturation data in our experiments, it is not feasible to fit all the oil-related parameters separately. Therefore, five parameters, in total, are fitted in this study: $fmmob$, $fmdry$ ($sfdry$), $epdry$ ($sfbet$), $epcap$ and $fncap$. Comparing $fmmob$ in the absence of oil to that incorporating the effect of oil when foam concurrently flows with oil gives the value of function F_3 . Similarly, comparison of $fmdry$ in the absence of oil and $sfdry$ altered by oil yields the value of function G_2 . The values of F_3 and G_2 , respectively, reflect the effects of oil on foam strength in the low-quality regime and foam stability in the high-quality regime (Eqs. 3.2, 3.4, 3.7 and 3.8).

Reme (1999) and Cheng et al. (2000) have sketched the parameter-fitting procedures for the STARS and UT foam models (Computer Modeling Group 2015; Rossen et al. 1999), respectively, without including the effect of oil. Here we use a method similar to that of Cheng et al. to fit model parameters to data, including the effects of oil on $fmmob$ and $fmdry$ ($sfdry$). Before fitting the parameters, one must specify foam-free relative-permeability functions for each phase. We here use Corey relative-permeability model based on relative-permeability data of Eftekhari and Farajzadeh (2017) for Bentheimer sandstone using the same type of surfactant and same concentration. **Table C-1** summarizes the fluid and transport properties used throughout the parameter-fitting.

Table C-1 Fluid and transport properties in porous media

Quantities	Parameter values
Water viscosity, μ_w	$0.7 \cdot 10^{-3}$ Pa·s
Gas viscosity, μ_g	$2.07 \cdot 10^{-5}$ Pa·s
Oil viscosity, μ_o	$5 \cdot 10^{-3}$ Pa·s
Water relative permeability, $k_{rw}(S_w)$	$0.713 \left(\frac{S_w - 0.135}{0.665 - S_{or}} \right)^{2.46}$
Gas relative permeability $k_{rg}(S_g)$	$0.94 \left(\frac{S_g - 0.2}{0.665 - S_{or}} \right)^{1.3}$
Oil relative permeability $k_{ro}(S_o)$	$0.5 \left(\frac{S_o - S_{or}}{0.665 - S_{or}} \right)^2$
Water-gas surface tension, σ_{wg}	0.03 N/m
Temperature, T	35°C

When oil is present, $S_{or}=0.1$, otherwise, $S_{or}=0$

Specifically, one can fit model parameters to data following the precedure step by step as described below. A major advantage of this method is each step has a clear physical meaning.

Step 1. Draw ∇p contours. For efficiently fitting parameters, one may need to smooth the ∇p contours. Then, pick up one representative ∇p contour and draw a vertical and horizontal straight line, which can best represent the data in the high- and low-quality regimes, respectively, for this contour, as illustrated in **Fig. C-1**.

This approach assumes the ∇p contours in low-quality regime are horizontal. However, in some cases, including this study, ∇p contours in the low-quality regime with or without oil tilt upward with increasing U_w (as in **Figs. 3.5** and **3.6**) (Kim et al. 2005). This means that fitted results could mismatch the low-quality regime data, especially for higher ranges of U_w . However, none of current foam simulation models can capture this behavior in the absence of oil. Therefore, it is necessary to improve current foam models to capture this upward-tilting ∇p trend for effectively fitting low-quality regime. This is beyond the scope of this study. Here we apply horizontal contours to represent low-quality-regime data throughout the model-fitting. **Figs. B-1, B-2, B-3** and **B-4** in Appendix B illustrate the representative contours drawn through data in both regimes in each case.

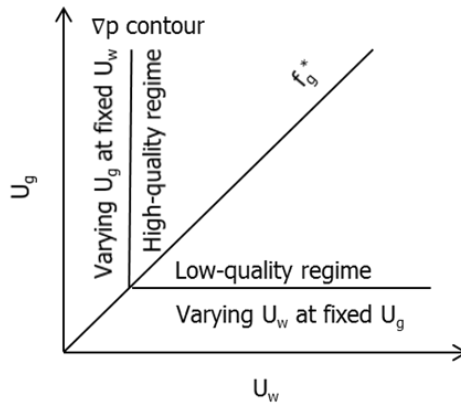


Figure C-1 Schematic of contour treatment in each regime for fitting model parameters to data.(adapted from Cheng et al. (2000)

Step 2. Determine limiting water saturation S_w^* . The vertical line in **Fig. C-1**, representing the high-quality regime data on the representative ∇p contour, corresponds to a specific value of U_w . Applying Darcy’s law for the water phase (**Eq. C-1**) at this value of U_w , along with $k_{rw}(S_w)$ from **Table C-1**, yields the limiting water saturation S_w^* :

$$U_w = \frac{kk_{rw}(S_w^*)}{\mu_w} \nabla p \dots\dots\dots (C-1)$$

Step 3. Calculate reference mobility reduction factor $fmmob^*$ (* denotes the factor without considering shear-thinning). As shown in **Fig. C-1**, the vertical and the horizontal lines intersect at one point, which marks the transition between regimes. Foam quality at this point, defined as $U_g/(U_g+U_w)$ in the absence of oil or $U_g/(U_g+U_w+U_o)$ in the presence of oil, is defined as the transition foam quality f_g^* . Parameter $fmmob^*$ is assumed

to be constant throughout the low-quality regime. Therefore this assumption applies also at f_g^* . Applying Darcy's law to the gas phase (Eq. C-2) at f_g^* using $k_{rg}(S_g)$ from Table C-1 with S_w^* known from previous step gives $fmmob^*$:

$$U_g = \frac{kk_{rg}^0(S_w^*)}{\mu_g} \frac{1}{1 + fmmob^*} \nabla p \dots\dots\dots (C-2)$$

where $k_{rg}^0(S_w^*)$ is the foam-free gas relative permeability at f_g^* , at which S_w^* is already known from step 2. The value of $fmmob^*$ obtained here neglects shear-thinning in the low-quality regime. This is considered in step 7.

Step 4. Set *epdry* to a large value (e.g., 20000). Parameter *epdry* controls the abruptness of foam collapse as S_w decreases towards S_w^* . Consistent with our experimental data, e.g. Fig. 3.5, an abrupt transition is assumed as in the model-fitting procedure of Cheng et al. (2000).

Step 5. Specify a reference capillary number *fmcap*. As shown in Eq. 3.5, no matter what value of *fmcap* is used in models, F_5 must be less than 1 for shear-thinning to have effect. Parameter *fmcap* in this study is calculated using Eq. 3.6, based on a value of ∇p smaller than all measured data in each case.

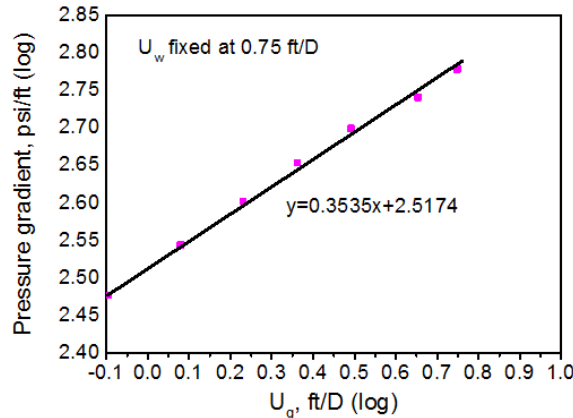


Figure C-2 log-log plot for ∇p v. U_g based on data of Fig. 3.5 at fixed $U_w=0.75$ ft/D.

Step 6. Capture shear-thinning in the low-quality regime through *epcap*. The model proposed by Rossen et al. (1999) characterizes shear-thinning in the low-quality regime via a parameter σ less than 1. The slope of a plot of $\log(\nabla p)$ v. $\log(U_g)$ is σ . Parameter *epcap* here can be obtained through Eq. C-3:

$$\sigma \cong \frac{1}{1 + epcap} \dots\dots\dots (C-3)$$

Plotting $\log(\nabla p)$ v. $\log(U_g)$ based on data of Fig. 3.5 at $U_w=0.75$ ft/D, as illustrated in Fig. C-2, gives a slope of 0.3535. Then, *epcap* is 1.83 from Eq. C-3.

Step 7. Adjust the reference mobility-reduction factor $fmmob$ accounting for shear-thinning. When considering shear-thinning in the low-quality regime, the value of $fmmob^*$ obtained above is the mobility reduction that incorporates the effect of shear thinning. Model parameter $fmmob$ can be obtained from $fmmob^*$ through **Eq. C-4**, using $fmcap$ and $epcap$ obtained in steps 5 and 6, based on ∇p of the representative ∇p contour:

$$fmmob^* = fmmob \cdot \left(\frac{fmcap}{N_{ca}} \right)^{epcap} \dots\dots\dots (C-4)$$

where N_{ca} is calculated from **Eq. 3.6** using the value of ∇p from the characteristic ∇p contours.

Step 8. Fit the effect of oil through functions F_3 and G_2 . As shown in **Figs. 3.6, 3.7** and **3.8**, oil impacts both high- and low-quality regimes, respectively, through its effect on S_w^* and reference-mobility-reduction factor $fmmob$ in each regime. Experimental data here suggest that oil has different magnitudes of effects on those two regimes, with the high-quality regime more susceptible to its influence. Therefore, oil-related parameters should be fitted separately based on data in each regime.

Specifically, when oil is present, steps 2 and 3 give S_w^* and $fmmob^*$, each of which now incorporates the effect of oil. Based on the fitted values of S_w^* and $fmmob^*$ in **Fig. 3.5** obtained in the absence of oil, applying **Eq. 3.8** yields the value of G_2 in the dryout model, accounting for the overall effect of oil on the S_w^* . Parameter $fmmob^*$ obtained in the presence of oil, divided by the value of $fmmob^*$ obtained in the absence of oil, gives the value of F_3 in wet-foam model, accounting for the effect of oil on gas mobility reduction in the low-quality regime. However, the non-linearly distributed contours in the high-quality regime of **Fig. 3.7** and **Fig. 3.8** suggest that S_w^* is not fixed throughout the high-quality regime, but varies with superficial velocity. Therefore, in order to fit the high-quality-regime data in presence of oil, one may have to fit S_w^* corresponding to each ∇p contour in the high-quality regime, instead of just fitting one representative ∇p contour. Nonlinear spacing of contours in the low-quality regime is fit by adjusting $epcap$ for oil, but observed behavior may reflect both shear-thinning and the effect of oil. The fit to $epcap$ in the absence of oil may not apply when oil flows with foam.

Step 9. Plot fitted results using model parameter values and compare to data. The experimental data demonstrate clearly that oil shifts both regimes. However, the modeling study of Tang et al. (2016) suggests that oil in the wet-foam model affects only the low-quality regime, while in the dryout model, it shifts only the high-quality regime. Therefore, the wet-foam model and dryout model are both needed to represent low- and high-quality-regime data.

FOAM MODEL FOR THEORETICAL ANALYSIS OF FOAM-OIL DISPLACEMENT

The widely used foam model STARS (Computer Modeling Group, 2015), is representative of implicit-texture models for foam. There are two algorithms in the STARS model to represent the effect of oil on foam: the “wet-foam” and the “dry-out” algorithms. We apply here the wet-foam algorithm, with its two key functions on the effects of water (S_w) and oil (S_o) saturations on foam.

Foam in the model lowers gas mobility by reducing foam-free gas relative permeability from its value in **Eq. 4.5**, through a mobility reduction factor FM :

$$k_{rg}^f = k_{rg} \cdot FM, \dots\dots\dots (D-1)$$

where superscript f denotes the value with foam, with k_{rg} given by **Eq. 4.5**.

FM comprises a series of functions F_i ($i=1, 2, 3\dots$), accounting for impacts of a variety of factors on foam, e.g. surfactant concentration, water saturation, oil saturation, oil composition, shear-thinning behavior and salinity:

$$FM = \frac{1}{1 + fmmob \cdot F_1 \cdot F_2 \cdot F_3 \cdot F_4 \cdot F_5 \cdot F_6}, \dots\dots\dots (D-2)$$

where $fmmob$ is the maximum attainable reduction in gas mobility, referred to as the reference gas-mobility-reduction factor. This factor dominates foam stability in the low-quality regime shown in **Figs. 4.1** and **4.2**. In our analysis, two key functions, F_2 , a function of S_w , and F_3 , a function of S_o , are considered, to describe the impact of water and oil saturations. The factor FM is thus a function only of (S_w, S_o).

The water-saturation-dependent function, F_2 in the wet-foam representation is defined in STARS as follows:

$$F_2 = 0.5 + \frac{\arctan[epdry(S_w - fmdry)]}{\pi}, \dots\dots\dots (D-3)$$

where $fmdry$ represents the limiting water saturation S_w^* around which foam collapses; the abruptness of foam collapse is controlled by an adjustable parameter $epdry$. As experimentally supported by the sharp transition between the two regimes as in **Figs. 4.1** and **4.2**, a large value of $epdry$ is assumed, that makes an abrupt foam collapse at S_w around $fmdry$.

Mathematically, to simplify the calculation of derivatives of fractional flows in **Eq. 4.11**, the F_2 in **Eq. D-3** is approximated and replaced here by a fifth-order polynomial function:

$$p(x) = a + bx + cx^2 + dx^3 + ex^4 + fx^5, \dots\dots\dots (D-4)$$

where a, b, c, d, e and f are coefficients. Variable x is a function of S_w , given by:

$$x = 0.2 \times \text{epdry}(S_w - \text{fmdry}), \dots\dots\dots (D-5)$$

where parameters *epdry* and *fmdry* here have the same definitions as them in **Eq. D-3**.

Equation D-4 must satisfy the following six conditions, with which the six coefficients in **Eq. D-4** can be solved:

$$\begin{cases} p(-1) = 0; & p(1) = 1; \\ p'(-1) = 0; & p'(1) = 0; \\ p''(-1) = 0; & p''(1) = 0. \end{cases} \dots\dots\dots (D-6)$$

Equation D-3, for the impact of S_w on foam, is then replaced by the following polynomial function:

$$\begin{cases} p(x) = 0 & x < -1 \\ p(x) = \frac{1 + 1.875x - 1.25x^3 + 0.375x^5}{2} & -1 \leq x \leq 1. \\ p(x) = 1 & x > 1 \end{cases} \dots\dots\dots (D-7)$$

Figure D-1 shows the difference between F_2 in **Eq. D-3** and its polynomial approximation $p(x)$ in **Eq. D-7** using the parameter values in **Table D-1**, with respect to S_w . In a very narrow range of S_w around *fmdry*, the width of which depends on the value of *epdry* (**Eq. D-5**), $p(x)$ in **Eq. D-7** changes more abruptly than F_2 in **Eq. D-3**, as seen from the expanded view in **Fig. D-1**. The difference between the two functions is negligibly small, confirming that the polynomial function of **Eq. D-7** represents the arctangent function of **Eq. D-3** for the impact of S_w on foam. One difference is that foam collapses completely in this approximation at $S_w = \{ \text{fmdry} - [1 / (0.2 \times \text{epdry})] \}$, whereas foam does not collapse completely at any value of S_w in **Eq. D-3**.

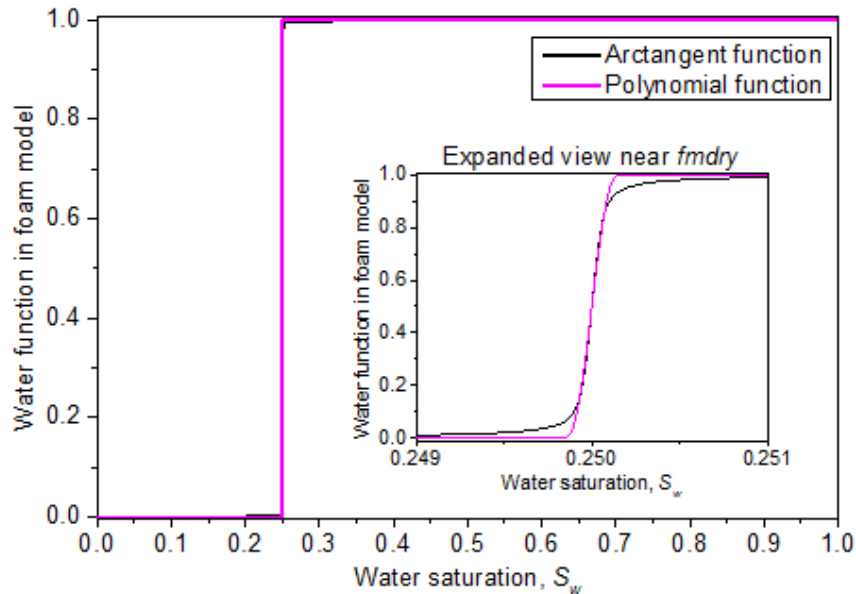


Figure D-1 Comparison between the arctangent function F_2 in **Eq. D-3** and polynomial approximation $p(x)$ in **Eq. D-7**. Parameters are referred to **Table D-1**.

The oil-saturation-dependent function F_3 in the wet-foam representation is defined as follows:

$$F_3 = \begin{cases} 1 & S_{or} \leq S_o \leq floil \\ \left(\frac{fmoil - S_o}{fmoil - floil} \right)^{epoil} & floil < S_o < fmoil \\ 0 & fmoil \leq S_o \leq 1 - S_{wc} - S_{gr} \end{cases} \dots\dots\dots (D-8)$$

where *epoil* is the oil exponent, and *fmoil* and *floil* are the upper- and lower-limiting oil saturations, respectively, between which the effect of S_o on foam is bounded. For $S_{or} \leq S_o \leq floil$, oil has no impact on foam, whereas, for $floil < S_o < fmoil$, oil destabilizes foam in a non-linear way. For $fmoil \leq S_o \leq 1 - S_{wc} - S_{gr}$, oil destroys foam completely.

Table D-1 provides the values of all model parameters used for Corey-type relative-permeability and foam-property interpolations. The same parameter values are utilized throughout all the cases presented, except those specified in **Table 4.1**. Saturations and saturation-related factors in **Figs. 4.3 — 4.15**, and **Figs. 4.18 — 4.22**, i.e. S_j , *fmdry*, *fmoil* and *floil*, are all normalized with respect to the total movable saturations through **Eq. 4.9**.

Table D-1. An overview of parameter values implemented in the Corey-type relative-permeability model and foam model.

Corey parameters and fluid properties						Foam model parameters		
k_{rw}^o	k_{ro}^o	k_{rg}^o	n_w	n_o	n_g	<i>fmmob</i>	<i>fmdry</i>	<i>epdry</i>
1	1	1	2	2	2	2000	0.3	32000
S_{wc}	S_{or}	S_{gr}	μ_w, cP	μ_o, cP	μ_g, cP	<i>fmoil</i>	<i>floil</i>	<i>epoil</i>
0.1	0.1	0	1	5	0.01	0.3	0.1	3

Note that superscript o represents the endpoint relative permeability of phases. Saturations and saturation-related factors shown here are all original values without being normalized.

FOAM MODEL FOR THEORETICAL ANALYSIS OF MULTIPLE STATES

The implicit-texture (IT) foam model in the STARS simulator includes two algorithms describing the effect of oil on foam (Computer Modeling Group 2015): the “wet-foam” representation and the “dry-out” representation. The modeling study of Tang et al. (2016) reveals that the two representations each describes the effect of oil on one foam regimes. The wet-foam representation captures the effect of oil only on the low-quality regime, while the dry-out representation depicts the effect of oil on the high-quality regime.

Below is a description of the wet-foam representation implemented in this study. The effect of foam on gas mobility, as defined in the model, is represented through its effect on gas relative permeability, k_{rg}^f . The dry-out representation (Computer Modeling Group 2015; Tang et al., 2016) also predicts a fold in the surface such as in **Fig. 5.8**. We believe displacements represented by that model would show similar phenomena to those investigated here.

Wet-foam representation

Foam in the STARS model scales gas mobility by modifying k_{rg} , the foam-free gas relative permeability, through a mobility-reduction factor FM :

$$k_{rg}^f = k_{rg} \cdot FM, \dots\dots\dots (E-1)$$

where superscript f denotes the presence of foam, respectively. k_{rg}^f with foam is usually referred to as effective gas relative permeability. The mobility scaling factor FM accounts for the effects of a series of physical factors on foam described by functions F_n ($n = 1, 2, 3\dots$), e.g. surfactant concentration, water saturation, oil saturation, capillary number, shear-thinning, or salinity:

$$FM = \frac{1}{1 + fmmob \cdot F_1 \cdot F_2 \cdot F_3 \cdot F_4 \cdot F_5 \cdot F_6 \dots}, \dots\dots\dots (E-2)$$

where $fmmob$ is the reference mobility-reduction factor, representing the maximum attainable gas mobility reduction.

This study considers two major factors dominating local-equilibrium foam flow behavior, water (S_w) and oil (S_o) saturations. The effect of S_w is captured through the function F_2 :

$$F_2 = 0.5 + \frac{\arctan[epdry(S_w - fmdry)]}{\pi}, \dots\dots\dots (E-3)$$

where $fmdry$ is the limiting water saturation, physically denoted as S_w^* (Rossen and Zhou, 1995), the water saturation around which foam collapses. Parameter $epdry$ determines the abruptness of foam collapse in a narrow range of S_w around $fmdry$. In the wet-foam model, $fmdry$ is a fixed constant, which is usually true in the absence of oil.

Oil here does not have an impact on foam stability (i.e., on $fmdry$), which dominates the high-quality regime. It affects foam only in the low-quality regime, through its effect on $fmmob$:

$$F_3 = \begin{cases} 1 & S_{or} \leq S_o \leq floil \\ \left(\frac{fmoil - S_o}{fmoil - floil} \right)^{epoil} & floil \leq S_o \leq fmoil \\ 0 & fmoil \leq S_o \leq 1 - S_{wc} - S_{gr} \end{cases}, \dots\dots\dots (E-4)$$

where S_{wc} , S_{or} and S_{gr} represent the residual saturations of water, oil and gas, respectively. **Equation E-4** is a piecewise smooth function depicting the effect of S_o through three factors $fmoil$, $floil$ and $epoil$. The factors $fmoil$ and $floil$ denote the upper- and lower-limiting values of S_o for stable foam. For $S_o > fmoil$, foam is killed completely ($F_3=0$). For S_o less than $floil$, oil has no effect on foam ($F_3=1$). For $floil < S_o < fmoil$, oil destabilizes foam in a non-linear manner.

Table E-1 summarizes the model parameters implemented throughout the study. Note that all of our illustrations in ternary diagrams, i.e. **Figs. 5.7, 5.9, 5.10, 5.13** and **5.15**, are plotted using normalized saturations rescaled as follows:

$$S_j = \frac{S_{j,a} - S_{jr}}{1 - S_{wc} - S_{or} - S_{gr}}, \dots\dots\dots (E-5)$$

where $S_{j,a}$ with subscript a denotes the absolute saturation of phase j and S_{jr} represents the residual saturation of phase j . Residual saturations of phase j , i.e. S_{wc} , S_{or} and S_{gr} , are not shown in the illustrations.

Table E-1 Model parameter values (without being normalized) used for Corey-type relative-permeability and foam interpolations.

Corey parameters and fluid properties						Foam model parameters		
k_{rw}^o	k_{rg}^o	k_{ro}^o	n_w	n_g	n_o	$fmmob$	$fmdry$	$epdry$
0.20	0.94	0.5	4.2	1.3	2.0	54000	0.316	6000
S_{wc}	S_{gr}	S_{or}	$\mu_w, Pa \cdot s$	$\mu_g, Pa \cdot s$	$\mu_o, Pa \cdot s$	$fmoil$	$floil$	$epoil$
0.2	0.2	0.1	$7 \cdot 10^{-4}$	$2.07 \cdot 10^{-5}$	$5 \cdot 10^{-3}$	0.2	0.12	4

Figure E-1 illustrates gas relative-permeability curves on semi-log scale using parameters in **Table E-1**, as described by the wet-foam representation above. Without foam, k_{rg} (green curve) is much greater than k_{rw} (dashed blue curve) for a wide range of S_w , indicating a large gas mobility that is usually unfavourable for oil displacements. With foam but without oil, k_{rg}^f (cyan curve) drops down suddenly and drastically, by a factor of

10^4 , within a narrow range of S_w around $fmdry$. The abruptness of the drop depends on the value of $epdry$ in **Eq. E-3**.

In **Fig. E-1** the effect of oil is introduced by fixing the ratio (u_o / u_w) , equivalent to fixing $fmdry$. Note that parameter $fmdry$, around which k_{rg}^f drops abruptly and suddenly, remains independent of the presence of oil and of (u_o / u_w) . The unchanging value of $fmdry$ reflects the fact that the wet-foam representation describes the effect of oil only on the low-quality regime. For $S_w > fmdry$, increasing the ratio (u_o / u_w) at fixed S_w raises S_o , as seen from **Eqs. 5.4** and **5.6**. That means increasingly weaker foam (smaller value of F_3 in **Eq. E-4**), causing k_{rg}^f in **Fig. E-1** to increase nonlinearly. As S_o increases enough to kill foam, k_{rg}^f rises largely because gas mobility is no longer restricted by foam. k_{rg}^f thereafter drops drastically down to zero as S_g approaches its residual saturation.

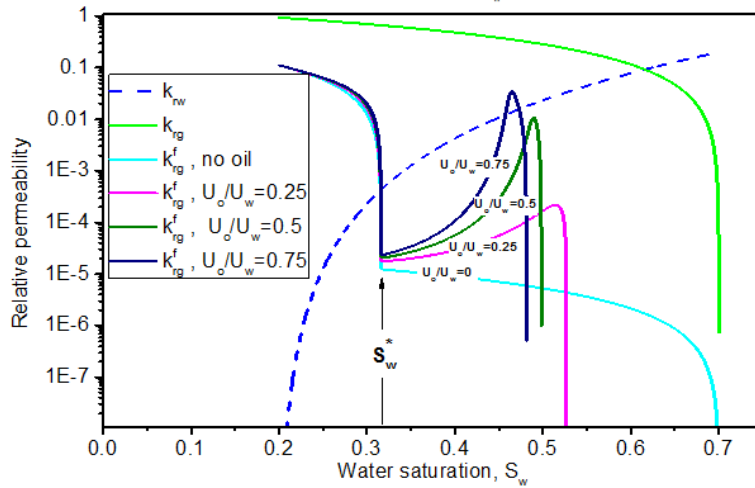


Figure E-1 Gas relative permeability k_{rg}^f with foam, as represented by the wet-foam model. Oil is introduced by fixing various ratios (u_o/u_w) , which is equivalent to fixing (f_o/f_w) . S_o increases with S_w along each curve at a fixed (u_o/u_w) , and the fixed value of S_{gr} corresponds to different values of S_w on the curves, which depend on the values of (u_o/u_w) . k_{rw} and k_{rg} are shown for a comparison with k_{rg}^f . All model parameters used for the illustration are in **Table E-1**.

APPENDIX F

CT IMAGING OF THREE-PHASE SATURATIONS USING DUAL-ENERGY

In our study, we implement 140 kv and 80 kv, denoted as 1 and 2 respectively in the following formulas.

Porosity is measured using single-energy beam 140 kv, calculated as follows:

$$\varphi = \frac{(CT_{wet})_1 - (CT_{dry})_1}{CT_w - CT_a} \dots\dots\dots (F-1)$$

$(CT_{wet})_1$ = CT number of 100% brine saturated (wet) core at 140 kv, HU.

$(CT_{dry})_1$ = CT number of 100% air saturated (dry) core at 140 kv, HU.

CT_w = CT number of brine in bulk at 140 kv, HU.

CT_a = CT number of air in bulk at 140 kv, HU.

Initial state in each experiment we conduct is at waterflood residual oil saturation S_{orw} , which is determined using 140 kv by:

$$S_{orw} = \frac{(CT_{Sorw})_1 - (CT_{wet})_1}{(CT_{oil})_1 - (CT_{wet})_1} \dots\dots\dots (F-2)$$

where:

$(CT_{Sorw})_1$ = CT number of core at S_{orw} at 140 kv, HU.

$(CT_{oil})_1$ = CT number of 100% doped-oil saturated core at 140 kv, HU.

During foam injection with oil, CT attenuation combines the effects of water, oil, gas and rock matrix. For each voxel, the expressions for CT number can be written as follows:

$$(CT_{wog})_1 = (CT_{wet})_1 S_w + (CT_{dry})_1 S_g + (CT_{oil})_1 S_o, \dots\dots\dots (F-3)$$

$$(CT_{wog})_2 = (CT_{wet})_2 S_w + (CT_{dry})_2 S_g + (CT_{oil})_2 S_o, \dots\dots\dots (F-4)$$

$$S_g = 1 - S_w - S_o, \dots\dots\dots (F-5)$$

where:

$(CT_{wog})_1$ = CT number of fluid saturated core involving three phases at 140 kv, HU.

$(CT_{wog})_2$ = CT number of fluid saturated core involving three phases at 80 kv, HU.

$(CT_{wet})_1$ = CT number of 100% brine saturated (wet) core at 140 kv, HU.

$(CT_{wet})_2$ = CT number of 100% brine saturated (wet) core at 80 kv, HU.

$(CT_{dry})_1$ = CT number of 100% gas saturated (dry) core at 140 kv, HU.

$(CT_{dry})_2$ = CT number of 100% gas saturated (dry) core at 80 kv, HU.

$(CT_{oil})_1$ = CT number of 100% doped-oil saturated core at 140 kv, HU.

$(CT_{oil})_2$ = CT number of 100% doped-oil saturated core at 80 kv, HU.

Substituting S_g in **Eq. F-4** into **Eqs. F-2 and F-3**, we solve for expressions for saturations S_o and S_w :

$$S_o = \frac{[(CT_{wog})_1 - (CT_{dry})_1][(CT_{wet})_2 - (CT_{dry})_2] - [(CT_{wog})_2 - (CT_{dry})_2][(CT_{wet})_1 - (CT_{dry})_1]}{[(CT_{oil})_1 - (CT_{dry})_1][(CT_{wet})_2 - (CT_{dry})_2] - [(CT_{oil})_2 - (CT_{dry})_2][(CT_{wet})_1 - (CT_{dry})_1]}, \dots\dots\dots (F-6)$$

$$S_w = \frac{[(CT_{oil})_2 - (CT_{dry})_2][(CT_{wog})_1 - (CT_{dry})_1] - [(CT_{oil})_1 - (CT_{dry})_1][(CT_{wog})_2 - (CT_{dry})_2]}{[(CT_{oil})_2 - (CT_{dry})_2][(CT_{wet})_1 - (CT_{dry})_1] - [(CT_{oil})_1 - (CT_{dry})_1][(CT_{wet})_2 - (CT_{dry})_2]} \dots\dots\dots (F-7)$$

To measure CT_{oil} , one has to disconnect the core from the coreholder, completely dry it in an oven and then re-saturate the core with oil until $S_o = 100\%$. This will unavoidably change the original position of the core where reference CT scans are taken, e.g. CT_{dry} and CT_{wet} . In our CT measurements, to avoid this risk, we estimate CT_{oil} using CT scan of the core at S_{wc} achieved by oil flood, as follows:

$$(CT_{oil})_1 = \frac{(CT_{swc})_1 - (CT_{wet})_1}{1 - S_{wc}}, \dots\dots\dots (F-8)$$

$$(CT_{oil})_2 = \frac{(CT_{swc})_2 - (CT_{wet})_2}{1 - S_{wc}}, \dots\dots\dots (F-9)$$

where S_{wc} obtained by material balance is 0.2 ± 0.02 and:

$(CT_{swc})_1$ = CT number of core at S_{wc} achieved by oil flood at 140 kv, HU.

$(CT_{swc})_2$ = CT number of core at S_{wc} achieved by oil flood at 80 kv, HU.

In our actual calculations of phase saturations, initial state S_{orw} is determined by replacing $(CT_{oil})_1$ in **Eq. F-2** with the right side of **Eq. F-8**. Similarly, S_o and S_w in **Eqs. F-6 and F-7** are finally calculated by replacing $(CT_{oil})_1$ and $(CT_{oil})_2$ with the right sides of **Eqs. F-8 and F-9**, respectively.

MICROFLUIDIC DEVICES IN THE LITERATURE

Figure G-1 shows images of the microfluidic devices from the literature, that were used to obtain the data in Figs. 7.2 and 7.3.

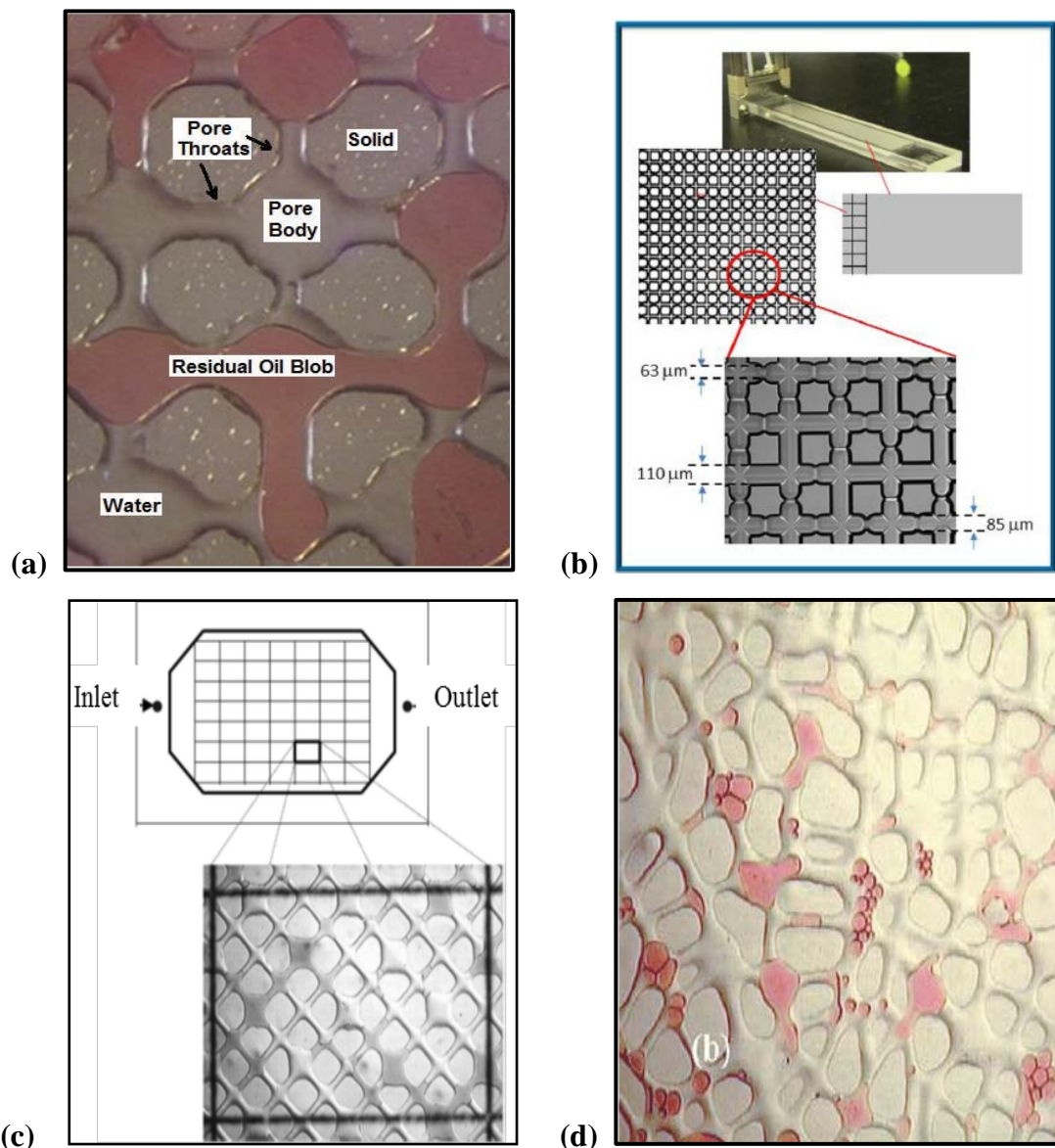


Figure G-1. Pore geometry of the microfluidic devices as used in Figs. 7.2 and 7.3: (a) Ibrahim (2009); (b) Yeganeh et al. (2016); (c) and (d) model A and B, respectively, in Jeong et al. (2003).

SCIENTIFIC CONTRIBUTIONS

Journal Articles:

- **Tang, J.**, Smit, M., Vincent-Bonnieu, S., & Rossen, W. R. (2019). New Capillary Number Definition for Micromodels: the Impact of Pore Microstructure. *Water Resources Research*.
- **Tang, J.**, Ansari, M. N., & Rossen, W. R. (2019). Quantitative Modeling of the Effect of Oil on Foam for Enhanced Oil Recovery. *SPE Journal*.
- **Tang, J.**, Vincent-Bonnieu, S., & Rossen, W. (2018). Experimental Investigation of the Effect of Oil on Steady-State Foam Flow in Porous Media. *SPE Journal*.
- **Tang, J.**, Castañeda, P., Marchesin, D., Rossen, W.R. (2019). Three-Phase Fractional-Flow Theory of Oil Displacement by Foam with Multiple Steady States. To be submitted to journal.
- **Tang, J.**, Castañeda, P., Marchesin, D., Rossen, W.R. (2019). Foam Flow with Oil in Porous Media: Insights from Three-Phase Fractional-Flow Theory. To be submitted to journal.
- **Tang, J.**, Vincent-Bonnieu, S., Rossen, W.R. (2019). CT Coreflood Study of Transient Foam Flow with Oil. To be submitted to journal.
- Chen, L., Zhang, G., Ge, J., Jiang, P., **Tang, J.**, & Liu, Y. (2013). Research of the heavy oil displacement mechanism by using alkaline/surfactant flooding system. *Colloids and Surfaces A: Physicochemical and Engineering Aspects*, 434, 63–71.

Conference Proceedings and Talks:

- **Tang, J.**, Ansari, M. N., & Rossen, W. R. (2016). Modelling the Effect of Oil on Foam for EOR. Presented at the *EAGE IOR 2016 – 15th European Conference on the Mathematics of Enhanced Oil Recovery*, Amsterdam, the Netherlands.
- **Tang, J.**, Vincent-Bonnieu, S., & Rossen, W. R. (2016). The Effect of Oil on Steady-State Foam Stability in Porous Media. Poster Presented at *InterPore conference programs – Interpore Benelux Day*, Venlo, the Netherlands.

SCIENTIFIC CONTRIBUTIONS

- **Tang, J.**, Vincent-Bonnieu, S., & Rossen, W. R. (2017). Effect of Oil on Steady-State Foam Flow Regimes in Porous Media. Presented at the *EAGE IOR 2017 - 19th European Symposium on Improved Oil Recovery*, Stavanger, Norway.
- **Tang, J.**, Vincent-Bonnieu, S., & Rossen, W. R. (2017). Experimental Investigation of the Effect of Oil on Steady-State Foam Flow in Porous Media. Presented at *9th International Conference on Porous Media & Annual Meeting*, Rotterdam, the Netherlands.

ACKNOWLEDGEMENTS

*The true friendship leads us back to the light,
when we are in the darkness.*

Every thesis has a story of both science and life. My story of Ph.D. would never have a beautiful end without the accompany of all individuals over last four years. It is all of you that bring me numerous unforgettable memories during this journey. I'd like to take this opportunity to express my sincere gratitude to all those that help me, support me, and encourage me in my study and daily life.

Prof. **Bill Rossen**, the first one I'd like to thank to. It is my great fortune to have a promotor like you, full of knowledge and enthusiasm. I greatly appreciate your guide in both my study and life. Your training of last four years opens the window of research to me. My discussions and new ideas are always welcomed, and your inputs and brainstormings give me a broad mind about the subject I have been working on. Thanks to you also for your patience in coaching me the academic writing, which develops my rigorous attitude to science. Near the end of my PhD, I appreciate that you support me to visit the national mathematical institute in Brazil that enriches my experience. In addition to study, I am very grateful for your discussions and advices on my future career path. Finally, you have my heartfelt thanks for offering me a postdoc position, to continue my further exploration of the mystery of foam in your group. All these motivate my passion for pursuing research and bring me a lot of joys in exploring unknowns. Like you said, "foam is a small group but there are people who love it". I am very happy to be one of them through you.

Dr. **Sebastien Vincent-Bounnieu**, thanks to you for your support and help in my study. You have been involved in my weekly meeting since the second year of my Ph.D. study. I greatly appreciate your inputs and discussions on my project, especially from the point of practical aspects. In addition, thank you for setting up an internship for me at Shell Global Solutions International. This opportunity brings me first experience of the research in the industry. Your inputs and perspectives would be a valuable reference in my future career.

Prof. **Dan Marchesin**, you have my gratefully acknowledgement for hosting me as a visiting scholar at Instituto Nacional de Matemática Pura e Aplicada (IMPA). It is my great fortune to work with brilliant mathematicians like you and Pablo, which gives me a broader view of multi-disciplinary context of the subject. This journey ends up with two of my most international papers: a student from China, advised by a professor from US in the Netherlands, visits IMPA in Brazil, working on a project in collaboration on with professor from Brazil and a professor from Mexico. I will keep your words in mind "science should be open to everyone", that you fulfill with your own practice all your life.

Dr. **Pablo Castañeda**, my daily supervisor and friend during my visiting of IMPA. I believe I would end up with nowhere without your help during my short journey at IMPA. This collaboration is greatly rewarded. Especially,

ACKNOWLEDGEMENTS

it is very joyful for me to have those discussions with you from two very different worlds, especially when mathematician's mind hits engineer's mind. Thanks also for your kind help in my writing on the work we did.

Prof. **Hans Bruining**, I owe you my deepest thanks for setting up the collaboration between Bill's and Dan's group, so that I could have a chance to visit IMPA. I am impressed by your passion to research. Your help and discussions are greatly appreciated. Especially, you sacrifice number of evenings to teach me those abstract mathematical concepts on the wave curve method. As you said, "mathematicians has a number of ways to confuse engineers" (of course, just a joke). Your explanations in a physical way make my life a lot easier during my visit at IMPA.

Dr. **Janice Rossen**, my sincere thanks to you for your encouragement and caring during my PhD study. Every time we meet, your being such energetic to life motivates me a lot. I appreciate your kinds words that calm me down and relieve some of my stress this period. Thank you also for your generosity about the CDs you give me. When I look back this journey in the future, all these would be my most precious memories.

Dr. **Sian Jones**, thanks for your helpful discussion and support. Whenever I bring up questions or need any help, you are always happy to give any support you can.

Yuhua, my elder brother and life mentor. Since my college, over 11 years have gone at a blink of eyes. Without your help at the moment, I could never have a chance to join the field of petroleum engineering of my big interest. You are one of the few that changes my life path. Although we didn't have much chance to talk, your words always wake me up and let me see the way ahead clearer. I am sincerely thankful for all you did for me.

No experimental work could be possible without the support of technicians in the laboratory. I express my great gratitude to **Michiel, Jens, Ellen, Jolanda, Wim, Karl-Heinz, Joost, Marc and Dirk**. In particular, my thanks to **Michiel** for building up the experimental setup and technical support in training me in operating the setup, and to **Ellen** for your assistance with my CT coreflood experiments.

Sincere thanks to all committee members for your time and efforts in reviewing my thesis, Prof. dr. Peter King, Dr. Voskov, Dr. Vincent-Bonnieu, Prof. dr. Marchesin, Prof. dr. Zitha, Prof. dr. Bakker.

I also thank Lydia, Margot, Marijke, Marlijn and Ralf for their administrative assistance during my Ph.D. study. Every time I write off myself, it is the kind encouragement of my friends that leads me back to the light. The experience I share with all of you over last four years makes the journey an unforgettable memory in my life. I'd like to express my thanks to: **Jiakun, Chris, Eduardo, Rahul, Bander, Rodrigo, Daniel, Matteo, Matei, Rafael, Siavash, Amin, Mojtaba, Ahmed, Swej, Guanqun, Kai, Xiaocong, Yang, Meng, Yue, Yansheng, Quan, Xuefeng, Anna, Siddharth, Jiande, Yang Yang, Yi Guo, Tong Yuan, Youhao, Mohsen, Durgesh, Martijn, Mark, Lidong, Dongxing, Bo Ren, Shuhua, Chao Zhang, Longlong, Sixue, Runhai, Yazhou, Jian Fang, Alexei, Kiarash, and Alexei**. I am very thankful to **Chris** for your help in my culture transition and those precious memories in celebrating new year and going for running. Thanks to **Chris** also for your help with the

AKNOWLEDGEMENTS

Dutch translation of the summary. **Matei**, my sincere thanks goes to you, I cherish those nights with you out for beers, and all the unforgettable moments we share together, SPE black-tie banquet and “running squad”. We still have one deal pending that you would come to visit me in China and I would go to see you in Romania; hope this will happen in the near future. **Yansheng**, many thanks for your host every time I visited Peking, and I am looking forward to our next trip to Great Wall. Our last trip there went back to five years ago; now we may have a different feeling.

Xuhong, my dearest beloved. “1 universe, 9 planets, 204 countries, 809 islands, 7 seas, and I had the privilege of meeting you”. This is more than true for me, to know you in the other corner of the world. Thanks for your accompany and understanding. People say that the world is very small. Since we met, I realize this world is actually very large because there are so many beautiful views we have not seen together. And I am happy to weave a lovely and warm story with you in our following journey wherever it leads us.

Last, but not least, my special thanks to my **parents**. You have done all that you can for me but rarely asked anything from me. Words are never sufficient to express my gratitude. You give me the courage to see the world and strength to face all difficulties ahead. Staying abroad far away from my family back in China, it has been a big pity that I could not accompany you as much as I should. I am very grateful to my **two sisters**, that both have their own happy family now, for their accompany and caring to our parents all the time.

Jinyu

Delft, February 2019

SUMMARY

Foam is a promising enhanced oil recovery (EOR) technology and combines various benefits of other EOR methods, e.g. gas injection, chemical flooding and thermal methods. The engineering application of foam injection into geological formations mainly rests on its unique microstructure and functionality of dramatically reducing gas mobility; this improves greatly the sweep efficiency of gas EOR.

Most oils present in reservoirs destabilize foam. A key to success of foam EOR is the effectiveness of foam for gas-mobility control with oil, i.e. its stability and strength. However, the interaction between foam and oil remains a long-standing challenge. The central goal of our study concerns understanding and modeling the effect of oil on foam over EOR processes. We investigate this subject with a focus on steady-state behavior (Chapters 2 and 3) and transient behavior (Chapters 4, 5 and 6) of foam flow through porous media with oil, from both theory and lab measurements. These findings can be a crucial reference for foam EOR design in subsurface fields.

It is worthwhile to understand first what foam models suggest regarding foam-oil interaction, before conducting coreflood tests that are greatly time-consuming. Current foam models reported in the literature fall into two groups: population-balance (PB) models and implicit-text (IT) models. The development of PB models in representing the foam-oil interactions are still at early stage. The most widely used model for simulating foam EOR processes is the IT foam model STARS, representative of current IT models. The STARS foam model includes two algorithms in delineating the effect of oil on foam: the “wet-foam” algorithm and “dry-out” algorithm. We propose a practical approach to represent the oil effect in both modeling and lab measurements, and show how the effect of oil is represented in each algorithm, in Chapter 2. Specifically, we examine how the introduction of oil shifts the two foam regimes on a pressure-gradient contour plot as a function of gas and water superficial velocities, with respect to oil-related factors. The wet-foam algorithm describes the effect of oil only on the low-quality regime, and dry-out algorithm only the high-quality regime. The specific effects of oil on foam as represented in the two algorithms can help to guide foam EOR simulation and interpretation of lab data.

Steady-state foam corefloods with oil (Chapter 3) demonstrate that the two foam regimes originally found for foam without oil also apply to foam with oil. Most significantly, these two foam regimes with oil can be used as a starting point for deeper exploration of foam dynamics with oil in geological formations. Specifically, the shift in these two foam regimes with oil relative to that without oil suggests oil affects both regimes with a greater impact on the high-quality regime. The STARS foam model shows a good match to our steady-state data, which supports its validity in representing foam EOR with oil. In particular, both wet-foam and dry-out algorithms are needed to fit the data in both regimes. The fitted results reveal that the presence of oil reduces foam stability (which controls the high-quality regime) by increasing the limiting-water saturation S_w^* below which foam collapses abruptly, and weakens foam strength (that dominates the low-quality regime) by decreasing the

reference gas-mobility-reduction factor, $fmmob$. Given the lack of direct data on oil saturations in our steady-state measurements, the quantitative correlation between oil saturation and foam stability (S_w^*) may be subject to some uncertainty. The estimation of oil-related factors in the foam model was never solved before; this caused a large uncertainty in simulating foam EOR. For the purpose of field-scale foam EOR simulation, one can collect data on the two regimes with oil saturations directly measured through imaging techniques. The oil-related factors can be estimated by fitting the STARS foam model to data, to improve the reliability of simulation results.

Transient foam behavior with oil is investigated through three-phase fractional-flow theory (Chapters 4 and 5) and CT corefloods (Chapter 6). Fractional-flow theory, aka the Method of Characteristics (MOC), is a powerful analytical approach that can provide crucial physical insights into a displacement and act as a benchmark to numerical simulation results, in spite of its simplifications. In Chapter 4, we use the wave curve method (WCM) in this theory to find theoretical solutions for the structures and features of foam displacement with oil. The solutions are solved for four representative scenarios with different combinations of injection (J) and initial (I) conditions, that each either allow or kill foam. The desirability of foam-oil-displacement structure is revealed mainly from the mobility ratio of displacing to displaced fluids at the displacement front, the propagation velocity of the foam bank and the time required to recover all oil. More importantly, we find that upon foam injection, oil saturation within an oil bank, if created, never exceeds the upper limit for stable foam $fmoil$; this is also true for an initial state I that kills foam, where waterflood ahead of foam may reduce oil saturation lower than $fmoil$. Conventional finite-difference simulation suggests that oil saturation within the oil bank displaced by foam can be greater than $fmoil$ in some cases. This contradiction reflects a numerical artifact which may result from the pressure or pressure-gradient calculation using neighboring grid blocks. We also analyze the effects of oil-related factors on foam-bank propagation in an oil displacement, to guide the optimization of foam EOR design.

Transient foam dynamics is a result of combined effects of water (stabilizing foam) and oil (destabilizing foam). Both wet-foam and dry-out algorithms in the STARS model predict multiple steady states (as in Chapter 2), a phenomenon that may occur some short distance from the injection well where foam and oil flow co-currently. These multiple steady states fit the same fractional flows of phases, but possess very different foam apparent viscosities (i.e. the inverse of total relative mobility); this means that some injection conditions correspond to multiple possible states with different apparent viscosities. A practical question arising from this phenomenon is which of the multiple possible states makes the displacement at a given initial condition of a reservoir.

We address the issue of multiple steady states using the wave curve method (WCM) and three-phase fractional-flow theory from the perspective of wave propagation (Chapter 5). Our crucial finding is that the wave curve method solves a problem definition different than physical corefloods with specified injection rates of phases. In physical corefloods, starting at time $t_D = 0$, injection state J is injected at position $x_D = 0$ and displaces initial state I present for $0 < x_D \leq 1$. In the WCM, J at $t_D = 0$ is injected from $x_D \ll 0$ and displaces initial state of I present for $0 < x_D$, with J initially present for $x_D \leq 0$. This distinction makes the WCM capable of identifying the unique displacing state among multiple possible states that fit same injected fractional flows. Among these

SUMMARY

multiple possible injection states, only the state that gives a composition path from J to I with only positive wave speeds makes a physically acceptable displacement. Those states that give negative wave velocities along a composition path do not correspond to the physical injection conditions in that the injected state at $x_D = 0$ deviates from the injected fractional flows upon injection, caused by the negative wave velocities. The choice of the displacing state shows a dependence on initial state. More fundamentally, a boundary curve in a ternary saturation space is defined that captures the nature of the displacement on initial state. These findings can assist in predicting the displacing state (with high or low foam apparent viscosity) to particular initial state in an oil reservoir and optimizing the design to achieve desired strong-foam displacement with high apparent viscosity.

To understand transient foam flow with oil in porous media as a function of oil type and saturation, we conduct a CT coreflood study using two representative model oils: hexadecane (C_{16}), benign to foam stability, and a mixture of 80 wt% C_{16} and 20 wt% oleic acid (OA), very harmful to foam stability. To understand the impact of oil type and saturation on foam generation and propagation with each model oil, we examine foam dynamics in two types of injection, i.e. co-injection of surfactant solution and gas to generate foam in situ, and direct injection of pre-generated foam. In-situ-generated foam flow with C_{16} shows transient dynamics similar to that of pre-generated foam and creates an oil bank. The less-harmful oils therefore have similar impacts on foam generation and propagation. Similar behavior could be expected in reservoirs with heavy oils that are normally benign to foam stability. However, in contrast with C_{16} , a model oil possessing 20 wt% OA has very different effects on foam generation and propagation. In particular, the presence of this harmful oil prevents the initial generation of strong foam. Depending on oil type in a given reservoir, this may suggest a risk of failure of foam generation using co-injection of phases or SAG (Surfactant-Alternating-Gas). Pre-generated foam with 20 wt% OA in the model oil shows two stages of propagation, i.e. primary propagation with weak foam that displaces most oil, followed by much stronger foam at lower oil saturation. These findings may help to select candidate oil reservoirs for foam EOR and interpret the transient dynamics of foam, both generated in situ and pre-generated, with oil in geological formations. In addition, our results show that current IT foam models cannot distinguish the very-different results between in-situ-generated foam and pre-generated foam with very harmful oils, which need to be improved to enhance the predictability of IT models in foam EOR simulations.

Microfluidic studies are appealing because flow processes and phase interactions can be visualized directly. The capillary number (N_{ca}), representing a ratio of viscous force to capillary resistance, is commonly used as a criterion for mobilization of non-wetting phase. We show that the conventional N_{ca} definitions originally proposed for 3D geological formations do not work for 2D micromodels given the very different flow geometries between the two types of networks. There is in general no simultaneous multiphase flow in 2D pore networks, and the permeability of micromodels is not controlled by the geometrical factors that control capillary trapping, i.e. pore throats and pore bodies. Direct application of the conventional N_{ca} definitions to microfluidic experiments may lead to misleading prediction of mobilization in geological formations. We propose (in Chapter 7) a new N_{ca} definition for micromodels, based on a force balance across a ganglion trapped in a single pore. The validity of the new N_{ca} definition in describing mobilization of nonwetting phase in micromodels is confirmed using data in the literature collected in micromodels with a variety of pore geometries. The new N_{ca} definition thus can be used as an effective criterion for non-wetting-phase mobilization in microfluidic evaluations.

Finally, based on the findings in our study, we give some recommendations for further investigation of foam-oil interactions in EOR processes (Chapter 8). In particular, it is necessary to check the reliability of IT foam models in predicting transient foam flow using foam-simulation parameters estimated from steady-state data. In addition, all our foam corefloods studies are conducted in water-wet conditions. It is worthwhile to investigate the impact of wettability on foam dynamics, to understand foam flow through oil-wet reservoirs such as carbonates. Miscibility of gas in foam with oil is not examined in our study. Without miscibility, oil interacts with foam through its interaction with aqueous lamellae. With miscibility, oil interacts with both aqueous lamellae and gaseous phases. Further investigation is needed to determine the behavior of foam with oil at miscible conditions.

SAMENVATTING

Schuim is een veelbelovende verbeterde oliewinningstechnologie (Engels, enhanced oil recovery, EOR) en combineert verschillende voordelen van andere EOR-methoden, b.v. gasinjectie, chemische overstroming en thermische methoden. De technische toepassing van schuiminjectie in geologische formaties berust hoofdzakelijk op zijn unieke microstructuur en functionaliteit van het drastisch reduceren van de gasmobiliteit; dit verbetert de sweep-efficiëntie van gas-EOR aanzienlijk.

De meeste oliën die in reservoirs aanwezig zijn, destabiliseren schuim. Een sleutel tot succes van schuim EOR is de effectiviteit van schuim voor gas-mobiliteitscontrole met olie, d.w.z. de stabiliteit en sterkte ervan. De wisselwerking tussen schuim en olie blijft echter een langdurige uitdaging. Het centrale doel van onze studie is het begrijpen en modelleren van het effect van olie op schuim binnen EOR-processen. We onderzoeken dit onderwerp met een focus op steady-state gedrag (Hoofdstukken 2 en 3) en transiënt gedrag (Hoofdstukken 4, 5 en 6) van de schuimstroom door poreuze media met olie, van zowel theorie als laboratoriummetingen. Deze bevindingen kunnen een cruciale referentie zijn voor het schuim-EOR-ontwerp in ondergrondse velden.

Het is de moeite waard om eerst te begrijpen wat schuimmodellen aangeven met betrekking tot schuim-olie interactie, voordat het uitvoeren van coreflood-tests die zeer veel tijd in beslag nemen. De huidige schuimmodellen die in de literatuur worden vermeld, vallen in twee groepen uiteen: populatie-evenwicht (Engels, population balance, PB) -modellen en impliciete textuur (IT) -modellen. De ontwikkeling van PB-modellen voor het modelleren van de schuim-olie-interacties bevindt zich nog in een vroeg stadium. Het meest gebruikte model voor het simuleren van EOR-schuimprocessen is het IT-schuimmodel STARS, dat representatief is voor de huidige IT-modellen. Het STARS-schuimmodel bevat twee algoritmen voor het afbakenen van het effect van olie op schuim: het "natschuim" -algoritme en het "uitdroog" -algoritme. We stellen een praktische benadering voor om het olie-effect in zowel model- als laboratoriummetingen weer te geven en laten zien hoe het effect van olie in elk algoritme wordt gemodelleerd in hoofdstuk 2. Specifiek onderzoeken we hoe de introductie van olie de twee schuimregimes op een drukgradiënt contourplot verschuift als een functie van gas- en watersuperficiële snelheden, met betrekking tot oliegerelateerde factoren. Het natte-schuim-algoritme beschrijft het effect van alleen olie op het lage kwaliteitsregime het dry-out-algoritme alleen op het hoge kwaliteitsregime. De specifieke effecten van olie op schuim, zoals weergegeven in de twee algoritmen, kan helpen om schuim EOR-simulatie en interpretatie van laboratoriumgegevens te begeleiden.

Steady-state schuimcorefloods met olie (hoofdstuk 3) tonen aan dat de twee schuimregimes die oorspronkelijk werden gevonden voor schuim zonder olie ook van toepassing zijn op schuim met olie. Het belangrijkste is dat deze twee schuimregimes met olie kunnen worden gebruikt als een startpunt voor een diepere verkenning van schuimdynamica met olie in geologische formaties. Met name de verschuiving in deze twee schuimregimes met olie ten opzichte van die zonder olie suggereert dat olie beide regimes beïnvloedt met een grotere impact op het

hoge kwaliteitsregime. Het STARS-schuimmodel komt goed overeen met onze steady-state-gegevens, wat de validiteit ervan in de voorstelling van schuim-EOR met olie ondersteunt. Zowel natschuim- als dry-out-algoritmen zijn nodig om de gegevens in beide regimes te fitten. De gefitte resultaten tonen aan dat de aanwezigheid van olie de schuimstabiliteit vermindert (die het hoge kwaliteitsregime regelt) door de verzadiging van de beperkende waterverzadiging S_w^* te verhogen waaronder schuim abrupt instort, en de schuimsterkte (die het lage kwaliteitsregime domineert) verzwakt door het verminderen van de referentie gas-mobiliteitsreductiefactor, f_{mob} . Gezien het gebrek aan directe gegevens over olieverzadiging in onze steady-state metingen, kan de kwantitatieve correlatie tussen olieverzadiging en schuimstabiliteit (S_w^*) mogelijk enige mate van onzekerheid bevatten. De schatting van olie-gerelateerde factoren in het schuimmodel is nooit eerder opgelost; dit veroorzaakte een grote onzekerheid bij het simuleren van schuim EOR. Ten behoeve van veldschaal-EOR-simulatie kan men gegevens over de twee regimes verzamelen met olieverzadigingen die direct worden gemeten door middel van beeldvormingstechnieken. De olie-gerelateerde factoren kunnen worden geschat door de parameters van het STARS-schuimmodel te fitten aan gegevens om de betrouwbaarheid van simulatieresultaten te verbeteren.

Transiënt schuimgedrag met olie wordt onderzocht door driefase fractionele stromingstheorie (Hoofdstukken 4 en 5) en CT corefloods (Hoofdstuk 6). Fractionele stromingstheorie, oftewel de Methode van Karakteristieken (MOC), is een krachtige analytische benadering die cruciale fysieke inzichten in een verplaatsingsproces kan bieden en die, ondanks de vereenvoudigingen, een maatstaf is voor numerieke simulatieresultaten. In Hoofdstuk 4 gebruiken we de wave curve-methode (WCM) binnen deze theorie om theoretische oplossingen te vinden voor de structuren en kenmerken van schuimverplaatsing met olie. De oplossingen zijn opgelost voor vier representatieve scenario's met verschillende combinaties van injectie- (J) en initiële (I) voorwaarden, die elk schuim toelaten of vernietigen. De wenselijkheid van schuim-olie-verplaatsingsstructuur wordt voornamelijk bepaald door de mobiliteitsverhouding tussen de verplaatsende en de verplaatste vloeistoffen aan het verplaatsingsfront, de voortplantingssnelheid van de schuimbank en de tijd die nodig is om alle olie te winnen. Wat nog belangrijker is, is dat na het injecteren van schuim de olieverzadiging in een oliebank, indien gecreëerd, nooit de bovengrens overschrijdt voor een stabiele waarde van f_{moil} ; dit geldt ook voor een beginstadium I dat schuim vernietigt, waarbij een watervloed vóór de schuiminjectie de olieverzadiging die lager is dan f_{moil} kan verminderen. Conventionele eindige-verschil-simulatie geeft aan dat de olieverzadiging in de oliebank die door schuim wordt verplaatst, in sommige gevallen groter kan zijn dan f_{moil} . Deze tegenspraak weerspiegelt een numeriek artefact dat kan resulteren uit de druk- of drukgradiëntberekening met behulp van aangrenzende rasterblokken. We analyseren ook de effecten van oliegerelateerde factoren op de verspreiding van schuim in een olieoverplaatsingsproces om de optimalisatie van het schuim-EOR-ontwerp te begeleiden.

Transiënte schuimdynamiek is het resultaat van gecombineerde effecten van water (dat schuim stabiliseert) en olie (dat destabiliserend werkt op schuim). Zowel natschuim- als uitdroogalgoritmen in het STARS-model voorspellen meerdere stabiele toestanden (zoals in hoofdstuk 2), een verschijnsel dat zich binnen korte afstand van de injectieput kan voordoen, waar schuim en olie gelijktijdig vloeien. Deze meervoudige stationaire toestanden passen in dezelfde fractionele stroming van fasen, maar bezitten zeer verschillende schijnbare viscositeiten van het schuim (dat wil zeggen het omgekeerde van de totale relatieve mobiliteit); dit betekent dat

sommige injectiecondities overeenkomen met meerdere mogelijke toestanden met verschillende schijnbare viscositeiten. Een praktische vraag die voortkomt uit dit fenomeen is welke van de meerdere mogelijke toestanden de verplaatsing maakt bij een gegeven initiële toestand van een reservoir.

We behandelen de kwestie van meerdere stabiele toestanden met behulp van de golfcurve-methode (WCM) en driefasige fractionele stromingstheorie vanuit het perspectief van golfvoortplanting (hoofdstuk 5). Onze cruciale bevinding is dat de methode van de golfcurve een probleemdefinitie oplost die anders is dan fysieke corefloods met gespecificeerde injectiesnelheden van fasen. Bij fysieke corefloods, beginnend op tijdstip $t_D = 0$, wordt injectie-toestand J geïnjecteerd op positie $x_D = 0$ en verdringt de aanvankelijke toestand I die aanwezig is voor $0 < x_D \leq 1$. In de WCM wordt J geïnjecteerd op tijdstip $t_D = 0$ uit $x_D \ll 0$ en vervangt de initiële toestand van I die aanwezig is voor $0 < x_D$, met J initieel aanwezig voor $x_D \leq 0$. Dit onderscheid maakt de WCM in staat om de unieke verdringingstoestand te identificeren binnen de meerdere mogelijke toestanden die op dezelfde geïnjecteerde fractionele stromen passen. Van deze meerdere mogelijke injectietoestanden, maakt alleen de toestand die een pad geeft van J naar I met alleen positieve golfsnelheden een fysiek acceptabele verplaatsing. Die toestanden die negatieve golfsnelheden langs een pad geven komen niet overeen met de fysieke injectieomstandigheden doordat de geïnjecteerde toestand bij $x_D = 0$ afwijkt van de geïnjecteerde fractionele stromen na injectie, die veroorzaakt wordt door de negatieve golfsnelheden. De keuze van de verplaatsingstoestand toont een afhankelijkheid van de initiële toestand. Meer fundamenteel wordt een grenscurve in een ternaire saturatie-ruimte gedefinieerd die de aard van de verplaatsing in de initiële toestand vastlegt. Deze bevindingen kunnen helpen bij het voorspellen van de verplaatsingstoestand (met hoge of lage schijnbare viscositeit van het schuim) naar een bepaalde begintoestand in een oliereservoir en het optimaliseren van het ontwerp om gewenste sterke schuimvervanging met hoge schijnbare viscositeit te bereiken.

Om de transiënte schuimstroming met olie in poreuze media te begrijpen als een functie van het olietype en de verzadiging, voeren we een CT-onderzoek uit met behulp van twee representatieve modeloliën: hexadecaan (C_{16}), dat goed is voor schuimstabiliteit en een mengsel van 80 gew% C_{16} en 20 gew.% oliezuur (Engels oleic acid, OA), wat zeer schadelijk is voor de schuimstabiliteit. Om de impact van olietype en verzadiging op schuimvorming en -propagatie met elke modelolie te begrijpen, onderzoeken we de schuimdynamica binnen twee soorten injectie, namelijk co-injectie van een oplossing van oppervlakte-actieve stof en gas om in situ schuim te genereren, en directe injectie van pre-gegenereerd schuim. De in-situ gegenereerde schuimstroming met C_{16} vertoont transiënte dynamica die vergelijkbaar is met die van pre-gegenereerd schuim en creëert een oliebank. De minder schadelijke oliën hebben daarom vergelijkbare effecten op de schuimvorming en -propagatie. Vergelijkbaar gedrag kan worden verwacht in reservoirs met zware oliën die normaal goedaardig zijn voor schuimstabiliteit. In tegenstelling tot C_{16} heeft een modelolie met 20 gew.% OA echter zeer verschillende effecten op schuimvorming en -propagatie. In het bijzonder voorkomt de aanwezigheid van deze schadelijke olie de eerste generatie van sterk schuim. Afhankelijk van het olietype in een bepaald reservoir, kan dit wijzen op een risico van falen van de schuimvorming bij co-injectie of SAG (Surfactant-Alternating-Gas) processen. Pre-gegenereerd schuim met 20 gew.% OA in de modelolie vertoont twee stadia van propagatie, d.w.z. primaire voortplanting met zwak schuim dat de meeste olie verdringt, gevolgd door veel sterker schuim bij lagere

olieverzadiging. Deze bevindingen kunnen helpen bij het selecteren van kandidaat-oliereservoirs voor schuim-EOR en voor het interpreteren van de tijdelijke dynamica van schuim, zowel bij in-situ gegenereerd als bij pre-gegenereerd schuim, met olie in geologische formaties. Bovendien laten onze resultaten zien dat de huidige IT-schuimmodellen niet de zeer verschillende resultaten kunnen onderscheiden tussen in-situ gegenereerd schuim en pre-gegenereerd schuim met zeer schadelijke oliën, die moeten worden verbeterd om de voorspelbaarheid van IT-modellen in schuim EOR te verbeteren simulaties.

Microfluidische studies zijn aantrekkelijk omdat stroomprocessen en fase-interacties direct kunnen worden gevisualiseerd. Capillair getal (*Nca*), dat een verhouding van viskeuze kracht tot capillaire weerstand weergeeft, wordt gewoonlijk gebruikt als een criterium voor mobilisatie van de niet-bevochtigende fase. We laten zien dat de conventionele *Nca*-definities die oorspronkelijk werden voorgesteld voor 3D-geologische formaties niet werken voor 2D-micromodellen, gezien de zeer verschillende stromingsgeometrieën tussen de twee soorten netwerken. Er is in het algemeen geen simultane multifasestroming in 2D-porie-netwerken en de permeabiliteit van micromodellen wordt niet geregeld door de geometrische factoren die de capillaire vangst regelen, d.w.z. de smalste en breedste doorgangen van de poriën. Directe toepassing van de conventionele *Nca*-definities op microfluidische experimenten kan leiden tot een misleidende voorspelling van mobilisatie in geologische formaties. We stellen voor (in hoofdstuk 7) een nieuwe *Nca*-definitie voor micromodellen, gebaseerd op een krachtbalans over een ganglion dat is gevangen in een enkele porie. De validiteit van de nieuwe *Nca*-definitie bij het beschrijven van de mobilisatie van de niet-bevochtigende fase in microfluidische studies wordt bevestigd met behulp van gegevens in de literatuur die zijn verzameld in micromodellen met een verscheidenheid aan poriëngeometrieën. De nieuwe *Nca*-definitie kan dus worden gebruikt als een effectief criterium voor mobilisatie van de niet-bevochtigende fase in microfluidische evaluaties.

Ten slotte geven we, op basis van de bevindingen in onze studie, enkele aanbevelingen voor verder onderzoek van schuim-olie interacties in EOR-processen (Hoofdstuk 8). In het bijzonder is het noodzakelijk om de betrouwbaarheid van IT-schuimmodellen te controleren bij het voorspellen van een transiënte schuimstroming met behulp van schuimsimulatieparameters geschat op basis van steady-state gegevens. Bovendien worden al onze schuim-corefloods uitgevoerd in omstandigheden waar water de bevochtigende fase is. Het loont de moeite om de impact van de bevochtigbaarheid op de schuimdynamiek te onderzoeken, om de schuimstroom door olie-bevochtigende reservoirs zoals carbonaten te begrijpen. Mengbaarheid van gas in schuim met olie wordt niet onderzocht in ons onderzoek. Zonder mengbaarheid werkt olie samen met schuim door zijn interactie met waterige lamellen. Met mengbaarheid werkt olie samen met zowel waterige lamellen en gasvormige fasen. Verder onderzoek is nodig om het gedrag van schuim met olie bij mengbare omstandigheden te bepalen.